Use of remote sensing to assess supra-glacial lake depths on the Greenland Ice Sheet.

Cordero-Llana, Laura

Swansea University
Prifysgol Abertawe

Use of remote sensing to assess supra-glacial lake depths on the Greenland Ice Sheet

Laura Cordero-Llana

Submitted in fulfilment of the requirements for the degree of Doctor of Philosophy

Swansea University
Department of Geography

November, 2012.

ProQuest LLC.
789 East Eisenhower Parkway
P.O. Box 1346
Ann Arbor, MI 48106 – 1346

Abstract

The influence that supra-glacial lakes have had in the recent mass loss at the margins of the Greenland ice sheet has been widely studied. Lakes can drain to the base of a glacier, lubricating the bed, and enhancing acceleration of the glacier and hence ice thinning. Recent studies suggested that melt extent is not directly linked to the dynamic loss but it has been proven to be linked to peak summer speed ups of the ice sheet front.

Large volumes of water are necessary to propagate cracks to the glacial bed via hydrofractures. Hydrological models showed that lakes above a critical volume can supply the necessary water for this process, so the ability to measure water depth in lakes remotely is important to study these processes. The aim of this thesis was to test the current models used for water depth calculations based on the optical properties of water. An optimisation model to estimate water depths was developed. Atmospherically-corrected data from ASTER and MODIS were used as an input to the water reflectance model. As a reference dataset, ICESat measurements were used to obtain lake geometries over empty lakes. Differences between modelled and reference depths are used in a minimisation model to obtain parameters for the water-reflectance model, yielding optimised lake depth estimates. The key contribution of this research was the development of a Monte Carlo simulation. This method allows the quantification of uncertainties in water depth and hence water volume, for the first time. This robust analysis provided better understanding of the sensitivity of the model to the input parameters. There is scope to improve current models of depth estimations if more extensive field observations are done.

Acknowledgements

After spending the last months thinking about all the people I was going to thank for just being there, it turns out that I just want to print and that the detailed acknowledgements will have to be shorter.

I would like to start with Tavi Murray, Kilian Scharrer and Nick Selmes for being very supportive and encouraging and for taking the role of supervising in a very close way. Thanks Tavi for teaching me the big picture of glaciology and for keeping the interest. Thanks Kilian for being full of ideas, crazy or not they were there and for bringing always the funny side of problems. Sorry Tavi and Kilian because, even though you were my first two supervisors, I have to especially thank Nick for just being there ALL the times, even if it was on Skype. I personally don't think I would have being able to finish without your help and support. I do not have enough words to say thank you. Thank you Adam Booth for providing the idea of using the Monte Carlo simulation in this thesis, and for all the help you gave me. I thank FUNDESFOR and the Leverhulme Trust for funding my PhD.

Especial thanks to Steve Shaw for being the most patient and efficient IT person I have never met. I will always be infinitely grateful to the Geography Department (Biology and Aquaculture too, apart from the smell) for being such a great place to work. The number of people that I feel close or that have made my life better is too big to list here. Even if I "belonged" to the Glaciology Group, I have to say that always felt part of all, or you always made me feel part of all.

I do not know how many people I am going to forget now, but I will try. Thank you Adam for more than words can say, even if we are apart now, I hope we can get closer again. Sarah Thompson and Anna Hughes...how many memories and more to come, just thank you for being there, for the swimming, for the spa, for the cake making, for the trips, for all. Thank you Nick again and Pete Abbott for being the best neighbours ever, and amazing friends. Tim James (guapo), what can I say, you are the perfect combination of a teenager-adult I know, even if you haven't been involved in my PhD directly I feel your presence has helped me being happy (BFF). Cristina Santín, nena I don't know what I would have done without you, my half Asturian friend, thank you for being there, for the gossip, for being such a good person in the bad moments and being even better in the goods ones. Thank you also to Carlos and María Cabo (my disable lesbian girlfriend). Sara Barrento, Laurance Dyke, Yoann Drocrout, Kilian Scharrer and Tatjana Enzinger, Ed Pope, Mary Gagen, Claudine, Vicky, Per and Mariane...who else? I don't know but you are such a sick group of people, I would never forget you. Benny and Mariluz thank you for making the beginning so amazing. Mariluz mi flor.

In the Asturian side, thank you Lucía Abello, my best friend since we were 8 years old and "lo que nos queda", I wish you were here so many times. Laura Marco thank you for being such a good person and better friend. Sara López, what can I say? I wish you were with us, I think having you in our lives is better than not having you. I hope one day you come back to us. Rober y Carmen I love you almost as much as I love you wife and your mum. Pablo el altu, Chiri, Diego (mi sol), Tati, Sonia, Xoel,...you will always be there.

Mis almejas (my clams) Raquel, Rosa, Cruz, Crispi, Mónica and Uca, for the university years and for the post-university years. I have the best memories of those years fighting for the Physics degree, all together, and all that came after, for thousands of moments with you in the future. Also thank you Jorge, Zama, Chus, Berto, Miguel y Fonsete you are the best paisanos ever.

Finally to my family, I could not be more lucky of having you all, I could not name

all of you here but I will try, Esthercita, Irene, Cecilia, Seni, Delia, Toni, Sergio, Natalia, Goyi, Ana, Cristal, Guillermo, Nesi, Jose, Erica, Nadia and the little ones. Especial thanks to my parents for all, even if we are not the most open family talking about feelings, everyday I am away I feel closer to you. Thanks even more to my brother Óscar, who has make my life better, I could not imaging not having you close.

I dedicate this thesis to my last grandparents, even if they decided to leave just before I finished, güelito y güelita I wish I could have enjoyed you more.

Agradecimientos

Después de pasar los últimos meses pensando en toda la gente que iba a agradecer por estar ahí, resulta que ahora solamente quiero imprimir y que los agradecimientos detallados tendrán que ser más cortos.

Quisiera empezar por Tavi Murray, Kilian Scharrer y Nick Selmes por ser de gran ayuda y muy alentadores y por ejercer el papel de supervisores de una manera muy cercana. Gracias Tavi por enseñarme glaciología y por mostrar tanto interés. Gracias Kilian por tantas ideas, locas o no siempre las tenías y por sacar el lado cómico de los problemas. Tavi y Kilian lo siento pero, aunque fuisteis mis primeros supervisores, tengo que agradecerle especialmente a Nick por estar ahí SIEMPRE, incluso por Skype. Personalmente no creo que hubiese podido acabar sin tu ayuda y apoyo. No tengo suficientes palabras para agradecértelo. Gracias Adam Booth por tener la idea de aplicar la simulació de Monte Carlo en esta tesis, y por toda la ayuda que me diste. Gracias a FUNDESFOR y The Leverhulme Trust por subvencionar mi doctorado.

Agradezco especialmemnte a Steve Shaw por ser el ténico informático más paciente y eficiente que conozco. Siempre le estaré agradecida al Departamento de Geografía (Biología y Acuacultura también, a pesar del olor) por ser un lugar tan especial en el que trabajar. El número de personas con las que me siento cerca o que han hecho mi vida mejor es demasiado grande como para listarlo aquí. A pesar de "pertenecer" al Grupo de Glaciología, tengo que decir que siempre me he sentido parte de todos, o vosotros siempre me hicisteis sentir parte vuestra.

No sé cuánta gente voy a olvidar ahora. Gracias Adam por todo, aunque ahora estemos lejos, espero que podamos acercarnos otra vez. Sarah Thompson y Anna Hughes...cuántos recuerdos y más que vendrán, gracias por estar ahí, por la piscina, por el spa, por las tartas, por los viajes, por todo. Gracias otra vez Nick y Pete Abbott por ser los mejores vecinos del mundo y mejores amigos. Tim James (guapo), qué puedo decir?, eres la combinación más perfecta de adolescente-adulto que conozco, aunque no fueses parte de mi tesis, siento que tu presencia me ayudó a ser feliz (BBF). Cristina Santín, nena no sé qué hubiera hecho sin tí, mi amiga mitad asturiana, gracias por estar ahí, por los cotilleos, por ser una persona tan especial en los malos momentos e incluso mejor en los buenos. Gracias Carlos y María Cabo (mi novia minusválida). Sara Barrento, Laurance Dyke, Yoann Drocrout, Kilian Scharrer y Tatjana Enzinger, Ed Pope, Mary Gagen, Claudine, Vicky, Per y Mariane...quién más? No lo sé pero sois un grupo muy "sick" de gente. Benny y Mariluz, gracias por hacer el principio tan especial. Mariluz mi flor.

En la parte asturiana, gracias Luía Abello, mi mejor amiga desde los 8, "y lo que nos queda", ojalá estuvieras aquí. Laura Marco gracias por ser una persona tan buena y mejor amiga. Sara López, qué puedo decir? Desearía que estuvieras con nosotras, creo que tenerte en nuestras vidas es mejor que no tenerte. Espero que algún día vuelvas. Rober y Carmen os quiero casi tanto como quiero a la tu muyer y a tu mamá. Pablo el altu, Chiri, Diego (mi sol), Tati, Sonia, Xoel,...siempre estaréis ah.

Mis almejas: Raquel, Rosa, Cruz, Crispi, Mónica y Uca, por los años de universidad y por los de después. Tengo los mejores recuerdos de esos años luchando por el título de física, todas juntas, y todo lo que vino después, por cientos de momentos que nos quedan juntas. Gracias también a Jorge, Zama, Chus, Berto, Miguel y Fonsete, sois los mejores paisanos del mundo.

Finalmente a mi familia, no podría ser más afortunada de teneros a todos. No puedo nombraros a todos, pero voy a intentarlo: Esthercita, Irene, Cecilia, Seni, Delia, Toni, Sergio, Natalia, Goyi, Ana, Cristal, Guillermo, Nesi, Jose, Erica, Nadia y los peques. Gracias a mis padres por todo, aunque no seamos la familia más abierta

del mundo, cada día que estoy lejos me siento más cerca de vosotros. Gracias a mi hermano Óscar, quien ha hecho mi vida mejor, y no podría imaginar no tenerte cerca.

Dedico esta tesis a mis últimos abuelos, aunque decidieran marcharse justo antes de que acabara, guüelito y güelita ojalá os hubiera disfrutado más.

Contents

List of Figures

List of Tables

List of Symbols

A_d	Bed albedo
a_w	Absorption coefficient for pure water
b_m^{fw}	Backscattering coefficient for molecular scattering in freshwater
d_{max}	Diameter maximum
d_{min}	Diameter minimum
$\dot{\epsilon}_{xx}$	Longitudinal strain rate
D_u	Distribution factor for upwelling irradiance
g	Effective attenuation coefficient
k	Electrodynamic absorption coefficient
K_d	Diffuse attenuation coefficient for downwelling light
L	Water-leaving spectral radiance
$L(0, \lambda)$	Spectral radiance at zero depth

λ	Wavelength
L_*^E	Elastic scattering
L_*^I	Inelastic scattering
ρ_i	Density of ice
R_∞	Reflectance of optically deep water
R_w	Reflectance at the water surface
V	Volume
V_{ICESat}	Volume derived from ICESat
V_{optim}	Volume derived from the optimisation model
V_{total}	Volume total
z	Lake depth
Z_{ASTER}	Depth derived from ASTER
Z_{Best}	Depth derived from the minimisation model
Z_{ICESat}	ICESat depth
Z_{MODIS}	Depth derived from MODIS
$Z_{optimised}$	Depth derived from the optimisation model

List of Abbreviations

AOP	Apparent Optical Properties
ARSF	Airborne Research and Survey Facility
ASTER	Advanced Spaceborne Thermal Emission and Reflection Radiometer
AVHRR	Advanced Very High Resolution Radiometer
AZGCORR	Geocorrection software for hyperspectral data
BRDF	Bidirectional Reflectance Distribution Function
CASI	Compact Airborne Imaging Spectrometer
CCD	Charge Coupled Device
DAO	Data Assimilation office
DEM	digital elevation model
EGM2008	Earth Gravitational Model
Envisat	Environmental Satellite

EOS	Earth Observing System
EROS	Earth Resources Observation and Science
ERS	European Remote Sensing
ETM	Enhanced Thematic Mapper
FWHM	Full Width Half Maximum
FOV	field of view
GDEM	Global Digital Elevation Model
GLAS	Geoscience Laser Altimeter System
GOT99.2	Global Ocean Tide Model
GPS	Global Positioning System
GRACE	Gravity Recovery and Climate Experiment
GrIS	Greenland Ice Sheet
HDF	Hierarchical Data Format
IKONOS	Earth observation satellite
ICESat	Ice, Cloud, and land Elevation Satellite
IOP	Inherent Optical Properties
IQR	Interquartile Range

JAROS	Japan Resources Observation System Organization
LEFM	Linear Elastic Fracture Mechanics model
LIDAR	Light Detection And Ranging
LPDAAC	Land Processes Distributed Active Archive Centre
LUT	look-up table
MISR	Multi-angle Imaging SpectroRadiometer
MODIS	Moderate Resolution Imaging Spectroradiometer
NASA	National Aeronautics and Space Administration
NERC	Natural Environment Research Council
NCEP	National Centres for Environmental Prediction
NE	North East
NGA	National Geospatial-Intelligence Agency
NSIDC	National Snow and Ice Data Center
NW	North West
PAD	precision attitude determination
PDD	positive degree day model
POD	precision orbit determination

QA	Quality Assurance
RMSE	Root Mean Square Error
RSS	Root Sum Squares
RTC	radiative transfer code
RTE	radiative transfer equation
SE	South East
SPOT	System Pour l'Observation de la Terre
SSE	Sum of Squared Error
SW	South West
SWIR	Shortwave Infrared Radiometer
TIR	Thermal Infrared Radiometer
TM	Thematic Mapper
TOA	Top of Atmosphere
TOF	Time-of-flight
TOMS	Total Ozone Mapping Spectrometer
USGS	United States Geological Survey
UTC	Coordinated Universal Time

UTM	Universal Transverse Mercator
VNIR	Visible Near Infrared Radiometer
WGS	World Geodetic System

Chapter 1

Introduction and aims

In this first chapter a brief introduction to the thesis is presented, showing the motivation for it, the objectives that are achieved and how the thesis is structured.

1.1 Motivation

The observed increase in mass loss from the Greenland ice sheet (GrIS) during the last decade (van de Wal *et al.*, 2008; Velicogna, 2009; Rignot and Kanagaratnam, 2006; Schrama and Wouters, 2011) is of great concern for the future contribution of the GrIS to sea level. In the GrIS the majority of ice lying on bedrock is above sea level, which means that if completely melted, sea level would rise a global average of 7.3 m (Lemke *et al.*, 2007). Previously it was thought that ice sheets took thousands of years to respond to an external forcing, hence the recent dramatic changes occurred mainly on the outlet glaciers were not predicted by previous models (Bamber *et al.*, 2007).

Understanding what are the mechanisms that are driving the recent mass loss is an important task; many studies have shown that glacier dynamics, melting and ocean-ice sheet interactions play and important role in the mass balance. Quantify-

ing these mechanisms over the entire GrIS is an unrealistic task; thus remote sensing techniques present a significant progress to monitor the ice sheet.

It is thought that supra-glacial melt-water lakes on the surface of the GrIS play an important role on the ice sheet dynamics by enhanced lubrication of the ice-bedrock interface (Krawczynski *et al.*, 2009; Das *et al.*, 2008; Lüthje *et al.*, 2006). Melt-water lakes are a common feature on the surface of the GrIS, which form seasonally (Box and Ski, 2007; McMillan *et al.*, 2007) and specifically in the ablation zone in topographic depressions. It seems that increasing melt-water penetration to the base of a glacier increases sliding velocities as a result of raising water pressure near the bed (van de Wal *et al.*, 2008). However, a study of drainage events across the GrIS, showed an inverse relationship between drainage events and the areas where increase mass loss was detected by the Gravity Recovery and Climate Experiment (GRACE) and the Ice, Cloud, and land Elevation Satellite (ICESat) (Selmes *et al.*, 2011). Surface melt-water causes a positive feedback on ice velocity, although is thought to be a seasonal effect that could have a minimal repercussion for the response of the ice sheet to climate warming (van de Wal *et al.*, 2008; Sundal *et al.*, 2011). Until the influence of changes in melting on the velocity of the ice sheet are completely established, the response of Greenland to the climate warming is still unclear. Therefore is still important to quantify the melt-water stored on the surface of the GrIS as a potential for lake drainage events and also for annual evolution of melt-lake extent across the ice sheet. Furthermore, the estimation of the volume of individual lakes can help assessing the potential formation of hydrofractures and hence drainage to the bed (Krawczynski *et al.*, 2009). This thesis investigates the application of different types of remote sensing imagery to derive a volume estimate of melt-water stored on the surface of the GrIS.

1.2 Aim and objectives

The aim of this thesis is to estimate the volume of melt-water stored in supra-glacial lakes on Greenland, using a combination of remote sensing platforms. This is achieved with the following objectives:

- Use of an archive of supra-glacial lakes that provides the annual maximum area of melt extent over the period of 2005-2009, to locate the lakes.
- Use of ICESat altimetry measurements of empty lakes, to assess the accuracy of the water reflectance model applied to the Advanced Spaceborne Thermal Emission and Reflection Radiometer (ASTER) imagery in deriving melt-lake depth.
- Optimising the water reflectance model, to derive the best set of the optical parameters for the ASTER imagery.
- Testing different spectral bands of ASTER imagery, to select the best fit with respect to ICESat depth measurements.
- Applying the optimised set of parameters to the Moderate Resolution Imaging Spectroradiometer (MODIS) archive, to up scale the depth estimates to catchment (or larger) area.

1.3 Structure of the thesis

The thesis is divided in nine chapters. In the following sections a brief description of each chapter is presented.

1.3.1 Introductory chapters

Chapter 2 presents the motivation for this glaciological project, showing previous studies that emphasised the importance of a quantification of the volume of melt-water stored on the surface of Greenland ice sheet.

Chapter 3 shows the principles of the different remote sensing platforms used in this thesis, MODIS, ASTER and ICESat. Chapter 3 also shows the advantages and disadvantages that each of the satellites in the application to melt-water depth estimates; including previous results obtained from optical imagery as a tool to infer water depth, based on the optical properties of fresh water.

1.3.2 Methods chapter

Chapter 4 introduces the basis of the water reflectance model and how each of the parameters driving the model are obtained based on the optical properties of water and depending of the wavelength. It also explains how the ICESat depths are used to validate the model, including a description of the Monte Carlo simulation, which is used to solve the radiative equation and assess its uncertainties.

1.3.3 Results chapters

Chapter 5 presents melt-water depth estimations obtained from the water reflectance model applied to ASTER imagery. Following this, the optimisation results after applying a minimisation model between ASTER derived depths with ICESat measurements are presented, which will be compared with the initial results and then from that uncertainties will be discussed. From there a global set of parameters will be obtained from the mean of all the optimised set of parameters of each lake.

Chapter 6 follows the results obtained and using the global set of parameters, a volume estimate for each lake is presented a compared with the lake volume estimated derived from the model before the optimisation. It also explores the application of MODIS imagery to up scale the model to at least regional level (South West Greenland).

Chapter 7 introduces the potential of applying the water reflectance model on water-filled crevasse depth estimations, using a hyperspectral sensor, the Compact Airborne Imaging Spectrometer (CASI).

1.3.4 Discussion and conclusion chapters

In Chapter 8 a detailed examination of the optimisation method is presented, compared with previous published studies. Major limitations are also discussed, separated into instrument spatial/temporal resolutions and the water reflectance assumptions.

Chapter 9 concludes this thesis, summarising the results and the discussion. It also present how future work could improve this method.

Chapter 2

Supra-glacial lakes in Greenland

2.1 Introduction

The increasing mass-loss from the margins of the Greenland ice sheet (GrIS) during the last decade, which has been broadly reported (van de Wal *et al.*, 2008; Velicogna, 2009; Rignot and Kanagaratnam, 2006; Schrama and Wouters, 2011; Sørensen *et al.*, 2011; Schrama *et al.*, 2011) was introduced in the previous chapter, where the need for a better understanding of the processes governing the ice sheet mass balance, since the mass balance is a key control of sea level (Thomas *et al.*, 2008) was highlighted. Changes observed at the margins of the GrIS (see Figure 2.1) show that dynamic response to higher temperatures could have more importance in the mass balance of the ice sheet than previously thought (Alley *et al.*, 2005a). A combination of mass balance estimates of the Greenland ice sheet since 1958 to present show high correlation ($R^2 = 0.83$) between surface mass balance and ice discharge (Rignot *et al.*, 2008).

Ice sheet models developed to simulate future of sea level seldom include surface melt-water as an influence on ice dynamics (Das *et al.*, 2008). The main uncertainties are the time-scales and routes through which surface melt-water gets to the ice

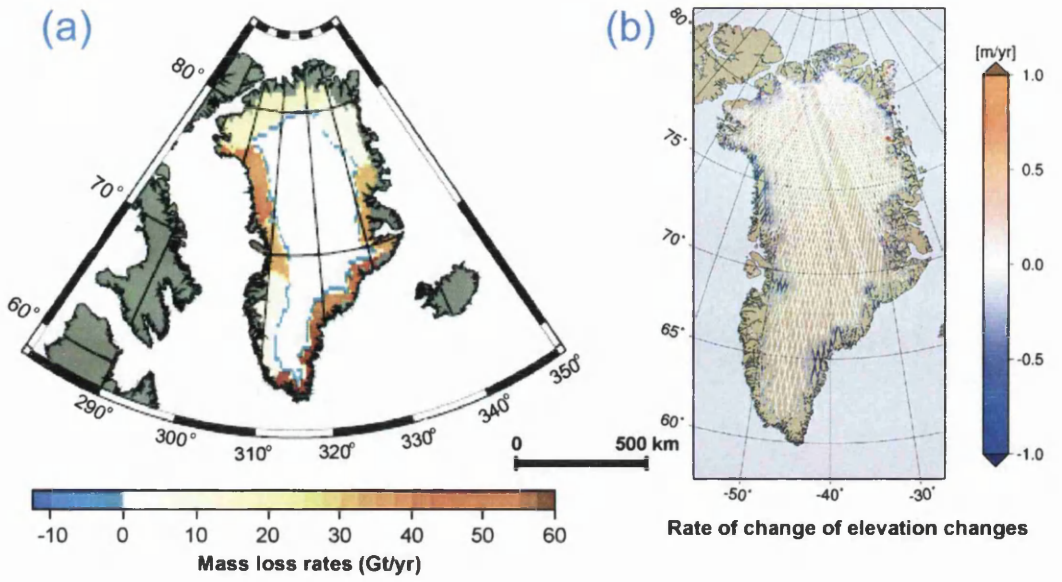

Figure 2.1: Two examples showing the observed mass loss on the GrIS from two different satellites; (a) Mass loss rates between 2003-2010 derived from the Gravity Recovery and Climate Experiment (GRACE), where the red in the colour bar corresponds to negative mass change rates (from Schrama *et al.* (2011)); (b) Rate of elevation changes derived from the Ice, Cloud and land Elevation Satellite (ICESat) measurements, and corrected for elevation changes caused by firn compaction, vertical bedrock movement and ICESat intercampaign bias, over the period 2003-2009 (from Sasgen *et al.* (2012)).

sheet base and the effect on basal motion. It has been shown that outlet glaciers and ice streams can present faster response than expected, therefore previous models that only included the slow movements of the ice and ice shelves, ignoring these rapid dynamic events are not accurate (Lemke *et al.*, 2007).

It has been suggested that supra-glacial melt-water stored in lakes on the surface of the GrIS play an important role in ice sheet dynamics by enhanced lubrication of the ice-bedrock interface (Krawczynski *et al.*, 2009; Das *et al.*, 2008; Lüthje *et al.*, 2006), which was first hypothesised for drainage events in Greenland by Zwally *et al.* (2002a). Melt-water lakes are a common feature on the surface of the GrIS, which form seasonally (Box and Ski, 2007; McMillan *et al.*, 2007; Selmes *et al.*, 2011) specifically in the ablation zone in topographic depressions. In this chapter, field observations and previous models trying to understand the implications of lake

drainage and melt-water stored on the surface of the GrIS on the ice sheet mass balance are introduced.

Section 2.2 introduces the main characteristics of the hydrological system of the GrIS.

Section 2.3 describes supra-glacial lakes on the GrIS, how they form and drain as well as well as field observations of lakes on the GrIS. Then Section 2.4 introduces the process by which the water reaches the bed. Different models applied to determine how hydrofractures develop are also presented in this section.

Different techniques are used to estimate lake depth, area and volume, which are introduced in Section 2.5, although a detailed description of the techniques will be introduced in Chapter 4. Also the results obtained from the different studies are introduced together with their implications.

2.2 Hydrology of the GrIS

The GrIS flows outward from its interior through a combination of internal deformation and basal sliding, losing mass around its edges through melt-water runoff and iceberg calving (Das *et al.*, 2008). Figure 2.2 summarises the two major ice dynamic mechanisms that potentially can cause a rapid change in ice sheet mass balance in the case of a calving front with a floating tongue, which are (1) perturbation of the force at the downstream terminus of the outlet glacier, and (2) lubrication of the bed (Bell, 2008). Climate warming could lead to earlier and expanded surface lake formation and as a result, links to the bed could happen earlier in the melt season and over a larger area (Das *et al.*, 2008). Nevertheless, whether the increasing area of surface melt could result in a greater area of well-lubricated ice-sheet bed and increased ice velocities is still unresolved (Bell, 2008).

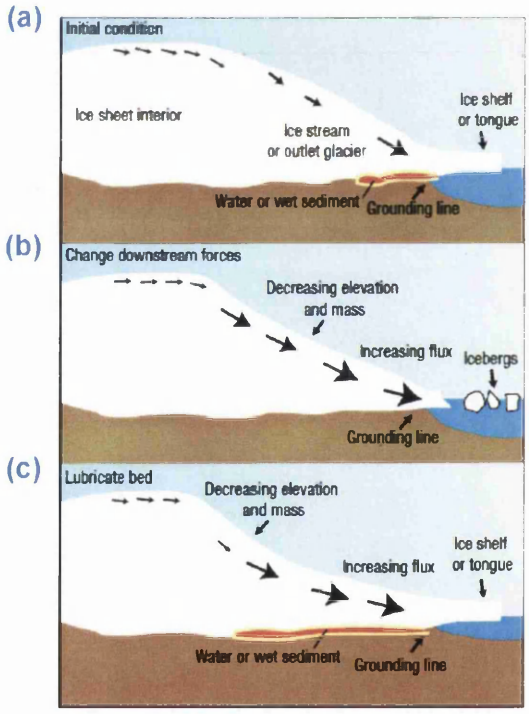

Figure 2.2: Summary of the ice dynamic mechanisms for fast ice-sheet flow. (a) The presence of an ice tongue provides a longitudinal compressive force, effectively slowing the flow of the ice stream. (b) Removing the ice tongue will produce increased ice-sheet velocities. (c) Lubricating the bed with either a water-saturated till or basal water will also yield increased ice sheet velocities (Modified from Bell (2008)).

The supra-glacial hydrological system combines lakes, channels and moulins (Figure 2.3). Supra-glacial lakes behave as a temporally storage of melt-water on the surface of the ice sheet. Supra-glacial channels can act as connectors between lakes and also between lakes and moulins (Johansson, 2012). The hydrological system in the ablation area was proposed to be similar to the one in Alpine systems, with in spring causing a strong melt/velocity feedback while in late summer there is a strong an instantaneous coupling between the surface and basal hydrology (Shepherd *et al.*, 2009), *i.e.* the drainage systems become increasingly efficient as hydrological connection between the ice surface and the ice sheet bed are made further inland, draining vast volumes of water and sediment (Bartholomew *et al.*, 2011). This more efficient drainage experiments fewer speed ups ans water is transported at lower pressure. Sundal *et al.* (2011) showed that for high rate melt years, the mean summer velocity is lower. Sudden drainages of lakes can overwhelm this system and still cause accelerations on ice flow (Das *et al.*, 2008). Routing of seasonal runoff at the ice sheet surface plays an important role in the magnitude and extent of seasonal ice sheet speed up (Palmer *et al.*, 2011), although the degree of speed up in late-summer presents spatial variations and the effect extends far inland, up to 100 km.

2.3 Supra-glacial lakes description

Echelmeyer *et al.* (1991) identified lakes near the firn line of Jakobshvans Isbrae, West Greenland. They observed numerous lakes between 600 m and 1,450 m elevation, with lakes below 1,150 m forming on bare glacial ice. Between 1,150 and 1,300 m lakes are within the superimposed ice zone and above that elevation many of the lakes are in the wet-snow facies. The low albedo of lakes in areas of saturated firm produce greater radiation absorption and thus increases the melting, which allows for the perpetuation of lakes (Echelmeyer *et al.*, 1991; Lüthje *et al.*, 2006). Tedesco *et al.* (2011) reported that warm conditions together with the positive albedo feedback mechanism contribute to large negative surface mass balance

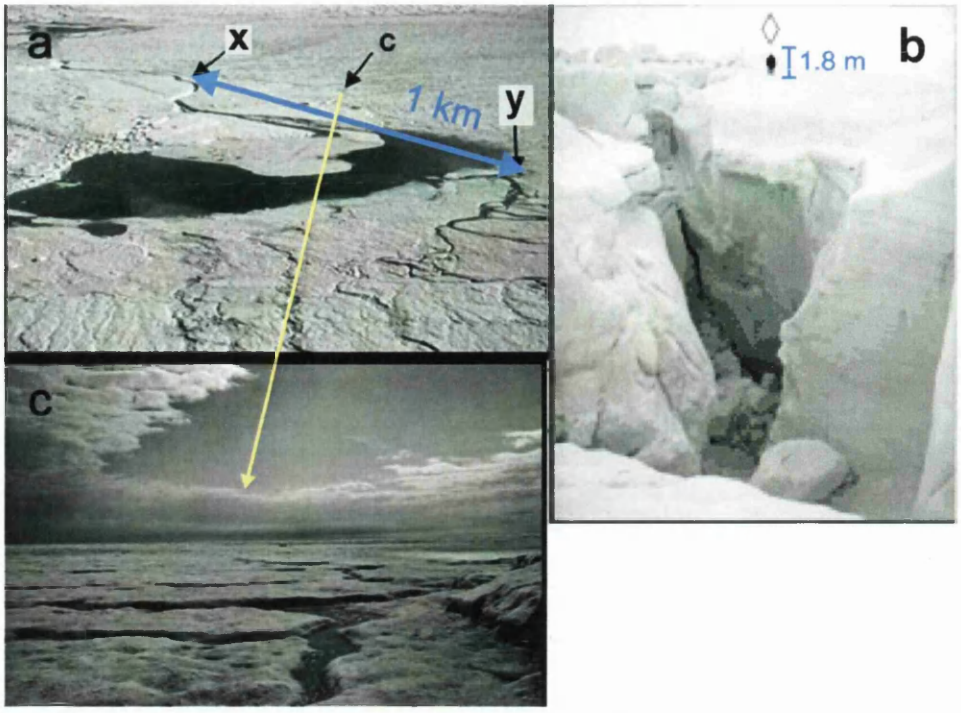

Figure 2.3: Photographs from a field site on the GrIS during August 2003: (a) A supra-glacial lake at 67°20' N, 48°57' W at an altitude of 1,240 m. **x** and **y** delimit the scale of the picture. (b) Photography from a large hole found in the bed of another lake at 68°43' N, 49°30' W, after it drained in 2007 (modified from (Das *et al.*, 2008)). (c) A small river (0.5 m wide), of the type typically found all around the lake (modified from Lüthje *et al.* (2006)), which corresponds with river **c** in photograph (a).

anomalies, although they also reported that low rates of summer accumulation can also help to reduce the albedo. Lowering of albedo has being also recently reported in west Greenland, where areas of increased crevassing might enhance surface ablation through increased absorption of solar radiation (Colgan *et al.*, 2011).

Supra-glacial lakes are formed during the ablation season. There are lakes that are classified as fast draining, others which disappear by refreezing, which are very common, and others which drain supra-glacially (Selmes *et al.*, 2011). Lakes that drained over 1.4 hours have been observed (Das *et al.*, 2008) (See Figure 2.3(e)); another lake in the Canadian Arctic (79°40'N, 74°00'W) (Boon *et al.*, 2003; Boon and Sharp, 2003) drained abruptly two days after an extreme melt event, where the water levels increased to at least 5 times that of the normal daily cycle. The observations of

Boon *et al.* (2003) confirmed that the high melt rates during the event caused large volumes of water to being routed through the englacial/sub-glacial drainage system. The surface layer of the glacier, which presented cryoconite holes up to 0.2 m deep, was removed by melting, and the resulting bare ice surface was covered with a thin film of water. This event observed by Boon *et al.* (2003) occurred relatively late in the melt season, when the link between the surface and the bed reached greatest efficiency.

The positive feedback over ice velocity is thought to be a seasonal effect that could have a minimal repercussion for the response of the ice sheet to climate warming (van de Wal *et al.*, 2008; Sundal *et al.*, 2011). Even in spring, the melt/velocity relationship can be decoupled. The impact of an early-season melt event on drainage development would be limited by the need to warm the snow pack to $0^{o}C$ before melt can occur, and by the refreezing of melt-water within the snowpack, which delays runoff response. However, early-season melt events could influence the dates when runoff and sub-glacial outflow are initiated (Boon *et al.*, 2003). The observations of Hoffman *et al.* (2011) showed that direct input of runoff and supra-glacial streams to moulins could drive the seasonal velocity response rather the sudden lake drainages. Despite ice velocities in the ablation zone, where ice thickness is around 1,000-1,500 m, reacting in less than a week to melt-water rates, annual velocities react slowly to ice thickness changes and surface slope. However, the mechanism that controls the drainage of a lake is not yet well understood nor how is it linked with the hydrology of the area.

Propagation of water-filled crevasses to the glacier bed seems to play a major role in the seasonal establishment of the surface-bed connection, but is not the only process responsible for establishing sustained drainage connection. One theory is that the rate of fracture propagation is controlled only by the melt-water necessary to keep the fracture full and that supra-glacial lakes can supply enough water needed to transmit the fractures to the bottom of the ice sheet. Local Global Positioning

System (GPS) observations coupled with seismic and water-level sensors in south west of Greenland (Das *et al.*, 2008), showed a lake draining rapidly during July 2006 and again in 2007 (Figure 2.3(e)).

A recent study found that the rapid lake drainage events reported can not explain the distribution of significant dynamic mass loss in the more varying areas of Greenland (Selmes *et al.*, 2011). From the period 2005-2009, the SW and NE accounted for 68% of the total fast draining lakes (Selmes, 2011), and since the SE, where those rapid changing glaciers are (like Helheim and Kangerdlugssuaq), only contained 2% of the total lakes (Selmes *et al.*, 2011) (Figure 2.4). Therefore, at least for the south east other mechanisms must be found to explain the mass loss. Better knowledge of both melt generation and the understanding of the sub-glacial hydrologic system at longer temporal resolutions could help predict the future dynamics of the ice sheet in response to variations in surface melt (Hoffman *et al.*, 2011).

2.4 Hydrofractures

Water-filled cracks are thought to be an effective mechanism to direct hydrofractures to the bottom of an ice sheet (Krawczynski *et al.*, 2009). Weertman (1973) showed that due to the density contrast between ice and water, a water-filled crack will continue to propagate until it reaches the bed of an ice sheet. Moreover, if a crack remains water-filled during its evolution, the propagation depth is limited only by the volume of water available to fill the crack (Krawczynski *et al.*, 2009). Supra-glacial lakes can provide the large volumes of water required to propagate fractures to the bed (Bamber *et al.*, 2007); Krawczynski *et al.* (2009) estimated that lakes with a diameter of around 250 to 800 m and from 2-5 m deep store sufficient volume of water to drive a water-filled crack to the base of a 1 km-thick ice sheet. Furthermore, moulins that form in lake basins lie near the confluence of melt-water streams and will continue to be supplied with surface melt-water after the lake drains, routing

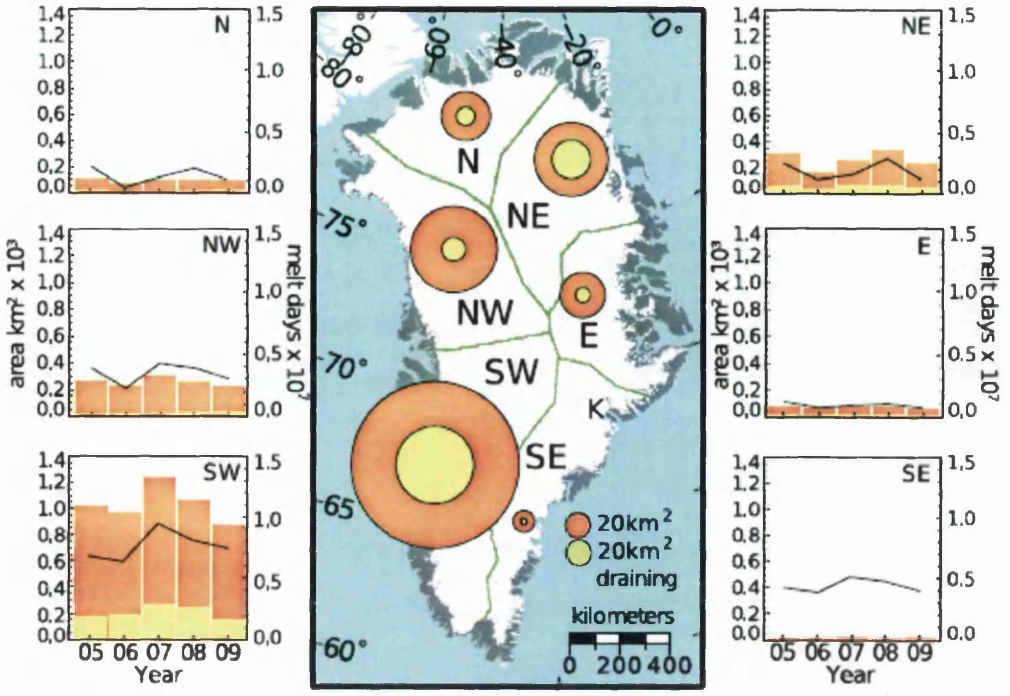

Figure 2.4: Summary of fast draining lakes on the GrIS from an automate method developed by Selmes *et al.* (2011), which used MODIS satellite data. Total area of lakes (red); total area of lakes that drained suddenly (yellow). The circles show the mean area values of the period 2005-2009. Bar plots show the interannual variation of lake area and drainage events and also melt intensity (black line) (From Selmes *et al.* (2011)).

water to the bed and delaying closure while sufficient melt-water continues flowing through the summer (Das *et al.*, 2008). Many studies have tried to model crack depths and geometry; from those two main models are introduced.

Nye crevasse model

Nye (1957) developed this model based on the balance between the longitudinal tensile strain rate and creep closure due to ice overburden pressure (Mottram and Benn, 2009).

$$d = \frac{2}{\rho_i g}\left(\frac{\dot{\epsilon}_{xx}}{A}\right)^{\frac{1}{n}} \tag{2.1}$$

Where d [m] the is crevasse depth, $\dot{\epsilon}_{xx}$ [s^{-1}] is the longitudinal strain rate, A [$kPa^{-3}s^{-1}$] and n are flow-law parameters, ρ_i [kgm^{-3}] is the density of ice and g [ms^{-2}] is the gravitational acceleration. Equation 2.1 is a version from Paterson (1994) as the crevasse depth derived from Nye's model assumed crevasses free of water (Weertman, 1973). It has been calculated that once there is water in a crevasse, this can increase its depth; a water-filled crevasse up to minimum of 97.4% of its depth can penetrate to the glacier bed (Weertman, 1973).

The Lineal Elastic Fracture Mechanics (LEFM) model

The LEFM model uses a stress intensity factor to describe the elastic stresses near the tip of the fracture. This factor provides the depth to which crevasses will penetrate to the ice sheet bed (van der Veen, 2007). At this depth the stress intensity factor equals the fracture roughness of ice. Fractures that have propagated deep enough (>10-100 m) will continue to propagate to the bed and probably along the bed if they remain water-filled. This suggests that storage of water at the surface, in lakes or in extensive but shallow crevasses is a normal prerequisite to moulin formation through cold ice (Alley *et al.*, 2005b). Warming of glacier ice due to initial refreezing events increases the likelihood of a permanent surface-bed connection developing during subsequent events. In addition, surface water ponding raises the water pressure at the crevasse tip; this stored water contributes to crevasse enlargement by wall melting when it eventually drains (Boon and Sharp, 2003).

In Greenland, the distribution of water beneath the wet and fractured margins of

the Greenland ice sheet is difficult to determine and the fraction of the increasing ice-sheet velocities caused by increased surface melt-water lubricating the bed remains unknown (Bell, 2008). On the other hand in Svalbard, deep fracture systems have been investigated in areas with extensional stress and ready availability of melt-water (Benn *et al.*, 2009). In that study, 60 m deep vertical fractures were found through cold ice to the bed. From their findings Benn *et al.* (2009) hypothesized that, if near-surface deviatoric stresses are relative low, then supra-glacial lakes could be necessary for hydrofracturing by providing an elevated head of water and a storage reservoir; however if stresses are sufficient to open deep surface crevasses then lakes would not be a necessary condition for the initiation of hydrofractures.

2.5 Depth, area and volume of supra-glacial lakes from previous studies

An estimate of total water volume stored in supra-glacial lakes is crucial for assessing the potential formation of hydrofractures and hence drainage to the bed (Krawczynski *et al.*, 2009); however a volume estimate of melt-water is challenging for several reasons; like mixed pixels (water/ice) due to sensor resolution; sensor related uncertainties (e.g. cloud cover, sun angle) and the need of an accurate method to derived water depth remotely.

Lake area can be relatively straight-forward derived from spectral differences between water and snow/ice (Lüthje *et al.*, 2006; McMillan *et al.*, 2007), although due to spatial and temporal limitations from the sensors (like cloud cover), a full volume coverage of the GrIS is yet impractical. Nevertheless, Selmes *et al.* (2011) developed an automate algorithm to map all the lakes detectable by the spatial resolution of MODIS imagery (250 by 250 m), producing an inventory of supra-glacial lakes over the entire GrIS from 2005 to 2009. This inventory contained the temporal evolution

of the lakes, with lake formation and drainage, if it occurred, and area extent of the lakes throughout the melt season. Therefore until an accurate method of deriving lake depth for the entire GrIS can be combined with lake inventories, such us those from Selmes *et al.* (2011), it is not possible give an accurate volume quantification of the water stored on the GrIS.

Water depth derived from models based on the optical properties of water column (Smith and Baker, 1981) were previously developed for coastal bathymetry studies (Lyzenga, 1978; Maritorena *et al.*, 1994; Philpot, 1989). Recently, estimates of water depth have been made for single or specific melt lakes on the GrIS from high-resolution optical satellite images, such as the Advanced Spaceborne Thermal Emission and Reflection Radiometer (ASTER) (Georgiou *et al.*, 2009; McMillan *et al.*, 2007; Sneed and Hamilton, 2007, 2011; Tedesco and Steiner, 2011), where they used the Radiative Transfer Equation (RTE) (Lyzenga *et al.*, 2006; Stumpf *et al.*, 2003) to derive the melt-water depth. These studies compare depths and volume estimations from satellite imagery (Box and Ski, 2007) with either *in situ* measurements or Light Detection And Ranging (LIDAR) observations (Georgiou *et al.*, 2009).

The RTE is based on the *Bouguer Lambert Beer law*, which states that the water-leaving spectral radiance decays exponentially with water depth. Satellite-based studies use the surface pixel reflectance to derive water depth; hence they transform the radiance into reflectance and solve the RTE for depth (Philpot, 1989). The RTE is derived in Chapter 4 and it depends on three physical parameters that will also be introduced in that chapter. R_∞ is the reflectance of optically deep water; A_d is the bottom albedo and g is the effective attenuation coefficient.

2.5.1 Summary of previous studies estimates

Several different approaches have been used to study lakes on the GrIS and they can be categorised as field, remote sensing and modelling studies.

Field studies

Field observations of lake depth around Jakobshavn Isbrae area were of the range of 0-20 m (Echelmeyer *et al.*, 1991), with the deepest corresponding to crevassed areas, and maximum lake area around 10 km^2. Whereas Das *et al.* (2008) reported a maximum lake extent 5.6 km^2 and a volume of 0.044 $\pm$ 0.01 km^3 with a relative maximum depth of 10 m for a single lake.

Remote sensing studies

Currently remote sensing based studies have focussed on either one supra-glacial lake or an specific area of interest, mainly the south west of the GrIS, because as shown previously in Figure 2.4, the south west presents the biggest concentration of lakes of the whole GrIS.

Despite the relative coarse spatial resolution of MODIS imagery, it has been used for depth/volume quantifications. An example is Box and Ski (2007) where the volume of individual lakes was calculated to be around 10^6 to 10^8 m^3 on average with the maximum estimated depth around 12 m. That study did not quote any uncertainties in their calculations. Sundal *et al.* (2009) also used MODIS observations, although like Selmes *et al.* (2011) they used MODIS to monitor lake area, showing interannual area variations from 1 to 9 km^2, with a 1.6% of uncertainty. Selmes *et al.* (2011) estimated a median lake area of 0.56 km^2 for south west Greenland.

ASTER and Landsat have higher spatial resolution than MODIS (15 and 30 m respectively). Studies using these satellites derived lake depths based on the RTE of around 4 m, areas of tens of km^2 and volumes of around $2x10^7$ m^3 for two specific lakes (Sneed and Hamilton, 2007). In a recent study the same authors used *in situ* measurements as true depth validation (Sneed and Hamilton, 2011); both true and satellite derived depths were of the same order of magnitude, with a maximum depth of 4.2 m, although no uncertainties were reported to the estimations. Georgiou *et al.* (2009) showed the temporal evolution of a lake from 2002-2005 using ASTER observations and LIDAR from 1995 as a comparison. They compared the maximum depth given by ASTER with the LIDAR, assuming a ± 1 m and accounting for inter-annual variations of ablation and accumulation. They observed that A_d uncertainty reduces with depth as well as depth uncertainty. On the other hand Tedesco and Steiner (2011) found a Gaussian-like behaviour of A_d, with this variability being intrinsic to that albedo of the lake bottom, which consisted of large patches of cryoconite. In the study by Georgiou *et al.* (2009), the maximum lake volume observed was 18.6 ± 3.7 $x10^6$ m^3 in 2005 from ASTER. Airborne laser altimetry was used as a ground-truth measurement of the optical remote sensing observations, although usually with different times and years as to the satellite, even with a decade of difference like in McMillan *et al.* (2007) and Georgiou *et al.* (2009) where they used data acquired on 24 May 1995. McMillan *et al.* (2007) estimated that the average depth of filling lakes increases from $1.5\pm$ 0.7 m to $3.9\pm$ 1.1 m between July-August 2001, which is of the order of the one they derived from airborne laser altimetry (4.4 $\pm$ 0.9 m).

Models

Recent models have also try to simulate the growth of supra-glacial lakes. A model was developed for lake growth on west Greenland and is based on routing runoff estimated by a regional climate model across a DEM of the ice sheet surface (Leeson *et al.*, 2012). The 100x100 m cell size model can predict the location of 66%

of observed lakes greater than 0.125 km^2. They used the diameter-area relationship first used by Krawczynski *et al.* (2009). The 1D model presented by Lüthje *et al.* (2006) studied the evolution of supra-glacial lakes showing that the surface ablation beneath the lake was enhanced by 110% in 1999 and 170% in 2001 compared with the ablation for bare ice. Nevertheless, from satellite imagery they showed that less than 1% of the ablation region in that region of Greenland is covered by supra-glacial lakes, therefore the large amount of melt beneath the lakes is minimal with respect to the total area. They also found the lake formation was more or less independent of the melt extent and their maximum modelled lake depth was around 10 m. Another approach is the use of regional weather data, for example McMillan *et al.* (2007) used the positive degree day model (PDD) to derive average lake depths, showing an average depth of filling lakes of 1 $\pm$ 0.7 m increasing to 3.9$\pm$1.1m on August. This study suggested that the uncertainties of area measurements (around 9%) were dependant upon both the satellite resolution and the perimeter of each lake.

2.6 Chapter Summary

A relationship between the production of melt-water at the surface of the GrIS and the velocity of ice flow has been reported. Melt-water at the surface is thought to propagate through hydrofractures to the ice sheet bed. When water reaches the bed the water is thought to reduce the effective pressure, which allows the ice sheet to accelerate. This mechanism was called *the Zwally Effect* and previously was thought to be governing the ice sheet dynamics (Zwally *et al.*, 2002a) and the recent observed mass loss (Figure 2.1). Recent studies have shown though that recent mass loss is not directly linked to supra-glacial lake drainage events (Selmes *et al.*, 2011; Hoffman *et al.*, 2011). Nevertheless field studies Das *et al.* (2008) showed that supra-glacial lakes could drain to the bed within a couple of hours and cause localised speed-ups. This confirmed that connections between surface and bed hydrological systems can

be established over short-time scales. Drainage can also mean that melt-water is transported from one lake to another (Johansson, 2012). Therefore a wide quantification of water stored on supra-glacial lakes is important for a better understanding of the dynamic response of the GrIS, to recent climate change.

A total estimate of water stored on supra-glacial lakes over the entire ice sheet each year is yet unknown. Previous studies focussed on individual lakes. There are models that simulate the evolution of lakes during different years, which is a step forward for the volume quantification. Also the inventory developed by Selmes (2011) is an unique tool for lake area monitoring and distribution. If a global set of the three physical parameters that govern the RTE on (A_d, R_∞ and g) could be derived and applied to every lake, the water reflectance model from Sneed and Hamilton (2007) could be up-scaled to the entire ice sheet and together with Selmes (2011) lakes inventory a volume of water stored in melt-water lakes could be obtained. This thesis explores the possibility of an optimisation of the parameters derived from ASTER images of melt-water lakes and validated with Ice, Cloud, and Land Elevation Satellite (ICESat) laser altimetry data over empty lakes, as an in put to the simple reflectance model for fresh water. Since knowing the uncertainties derived from the model is crucial to discuss its limitations and future applications, a Monte Carlo Simulation is applied, which allowed us to study the sensitivity of the parameters to the model.

Chapter 3

Data sources

3.1 Introduction

This chapter presents the different datasets used in this thesis and explains the motivation for choosing them. The primary data were ICESat elevation measurements. ICESat data are introduced in Section 3.2. ICESat data were used as a validation of the results obtained from the ASTER and MODIS data (Section 3.3 and 3.4 respectively). In section 3.5 CASI sensor is introduced, which was used in the last results chapter (Chapter 7). For each of the different data sources a sensor description, type of data product, instrument errors and why the corresponding sensor was suitable for this thesis are included. Finally, in Section 3.6 Landsat 7 data is included.

3.2 ICESat

3.2.1 Satellite description

The Geoscience Laser Altimeter System (GLAS) launched onboard the ICESat satellite on January 2003 and developed by the National Aeronautics and Space Admin-

istration (NASA) - Goddard. ICESat mission ended in October 2009. It was the first laser satellite designed specifically to observe changes in the polar ice sheets. For this reason the satellite was operated in near-polar and non-sunsynchronous orbit at an altitude of 600 km. With a 94° orbital inclination, ICESat reached a maximum latitude of 86° north and south of the equator. GLAS/ICESat emitted around 3.4 million pulses per day, usually 1/3 of ICESat's laser pulses were over land and ice, and around 1/2 over the ocean surface were obscured by opaque clouds (Urban and Schutz, 2005). GLAS/ICESat was a nadir-looking sensor and had three lasers mounted in a rigid optical bench (Schutz *et al.*, 2005). Apart from the 3-laser system, the system onboard ICESat included a Global Positioning system (GPS) and a Star Tracker (ST) (Wang *et al.*, 2011). The 3-laser system worked in two wavelengths, 1,064 nm (near infrared channel) for surface altimetry and dense cloud heights with a laser pointing angle determination system and 532 nm (green channel) LIDAR for the vertical distributions of clouds and aerosols.

The general idea of how the laser altimeter installed in ICESat worked is that, at a frequency of 40 Hz, the transmitted laser pulse illuminated a spot on the Earth's surface with a 60 m averaged footprint (Zwally *et al.*, 2002b), 172 m footprint separation (Fricker *et al.*, 2005a) and along-track spacing of approximately 7 Km at 60° and 2.5 km at 80° latitude (Zwally *et al.*, 2002b). Figure 3.1 summarises how the laser altimeter instrument operated from space.

The primary objective of the GLAS/ICESat instrument was to measure ice sheet elevations and their temporal variations, with a proposed minimum variation detection of 1.5 cm/year (Fricker *et al.*, 2005b). Other objectives were measures of cloud and aerosol profiles, land elevation and vegetation cover, and sea ice thickness. The different datasets are freely available from the National Snow and Ice Data Centre (NSIDC) (`http://nsidc.org/data/icesat/order.html`).

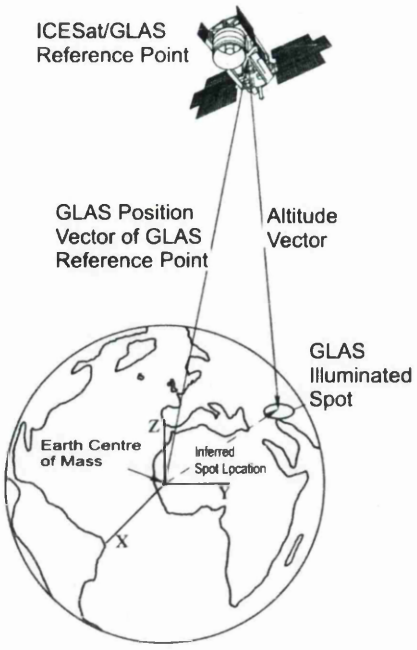

Figure 3.1: Illustration showing the laser altimetry concept (modified from Schutz and Zwally (2008) and Schutz (2002)).

GLAS/ICESat presents two levels of products, which are summarised in Table 3.1, with level-1 products (GLA01 to GLA06) storing altimetry, atmospheric, and engineering-related raw data; whereas level-2 products (GLA12 to GLA25) contain validated and corrected data. Based on the waveform of the received laser pulse and other instrument records, 15 different sets of data are available (Wang *et al.*, 2011).

The NSIDC provides different data releases, each of them presenting improvements on data management. For practical reasons Release 31 was chosen for analysis in this thesis, since it was the latest release available during the time that research took place. A summary of the main characteristics of Release 31 for the altimetry products (GLA05, 06, 12, 13. 14 and 15) are as follows;

1. The DEMs over Greenland and Antarctica used in previous releases have been replaced with the ICESat-derived DEM, with the GLAS-derived 1 km and 500 m (respectively) DEMs on GLA06, 12-14.

2. The Geoid has been updated to Earth Gravitational Model EGM2008. EGM2008

Table 3.1: GLAS data products offered by NSIDC (modified from Schutz (2002)).

Product ID	Product name
GLA01	L1A Global Altimetry
GLA02	L1A Global Atmosphere
GLA03	L1A Global Engineering
GLA04	L1A Global Stellar Reference and GPS
GLA05	L1B Global Waveform-based elevation corrections
GLA06	L1B Global Elevation
GLA07	L1B Global Backscatter
GLA08	L2 Global Boundary layer and elevated aerosol layer heights
GLA09	L2 Global Cloud heights for multiple layers
GLA010	L2 Global Aerosol vertical structure
GLA011	L2 Global Thin Cloud/Aerosol optical depths
GLA012	L2 Polar ice sheet altimetry
GLA013	L2 Sea ice altimetry
GLA014	L2 Global land surface altimetry
GLA015	L2 Ocean altimetry

was developed by the USA National Geospatial-Intelligence Agency (NGA) and combines gravitational information from the Gravity Recovery and Climate Experiment (GRACE) satellite, with 5' x 5' resolution (Pavlis *et al.*, 2008). The new geoid file contains the Earth Gravitational Model EGM2008 referenced to the Topex-Poseidon ellipsoid, with mean tides applied. Elevations have had ocean tide and load tide corrections applied using the GOT99.2 global ocean model (Ray, 1999).

3.2.2 GLAS/ICESat Laser operational periods

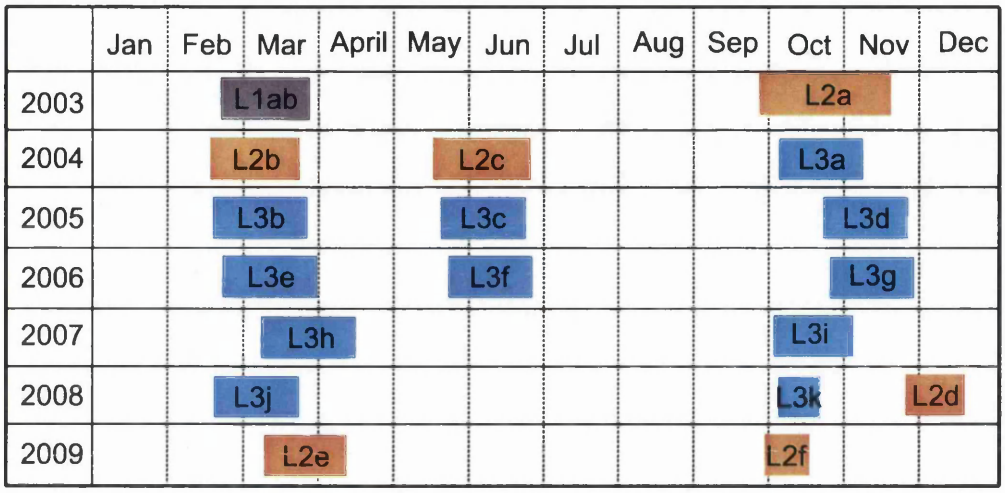

Figure 3.2: Missions of ICESat. Different colours stand for different lasers: Purple, Laser 1; red, Laser 2; blue, Laser 3; and the lengths of the bars show the durations of different missions (modified from Wang *et al.* (2011)).

The three lasers that formed GLAS/ICESat operated one at a time throughout the mission. To maximise the mission lifespan, the three lasers were operating individually, with 33-day to 56-day campaigns per year, varying from 1 to 3 times per year. In total GLAS/ICESat recorded 18 campaigns distributed in seven years as summarised in Figure 3.2, usually one during spring and the other during autumn. Blank spaces on ICESat coverage maps are places where no elevation data were recorded. This was usually due to atmospheric issues and also due to ICESat's 8-day and partial 91-day sampling patterns. The 8-day repeat orbit was chosen to secure frequent repeats of the ground calibration sites during Laser 1 ; whereas the 91-day orbit was used to allow dense data for research purposes for lasers 2 and 3 (Wang *et al.*, 2011).

3.2.3 ICESat's elevation data

The elevation derived from ICESat altimetry is defined as the mean surface height of the laser footprint, which is the difference between the satellite height and the range

between the satellite and the surface (Brenner *et al.*, 2003). This value is estimated using an ice sheet specific algorithm and after instrument corrections, atmospheric delays and tide models are applied.

GLAS/ICESat estimates the surface elevation from the altitude of the satellite orbit above the Earth minus the range of the surface measured by the sensor (see Figure 3.3). GLAS determines the range via photon time-of-flight (TOF) in the altimetry and atmospheric backscatter channels of the altimeter. First, a Gaussian pulse is emitted at time t_1 from the laser and at time t_2 the echo pulse is reflected back from the surface in the sensor. The total round-trip of the photons is estimated as $\Delta t = t_2 - t_1$ (Mitchell, 2009). Then, the range to the mean surface within the laser footprint is determined from $R = c\Delta t/2$, with c being the speed of light ($\approx 3\times10^8$ m/s). If the transmitted pulse is close to a Gaussian shape, then the surface is a mean slope plus random height variations, and if there is no atmospheric forward scattering, then the return signal shape would be close to a Gaussian (Brenner *et al.*, 2003). Over the oceans, sea ice and most of the ice sheets, the echo is expected to be a single Gaussian (Zwally *et al.*, 2002b).

Level-0 data contains voltages recorded by the altimeter system and from there, as illustrated in Figure 3.3, Level-0 data are translated into Level-1 range data. As mentioned above, Level-1 data contain global altimetry range and atmospheric backscatter information (Mitchell, 2009).

The GLAS measurement is the scalar distance between a reference point in the sensor and the Earth's surface (Zwally *et al.*, 2002b). The precision attitude determination (PAD) data were combined with the precision orbit determination (POD) and laser-ranging data to give the location of each footprint on the surface of the Earth, along with the topographic elevation at that point; this process is known as geolocation (Schutz, 2002). The geolocation results were reported in the location

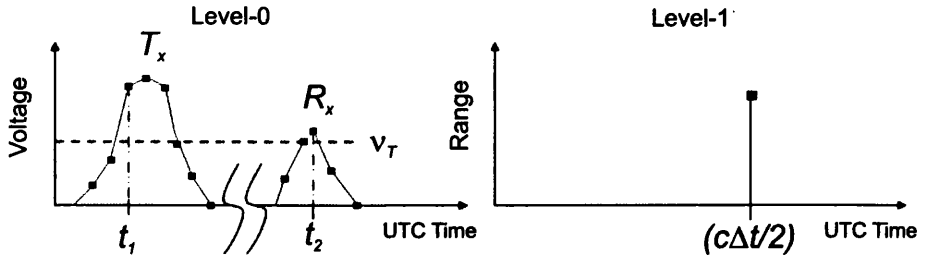

Figure 3.3: Translation of Level-0 data into Level-1 data (from (Mitchell, 2009)). The graph on the left shows the Gaussian pulse emitted at time t_1 (T_x) and the echo pulse reflected back from the surface to the sensor at time t_2. The graph on the right shows the output of Level-1 showing the range to the mean surface within the laser footprint (R). UTC stands for Coordinated Universal Time.

data given on the ICESat Level 2 data products (see Table 3.1) (Sirota *et al.*, 2005).

As mentioned above, for the purpose of this thesis, only the GLA012 altimetry product was used. The files contained a record number, spatial and temporal coordinates, the surface elevation in meters with respect to the ellipsoid at the spot location determined by range using the ice sheet specific algorithm (described above) and the height of the geoid above the ellipsoid. To obtain the elevation above sea-level, the geoid values were subtracted for each of the elevation measurements. ICESat data files also contained a correction to elevation for saturated waveforms, which was applied to the elevation values following product guidelines. After correcting the dataset for the geoid and saturation, the final elevation data were projected into North Polar Stereographic Projection for practical issues, which is characterised by a central meridian of -45° and standard parallel of 71° and WGS1984 as the Geographic Coordinate System. This dataset of elevation measurements across Greenland forms the base of this thesis; ICESat elevation measurements were transformed into empty lake depth and then applied as a validation for the model used.

3.2.4 Sources of errors

The accuracy of the derived surface elevation depends on timing, range errors, instrument saturation, atmospheric forward scattering, field of view shadowing and pointing errors. The laser pointing errors depend on the slope and surface roughness, as shown in Figure 3.4. The accuracy and precision of ICESat altimetry data were estimated to be about 14 cm and 2 cm, respectively (Shuman *et al.*, 2006; Wang *et al.*, 2011). The error budget for GLAS/ICESat elevation measurements is detailed in Table 3.2,and it is valid for ice, land and ocean/lake applications.

Table 3.2: GLAS single-shot error budget (modified from Mitchell (2009) and Zwally *et al.* (2002b)). For the error budget estimation it was assumed 1° surface slope and laser pointing error 1.5 arcsec.

Error Source	Contribution (cm)
GLAS range measurement precision per pulse	10
Radial orbit error (based on GPS)	5
Attitude/pointing determination error (based on PAD system)	7.5
Atmospheric delay error	2
Atmospheric forward scattering	2
Other (solid tides and ocean loading over ice sheets; ice sheet rebound)	1
Root Sum Squares (RSS)	13.8

The errors associated with the surface elevation determination by the GLAS/ICESat instrument have random and systematic nature. The components of the error budget are mostly uncorrelated with each other, so the Root Sum Squares (RSS) (Table 3.2) of the error budget is a reasonable representation of the overall error for a single pulse (Zwally *et al.*, 2002b). However, as mentioned above, the slope and roughness of the target surface have great impact on ICESat pointing precision. As an example, for 1 arcse .0cond pointing error; a 1° slope is equivalent to 5.1 cm of surface slope induced range error; a 2° slope is equivalent to 10.1 cm range error and a 3° slope is equivalent to 15.2 cm range error (Bae and Schutz, 2002; Yi *et al.*, 2005).

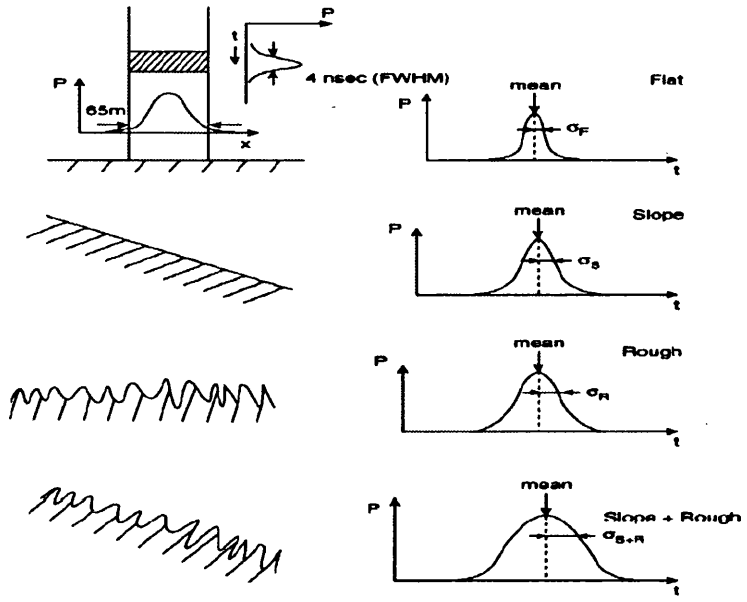

Figure 3.4: Example of how the received laser pulse varies as a function of the surface characteristics. The laser footprint diameter on the surface is nominally 70 m, and the width of the transmitted pulse is 4 ns (equivalent to 0.60 m in surface elevation). The returned pulse is broadened by the distribution of surface heights within the footprint. The surface height distribution is characterised by a mean surface slope and a surface roughness within the footprint (modified from Brenner *et al.* (2003)).

Since ICESat was launched (also pre-launch) many studies have carried out validation analysis of the sensor performance (Zwally *et al.*, 2002b; Fricker *et al.*, 2005b). Fricker *et al.* (2005b) chose the salar Uyuni on the Bolivian Altiplano as a terrestrial target to validate ICESat elevation measurements over the ice sheet, since it is a large salt flat, which is a stable surface that allows detailed surveying and present an albedo comparable to that of the ice sheets. They concluded that ICESat-derived elevations have an absolute accuracy (bias) of < 2 cm and precision (Standard Deviation) of < 3 cm over the salar. Nevertheless, these results were for ideal conditions and a small deviation from them causes errors to significantly increase. For instance, forward scattering in the atmosphere causes increased noise and negative elevation bias; moreover degradation of the transmitted energy with time affect the accuracy and precision of the elevation derivations.

Pre-launch estimations of effects of roughness and slope over the ice sheet made the

following assumptions:

1. The target surface was a Lambertian (diffuse) reflector, which is radiating constantly in a hemispherical solid angle.
2. It was also assumed that the surface reflectivity is uniform within the laser footprint.

The largest error source when estimating ICESat measurements is the precision of the pointing knowledge of the laser beam. The Laser Reference system is a major input required to calculate the beam point angle. The accuracy of ICESat elevation measurements was recently tested at the summit in Greenland (Siegfried *et al.*, 2011), and they discovered inter-campaign bias in the data; however it was concluded that the biases were within the satellite's objective of $\pm$ 0.15 m. The elevation data as a function of the bias highlights the need of parallel *in situ* calibrations of ICESat and therefore of any satellite.

3.2.5 Advantages of ICESat over other satellites

For the scope of this thesis, an accurate dataset covering the entire ice sheet was desirable. Since *in situ* measurements of supra-glacial lakes in the whole ice sheet of supra-glacial lakes were unfeasible, ICESat appeared to be an useful choice, due to its small footprint and with an absolute vertical accuracy of 0.15 m (Fricker *et al.*, 2005b), which was determined as the elevation bis for the GLAS data, calculating the weighted-mean difference between GLAS and the GPS elevation measurements (Siegfried *et al.*, 2011). Also the measurements over lakes had to be when empty, since the ICESat laser does not penetrate water. As mentioned above, ICESat campaigns were usually occurring in spring and autumn (Figure 3.2), which is when the lakes are likely to be empty. After an intensive search of overlapping lakes with ICESat tracks with a previously developed supra-glacial lakes archive (Selmes, 2011), it

was concluded that ICESat was a valid dataset to use as validation depth.

Some of the characteristics of laser altimetry over ice sheets follow radar altimetry; the basic measurement follows the same principle (determination of TOF of an electromagnetic pulse from the source to the surface and back) (Brenner *et al.*, 2003). However, there are two main characteristics that made laser and radar altimeters different; the smaller footprint of laser altimeters and the fact that they operated at much lower electromagnetic frequency. The accuracy of satellite radar altimetry techniques in the determination of land-surface elevation is limited by its large footprint, around 2-3km over ice. Also slope-induced error varies from several metres to tens of metres. The lower frequency of laser altimeter (40 Hz) means that there is no deep penetration below the surface (Brenner *et al.*, 2003); in contrast radar altimetry uses the K_u band (12-18 GHz), which can penetrate through snow to the snow/ice interface (Wang *et al.*, 2011). This effect increases in the dry snow zone and high accumulation areas. As an example Brenner *et al.* (2007) compared the accuracy and precision of different altimeter satellites over Antarctica and Greenland ice sheets; Figure 3.5 summarised their results, showing the unprecedented accuracy of ICESat elevation measurements.

One of the disadvantages of ICESat is that clouds and aerosols in the atmosphere affect the laser beam, which means that heavy clouds produce no ground returns and thinner clouds cause forward scattering (Brenner *et al.*, 2003). Nevertheless, elevations derived from ICESat in clear atmospheric conditions have shown higher accuracy and precision than results derived from the radar altimeters, such us ERS-2 (European Remote Sensing) and Envisat (Environmental Satellite). Brenner *et al.* (2007) showed that elevations derived from ICESat varied from 0.14 to 0.5 m as a function of surface slope.

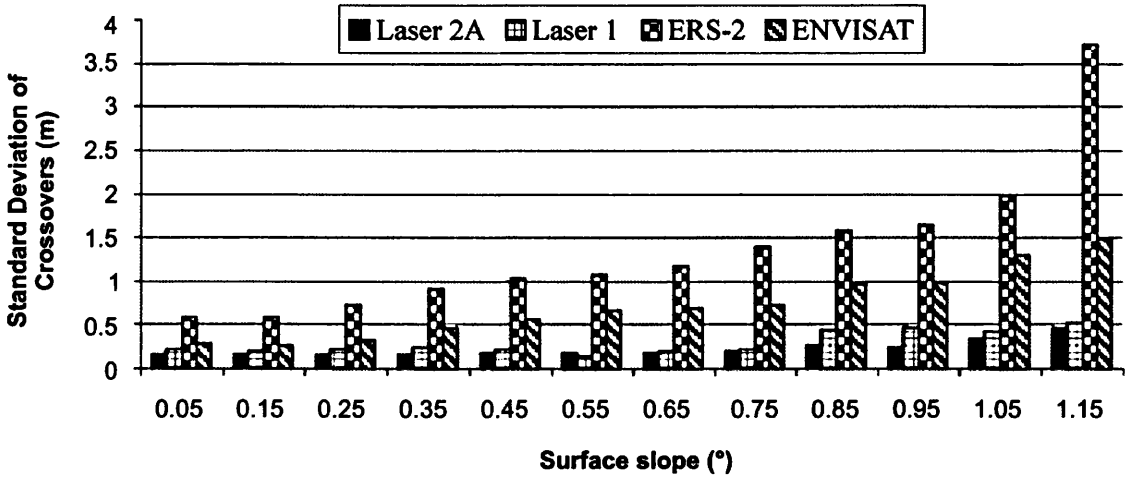

Figure 3.5: Laser (ICESat Laser 1 and 2A) and radar altimeter (ERS-2 and ENVISAT) elevation precision as a function of slope as measured by the standard deviation of the crossover residuals for a study in Greenland (Brenner *et al.*, 2007).

3.3 ASTER

3.3.1 Sensor description

ASTER is a multi-spectral visible/infrared instrument onboard the Terra satellite, and launched in December 1999. It is one of the five systems onboard Terra, which was the first Earth Observing System (EOS). ASTER sensor operates in a sun-synchronous polar orbit at 705 km of altitude and with a grounding track repeat cycle of 16 days. ASTER scenes have 60 km swath width and are georeferenced to the WGS-84 (World Geodetic System) datum and the Universal Transverse Mercator (UTM) projection. ASTER instrument was designed to collect the highest spatial resolution (15 m - 60 m) surface spectral reflectance, temperature, elevation and emissivity data of all the Terra sensors (Miura *et al.*, 2008).

The basic principle of ASTER instrument is to acquire quantitative spectral information of reflected and emitted radiation from the surface of the Earth at the spectral windows shown in Table 3.3 (ASTER, 2005). The ASTER sensor is composed of the following radiometers: Visible Near-Infrared (VNIR), Shortwave Infra-Red (SWIR)

and Thermal Infra-Red (TIR).

Table 3.3: ASTER bands specifications, table modified from (Yamaguchi *et al.*, 1998)

Subsystem	Band Number	Spectral Range (μm)	Spatial resolution (m)
VNIR	1	0.52 - 0.60	15
	2	0.63 - 0.69	
	3N	0.78 - 0.86	
	3B	0.78 - 0.86	
SWIR	4	1.600 - 1.700	30
	5	2.145 - 2.185	
	6	2.185 - 2.225	
	7	2.235 - 2.285	
	8	2.295 - 2.365	
	9	2.360 - 2.430	
TIR	10	8.125 - 8.475	90
	11	8.475 - 8.825	
	12	8.925 - 9.275	
	13	10.25 - 10.95	
	14	10.95 - 11.65	

The key features of ASTER sensor are as follows;

1. High spatial resolution (see Table 3.3).
2. Wide spectral range (see Table 3.3)
3. It can produce stereoscopic (three-dimensional) images and detailed terrain height models using the Visible Near Infra-Red (VNIR) telescope's backward

viewing band (Band 3B).

4. It is able to schedule on-demand data acquisition requests

The Japan Resources Observation System Organization (JAROS) is in charge of the development of the ASTER sensor. ASTER images were obtained though the on-line Data Pool at the NASA Land Processes Distributed Active Archive Centre User Services (LP DAAC), United States Geological Survey (USGS) - Earth Resources Observation and Science (EROS) Centre, Sioux Falls, South Dakota (`https://LPDAAC.usgs.gov/get\_data`). The standard data products are divided into 3 levels; Table 3.4 summarises the ASTER land products currently distributed from LP DAAC.

1. Level 0: Reconstructed, unprocessed instrument data at full resolution (Abrams, 2000).

2. Level 1A: Reconstructed, Unprocessed Instrument Data at full resolution. This product contains instrument data time-referenced (Abrams, 2000) and with geometric correction coefficients and radiometric calibration coefficients appended but not applied to Level 0 data (ASTER, 2005)

3. Level 1B: Registered Radiance at Sensor in $W/(m^2$ mm sr). This product contains radiometrically calibrated and geometrically coregistered data for all ASTER channels. It is created by applying the radiometric and geometric coefficients to the level 1A data. This product is the input to derived geophysical products (ASTER, 2005).

4. Level 2: Derived geophysical variables at the same resolution and location as Level 1 data (Abrams, 2000)

5. Level 3: The ASTER stereoscopic subsystem consists of nadir and backviewing telescopes operating in the VNIR (Abrams, 2000). The final products of this level include ASTER Global Digital Elevation Model (GDEM), DEMs,

15 orthorectified L1B radiance images and 15 orthorectified L1B radiance images plus DEM (`http://asterweb.jpl.nasa.gov/data\_products.asp`).

For the purpose of the thesis, where spectral reflectance values of water were needed at high spatial resolution, the Level 2 surface reflectance dataset (AST_07) was used. The next subsection presents a description of this dataset product.

Table 3.4: ASTER products table

Shortname	Level	ASTER Product	Grid Resolution (m)
AST_L1A	1A	Reconstructed Unprocessed Instrument Data	15, 30, 90
AST_L1AE	1A	Reconstructed Unprocessed Instrument Data (Expedited)	15, 30, 90
AST_L1B	1B	Registered Radiance at the Sensor	15, 30, 90
AST_L1BE	1B	Registered Radiance at the Sensor (Expedited)	15, 30, 90
AST_05	2	Surface Emissivity	90
AST_07	2	Surface Reflectance (VNIR and SWIR)	15, 30
AST_07XT	2	Surface Reflectance (VNIR and Crosstalk Corrected SWIR)	15, 30
AST_08	2	Surface Kinetic Temperature	90
AST_09	2	Surface Radiance (VNIR and SWIR)	15, 30
AST_09T	2	Surface Radiance TIR	90
AST_09XT	2	Surface Radiance (VNIR and Crosstalk Corrected SWIR)	15, 30
ASTGTM	3	ASTER Global Digital Elevation Model	30
AST14DEM	3	Digital Elevation Model (DEM)	30
AST14DMO	3	DEM and Registered Radiance at the Sensor (Orthorectified)	15, 30, 90
AST14OTH	3	Registered Radiance at the Sensor (Orthorectified)	15, 30, 90

3.3.2 Surface Reflectance product description

The AST_07 product contains surface reflectance at each of the nine VNIR and SWIR bands. The reflectance values are obtained after applying an atmospheric correction to radiances at the sensor (ASTER, 2002). The objective of atmospheric correction is to produce more accurate surface reflectance and to potentially improve the extraction of surface parameters from the sensor images (Chrysoulakis *et al.*, 2010).

Atmospheric correction consists of deriving a relationship between the surface radiance/reflectance and the top of the atmosphere (TOA) radiance from information of the scattering and absorption characteristics of the atmosphere (Information obtained from site `http://lpdaac.usgs.gov/get\_data`). The algorithm used to obtain surface reflectance is based on a look-up table (LUT); the LUT approach uses results from a Gauss-Seidel iteration radiative transfer code (RTC) (Thome, 1999) that assumes the Earth is flat with a homogeneous, Lambertian surface and a plane parallel, homogeneous atmosphere divided into optically thin layers (Thome *et al.*, 1998). The algorithm uses outside sources (like the Multi-angle Imaging SpectroRadiometer (MISR), MODIS or climatological means) for the atmospheric information required due to the fact that the sensor was not designed to collect atmospheric information. The atmospheric correction removes effects due to changes in satellite-sun geometry and atmospheric characteristics. The final results of this algorithm are in reflectance units (going from 0 to 1) with an accuracy as a function of the accuracy of input atmospheric characteristics and the surface slope. The absolute accuracy of this product is 0.01 for reflectance < 0.15 and 7% for reflectance values > 0.1 (ASTER, 2002).

3.3.3 Advantages of ASTER satellite

ASTER satellite provides images of 15 by 15 m pixels, which for the case of monitoring supra-glacial lakes is an useful resolution. Uncertainties risen from mixed pixels at the ice/water interface are still present with this sensor, but that is an uncertainty accounted for in the results derived from this sensor.

ASTER products provide atmospherically-corrected surface reflectance data, which requires no other basic processing before using them (Miura *et al.*, 2008). ASTER follows from previous sensors designed for higher spatial resolution surface charac-

terisation, which was begun with the Landsat Thematic Mapper (TM) and System Pour l'Observation de la Terre (SPOT), the Advanced Very High Resolution Radiometer (AVHRR). The global advantages of ASTER were that it increased the number of bands in comparison with those previous instruments, plus giving high-spatial resolution and same-orbit stereo capability (Thome *et al.*, 1998).

There are other satellites with higher spatial resolution than ASTER, like IKONOS or the System for Earth Observation (SPOT) with 4 m and 5 m respectively. However, IKONOS presents a 13.8 km swath in comparison with 60 km of ASTER, whereas SPOT has the same as ASTER. Nevertheless, more ASTER scenes with supra-glacial lakes were available for the study. For these reasons, a compromise between spatial resolution, temporal resolution and availability was made and ASTER was selected. Another reason is that MODIS imagery was used to locate supra-glacial lakes (Selmes *et al.*, 2011) and both MODIS and ASTER present the same flying time since they are both onboard the TERRA satellite, so that fact was very useful in terms of lake selection and scene quality comparison. The next section will introduce the MODIS sensor.

3.4 MODIS

3.4.1 Sensor description

The Moderate Resolution Imaging Spectroradiometer (MODIS) is an instrument operating on both the Terra and Aqua satellites. Terra was launched on December 1999 and Aqua on 2002. The MODIS instruments were designed to monitor terrestrial, atmospheric and oceanic phenomenology across the Earth. MODIS instrument provides high radiometric sensitivity in 36 spectral bands and Table 3.5 shows the first 7 bands only, because they are the ones used for land/cloud/aerosols

boundaries and of interest for this thesis. With a ± 55° scanning pattern at the EOS orbit of 705 km, the instrument presents a 2,330 km swath view and a ground repeated orbit of one or two days. MODIS was designed to provide long-term global measurements at moderate spatial resolution, between 250 m to 1 km.

Table 3.5: MODIS first seven bands

Band	Bandwidth (μm)	Pixel size (m)
1	0.620 - 0.670	250
2	0.841 - 0.876	
3	0.459 - 0.479	500
4	0.545 - 0.565	
5	1.230 - 1.250	
6	1.628 - 1.652	
7	2.105 - 2.155	

MODIS sensor has different data levels; Level 1A data set contains radiance count for all the channels, together with instrument and spacecraft ancillary data. Level 1A data are used as input for geolocation, calibration and processing. Then, Level 1B dataset contains calibrated and geolocated radiances in W/(m^2 mm sr) for all the channels generated from the previous level 1A. One of the applications of MODIS is for the acquisition of land parameters, which requires that the TOA radiance to be transformed to surface reflectance. This process is called atmospheric correction; which is based on the same theory as the algorithm applied for ASTER. The atmospheric correction algorithm uses MODIS products as inputs (see Table 3.6). Other results are DEMs, Data Assimilation office (DAO) for surface pressure, water vapour, and ozone.

After applying the required algorithms MODIS level 1B radiance are corrected for

Table 3.6: List of MODIS products used as an input to the atmospheric correction algorithm (modified from (Vermote and Vermeulen, April 1999)) (*Bidirectional Reflectance Distribution Function).

MODIS products	Characteristics
MOD02	Geographically registered and calibrated radiances
MOD03	Geographically registered and calibrated radiances
MOD35	Cloud mask
MOD04	Spectral aerosol optical thickness
MOD05	Precipitable water
MOD07	Ozone
MOD43	Surface BRDF*

atmospheric effects and then transformed into a surface reflectance dataset. The result is an estimate of the surface spectral reflectance for each band as it would have been measured at ground level if the atmospheric scattering and absorption were not present (Vermote *et al.*, 1997; Vermote and Vermeulen, April 1999). The algorithm is applied to bands 1 to 7 and it includes corrections for the effect of atmospheric gases, aerosol, and thin cirrus clouds, and it is applied to all non-cloudy level 1B pixels that pass the level 1B quality control. The atmospheric correction assumes that the signal received at the sensor is the result of the mixed reflectance of the pixel and reflectance values from surrounding pixels, each weighted by their distance from the target. This effect is known as the adjacent effect. In the case of MODIS ten pixels are used to correct this effect. Moreover, because the atmospheric point spread depends on the view angle; this is also taken in to account with their relationship. There are some characteristics of MODIS sensor that allow us the provide more accurate results from the atmospheric correction than previously (Vermote and Vermeulen, April 1999);

1. The seven channel in the spectral interval 0.41 to 2.1 μm, which allows the estimation of aerosol optical thickness.

2. The bandwidths in the reflectance channels are smaller so they do not overlap with the water vapour absorption bands, with the exception of 0.659 μm and 2.1 μm. This results in a reduction of the error introduced by water vapour absorption.

3. Another improvement is the pixel reduction to 250 m in MODIS from the previous 1 km in the Advanced Very High Resolution Radiometer (AVHRR), which increases the detection of cloud pixels and reduces the subpixel cloud mixing.

4. Finally, apart of the seven reflectance channels, two other MODIS channels, 3.75 μm and 1.38 μm, are used for determining aerosol optical thickness and for detecting thin cirrus and stratospheric aerosols respectively.

The output algorithm is the MOD09, which process daily the 7 land bands at 250 m (Bands 1 and 2) and 500 m (Bands 3-7). The product is the estimates of the surface reflectance, QA (Quality Assurance) bit fields and QA metadata for each dataset. This MODIS product was the one used in this thesis and Table 3.7 gives the different accuracy for each band derived from the atmospheric correction algorithm.

Table 3.7: Total theoretical accuracy of MODIS surface reflectance (from Vermote and Vermeulen (April 1999)).

Band	Absolute error	Relative error % (range)
1	0.005	10 - 33
2	0.014	3 - 6
3	0.008	50 - 80
4	0.005	5 - 12
5	0.012	3 - 7
6	0.006	2 - 8
7	0.003	2 - 8

3.4.2 Justification for data choice

For the purpose of this thesis two different products derived from MODIS were used. First an archive of 2,600 supra-glacial lakes across Greenland derived by Selmes (2011) from MODIS imagery, which includes lake evolution during summer months from 2005-2009 (Selmes *et al.*, 2011). The second product used was MOD09 reflectance values as an input for the model derived in this thesis. Even though ASTER reflectance values are the ones used for the model, since MODIS swath width is bigger and both sensor flown onboard Terra and have equivalent channels, in some cases the ASTER dataset was substituted by MODIS, as it will be explained in the following chapter.

The main advantages of using MODIS is the high temporal resolution, which allows a continuous monitoring of Greenland. MODIS reflectance data were rejected as a main source due to its coarse spatial resolution: 250 m. The reason is that in order to obtain an accurate estimate of lake depth and hence volume, the spatial resolution of the pixels has to be as high as possible to avoid mixed pixels. That is why ASTER was chosen instead.

3.5 CASI

The Compact Airborne Spectrographic Imager (CASI) is a VIS/NIR pushbroom (along track) imaging spectrograph with a reflection grating and a 2D Charge Coupled Device (CCD) solid-state array detector. The instrument operates by looking down in a fixed direction and imaging successive lines of the scene under the platform, building up a two-dimensional image as the platform moves forward. The CASI instrument has been used in a variety of applications from forest cover mapping to pollution monitoring (`http://geo.arc.nasa.gov/sge/jskiles/top-down/OTTER/OTTER_docs/CASI.html`).

This instrument was flown on an aircraft by the Natural Environment Research Council (NERC ARSF) Project on the 19^{th} and 24^{th} of July 2007 over the Helheim glacier in south east Greenland. The data collected during those flights was used in this Thesis (Chapter 7). The NERC ARSF provides the UK environmental research community with high spectral and spatial resolution data from the CASI instrument.

3.5.1 Sensor description

The CASI "hyperspectral imager" with a spectral range of 400-915 nm, is fully programmable prior to, and during flight operations, and can be operated in a series of different modes depending on the requirements of the project application (`http://www.neodc.rl.ac.uk/index.php?option=displaypage&Itemid=71&op=page&SubMenu=-1`). The operational modes are:

1. **Spatial Mode**: 512 pixels across swath, up to 18 spectral bands fully programmable.

2. **Spectral Mode**: Full spectrum (288 channels) for up to 39 look directions spread across swath (between 4 an 16 pixel spacing between look directions). This also includes a monochromatic image at full spatial resolution (the Scene Recovery Channel).

3. **Enhanced Spectral Mode**: Full spectrum (288 channels) in a block of 101 adjacent spatial pixels.

4. **Full frame**: 512 pixels across swath by 288 spectral pixels (around 1-2 seconds of integration time). This limits this mode to laboratory calibration or ground-based field use.

The original specifications of CASI presented an imaging area of the array of 512 x 288 pixels. The 512 spatial pixels across the field of view (FOV) of 38.4° degrees

across track give a 1.23 meter ground resolution (cross track) per 1 km above ground level altitude. The along track ground resolution is approximately the product of the integration time and the aircraft speed. The required integration time is directly proportional to the number of bands collected in spatial mode or in spectral mode the number of views. The spectral range of the CASI instrument is shown in Table 3.8. The spectral resolution was 2.5 nm FWHM (Full Width Half Maximum). The 2.5 nm FWHM is nominal, the bandwidth changes significantly with wavelength. Channel to wavelength registration is subject to slight deviations (3 nm) at large view angles due to spectral sag.

Table 3.8: CASI bands list.

Band number	Wavelength central frequencies (nm)	FWHM* (nm)
1	448.46	10.51
2	488.94	9.58
3	551.17	5.82
4	606.95	6.78
5	649.63	3.95
6	669.6	4.91
7	700.09	4.92
8	709.63	4.92
9	740.24	4.93
10	748.86	3.98
11	761.34	3.02
12	779.60	3.99
13	819.14	4.97
14	863.75	4.99
15	940.04	5.04

3.5.2 Data processing details

CASI delivered data are Level 1b HDF (Hierarchical Data Format), which means that the radiometric calibration algorithms have been applied and that the navigation information has been appended. These Level 1b (or Level 2) files need to be geocorrected with the AZGCORR software, which produces a Level 3 file. The CASI atmospheric corrections and geocorrection processes will be detailed in the methodology (Chapter 4).

3.5.3 Data quality

For the geocorrection process a LIDAR DEM produced during the flight is used. That DEM is not tested for geometric error; nevertheless screen-shots of the Level 3 outputs generated by NERC ARSF were included in the data distribution to indicate the expected accuracy. Some bands show missing pixel lines where the instrument has bad pixels. These have been removed automatically where detected in the calibration process applied by NERC ARSF, but some remain.

3.5.4 Justification for data choice

For the purpose of this thesis CASI geocorrected data were used in Chapter 7. The CASI reflectance obtained from the geocorrection process was used an input for the water reflectance model developed in Chapter 5. It is a an application of the model to derive the depth of water in crevasses. Due to the high spatial resolution of CASI (10 by 10 m in this study), this sensor appeared to be useful for this purpose, since crevasses can be very narrow features.

3.6 Landsat 7

The last data source described here is Landsat 7, which is one of the latest National Aeronautics and Space Administration (NASA) satellite in a series that has produced uninterrupted multispectral record of the Earth's land surface since 1972 (Figure 3.6). Landsat 7 data are free available from the United States Geological Survey Global Visualisation Viewer (USGS GLOVIS) (`http://glovis.usgs.gov/`).

System	Launch (End of service)	I(s)	Resolution (meters)	Communications	Alt. Km	R Days	D Mbps
Landsat 1	7/23/72 (1/6/78)	RBV MSS	80 80	Direct downlink with recorders	917	18	15
Landsat 2	1/22/75 (2/25/82)	RBV MSS	80 80	Direct downlink with recorders	917	18	15
Landsat 3	3/5/78 (3/31/83)	RBV MSS	40 80	Direct downlink with recorders	917	18	15
Landsat 4*	7/16/82	MSS TM	80 30	Direct downlink TDRSS	705	16	85
Landsat 5	3/1/84	MSS TM	80 30	Direct downlink TDRSS**	705	16	85
Landsat 6	10/5/93 (10/5/93)	ETM	15 (pan) 30 (ms)	Direct downlink with recorders	705	16	85
Landsat 7	4/99	ETM+	15 (pan) 30 (ms)	Direct downlink with recorders (solid state)	705	16	150

I(s) = Instrument(s)
R = Revisit interval
D = Data rate
*TM data transmission failed in August, 1993.
** Current data transmission by direct downlink only. No recording capability.

Figure 3.6: Table showing the key mission characteristics of the Landsat Program, where the product used in this thesis is highlighted in red (`http://landsathandbook.gsfc.nasa.gov/pdfs/Landsat7_Handbook.pdf`).

The Landsat 7 satellite was launched on April 1999. This satellite was designed for a 705 km, sun synchronous, earth mapping orbit with a 16-day repeat cycle. Its payload is a single nadir pointing instrument, the Enhanced Thematic Mapper Plus

(ETM$^+$). The ETM$^+$ is a derivative of Thematic Mapper (TM) engineered for previous missions (Landsat 4 and 5), although is more closely related to the Enhanced Thematic Mapper(ETM), which was lost during the Landsat 6 failure. The primary performance related changes of the ETM$^+$ over the TM's are the addition of the panchromatic band (Table 3.9) and two gain ranges, the improved spatial resolution for the thermal band, and the addition of two solar calibrators.

The ETM$^+$ design provides for a nadir-viewing, eight-band (Table 3.9) multispectral scanning radiometer capable of providing high-resolution image information of the Earth's surface when operated from Landsat 7, a 3 axis stabilized spacecraft located in a near polar, sunsynchronous and circular orbit at a 705 km nominal altitude, with an orbit inclination of 98.2°. The ETM$^+$ was designed to collect, filter and detect radiation from the Earth in a swath 185 km wide as it passes overhead and provides the necessary cross-track scanning motion while the spacecraft orbital motion provides an along-track scan.

Table 3.9: Landsat 7 ETM$^+$ spectral characteristics (`http://landsathandbook.gsfc.nasa.gov/pdfs/Landsat7_Handbook.pdf`).

Satellite	Sensor	Band number	Bandwidths (nm)	Resolution (m)
Landsat 7	ETM$^+$	1	450-520	30
		2	520-600	30
		3	630-690	30
		4	760-900	30
		5	1,550-1,750	30
		6	10,400-12,500	60
		7	2,080-2,350	30
		Panchromatic	500-900	15

The goal of the Landsat 7 program was to achieve radiometric calibrations of the

data to ± 5% uncertainty over the 5-year life of the mission. Pre-launch, the mission design supported this requirement through hardware design changes, and instrument characterizations. When the satellite was on orbit, this 5% requirement was supported by a monitoring and calibrations program, and the implementation of any necessary changes to the ground processing of the data.

3.6.1 Justification for data choice

For the purpose of this thesis Landsat 7 was a useful tool to validate CASI modelled results on Helheim glacier. This was due to the availability of scenes that coincided with the CASI flights, with a few days difference and also with field observations by Sneed and Hamilton (2007). Landsat 7 radiometric data were atmospherically corrected in order to obtain reflectance values for the model applied in this thesis. The pre-processing of Landsat 7 scenes is presented in Chapter 4.

3.7 Chapter Summary

The main data source in this thesis was ICESat altimetry measurements (GLA12). This satellite was chosen due to it high accuracy in elevation measurements and the convenient campaigns operational periods, coinciding with the season when lakes might be empty, which allowed lake depth approximation from ICESat elevations. The other important data source was ASTER surface reflectance (AST_07), which was used as an input to the water reflectance model used in this thesis to estimate water depth from the optical properties of water. MODIS imagery was an important source for lake location and evolution, obtained from the archive developed by Nick Selmes. Finally CASI and Landsat 7 data were used as an application of the model develop in this thesis and hence as a test of itself.

Chapter 4

Methodology

4.1 Introduction

In this chapter the methodology used to derive melt-water depth of supra-glacial lakes on the GrIS is described. In the previous chapter the data sources from the different remote sensing sensors used as an input to these methods were introduced. The main sections of this chapter are the water reflectance model used in this thesis as an approach for water depth estimation (Section 4.2) and the statistical analysis of the model carried out via a Monte Carlo simulation approach (Section 4.5). Also, an application of the water reflectance model for water-filled crevasses over the front of the glaciers is introduced in Section 4.6. Chapters 5, 6 and 7 present the results derived directly from this chapter.

4.2 Derivation of water depth from optical imagery

An estimate of total water volume stored in supra-glacial lakes is crucial for assessing the potential formation of hydrofractures and hence drainage to the bed (Krawczynski *et al.*, 2009); however a volume estimate of melt-water is challenging for several reasons. Firstly, even though lake area can be derived from spectral differences between water and snow/ice (Lüthje *et al.*, 2006; McMillan *et al.*, 2007), due to spatial and temporal limitations from the sensors (like cloud cover), a full coverage of the GrIS is impractical (Selmes *et al.*, 2011). Secondly, estimation of lake volume also requires depth knowledge. Here is where the aim of this thesis comes in, starting with solving the integral form of the RTE for z (Equation 4.5).

Recent estimates of water depth have been made for single or specific melt-lakes on the GrIS from high-resolution optical satellite images, such as ASTER (Georgiou *et al.*, 2009; McMillan *et al.*, 2007; Sneed and Hamilton, 2007), where they use the RTE (Lyzenga *et al.*, 2006; Stumpf *et al.*, 2003) to derive the melt-water depth. These studies compare depths and volume estimations derived from satellite imagery (Box and Ski, 2007) with either *in situ* measurements or lidar observations (Georgiou *et al.*, 2009).

The difference in the spectral characteristics between ice/snow and water is the key tool for monitoring and mapping the area distribution of lakes, both spatially and temporally, on sea-ice and on the GrIS (Selmes *et al.*, 2011; Bartholomew *et al.*, 2011; McMillan *et al.*, 2007; Sundal *et al.*, 2009; Tedesco and Steiner, 2011; Leeson *et al.*, 2012). Figure 4.1 shows the theoretical difference in reflectance between glacier ice, snow, firn, and clear water on the visible near infrared part of the spectrum. The clear water curve is the one of interest in the current study. However, in order to provide a full picture of a lake and to quantify the potential of the water

stored draining to the lake bed, the volume stored is necessary, water depth estimations are also needed (Krawczynski *et al.*, 2009). A refinement of the existent water reflectance model for a wider quantification of water stored on melt-lakes across Greenland is the purpose of this thesis.

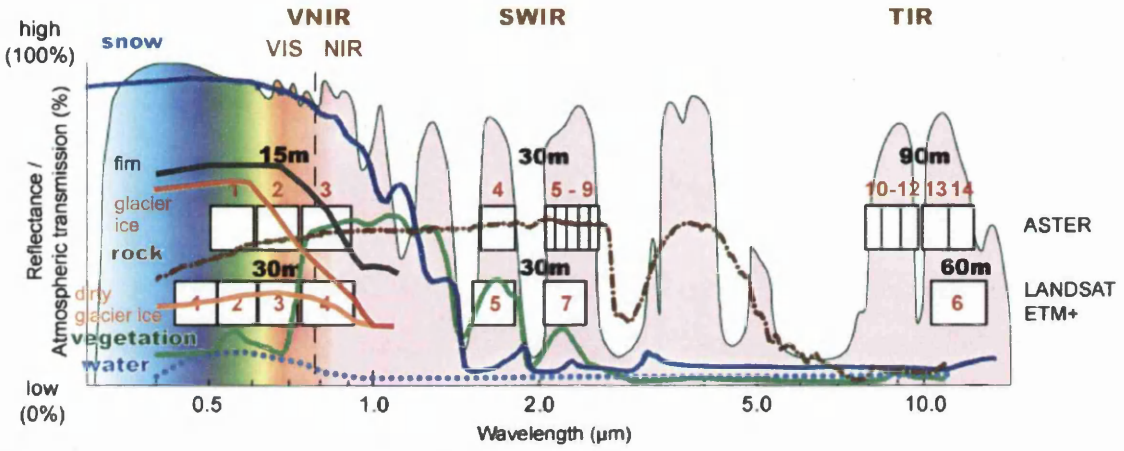

Figure 4.1: Spectral characteristics of water, snow and ice (coloured lines). Numbered boxes: wavelength range of the channels of the ASTER and the Landsat ETM^+ (and TM) sensors with their spatial resolution. Coloured area: atmospheric transmission; high values indicate that a high degree of solar radiation passes through the atmosphere, low values indicate that large parts of solar radiation are blocked by atmospheric gasses, (`http://www.esa.int/esaMI/Eduspace_Environment_EN/SEMPJ7TWLUG_0.html`).

Water depth has been estimated from the optical properties of water for supra-glacial lakes, coral reefs areas, for bathymetry mapping of coastal regions (Lyzenga, 1978; Smith and Baker, 1981; Philpot, 1989; Maritorena *et al.*, 1994; Stumpf *et al.*, 2003; Lyzenga *et al.*, 2006; Mishra *et al.*, 2004; Sneed and Hamilton, 2007, 2011) and in sea-ice melt-lakes studies (Morassutti and Ledrew, 1996).

In the field of supra-glacial lakes on the Greenland ice sheet, satellite imagery from ASTER (Sneed and Hamilton, 2007, 2011; Georgiou *et al.*, 2009) has been combined with *in situ* bathymetry measurements (Sneed and Hamilton, 2011; Box and Ski, 2007) and also multispectral measurements (Tedesco and Steiner, 2011) to measure lake depth. Figure 4.2 is an example of the different reflectance values given by three of the spectral bands from one of the ASTER scenes used in this thesis. The

reflectance at the lake surface given by ASTER is used as the main input to the water reflectance model described next.

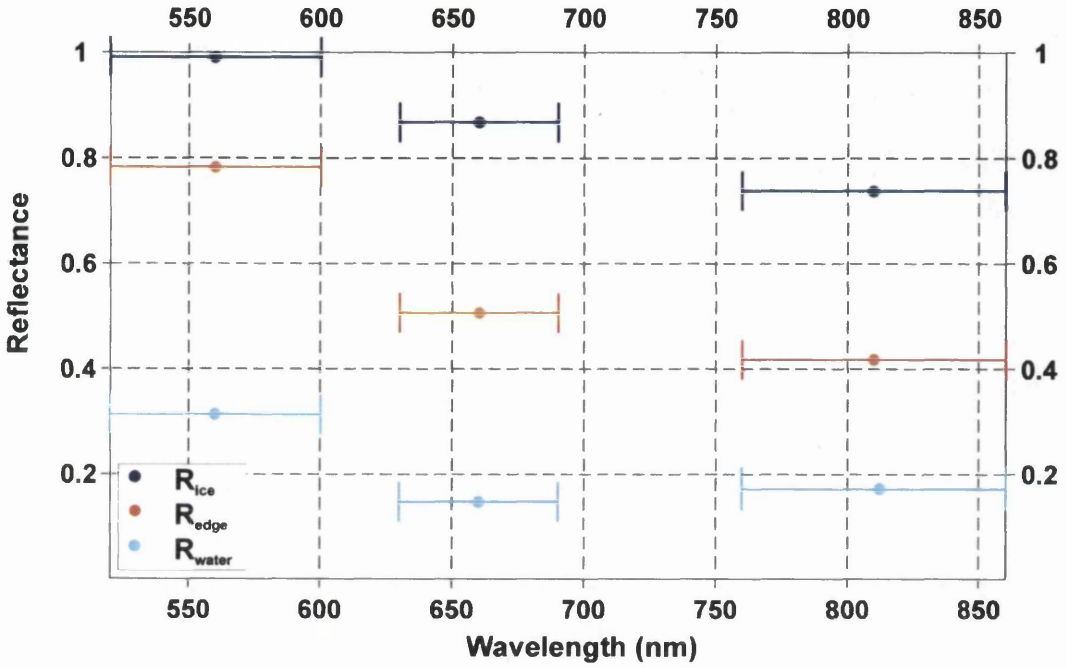

Figure 4.2: Example of the difference in the spectral characteristics of ice and water from an ASTER scene used in this thesis. Blue/red/light blue dots corresponds to ice/edge/water reflectance values for wavelengths between 520-860 nm, corresponding to the three windows of Band 1 2 and 3N of ASTER. The horizontal error bars just show the range of values that each of the bands take of the spectrum and the dot the mean wavelength value.

4.2.1 Theoretical background of the water reflectance model

The depth derivation approach from optical properties of water applied in this thesis is based on Equation 4.1, which is a simple radiative transfer model for optically shallow waters of the general form (Philpot, 1989) and states that the water-leaving spectral radiance $L(z, \lambda)$ decays exponentially with water depth z (see Figure 4.3). This relationship is some form of the *Bouguer-Lambert-Beer law*, which relates the transmission of light with the properties of the material (water in this study) that travels through. The focus of this thesis is the upward radiance after travelling

through the water in a two way form (see Figure 4.3).

$$L(z, \lambda) = L(0, \lambda) \times \exp(-K_\lambda z) \tag{4.1}$$

Where $L(0, \lambda)$ is the spectral radiance at zero depth and K_λ is the spectral attenuation (Lyzenga, 1978). The source radiance L is defined as the radiant flux per unit solid angle per unit projected area of surface [W m^{-2} sr^{-1}] (Zaneveld and Boss, 2003). The solid angle Ω is the surface area of a unit sphere covered by the surface's projection onto the sphere (`http://mathworld.wolfram.com/SolidAngle.html`). If the concept of radiance is applied in remote sensing, Figure 4.3 summarises the general case of a passive satellite, where the sensor receives the radiance that first is emitted by the sun, arrives to the water surface, travels through it, reflects on the bottom substrate and back to the water surface.

The knowledge of the physical parameters that define the water properties is needed to derive water depth. The optical properties of water are divided into two classes:

1. The Inherent Optical Properties (IOP) depend only upon the medium, which implies that they are not a function of the light field within the medium (Mobley, 1994). Examples of IOP relevant to this thesis are the absorption coefficient and beam attenuation coefficient.

2. The Apparent Optical Properties (AOP) are a function of both the medium (IOP) and of the geometric structure of the ambient light field. Examples of AOP relevant to this thesis are the reflectance measure by remote sensing and vertical diffuse attenuation coefficients (Mobley, 1994).

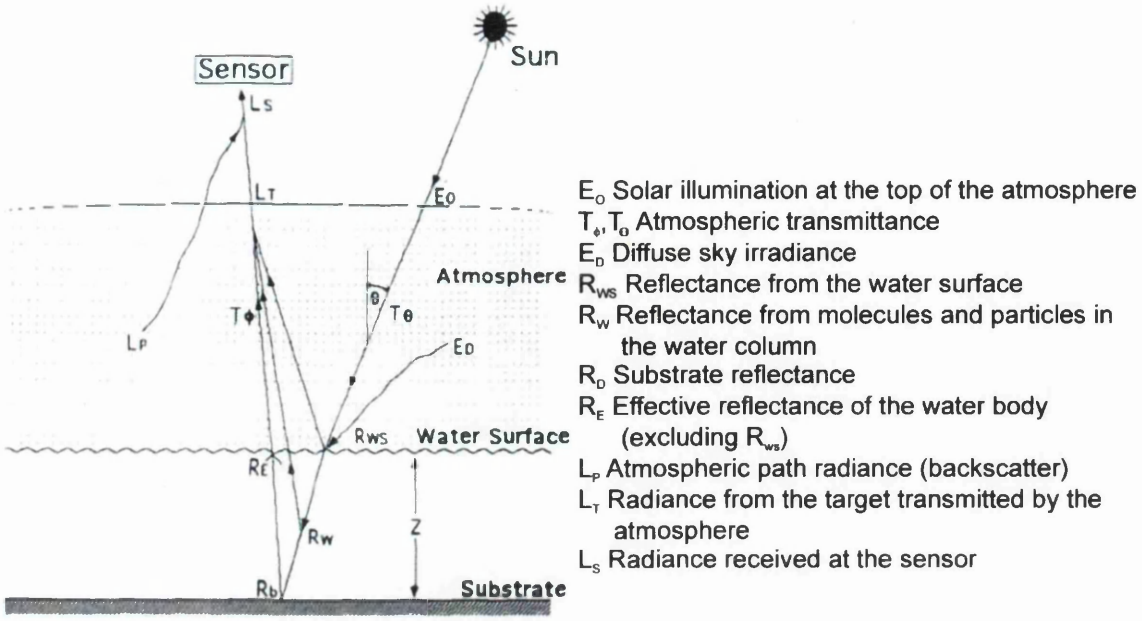

Figure 4.3: Radiance arriving at the sensor after travelling through the water, showing the difference factors that influence the amount of radiance reaching the sensor. (modified from Bierwirth *et al.* (1993)).

The IOP of water, water depth, and bottom type are the main physical agents governing the magnitude and spectral composition of the backscattered flux received by the sensor (Maritorena *et al.*, 1994). The *Bouguer-Lambert-Beer law* (Equation 4.1) is the integral form of the Radiance (or radiative) Transfer Equation (RTE) (see Equation 4.2), which drives the behaviour of radiance within natural bodies. After applying boundary conditions to the RTE, it is possible to predict the radiance distributions under the water surface, given the prior knowledge of the water's IOP, the incident light flux and the medium conditions (Mobley, 1994). The full derivation of the Bouguer-Lambert-Beer law from Equation 4.2 will not be shown in this thesis; however the basis of it will be explained next, together with the fundamental theorems that are used to derive it.

$$\frac{1}{\nu}\frac{\partial}{\partial t}\left(\frac{L}{n^2}\right) + \widehat{\xi}\cdot\nabla\left(\frac{L}{n^2}\right) = -c\left(\frac{L}{n^2}\right) + L_*^E + L_*^I + L_*^S[Wm^{-3}sr^{-1}nm^{-1}] \quad (4.2)$$

Where $\widehat{\xi}$ is the travelling direction of the photons, which travel at the speed of light $\widehat{\xi} = \vec{v}/\nu$; c is the total beam attenuation coefficient; and finally the three last terms of the Equation are the mathematical descriptions of elastic scattering (L_*^E), inelastic scattering (L_*^I) and true emission (L_*^S). The term L/n^2 comes from the *fundamental theorem of radiometry* (Equation 4.3);

$$\frac{L_2}{n_2^2} \approx \frac{L_1}{n_1^2} \tag{4.3}$$

This theorem states that 'the radiance divided by the square of the index of refraction is constant along any path'; which in turn derives from the n^2 law for radiance for the case of a beam with a normal incidence on air-water interface. The fundamental theorem of radiometry is only true for paths in a vacuum, since real media have some kind of absorption and scattering. However, in a vacuum $n_1 = n_2 = 1$, so Equation 4.3 stays as $L_1 = L_2$, which is a generalization of the radiance invariance law.

Before solving the RTE it is important to understand how the light travels through the water medium (Figure 4.3); the light is defined as a beam of photons travelling in all directions through the medium. Six processes are necessary and sufficient to describe an energy balance equation for a beam of photons travelling through the water body:

1. Loss/gain of photons through scattering without change in wavelength (elastic scattering).

2. Loss/gain of photons through scattering with change in wavelength (inelastic scattering).

3. Gain of photons through creation of photons by conversion of non-radiant energy to radiant energy (true emission).

4. Loss of photons through annihilation of photons by conversion of radiant energy to non-radiant energy (true absorption).

All these processes need to be written in a quantitative way so they can be included in the equations. The general RTE expresses the change in L/n^2 along a path with the sum of the physical terms causing that change (Mobley, 1994) (see Equation 4.2). Equation 4.2 is the most general form of the RTE for unpolarised radiance, where unpolarised mean that the photons present randomly orientated electric field directions.

The *Bouguer-Lambert-Beer law* (see Equation 4.1) is derived from the general RTE mentioned above (see Equation 4.2) assuming an idealised case of source-free and non-scattering media and then integrating it for the whole water depth. Satellite-based studies use the surface pixel reflectance to derive water depth; hence the Bouguer-Lambert-Beer law is usually transformed in terms of reflectance (Equation 4.4) (Lyzenga, 1978; Philpot, 1989; Maritorena *et al.*, 1994; Stumpf *et al.*, 2003; Sneed and Hamilton, 2007) and solved for water depth z (Equation 4.5). Note that there is a negative sign in Equation 4.5 ("-g")that does not come from Equation 4.4. This sign is added because depths are assumed negative.

$$R_w = R_\infty + [A_d - R_\infty] \times \exp(-gz) \tag{4.4}$$

$$\downarrow$$

$$z = (\ln(A_d - R_\infty) - \ln(R_w - R_\infty))/(-g) \tag{4.5}$$

Where R_w is the pixel reflectance at the water surface provided by the sensor, defined as the ratio of emergent radiance relative to the total irradiance (Bierwirth *et al.*, 1993); R_∞ is the reflectance at depth zero of the deep ocean; A_d is the bottom albedo and g [m^{-1}] is the effective attenuation coefficient. Because there is no analytical solution of this RTE, any analytical equation is an approximation (Maritorena *et al.*, 1994). Equation 4.5 is the form of the RTE on which this thesis is based. This thesis applied the simple reflectance model (Equation 4.5) for depth estimations, which is fully explained in the following subsection.

4.2.2 Types of Water reflectance models

The different types of water reflectance models are based on either one wavelength or on a combination of wavelengths. If the model is based on the knowledge of a single wavelength band the model linearises the relationship between the reflectance and the water depth; this is known as the simple water reflectance model, which accounts for almost the whole signal received from a sensor over clear shallow water. This model ignores scattering in the water and internal reflection at the water surface (Lyzenga, 1978). An extension of the single band model is the estimation of depth for various wavelengths. The use of more bands with inversion weighted by uncertainties could be expected to results in greater accuracy in comparison with the single band approach. However the multiple band approach was dismissed for the purpose of this thesis for simplification and as a first approach.

For the case of two bands with equal attenuation coefficients, the water reflectance model is equivalent to the ratio method, which considers a pair of bands so the ratio of the bottom reflectance in the two bands is the same for all the bottom types (Lyzenga, 1978; Lyzenga *et al.*, 2006). The main advantage of the ratio method is that it requires fewer empirical coefficients and it can tuned using available soundings (Stumpf *et al.*, 2003).

The model can be extended for a N-band system, although the disadvantage of this algorithm is that it is more complex and hence more difficult to implement (Lyzenga, 1978; Lyzenga *et al.*, 2006); furthermore this method introduces errors in depth determination from each of the bands (Bierwirth *et al.*, 1993).

For simplification and because the studies this thesis was motivated by used the single band reflectance model (Sneed and Hamilton, 2007, 2011; Tedesco and Steiner, 2011; Georgiou *et al.*, 2009), it was decided to proceed with the same method for comparison with our results.

4.3 Description of the single band water reflectance model applied for depth derivation

This thesis presents an optimisation of the parameters derived from ASTER images of melt-water lakes and validated with ICESat laser altimetry data over empty lakes (see Figure 4.4) on south west Greenland (sea map location in Figure 4.8), as an input to the simple reflectance model for fresh water (Equation 4.9).

A total estimate of water stored on the entire Greenland ice sheet each year is yet unknown. If a global set of the three physical parameters governing Equation 4.5 (A_d, R_∞ and g) can be derived and applied to every lake across the GrIS, the model can be up-scaled to the entire ice sheet and thus a volume of water stored in melt-water lakes can be derived. A total number of eleven lakes was used for this section, all of them located in the same area. The reason for so few lakes in the sample was due to the sparse subset of overlapping ASTER scenes and ICESat tracks for the same year.

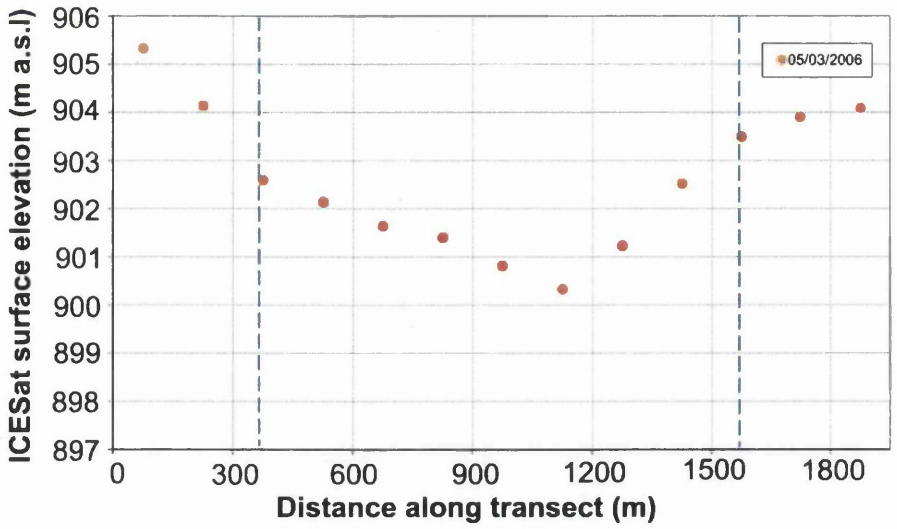

Figure 4.4: Example of an ICESat track over an empty lake giving the surface elevation above sea level, which is then transformed into lake depth to validate the ASTER depth derivations. In this case the lake in the graph is about 1,200 m long and 5 m deep.

The input value in Equation 4.5 is the returning signal at the surface of the lake from the ASTER scene (R_w), which comprise information about radiation between two media (water/atmosphere) and about the underlying bottom (Bierwirth *et al.*, 1993). Consequently, some assumptions are needed to apply Equation 4.5 in this study, which are based on previous studies (Sneed and Hamilton, 2007). *In situ* studies showed that the following assumptions are appropriate for this purpose (Sneed and Hamilton, 2011; Tedesco and Steiner, 2011); however further discussion is needed for individual assumptions, which is included Chapter 8, with the highest uncertainty related with mixed pixels due to the spatial resolution of the sensor used.

1. The fundamental assumption made is that the optical properties of the water are vertically homogeneous (Philpot, 1989).

2. Homogeneity of the lake bottom assuming ice as the substrate, which allow us to consider A_d constant across the lake.

3. Negligible particular matter within the water column.

4. No inelastic scattering.

5. Absence of wind, *i.e.* no waves on the lake surface.

6. Melt-water considered pure natural water, assumption needed for the determination of g.

In order to get an accurate comparison between estimated depth from the water reflectance model and observed depth (ICESat measurements), a transect was drawn for each lake in the ASTER scene following the ICESat track across the supra-glacial lake and the surface reflectance values from Band 1 in ASTER (R_w) are taken as an input to the water-reflectance model described below (Figure 4.5). A depth profile of each lake was obtained and then compared with the ICESat depth profile.

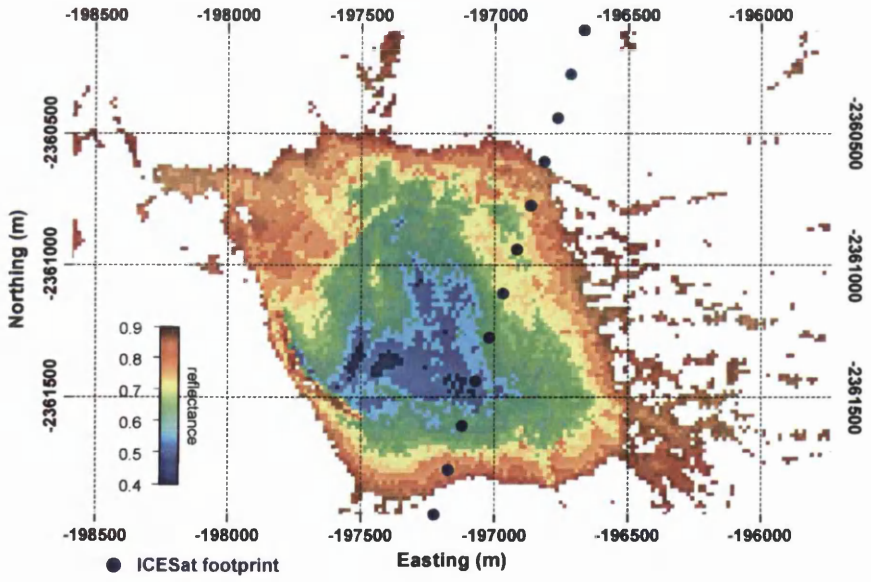

Figure 4.5: Example of a supra-glacial lake used in the study. Pixels show reflectance values of Band 1 from an ASTER image (scene taken on 26/06/2006). A transect of the reflectance along the ICESat track (dark blue circles) is used as an input for Equation 4.5, to estimate lake depth. Co-ordinates in polar stereographic projection.

To appreciate the relationship that exists between water reflectance and water depth given in the water model used in this thesis (Equation 4.5), Figure 4.6 shows the

surface reflectance values given by ASTER for the same transect as the one on Figures 4.4 and 4.5. From this transect, water depth will be derived using the water model explained above.

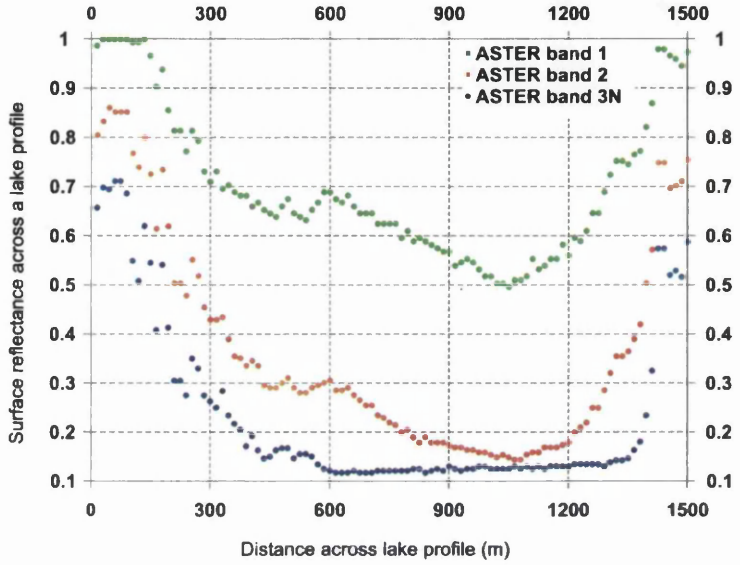

Figure 4.6: Reflectance (R_w) transect of a lake given by an ASTER scene for Band 1, 2 and 3N; clearly showing the attenuation/wavelength relationship.

4.3.1 Parameters determination

From Equation 4.5 it can be seen that four inputs are needed in order to solve it. The input surface reflectance R_w is given by the sensor ASTER. The other three inputs are the physical parameters A_d, g and R_∞. If the optical properties of the water body (R_∞ and g) are known, the increase in reflectance due to the presence of the bottom can be interpreted in terms of depth only if the albedo is known. The parameters are obtained as follows;

Reflectance at the water surface

The spectral Band 1 (520-600 nm) values of reflectance from the ASTER scenes is taken as the R_w. The reason for this is that there is strong absorption after wavelengths above 650 nm, which excludes the use of those bands for depth derivation (Tedesco and Steiner, 2011). The spectral absorption coefficient $a(\lambda)$ is inversely proportional to the wavelength and directly proportional to $k(\lambda)$ (Equation 4.6), which is collectively called one of the optical constants of water, although it depends strongly on wavelength;

$$a(\lambda) = \frac{4\pi k(\lambda)}{\lambda} \tag{4.6}$$

The physical explanation of the absorption curve (Figure 4.7) is that, for pure water at blue wavelengths (450-520 nm), photons are not energetic enough to excite electrons to higher levels of energy of the water molecule (Equation 4.7 shows the inverse relationship between the energy of a photon (q) and λ), and the photons do not have the right energy to interact easily with the molecule as a whole. Hence the photons do not interact strongly with the water molecules, and $a(\lambda)$ is at its minimum value. As the wavelength increases from blue to red and beyond, the photons begin having just the right energy to excite first the fundamental vibrational and then the rotational modes of the water molecules, and absorption once again increases rapidly in the infrared. The pronounced peaks in $a(\lambda)$ in the infrared result from these resonant excitations of molecular motions. At very long wavelengths, the photons are not energetic enough to excite molecular motions, and the absorption decreases (Mobley, 1994) (see Figure 4.7).

$$q = \frac{hc}{\lambda} \tag{4.7}$$

Where $h = 6.626x10^{-34}Js$ is the *Plank's constant* and $c = 3x10^{8}m/s$ is the speed of light (Mobley, 1994).

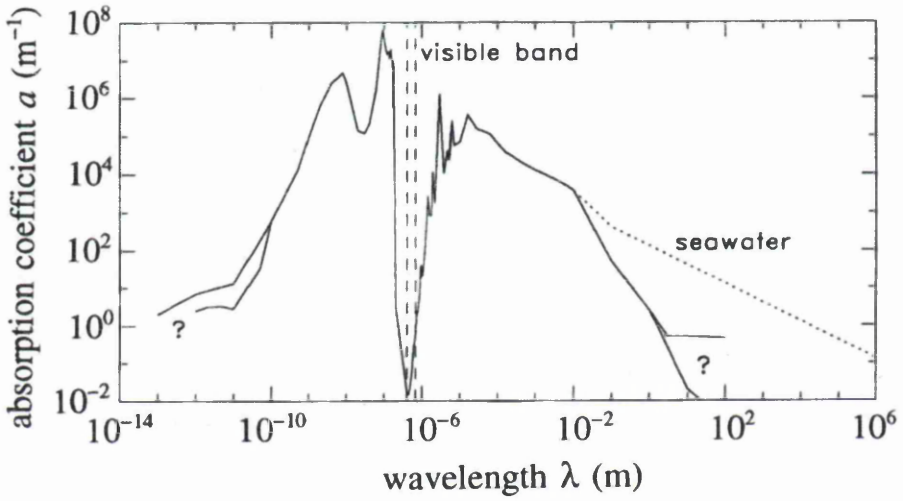

Figure 4.7: Spectral absorption coefficient for pure water (solid line) and for pure sea water (dotted line) as a function of wavelength. The visible band is the one relevant for the purpose of the thesis (from (Mobley, 1994)).

Band 1 in ASTER is the lowest wavelength range available, which corresponds with green, therefore this spectral band was chosen for R_w; also previous studies used that band also so it was used also for comparison (for example Sneed and Hamilton (2007)).

Bottom albedo

To determine A_d the difference in attenuation between spectral bands was taken into account. Due to the low attenuation in the blue and green (Band 1 in ASTER) bands in comparison with the red band (Band 3), A_d from ASTER Band 1 can be considered to have similar values to pixels at the lake shore. ASTER Band 3 was selected to locate adjacent pixels defining the lake edge, following Sneed and Hamilton (2007); where it was shown that, for a wavelength of 780 nm and water depth of 10 cm, the adjacent pixel of bare ice will show 40% lower reflectance than a neighbouring pixel with water. Thus locating two adjacent pixels with at least 40% difference in reflectance in Band 3, the reflectance value of the pixel at the shore of band 1 was then approximated as the bottom albedo A_d. The equation would be as follows (Equation 4.8);

$$A_d(\lambda_1) = R_\infty + [R_w(\lambda_1) - R_\infty] \times \exp(-gz) \tag{4.8}$$

With z = 10 cm; solving this equation was found how the approximation was valid because $A_d(\lambda_1, z = 10cm) \approx R_w(\lambda_1, z = 10cm)$ with a difference of less than 0.01.

The choice of the bottom albedo is the most important parameter in Equation 4.5, for instance a decrease of 1% in the bottom albedo, results in a 16% decrease in the melt-lake volume (Sneed and Hamilton, 2007). The sensitivity of depth estimation with variations in bottom albedo is demonstrated in the results and discussion chapters.

Effective attenuation coefficient.

The approach used to determine g was based on Smith and Baker (1981), who compiled a table (see Table 4.1) with the diffuse attenuation and the absorption coefficients for spectral bands between 200 and 800 nm. In that study the attenuation coefficient for clearest natural waters was related to the inherent optical properties of pure water. Many of the current studies about models based on the radiative transfer theory use the parameters derived in this study (for example Sneed and Hamilton (2007); Georgiou *et al.* (2009)). Optically pure water is defined as a medium that is free of dissolved and suspended particulate material. Water reflectance models established an inequality (Equation 4.9) that relates the diffuse attenuation coefficient for the clearest natural freshwater (K_w^{fw}) with the absorption coefficient for pure water (a_w) and the backscattering coefficient for molecular scattering in freshwater (b_m^{fw}).

A previous study (Maritorena *et al.*, 1994) demonstrated that to estimate the attenuation coefficient, a two-flow model can be applied, which consists of two streams of irradiance. For natural light fields, one of the streams defined as flowing downward through the optical media and the other as flowing upward (Ackleson and Klemas, 1986). The two-flow model applied by Maritorena *et al.* (1994) included the upwelling irradiance and the irradiance ratio (reflectance) between the bottom (with a given albedo) and the top layer. They validated the approximated solutions comparing with Monte Carlo simulations. In this model the effective attenuation coefficient is considered as a two-way attenuation coefficient $g \approx K_d + (aD_u)$ (Smith and Baker, 1981; Philpot, 1989; Maritorena *et al.*, 1994; Stumpf *et al.*, 2003; Sneed and Hamilton, 2007), where K_d is the diffuse attenuation coefficient for downwelling light, which corresponds with K_w^{fw} in Equation 4.9; a is the beam absorption coefficient, and D_u is the distribution factor for upwelling irradiance.

Table 4.1: Absorption ($a_w(\lambda)$) and scattering (b_m^{fw}) coefficients for pure water applied for the estimation of the effective attenuation coefficient g (Modified from Smith and Baker (1981)).

λ(nm)	$a_w(m^{-1})$	$b_m^{fw}(m^{-1})$
500	0.0257	0.0022
510	0.0357	0.0020
520	0.0477	0.0019
530	0.0507	0.0017
540	0.0558	0.0016
550	0.0638	0.0015
560	0.0708	0.0014
570	0.0799	0.0013
580	0.108	0.0012
590	0.0157	0.0011
600	0.244	0.0011
610	0.289	0.0010
620	0.309	0.0009
630	0.319	0.0009
640	0.329	0.0008
650	0.349	0.0007
660	0.400	0.0007
670	0.430	0.0007
680	0.450	0.0006
690	0.500	0.0006

$$K_w^{fw} \geq a_w + 1/2b_m^{fw} \tag{4.9}$$

Many observations exits for K_d but virtually none for D_u; the problem is that the vertical diffuse attenuation coefficient is not directly measurable and has specific values for each situation and geometry. Therefore a range of values $1.5K_d < g < 3K_d$ is usually taken, where the highest value is used in case of strongly absorbing waters (Philpot, 1989). This approximate solution assumes that all the attenuation coefficients can be replaced by a unique coefficient K.

In this thesis the expression approximated in Equation 4.10 was used, with K_w^{fw} estimated from Equation 4.9. g is taken as the mean of all the effective attenuation coefficients derived from that equation when applied for the wavelength range of the correspondent band width, in this case for Band 1 ASTER 520-600 nm (see Table 4.1). This approximation is thought to cause an underestimate of the actual attenuation suffered by the albedo difference, (A_d-R_∞) in Equation 4.4. This approximation will imply an overestimation of depths (Maritorena *et al.*, 1994). Nevertheless, the approximate formula (Equation 4.10) can be safely adopted in operations when interpreting or predicting the reflectance of shallow waters, in particular if g and R_∞ have been estimated from remotely sensed data.

$$g = K \approx 2K_w^{fw} \tag{4.10}$$

Reflectance of optically deep water

R_∞ was determined using a similar approach as in Georgiou *et al.* (2009) and Sneed and Hamilton (2007), who showed that by choosing ASTER images with ocean present, R_∞ could be approximated to the darkest pixel in the ocean. In our case no ASTER scenes had ocean present; nevertheless MODIS scenes with ocean present corresponding to the same day and time to the ASTER scenes used in the study were available; the dark pixel approximation was therefore made for those scenes. Reflectance values of deep water were taken from MODIS band 4 (545-565 nm), since it is the equivalent band to the ASTER band 1. Before carrying out the approximation, reflectance values from both sensors for the same target were compared, selecting an area of bare ice. Only images where those values were similar between sensors were selected, with less than 0.01 reflectance difference.

4.4 Water reflectance model validation

ICESat laser altimetry data acquired from eleven empty lakes in spring/autumn in the south-west of Greenland (Figure 4.8) were used to assess the accuracy of lake depth estimates derived from ASTER imagery based on the water reflectance model. Availability of both ASTER images and ICESat tracks crossing the empty lakes in the same year limited lake selection. Visible near infrared (VNIR) ASTER spectral bands with 15 m spatial resolution were used. For ICESat altimetry data, Release 31 from the product ICESat/Geoscience Laser Altimeter System (GLAS) (Zwally *et al.*, 2002b) was used. ICESat data provides elevation above sea level, with 60 m average laser footprint (Zwally *et al.*, 2002b), and 172 m footprint separation (Fricker *et al.*, 2005a).

To convert ICESat elevations to lake depth, the absolute elevation of the lake shore must be determined. To achieve this ASTER images of the lakes combined with

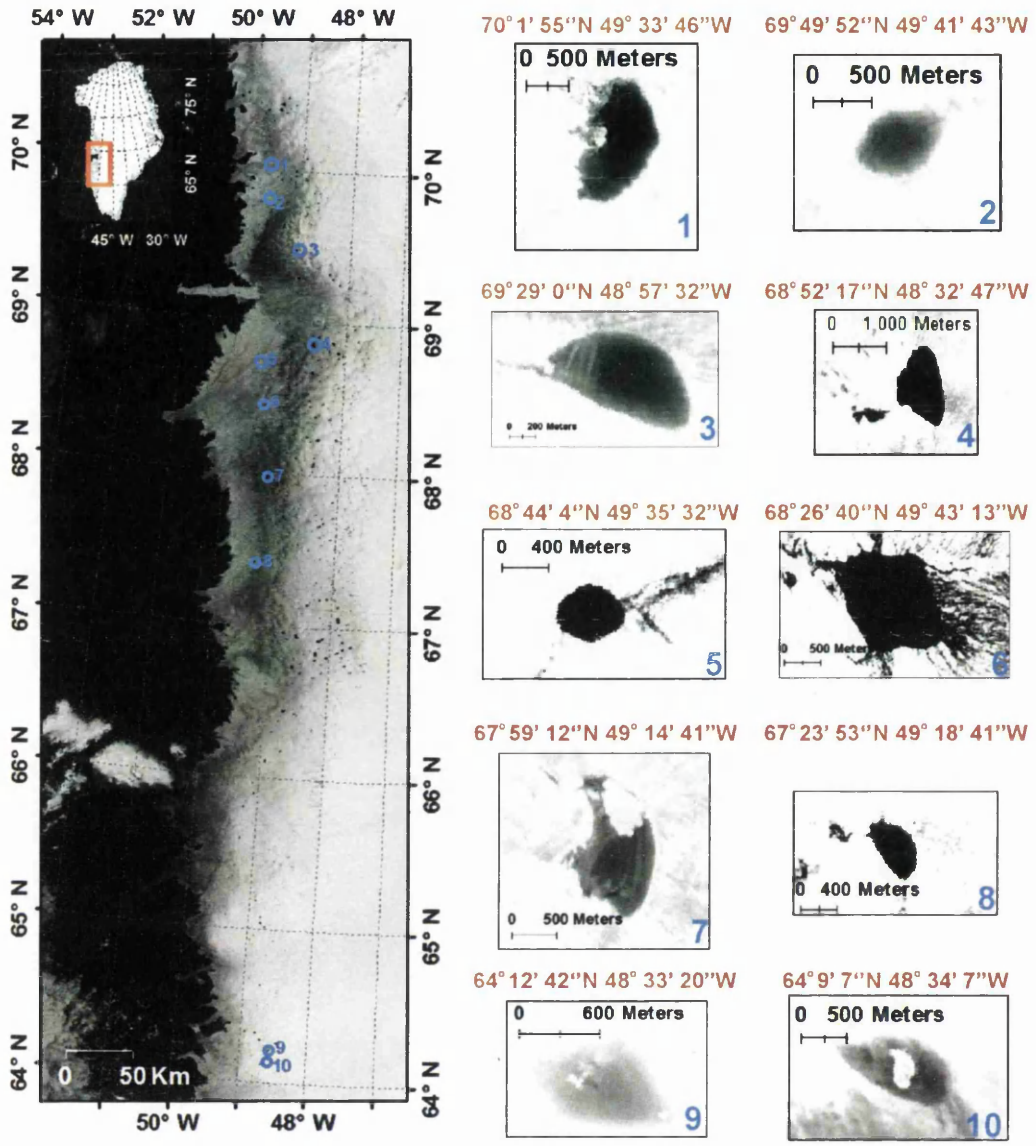

Figure 4.8: Location map of the lakes used for the water reflectance model, image background is a 250 m resolution MODIS Band 1 scene. Right side of the Figure shows ten snap shots of the lakes used in this Chapter; the scenes correspond to ASTER Band 1 scenes, which are the ones used as an input to the water reflectance model.

ICESat footprints were used to locate the margin of each studied lake and set that as zero depth. There are three causes of uncertainty in this method:

1. ASTER and ICESat data are not recorded on the same dates.

2. The separation between footprints in ICESat tracks prevents a precise lake shore demarcation.

3. ICESat vertical resolution decreases on slopes greater than 1°.

To account for these error bias in depth estimation, the vertical uncertainty in the ICESat elevation set as depth zero was selected to be ± 0.5 m, this was calculated looking the consecutive footprints and averaging the elevation difference for the available campaigns. Since the vertical resolution of ICESat laser is 0.15 m (Fricker *et al.*, 2005b; Siegfried *et al.*, 2011), 0.65 m of total vertical uncertainty is given to ICESat depth measurements in this study.

4.5 Statistical analysis

Modelled melt-water lake depth is a function of the physical parameters described above (A_d, g and R_∞), all of them dependent on the wavelength (λ) and each of them present a different source of errors. The overall uncertainty in the lake depth is crucial in order to understand how the parameters influence the final melt-lake depth estimates; moreover if the depth error is known, ICESat depth values can be compared with the model error range. For this purpose, a numerical differentiation could be used to perform a statistical analysis of the method; however the complexity of the analysed function (Equation 4.5) led the study to search for an alternative approach. Monte Carlo simulations are convenient for this purpose, since they can be applied to equations with multiple degrees of freedom and with independent variables (Metropolis and Ulam, 1949). In this study the parameters can be considered to be independent because the model was applied for one band, so λ is essentially constant. The Monte Carlo simulation used in this research was modified from an approach previously applied for Ground Penetrating Radar (GPR) analysis interested on precision of velocity (Booth *et al.*, 2011).

4.5.1 Monte Carlo approach

The Monte Carlo Method is a statistical approach to solve any problem in statistical physics using random positions, called samples (Krauth, 2006). Monte Carlo simulations provide a probability density function of an output variable, using as an input random permutation of samples within an imposed range of values for each variable. The ranges chosen are based on the errors associated with the given value, which are discretised in the simulation. In order to honour the Gaussian sampling regime, the Monte Carlo simulation should generate more depth manifestations than the number of possible permutations of the input variables, itself given by the product of the number of discrete samples in each variable range.

The Monte Carlo simulation was applied to Equation 4.5, although only A_d, g and R_∞ are taken as the three independent parameters that randomly varied within the error margin, respectively. R_w is the input value given by the ASTER sensor, as was considered fixed, so no Monte Carlo Simulation was applied to the pixel surface reflectance. However, R_w absolute error is still considered as established from AST07 product (Thome, 2001) (Table 4.2).

Table 4.2: Absolute errors of the four input variables to Equation 4.5. The three first columns correspond to the independent variables and the last one to the input varible.

δA_d	δg (m^{-1})	δR_∞	δR_w
$\pm$ 0.07	$\pm$ 0.15	$\pm$ 0.005	$\pm$ 0.07

The absolute error of each parameter was taken as the error range (Table 4.2); g error was based on Smith and Baker (1981) results; for R_∞ the absolute error was given by Vermote and Vermeulen (April 1999). A_d absolute accuracy was taken from Thome (2001). When error ranges for all the parameters were specified the simulation generated depths estimates for each pixel along the transect defined.

For each of the 4 input variables (R_w, A_d, g and R_∞), the error range was discretised into 20 samples, which showed a good compromise between model accuracy and computational effort. Consequently, a total of $20^4 = 160,000$ variable permutations were obtained, thus the Monte Carlo simulation generated 160,000 depth manifestations. The first approach taken was to assume a Gaussian distribution of random samples, which was imposed on the input parameters, making samples of each variable more likely to be located at the centre of the error range. In Chapter 5 different model scenarios will be applied to analyse the performance of the water reflectance model when the initial settings are altered. Figure 4.9 shows the distribution of random samples if a Gaussian distribution is imposed and in the case of a Box distribution. In a Box distribution all the permutations present the same probability.

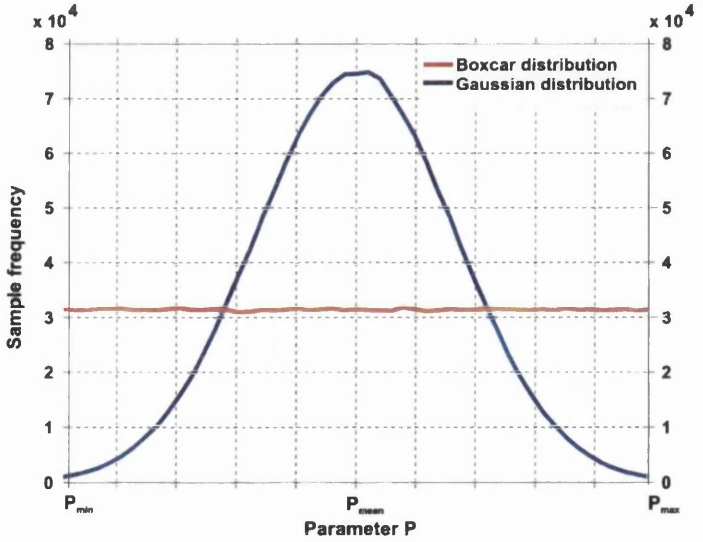

Figure 4.9: Histograms of boxcar (red line) and Gaussian distributions (blue line). The y-axis corresponds to the frequency that each of the values of the sample is sampled, and the x-axis corresponds to the different parameters P (A_d, g and R_∞) where the Monte Carlo approach is applied, with P_{min} corresponding to zero value and P_{max} corresponding to 1.

It is important to test after how many permutations the Monte Carlo simulation converges, to test whether 160,000 permutations are enough to make the simulation stable. Figure 4.10 presents the results from this test. The plot shows the residuals

(Equation 4.11) for different numbers of permutations, between 1 to around 10^6 in an increasing interval of 1. After 1,000 permutations it can be stated that the Monte Carlo simulation is stable for both Gaussian and Box distribution settings. In the case of Box after 100 permutations the model stabilises, whereas the Gaussian distribution needs more permutations.

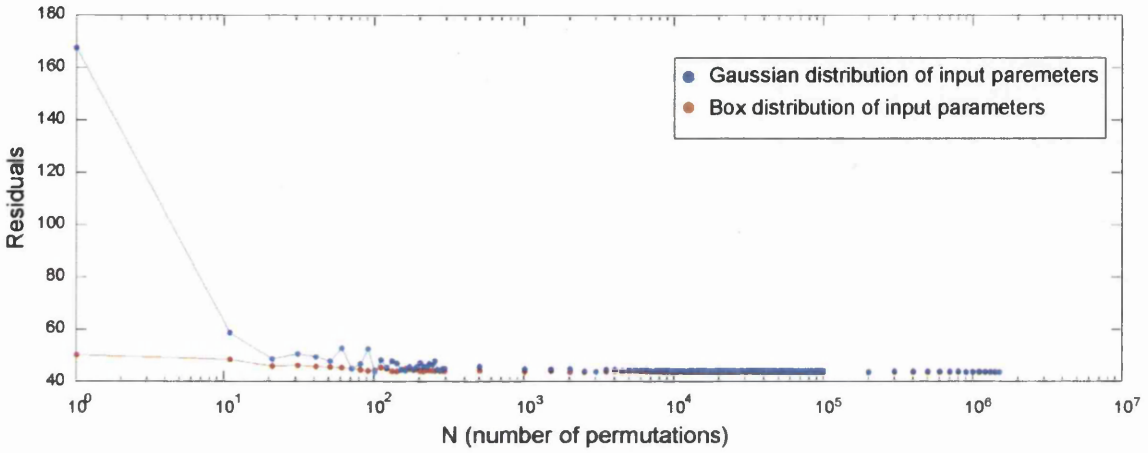

Figure 4.10: Residuals from Equation 4.11.

4.5.2 Optimisation of the Monte Carlo simulations using ICESat elevation data

Once depth and uncertainties were derived from the Monte Carlo simulation, the aim was to minimise the difference between ICESat measurements and ASTER derived depths; for that purpose a minimisation model was applied. The input values were the ICESat values across each transect. Since the ICESat circular footprint is known to be around 60 m in diameter, thirteen pixels of ASTER were selected for each footprint of ICESat (see Figure 4.11). Taking the mean value of the thirteen surface reflectance pixels, we had as many ASTER points as ICESat were included for each lake.

The Monte Carlo Simulation was run again, fixing the mean surface reflectance from ASTER and leaving the other three variables to vary within the same range

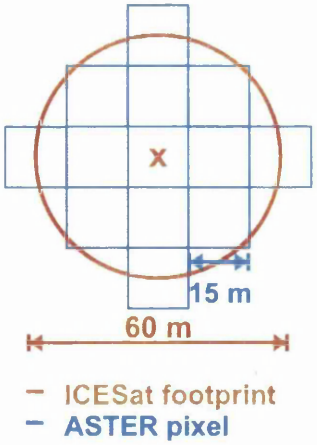

Figure 4.11: Selection of thirteen ASTER pixels (blue) chosen to overlap with ICESat elevation values for one footprint (red).

described in the previous section and again a Gaussian distribution was imposed on the input samples. The model outputs the best lake profile given by all the permutations of the input samples. The Monte Carlo simulation minimises the residuals between ICESat reference profiles (P_{ICESat}) and the modelled depths from the water reflectance model (P_{ASTER}) (Equation 4.11). The best profile for each lake is given by:

$$Best\,profile \Leftrightarrow \sum_{i} ((P_{ASTER}(i) - P_{ICESat})^2) = Minimum \qquad (4.11)$$

Where $P_{ASTER}(i)$ defines the output of the Monte Carlo simulation and P_{ICESat} the ICESat depth profile. From each of the eleven lakes the minimisation model generated a set of values for R_∞, A_d and g that gives the ASTER profile with minimum difference with respect to ICESat profile. Taking the median value of each parameter for the eleven lakes, one global set of parameters was obtained. This parameters set was used to estimate lake depth (Equation 4.5) again, this time with the optimised parameters as an input, so the water reflectance model results represent the best approximation to the observed depth profiles given by ICESat data.

4.5.3 Influences of the Monte Carlo approach over the input parameters to the model

Apart from how the depth profiles vary with the minimisation model, it is interesting also to show how the three input parameters (A_d, g and R_∞) evolve with the model; Figure 4.12 shows the variation of the three parameters within the first ten best profiles of the minimisation; the model performance is discussed in Chapter 8 (Figure 8.7). In Figure 4.12 the curves *Lake 1* and *Lake 2* correspond to two of the lakes used in this study and show how the minimisation model influences on each lake independently optimised. Curve *All the lakes* corresponds to the case of a global minimisation model applied to all the lakes at the same time, as if all the lakes were one. Those graphs show how the parameters vary randomly for each permutation, as expected from the Monte Carlo approach.

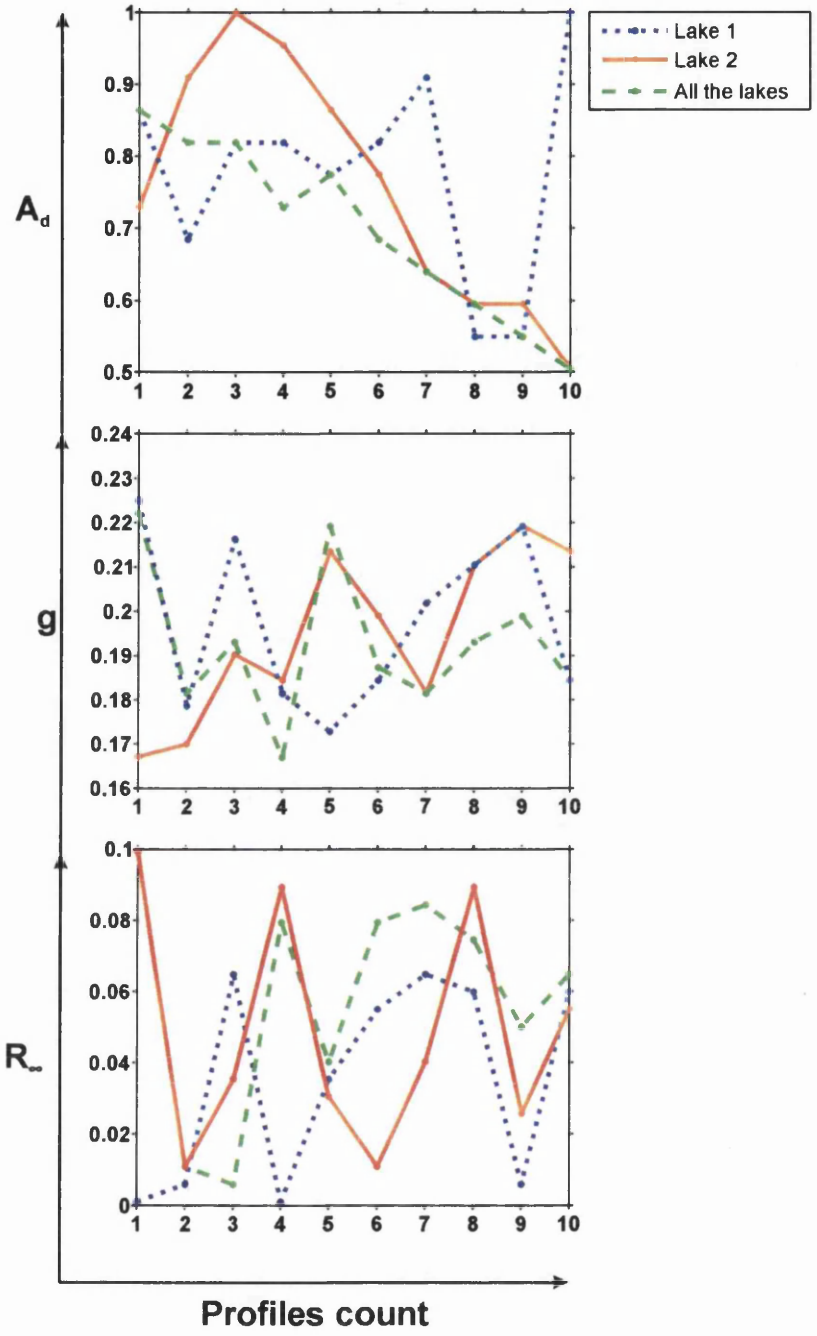

Figure 4.12: Variation of the three input parameters for the best profiles of the minimisation model derived using the Monte Carlo approach. The plots are for two sample lakes used previously in the study (blue dash line and red solid line) and for all the lakes minimised together (green dash line).

4.6 Application of the optimised model to CASI dataset

The last experiment carried out in this thesis explored the potential of applying the water-reflectance model for the quantification of water-filled crevasses depths using CASI hyperspectral aircraft data. The area chosen for this study was Helheim glacier on south east Greenland, owing to the availability of CASI observations. Both Landsat 7 and CASI were used for this experiment, which is presented in Chapter 7. Landsat 7 was firstly used to estimate lake depth from a lake found in Helheim, which also had field observations from Sneed and Hamilton (2011); therefore Landsat 7 modelled depths and the field observations were compared across two years and then with CASI The input data used for the water reflectance model is the surface reflectance given by the atmospherically corrected Landsat 7 scenes.

The Landsat 7 scenes were atmospherically corrected using the 6S radiative transfer approach, which was developed for the TERRA MODIS instrument (Vermote *et al.*, 1997). The version is a full version of the 6S used for MODIS because it includes the input data NCEP (National Centres for Environmental Prediction) water vapour and TOMS (Total Ozone Mapping Spectrometer) ozone (Masek *et al.*, 2012).

CASI hyperspectral dataset was chosen due to the high spatial resolution (less than 10 by 10 m) and due to the availability of the images for Helheim glacier. The scenes used from CASI dataset are from summer 2007. No ICESat campaigns exist that overlap with the crevasses or lakes found on this glacier, therefore *in situ* bathymetry surveys from previous studies were used as reference true depth estimations (Sneed and Hamilton, 2011).

The pre-processing involved in the CASI images is detailed below; the result was atmospherically corrected surface reflectance with a pixel size of 10 m by 10 m.

1. The first step was to atmospherically correct the CASI scenes. For this purpose the Atmospheric correction Module from ENVI software was used, which is the *Fast Line-of-sight Atmospheric Analysis of Spectral Hypercubes*(FLAASH) (ENVI, 2009).

2. Once CASI scenes were atmospherically corrected, the geocorrection was applied using AZGCORR software (AZGCORR, 2005), which is an airborne remote sensing geocorrection package designed by Azimuth Systems and provided by Natural Environment Research Council Airborne Research and Survey Facility (NERC ARSF) (`http://arsf.nerc.ac.uk/`).

3. Before applying the geocorrection the output pixel size needed to be specified; the recommendations from NERC ARSF were followed (`http://arsf-dan.nerc.ac.uk/trac/wiki/Processing/PixelSize#`) and an automatic pixel size calculator tool was applied, which depended on the altitude over the ground (`http://arsf-dan.nerc.ac.uk/trac/wiki/Processing/PixelSize`).

4. After applying the geocorrection, azexhdf tool (AZGCORR, 2005) was used to visualise the geocorrected CASI scenes. This tool was also provided by NERC ARSF.

The geocorrection applied to CASI scenes was not completely successful because in the output scenes the reference coordinate. The AZGCORR package was a novel tool for the research group where this thesis was developed, as well as the used of CASI hyperspectral aircraft dataset. Therefore it was not possible to completely solve the issues associated with the geocorrection, which were related to the reference coordinate system information contained in each scene that was lost after the geocorrection or the atmospheric correction. Nevertheless, for the purpose of this thesis, the geocorrected scenes were still useful. When comparing CASI, Landsat 7 and *in situ* depth measurements from Sneed and Hamilton (2011) from a lake located in Helheim glacier, the interest was focus on the depth profiles derived from

each sensor so even if the coordinates from CASI were missing, a complete lake pixel area comparison was possible. Also for interannual comparisons, lakes form in the same topographic depressions (Echelmeyer *et al.*, 1991) from one year to the next because they are influence by the bed topography and hence do not advert down glacier; therefore CASI scenes were still use for interannual comparisons, although only one year's campaign was available. The lack of coordinate system would be an issue for a direct comparison of pixel to pixel or for monitoring crevasse evolution within days, since crevasses move with the glacier flow.

4.7 Chapter summary

The theoretical background to the water reflectance model is included in this chapter. From the previously developed water reflectance model, a Monte Carlo simulation was applied to obtain a robust statistical analysis of the model and of all the three physical parameters involved in it. The objective of this analysis was to obtain a set of physical parameters that could be applied to each of the supra-glacial lakes on the surface of the GrIS, hence up-scaling the model and obtaining a quantification of the volume of water stored in them and the errors associated with the volumes. This is important to understand the quantification of potentially draining water to the glacier bed and its possible implications on glacial dynamics.

The study was only carried out for eleven lakes located in south west Greenland. This limitation was due to sparse data availability of both ICESat and ASTER, which needed to be from the same year. Data from ICESat was required from when lakes were empty which was possible since ICESat campaigns were in Spring and Autumn. For the case of ASTER, the scenes were usually between July and August, when lakes were water-filled.

In the last section of this chapter CASI hyperspectral imagery was introduced as a tool for quantifying water stored on crevasses. The reason for this is the small pixel sizes, (less than 10 m), which allow the detection of small and narrow crevasses. To achieve this the water reflectance model optimised previously was applied to this dataset. Helheim glacier was selected for this. There was not ICESat available to validate the results from this dataset, hence previous studies that carried out *in situ* measurements over these glaciers were used as a validation of the water-filled crevasses/lakes depth derived in this thesis.

Chapter 5

Lake depths from the water reflectance model

5.1 Introduction

The chapter presents both the water reflectance model, the process of sensitivity testing and refining of the water reflectance model and the results obtained from each step. All the results in this chapter are for the eleven lakes selected across south west Greenland (see map in Figure 4.8, Chapter 4).

Firstly, water-depth was derived from the water-reflectance at the surface from ASTER using parameters values based on previous studies (Sneed and Hamilton, 2011, 2007; Sundal *et al.*, 2009; Tedesco and Steiner, 2011; Smith and Baker, 1981) (Section 5.2.1). These depth estimates are referred to Z_{ASTER} (Figures 5.2, 5.3 and 5.4). As explained in the methodology chapter (Chapter 4) a Monte Carlo simulation was applied to Equation 4.5 (Chapter 4) in order to calculate the uncertainties in Z_{ASTER}.

Secondly, ICESat derived depths (Z_{ICESat}) are used as reference depths in a min-

imisation model, where the parameters used for Z_{ASTER} are the input to the model. Varying these parameters within their error range, the model gives the best set of values so that the residuals between the observed depths (Z_{ICESat}) and the modelled depths (Z_{ASTER}) are minimised (Section 5.2.2). For this minimisation model the Monte Carlo approach is applied again. The depths derived using the minimisation model are called Z_{BEST}.

The set of parameters used for Z_{BEST} (A_d, g and R_∞) are those that provided the best ASTER profile for each lake, *i.e.* the set giving the minimum residual between ICESat depth values and ASTER values. From this set of ideal parameters for each lake, a global set of parameters that could be used in any lake, was obtained by taking the median of the eleven values for each parameter. The water reflectance model was re-run for the eleven lakes and the results depths are referred to as "optimised model estimates" ($Z_{optimised}$) (Section 5.2.3).

In order to further understand the sensitivities of the water reflectance model and why the model tends to underestimate water depth with respect to reference depth Z_{ICESat}, especially in the deeper parts of the lakes, some variations of the model are applied (Section 5.3), referred to as model scenarios (Figure 5.6). First, the model is applied using the parameters and their respective uncertainties (absolute errors) derived from the sensor manufactures or the literature (Smith and Baker, 1981; Sneed and Hamilton, 2007).

To test if the cause of depth underestimation was the restriction of parameters to certain pre-chosen values, the next step was to run the model again allowing the parameters to vary within their physically possible values, although the values were varied so the depth equation gave real numbers. This change did improve the modelled depths with respect to the observed depths (Section 5.3.1), reducing the residuals between the model and the observed depths (Z_{ICESat}).

As explained in Chapter 3, the Monte Carlo simulation was assumed to have a Gaussian distribution, which means that the distribution of the input parameters with their error range has a Gaussian shape. This is an assumption based on the knowledge of the parameters from previous literature. To prove if this assumption is accurate, the model is run again, but this time assuming that the Monte Carlo simulation was a box distribution, which means that all the possible values that the input parameters can take have the same weight of probability (Section 5.3.2).

A very important choice for the optimisation model is whether the minimisation approach is applied independently to each lake and then taking the median of the set of parameters obtained, or if the minimisation model should be applied at the same time to all lakes, since the last aim of this thesis is to obtain a global model. Therefore, results of the model using both assumptions were obtained (Section 5.3.3).

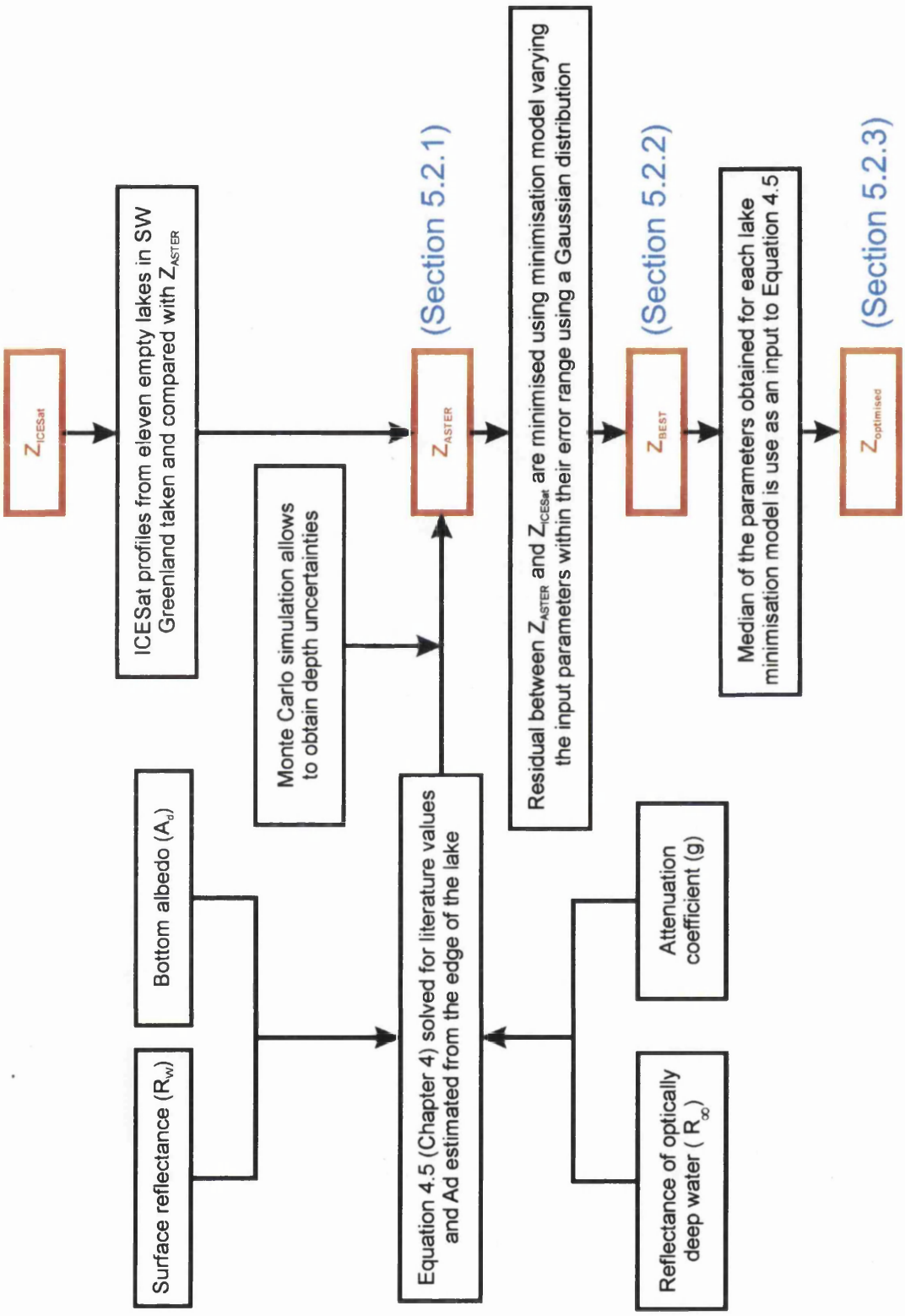

Figure 5.1: Diagram summarising all the steps that are involved in the initial model.

5.2 Initial model results

The development of the optimisation model was based initially on the scenario where the parameter's error range was taken as their absolute error; the probability distribution of the parameters was assumed Gaussian, and the minimisation model was applied independently to each of the eleven lakes.

5.2.1 Depths estimates based on previous literature

In this section, depth estimates for the eleven lakes from applying the water reflectance model to ASTER imagery are presented. The ASTER reflectance values (R_w) are from Band 1 and the input parameters to equation (Equation 4.5 in Chapter 4), were obtained as explained in the Chapter 4. Table 5.1 shows the values taken for each of the lakes as an input to the equation, applying the method showed in Figure 5.1. It is worth pointing out that while eleven lakes are referred to throughout this thesis, in fact then were measured but one (Lake ID 5) has two different ICESat measurements for the same year, so the estimates for that lake were taken twice and counted as two lakes called $5a$ and $5b$.

The results are presented in Figures 5.2, 5.3 and 5.4; this figure shows the median of the depth values obtained from the Monte Carlo simulation. A transect across each lake coinciding with the ICESat track was traced and the results (Z_{ASTER}) are plotted with a blue line. The range and interquartile range (IQR) are also plotted. The mean and the standard deviation were calculated, but for the results and discussion the median is chosen because the distribution is non-normally distributed.

Comparing the results obtained from ASTER observations with the ICESat depths (Figures 5.2, 5.3 and 5.4 blue lines), overall ICESat measurements tended to give

Table 5.1: List of the input parameters for the water reflectance model and their absolute error for each the lakes used in this first experiment described in Figure 5.1. Note that 5a/5b have the same values, this is because the same ASTER scene was used for both, varying only the ICESat reference track and hence reference depth values.

Lake ID	$A_d \pm 0.07$	$g \pm 0.15$ (m^{-1})	$R_\infty \pm 0.005$
1	0.697	0.196	0.011
2	0.835	0.196	0.010
3	0.770	0.196	0.015
4	0.757	0.196	0.012
5a/5b	0.873	0.196	0.011
6	0.855	0.196	0.011
7	0.677	0.196	0.012
8	0.757	0.196	0.013
9	0.992	0.196	0.010
10	0.887	0.196	0.010

deeper lakes than ASTER-derived depths. This discrepancy was not always the case in the shallow parts of the lake, where the sparse ICESat footprints do not resolve whether there is a stepped or smooth slope, whereas ASTER-derived depths give more detailed lake topography. Nevertheless, ICESat measures are within the lower range of the estimated values from the Monte Carlo simulation. The sum of the residuals between Z_{ICESat} and Z_{ASTER} taking the absolute value is 37.86 m, with a total of 44 footprints for all the lakes together.

Figure 5.2: Lake depth (m) *vs* distance along profile (m) for the eleven studied lakes. Red dots are Z_{ICESat} measurements for each footprint; vertical and horizontal red lines are the respective uncertainties. Blue lines are Z_{ASTER} derived from equation 4.5 (Chapter 4) and the input parameters on Table 5.1; the grey area and the blue dash lines are the range and IQR derived from the Monte Carlo simulation. Black dots are Z_{Best} profiles for each lake considering minimum difference between Z_{ICESat} and Z_{ASTER}, based on a Monte Carlo permutation of the parameters (R_∞, A_d, g). Green lines are $Z_{Optimised}$ profiles derived from equation 4.5 using as an input the set of optimised parameters (Table 5.3); green dash lines are the error range derived from the Monte Carlo simulation for the new set of parameters (NE to SW distance along profile (m)). Figure continues in Figures 5.3 and 5.4.

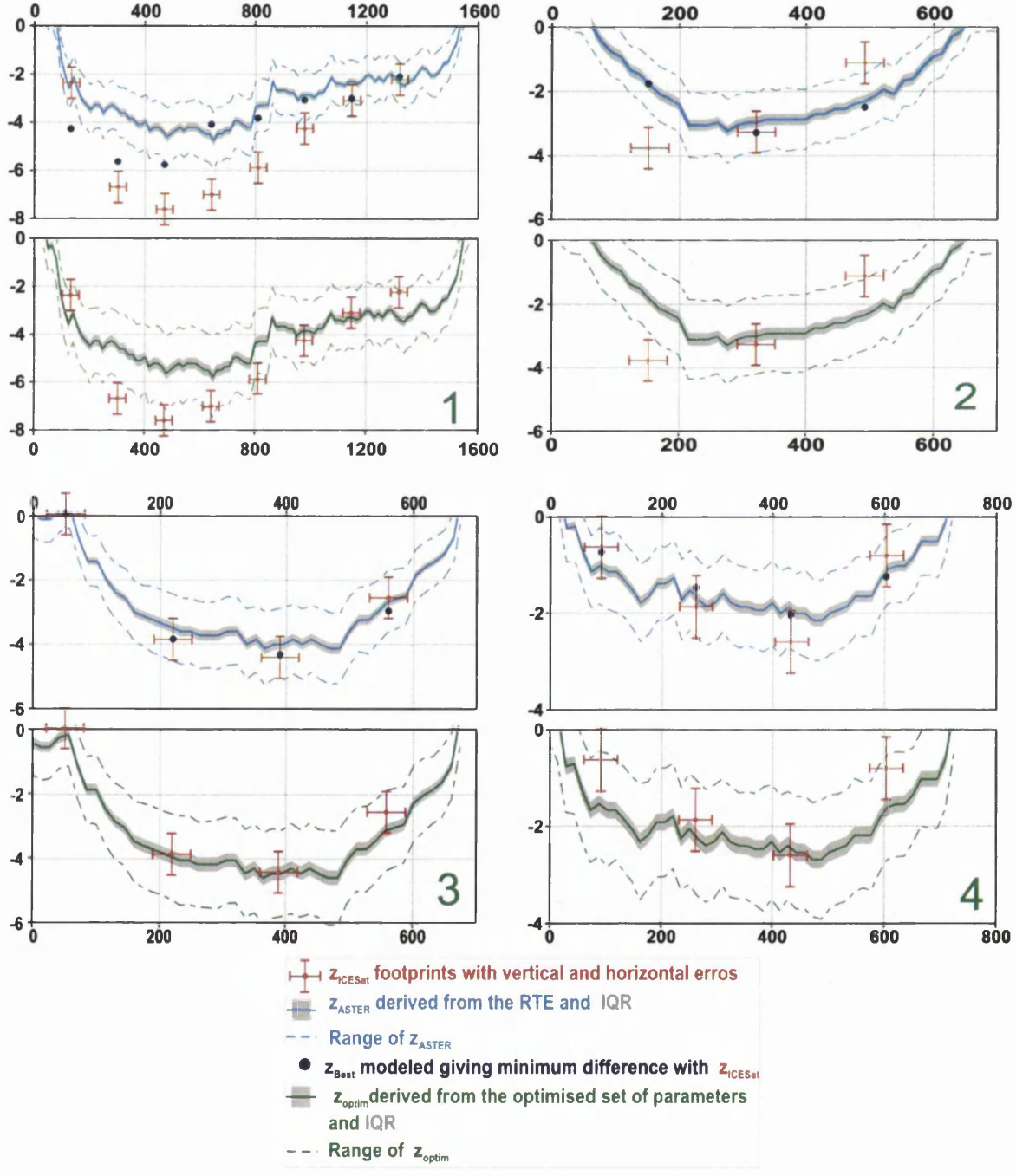

Figure 5.3: Lake depth (m) vs distance along profile (m) for the eleven studied lakes. Red dots are Z_{ICESat} measurements for each footprint; vertical and horizontal red lines are the respective uncertainties. Blue lines are Z_{ASTER} derived from equation 4.5 (Chapter 4) and the input parameters on Table 5.1; the grey area and the blue dash lines are the range and IQR derived from the Monte Carlo simulation. Black dots are Z_{Best} profiles for each lake considering minimum difference between Z_{ICESat} and Z_{ASTER}, based on a Monte Carlo permutation of the parameters (R_∞, A_d, g). Green lines are $Z_{Optimised}$ profiles derived from equation 4.5 using as an input the set of optimised parameters (Table 5.3); green dash lines are the error range derived from the Monte Carlo simulation for the new set of parameters (NE to SW distance along profile (m)). Continued Figure 5.2.

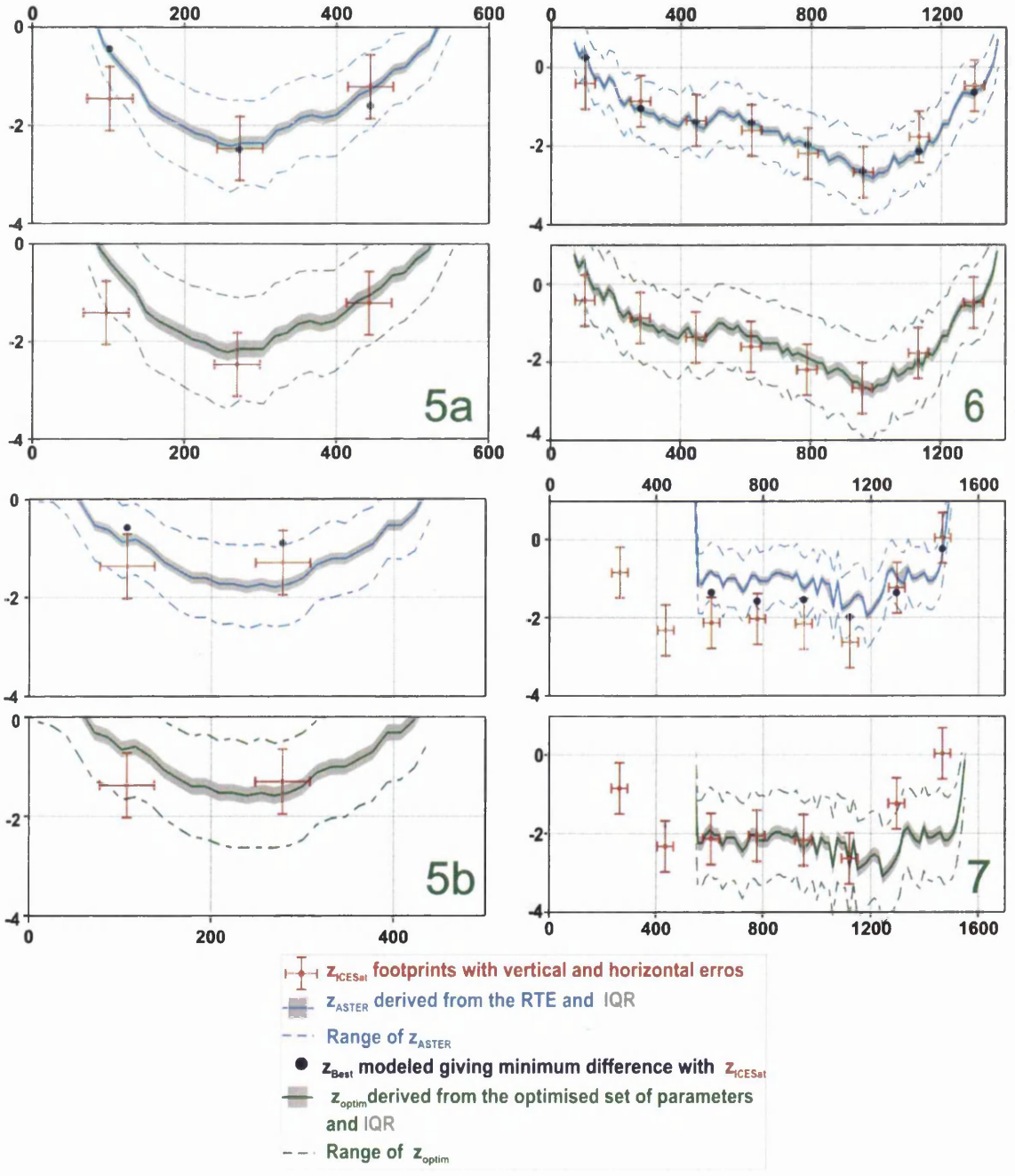

Figure 5.4: Lake depth (m) vs distance along profile (m) for the eleven studied lakes. Red dots are Z_{ICESat} measurements for each footprint; vertical and horizontal red lines are the respective uncertainties. Blue lines are Z_{ASTER} derived from equation 4.5 (Chapter 4) and the input parameters on Table 5.1; the grey area and the blue dash lines are the range and IQR derived from the Monte Carlo simulation. Black dots are Z_{Best} profiles for each lake considering minimum difference between Z_{ICESat} and Z_{ASTER}, based on a Monte Carlo permutation of the parameters (R_∞, A_d, g). Green lines are $Z_{Optimised}$ profiles derived from equation 4.5 using as an input the set of optimised parameters (Table 5.3); green dash lines are the error range derived from the Monte Carlo simulation for the new set of parameters (NE to SW distance along profile (m)). Continued Figure 5.2.

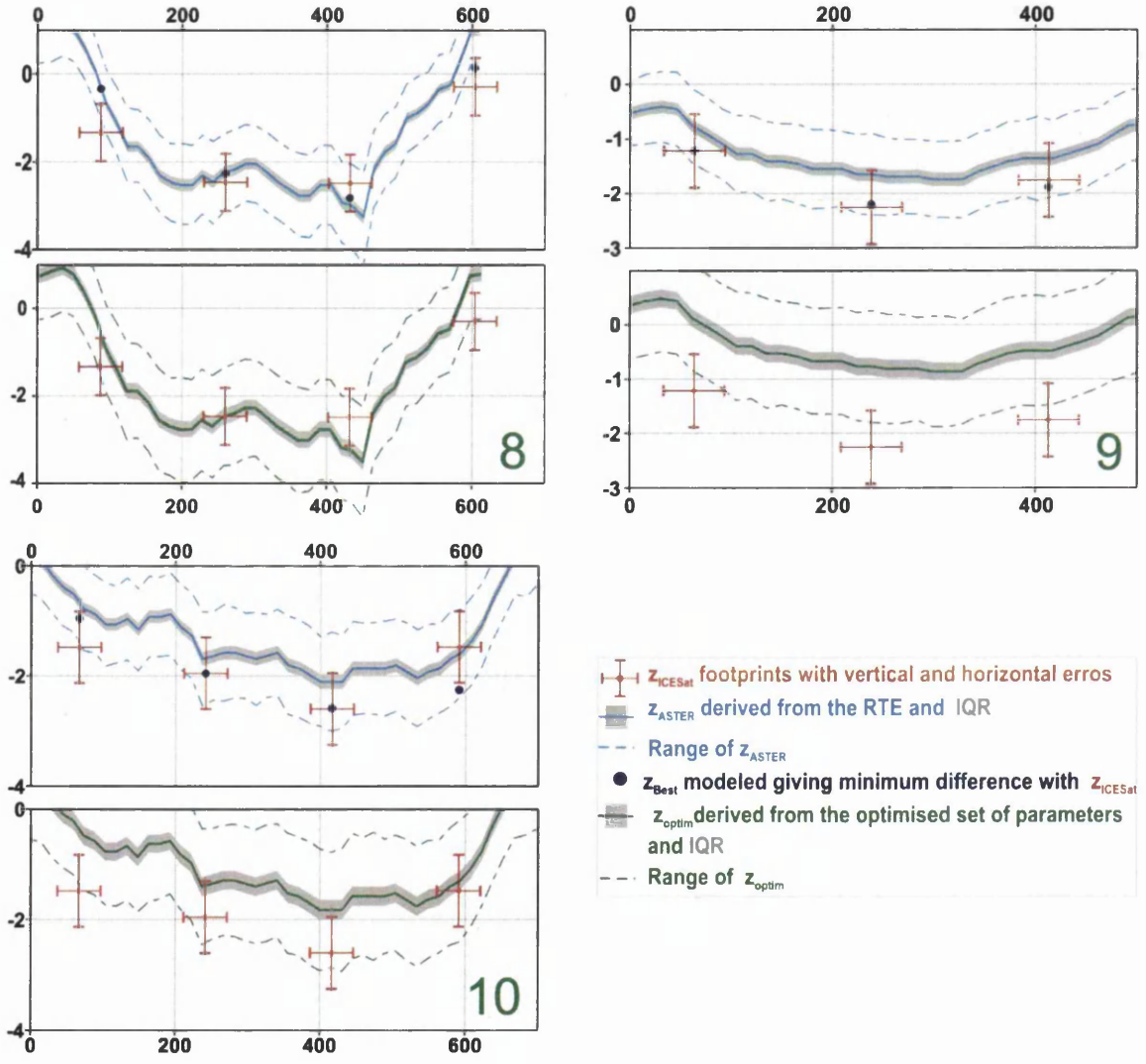

Even though Z_{ASTER} depths for the eleven lakes are derived based on Sneed and Hamilton (2007), the parameters used as an input differ from the ones used by the same authors in a more recent article (Sneed and Hamilton, 2011), where using the same model they derived the following parameters values: $A_d = 0.564$; $g = 0.118$ m^{-1}; $R_\infty = 0.038$. The median of the parameters in Table 5.1 differ around 42%, 66% and -71% respectively. This difference will be analysed in detail in the discussion (Chapter 8).

5.2.2 Minimisation model of ASTER depths based on ICESat reference depths

The second step of the optimisation process was to test if it was possible to tune the parameters so the modelled depths got closer to the observed values (Z_{ICESat}). For that purpose a minimisation model based on the Monte Carlo simulation was applied (Chapter 4). From the minimisation model, the combination of the three parameters (R_∞, A_d and g) within their uncertainties was chosen that gave the minimum difference between ICESat and the eleven best lake profiles. The best profiles for each lake (Z_{Best}) are shown in Figures 5.2, 5.3 and 5.4. The list of the best set of parameters for each lake is shown in Table 5.2. For a statistical comparison between these parameters and the ones from the original model see Figure 5.7. The median of the best parameters in Table 5.2 are used as the input parameters for the optimisation model (Section 5.2.3).

After applying the independent minimisation model the difference between modelled depth and observed depth decreases. Figure 5.5 compares the residuals for the original model and for the minimisation model, showing a clear reduction in residuals, with around 30% of the data points falling around the zero residual value for the minimisation model, whereas the original model shows 25%. Comparing the distribution shape of the residuals, the residuals for Z_{Best} seemed almost normally

Table 5.2: List of the parameters derived from the independent minimisation model.

Lake ID	A_d	g (m^{-1})	R_∞
1	0.738	0.167	0.015
2	0.893	0.175	0.007
3	0.732	0.167	0.019
4	0.731	0.167	0.017
5a	0.934	0.213	0.014
5b	0.861	0.225	0.007
6	0.831	0.181	0.006
7	0.724	0.170	0.015
8	0.810	0.223	0.011
9	0.936	0.225	0.006
10	0.949	0.178	0.012

distributed, with the centre in zero and ranging from [-2,+2]. For the original case the histogram is skewed to positive residuals, following the previous finding that the observed depths tend to be deeper than the model. In the case of the best profile the distribution is more symmetrical and the maximum residual is below 2 m, whereas the original model reaches 3.5 m. The sum of the residuals between Z_{ICESat} and Z_{Best} taking the absolute value is 24.93 m, which is around 34% of the residuals obtained with the original set of parameters (Table 5.1).

5.2.3 Optimisation model ASTER depths using the set of parameters derived from the minimisation model

In this subsection the results of the final step of the modelling process are shown. Taking the median of the eleven set of parameters obtained from the minimisation

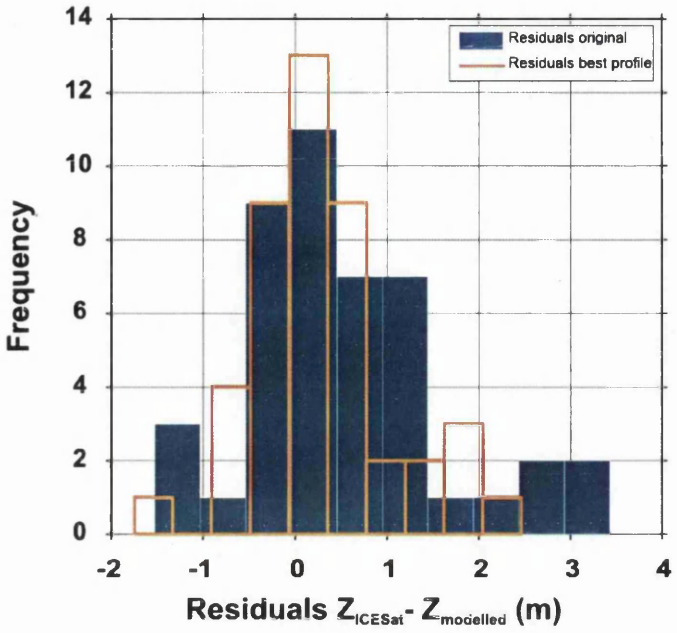

Figure 5.5: Histogram comparing the residuals derived from the independent minimisation model (Z_{ICESat}-Z_{Best}), unfilled red bars, with the residuals derived from the application of the water-reflectance model for the original parameters values (Z_{ICESat}-Z_{ASTER}), blue bars.

model (Table 5.2), a unique set of parameters was obtained (Table 5.3). With that set of parameters the water-reflectance model is run again for each lake, in this case the absolute error in the parameters is the uncertainty of the median value used (IQR), not the satellite errors. The results are shown in Figures 5.2, 5.3 and 5.4 as $Z_{Optimised}$.

The optimised results still do not meet ICESat depth measurements. Nevertheless the model did improve upon the initial depth values. The total absolute difference between the ICESat profiles and the optimised profiles is 29.53 m, which is 22% better than the difference between ICESat and ASTER differences from. Comparing $Z_{Optimised}$ with Z_{Best} the latter is better, however what is needed is an improvement over Z_{ASTER}, therefore some compromise over Z_{Best} should be acceptable to get the the global model.

5.2.4 Summary of the results for the optimisation model

The overall results of the minimisation model are shown in Figures 5.2, 5.3 and 5.4 where the observed depths (Z_{ICESat}) are compared with the profiles of the eleven lakes plotted for the three stages of the model; the original model (Z_{ASTER}), minimisation model (Z_{Best}) and optimisation model ($Z_{Optimised}$). The optimised model is not always an improvement on Z_{Best}, which is explained by the used of a global set of parameters.

5.3 Model variations

Some variations were applied to the optimisation model in order gain a deeper understanding of the Monte Carlo simulation and the water-reflectance model behave. The following subsections describe the different model scenarios applied in this chapter, the results obtained from, each model variation, and the process of selection of a final model to take forward to later sections of this thesis. Figure 5.6 summarises all the different scenarios introduced in this section.

5.3.1 Monte Carlo simulation varying the range of values of the input parameters

The first model variation was related to the uncertainties in the input parameters. In the previous Section (Section 4.2) where the optimisation model results were shown, the parameters were taken from Table 5.1. To allow the Monte Carlo Simulation to run, the range where each parameter was allowed to vary needed to be defined. In this first case, it was assumed that that range corresponded to the absolute error of each parameters, taken from satellite specifications or to previous studies (Scenario A, Section 5.2).

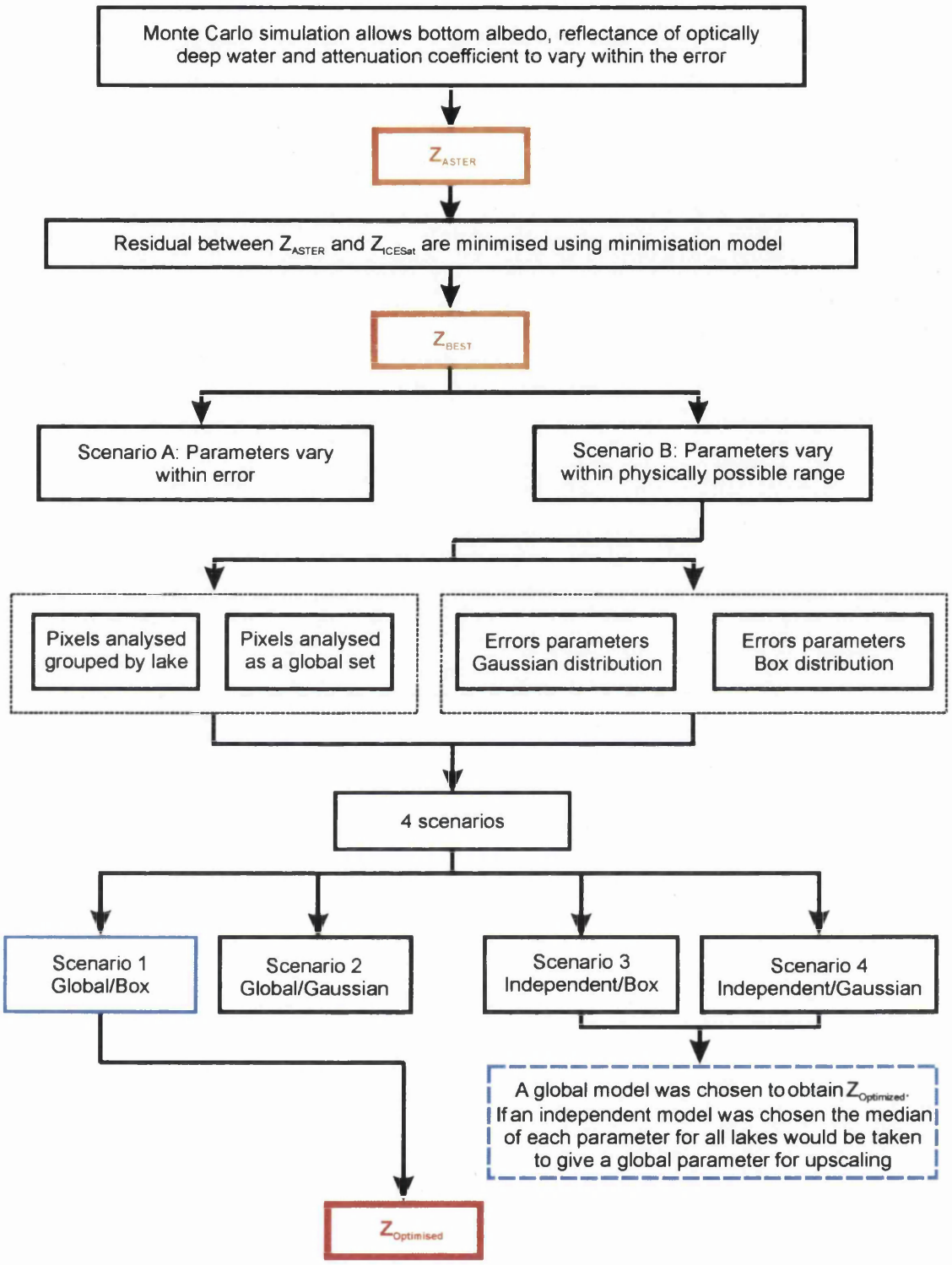

Figure 5.6: Summary of all the steps involved in the different scenarios applied in this section (Section 5.3). Note that Z_{ASTER} corresponds with the same model stage as in Figure 5.1.

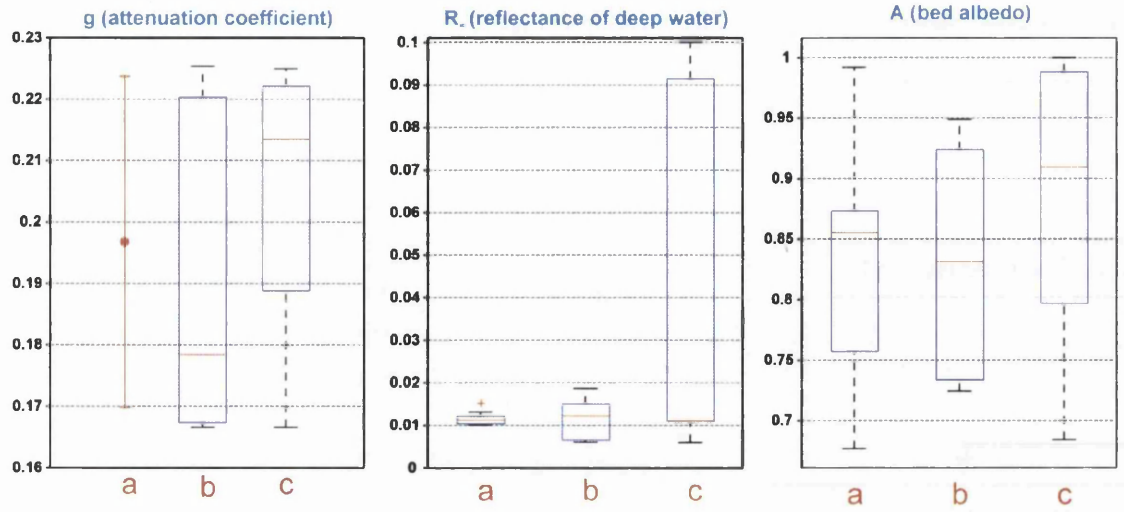

Figure 5.7: Box plots showing the difference in the parameters values for three different scenarios. The central mark is the median, the edges of the box are the 25^{th} and 75^{th} percentiles, the whiskers extend to the most extreme data points not considered outliers, and outliers are plotted individually. (a) corresponds to the parameters values given by the literature, *i.e.* the so called original model; (b) parameters derived from the minimisation model for the eleven lakes using Scenario A; (c) parameters derived from the minimisation model for the eleven lakes using Scenario B.

The next step was to broaden the range by allowing each of the three parameters to vary within their physically viable limits. This experiment was done to see whether the minimisation model could be improved with this new scenario (Scenario B). Figure 5.7 shows how the parameters are distributed and compared with the original parameters. A_d was the parameter that varied least, while the reflectance of deep water is the parameter varied the most, meaning that the model is highly sensitive to the bed albedo, as shown in previous studies (Sneed and Hamilton, 2007; Georgiou *et al.*, 2009).

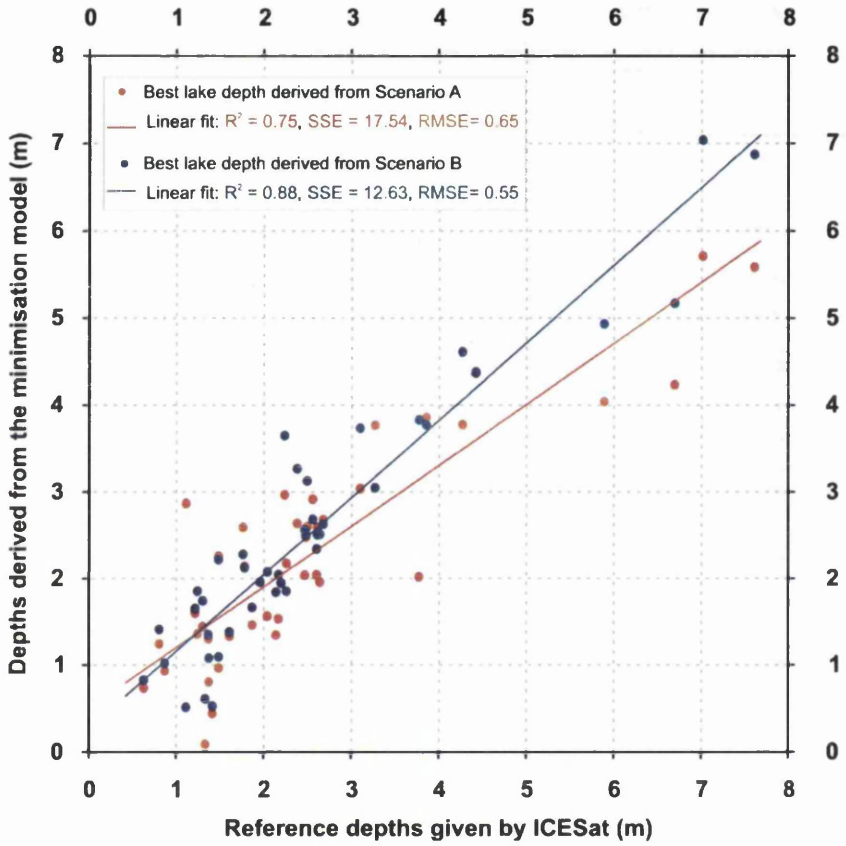

Figure 5.8: Comparison of Z_{ICESat} with depths derived from ASTER imagery after applying the minimisation model between Z_{ASTER} and Z_{ICESat} for each lake (Z_{Best}). Red dots correspond to Z_{Best} using Scenario A as an input to the minimisation model. Blue dots correspond with Z_{Best} using Scenario B. Both linear fits (blue and red lines) come from a Robust least squares method, where the extreme values are consider anomalous.

The best profiles derived from the minimisation model applied for each of the lakes for both scenarios A and B are compared in Figure 5.8. These results show that by using scenario B as an input to the minimisation model the best profiles are closer to the observed profiles. The linear fit for scenario B gives $R^2 = 0.88$, whereas scenario A gives a linear fit of $R^2 = 0.75$.

A significant observation is that previously modelled depths tended to underestimate lake depth, especially in the deeper parts of a lake. Even though scenario B still does not reach the values of deep ICESat footprints, it does gets closer to them. For example, for the deepest footprint out of the 44 used in this study, where ICESat depth is almost 8 m, modelled depth using Scenario B is around 7 m, more than 1 m deeper that the depth value obtained from the scenario A. For this reason in the next analysis where four further scenarios are tested (scenario 1, 2, 3 and 4), the error range for the parameters is assumed to be that corresponding to scenario B.

5.3.2 Monte Carlo simulation varying the probability distribution of the parameters

The probability distribution that the three input parameters present for the Monte Carlo simulation was firstly assumed to be Gaussian. Then the model was run again but this time assuming that the input distribution of the parameters was a Box distribution.

The results derived from a Box distribution and from a Gaussian are very similar, as shown in Figure 5.9.

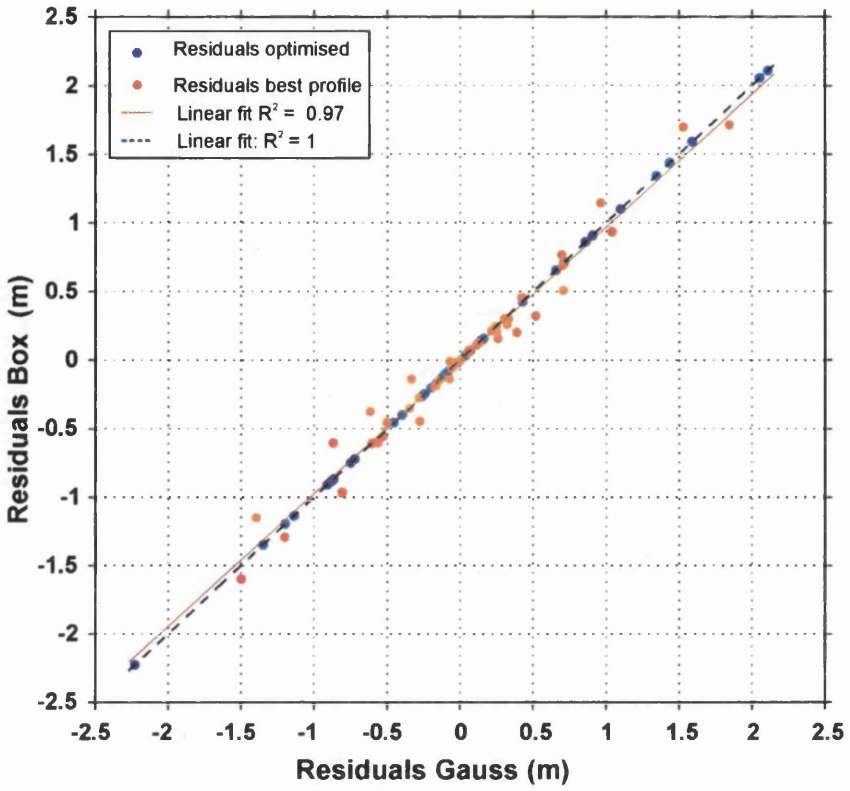

Figure 5.9: Comparison of Residuals derived from the minimisation model (Red dots) and the optimisation model (blue dots), varying the probability distribution of the input parameters; Gaussian (scenario 3) or Box (scenario 4). A simple linear fit is applied for both curves.

5.3.3 Optimised depths from a global and an independent minimisation model

In Section 5.2 the optimisation model was applied assuming that the minimisation approach was applied independently to each lake and the parameters averaged over the eleven lakes. This is referred to here as the independent model. An alternative model was also tested, and referred subsequently as the global model, which consisted in applying the minimisation model at the same time for all the lakes, which meant running the model for the 44 footprints at the same time, ignoring that they were from different lakes (Scenarios 1 and 2). This produced the optimised depths with no intermediate steps along with the set of parameters that provided the minimum residuals. The summary of these results are shown in Section 5.3.4.

A quick way of comparing results between the global/independent models with the original model is to look at the residuals that each generated. Figure 5.10 shows how for both scenarios global/independent, the residuals between the reference profiles (ICESat) and the modelled reduce in comparison with the original model, especially for the biggest residuals where they were reduced around 1 m for some of the footprints. The sum of the residuals for the global model is 27.78 m, whereas for the independent model is 29.53 m.

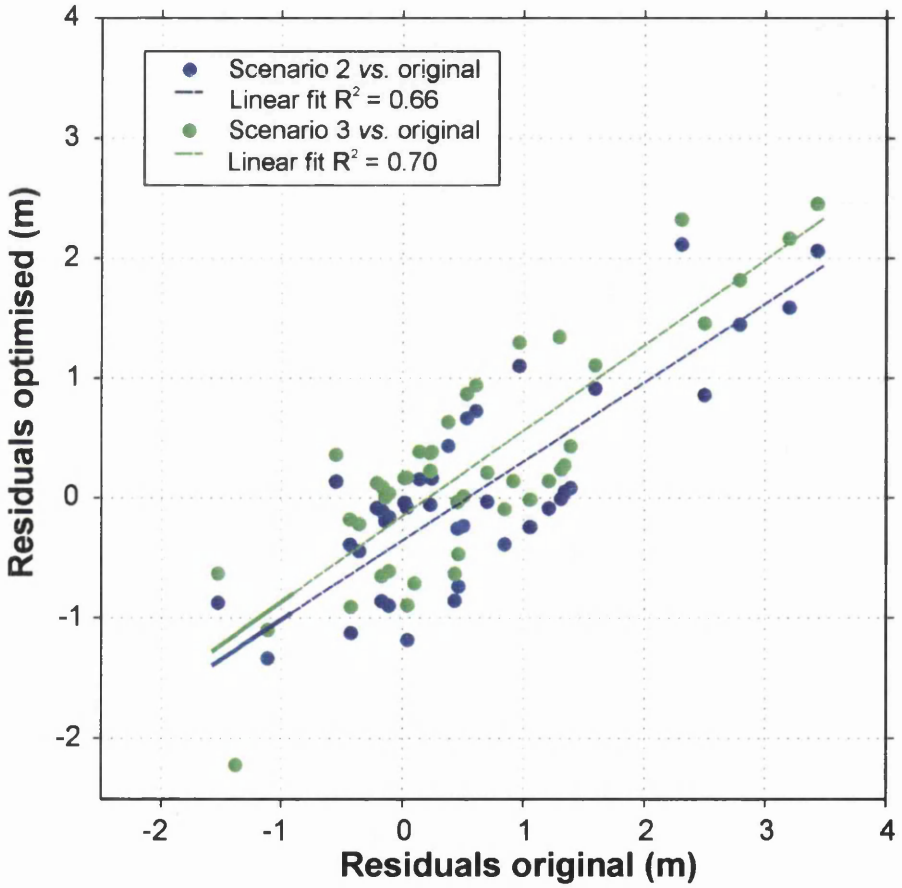

Figure 5.10: Comparison of Residuals derived from optimisation model (Z_{ICESat}-$Z_{Optimised}$) for two different scenarios (scenarios 2 and 3) with the residuals obtained with the original model (Z_{ICESat}-Z_{ASTER}). Blue dots correspond with the optimised model derived from scenario 2; green dots correspond with the optimised model derived from scenario 3. A simple linear fit is applied for both scatter plots.

5.3.4 Results summary from the different model scenarios

This section groups the results of the model for the 4 different scenarios that were considered in order to improve the optimisation model (Figure 5.6). Figure 5.11 summarises the optimisation models for each of the scenarios. Assuming a Gaussian or a Box distribution gives similar results when a global model is applied. Those results are also similar to the optimisation model assuming a Gaussian distribution but applying an independent model. The scenario that gives higher residuals is for a Gaussian distribution with an independent model (highest SSE).

The linear fits are done using a Robust linear squares fitting tool. They are plotted as an indication of how the points as a whole differ from the theoretical fit line when $(x_i = y_i)$. They show that for deep parts of the lakes (deeper than 3 m) the modelled depths are shallower than the observed depths in all cases. For the shallowest parts the points tend to do the opposite, giving deeper values for the modelled, although the high concentration of scatter points around the 2 m depth make this less clear.

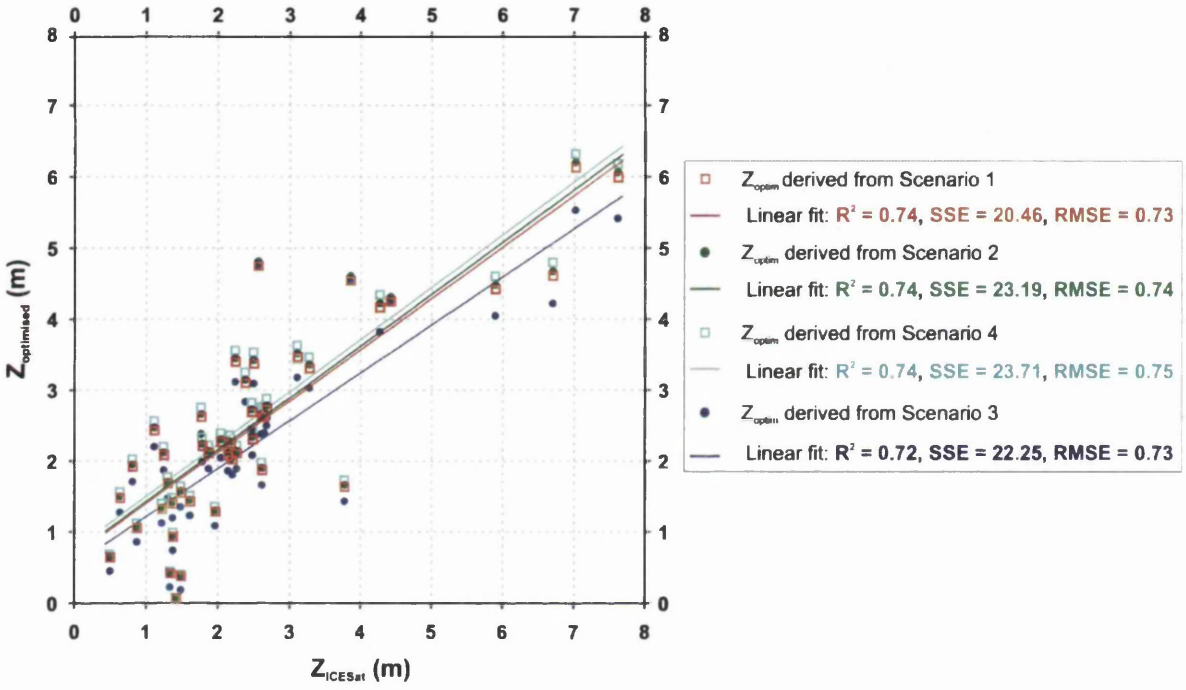

Figure 5.11: Comparison of depth values from ICESat footprints with depths derived from ASTER imagery after applying the optimisation model to different scenarios.

An examination of the residuals from each of the model scenarios was done (Figure 5.12), showing no clear scenario that produces smaller residuals. In addition, for all scenarios except number 3, the distribution of the residuals tends to be negative skewed, showing once more that the observed values are usually deeper than the modelled.

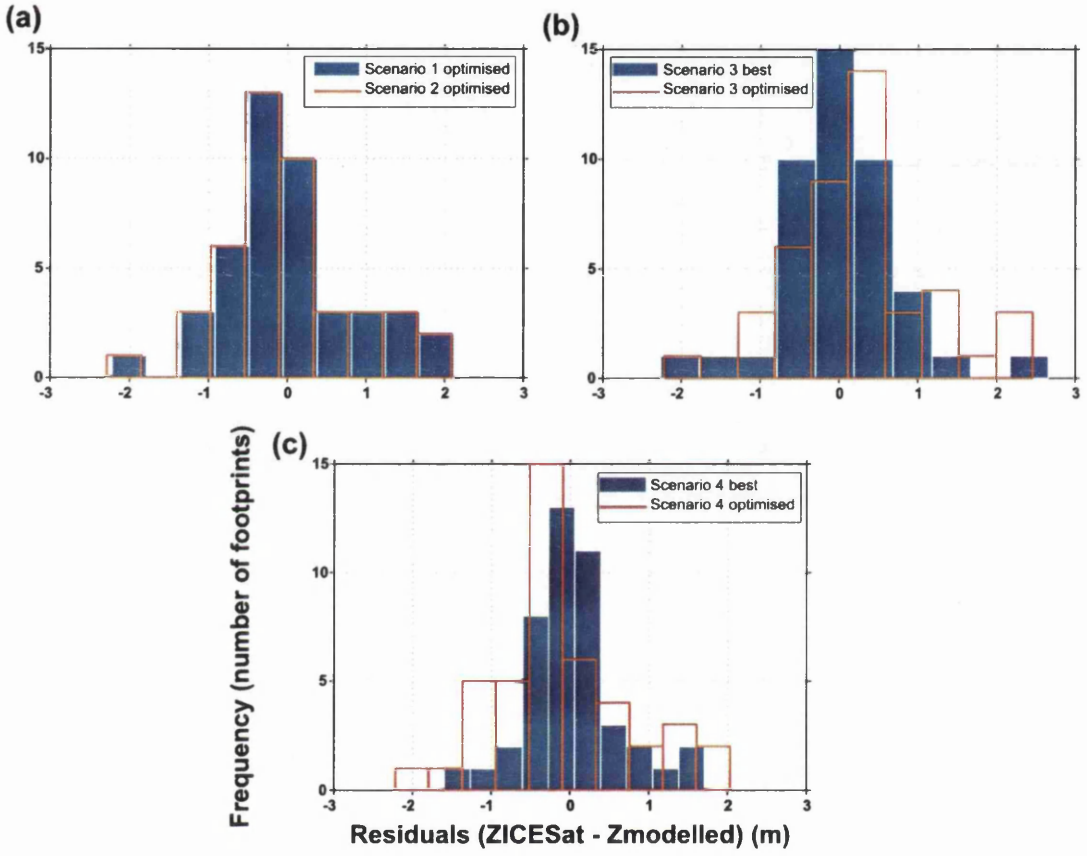

Figure 5.12: Histograms plot showing the different residual distribution for different model scenarios. Blue bars correspond with residuals derived from the minimisation model (Z_{ICESat} - Z_{Best}). Red unfilled bars correspond with Residuals derived from the optimisation model (Z_{ICESat} - $Z_{Optimised}$). It is worth noting that in plot (a) both blue and red bars correspond with optimised residuals, this is because the 'Optimised profiles (scenario 1) = Best profiles (scenario 1)' and the same applies for scenario 2. (a) Compares residuals from the optimised models for the cases of scenario 1 and scenario 2; (b) compares the residuals obtained from the minimisation model using scenario 3 with the residuals obtained from the optimisation model derived from the same scenario; (c) compares the residuals obtained from the minimisation model using scenario 4 with the residuals obtained from the optimisation model derived from the same scenario.

In Figure 5.12 the residual histograms for the best profiles of each scenario are also plotted, for comparison with the optimised. There are some variations in distribution, but in general the best profiles give better results than the optimised one. In the case of the Z_{Best} profiles, the sum of the absolute of the residuals for scenarios 1 and 2 (global model) are around 28 m; and for 3 and 4 (independent model) around 20 m. For the optimised profiles, scenarios 1 and 2 are the same as the best profiles, and for the 3 and 4 the sum is around 29 m. It seems that for the global model the sum of the residuals is around 1 m smaller than for the independent model. Remember that for the original model (Section 4.2.1) the sum of residuals was around 38 m, so even for the worst scenario, the improvement is greater than 25%.

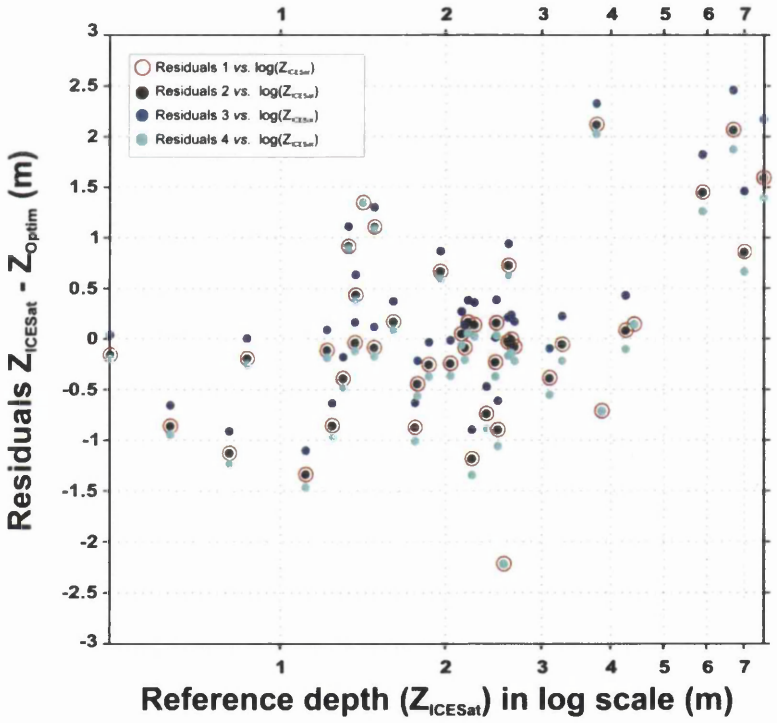

Figure 5.13: Scatter plot of the residuals obtained from the optimisation model for the 4 Scenarios as a function of the observed depth given by Z_{ICESat}. The X axis is in log scale.

The previous histograms show the range of distribution of the residuals but they do not show how these residuals are distributed with depth, *i.e.* it is interesting to see whether there is a correlation between the residual value and sign with the observed

depth. This information is plotted in Figure 5.13 for the four studied scenarios; this graph shows that for the deeper parts of the lake > 4 m, there is a positive correlation between the residuals and the observed depth. However, since only seven points represent this part, a conclusion is difficult to reach. For the shallower parts of the lakes the residuals tend to be concentrated in the zone of $\pm$ 1 m of residual. And for depths below 1 m, the correlation is negative.

The last part of this analysis shows the different set of parameters obtained for the different scenarios (Table 5.3). There are not major differences between the parameters obtained after the minimisation model for the four scenarios. The biggest variation occurs for the reflectance of deep water, was shown earlier to have the least influence on the water-reflectance model of the three parameters. Only for scenarios A and B are the difference bigger, where the error range of the input parameters was varied. For the other four scenarios the error range is fixed to the physically plausible limits for all cases. So in these scenarios the factors influencing the model are mainly the Gaussian/Box distribution of the input parameters and the global/independent minimisation methods.

Table 5.3: Table showing the value of the optimised parameters for all the different scenarios consider in this study.

Scenario description	A_d	$\mathbf{g}$ (m^{-1})	R_∞
Parameters from Scenario A	0.831 $\pm$ 0.095	0.178 $\pm$ 0.027	0.012 $\pm$ 0.005
Parameters from Scenario B	0.909 $\pm$ 0.096	0.213 $\pm$ 0.017	0.011 $\pm$ 0.040
Parameters from Scenario 1	0.864 $\pm$ 0.032	0.222 $\pm$ 0.011	0.099 $\pm$ 0.002
Parameters from Scenario 2	0.864 $\pm$ 0.038	0.219 $\pm$ 0.012	0.091 $\pm$ 0.003
Parameters from Scenario 3	0.864 $\pm$ 0.079	0.216 $\pm$ 0.018	0.016 $\pm$ 0.039
Parameters from Scenario 4	0.864 $\pm$ 0.096	0.219 $\pm$ 0.019	0.001 $\pm$ 0.045

5.4 Chapter Summary

This chapter introduces the results derived from the model developed to improve the water-reflectance model. The model uses a Monte Carlo simulation to minimised the residuals between the reference depths Z_{ICESat} and modelled depth based on ASTER imagery. To achieve this, the model finds the best set of the input parameters that give minimum residual error, varying the parameters within an established range. Section 5.2. shows the different steps carried out to achieve the optimised model. The optimised model provides an improvement with respect the original model, which was based on previous literature (Sneed and Hamilton, 2007). Despite the improvement, the difference between the expected depths and the modelled depths is significant, specially in the deepest parts of the lakes, where there is a systematic underestimation of depth from the model.

The discrepancies between the model and the observations could be due to many factors. In next section of this chapter (Section 5.3) different model scenarios were tested to better understand what are the main influences on the model. The first variation introduced was in the range distribution of the input parameters to the model; in Section 5.2 it was assumed initially that the range was the published error range of each parameter, either from the correspondent satellite specifications or from previous established tables (scenario A). The input parameters were allowed to vary within their physically viable limits, while excluding the combinations that did not produce physically real values for the water reflectance model. This scenario was called scenario B. The minimisation model gave better results when scenario B was applied, presumably because any possible restrictions that the previous Scenario could have were removed. Therefore for the next four scenarios, where other factors were altered, it was assumed that the input parameters varied following scenario B.

The following scenarios were combinations of changes in the probability distribution of the input parameters (Gaussian or Box distributions) with changes in the minimi-

sation method (global or independent minimisation). For the minimisation model, a Box distribution with an independent model provided profiles (Z_{Best}) closest to the observed values. This is probably because, in case the mean values of the input parameters chosen in the Gaussian distribution are not appropriate, the Box distribution still gives equal weight to all the values. In addition, with an independent minimisation model, the best profiles are for each lake so there is no influence from others. However, when applying the optimisation model to all four scenarios the differences between the four decreased. This is due to the fact that the parameters values do not vary much (Table 5.3), especially the bed albedo, which is the one the water-reflectance model is most sensitive to.

This chapter has demonstrated that the Monte Carlo Simulation provides a new method of accurately calculating an optimised depth based on the water reflectance model and using ICESat depth estimates as reference depths. Even though the modelled depths tend to underestimate lake depths, particularly for the deep parts of the lakes, the observed depths fall within the uncertainties of the modelled values. This means that taking into account the Monte Carlo-derived uncertainties, it is possible to model depths at a regional scale using the optimised model described in this chapter.

The different scenarios give an insight into the model behaviour. From these results a Box distribution of the parameters applied to a global model was chosen. The last objective was to obtain an optimised set of parameters that could be applied at a regional or ice-sheet scale across the surface of the GrIS; for that a global minimisation model appear to be most realistic. In the next chapter these results will be applied to derived water volume in a regional scale (south west Greenland) and from them an area-volume relationship will be investigated. Also the reflectance bands will be taken into account to see how the model performs at different wavelengths (Chapter 6). Following that chapter, another chapter will be introduced with an application of the model developed here to a higher resolution sensor (CASI) with

the objective of deriving water-filled crevasse depth (Chapter 7).

Chapter 6

Lake volume estimates

6.1 Introduction

This chapter will expand the results based on the optimisation model derived in the previous chapter (Chapter 5), showing the next obvious step after lake depth estimation, *i.e.*, estimation of lake volume. The quantification of the volume of water stored in supra-glacial lakes is important in terms of basal pressure at the base of the lake, potential drainage events and overflow (Box and Ski, 2007; Russell. *et al.*, 2011; Das *et al.*, 2008). For example, van der Veen (2007) stated that large volumes of water were necessary to propagate crevasses to the glacier bed via hydrofractures. Therefore lake volume knowledge is key to understand the processes that drive these events.

Firstly, volume estimates derived from the water-reflectance model are presented (Section 6.2). In order to be able to analyse how realistic these results are and considering ICESat limitations for this purpose, volume estimates based on the reference ICESat data using three different approaches, which will at least give the order of magnitude of the water stored and the uncertainty. After this comparison, the water-reflectance model was up-scaled, although it was only applied to lakes in

the south west of Greenland due to data limitations. The reason for this choice is, as discussed in depth later on in this chapter, lakes elsewhere could present different water characteristics. From the volume results the area $\propto$ volume relationship will be investigated to test whether it will be possible to estimate the volume without knowing lake depth, which would imply that *in situ* measurement would not be required, with lake area derived from satellites being sufficient (Selmes *et al.*, 2011; Liang *et al.*, 2012).

Secondly, analysis of MODIS scenes as an input to the water-reflectance model is presented (Section 6.3). Since the temporal coverage of MODIS imagery is higher than ASTER, further analysis from the optimisation model needs to be carried out; fox example annual variation of lake area (Selmes *et al.*, 2011), depth and hence volume. MODIS data cannot resolve the depth at the lake margins owing to the coarse resolutions of pixels (250 by 250 m). Nevertheless MODIS could be useful to compare depths on the centre of the lakes, where no mixed-pixels occur.

Thirdly, depth estimates derived from the three visible near-infrared ASTER bands (Band 1, Band 2 and Band 3N) are introduced (Section 6.4). This was done as a prove of concept, since in the methods chapter it was already explained why Band 1 is more suitable than bands with wavelengths 650 nm (Chapter 4). This was because at those higher wavelengths there is strong absorption by water (Tedesco and Steiner, 2011).

Finally, fourteen empty lakes were found in some of the ASTER scenes (Section 6.5)). This will be used to estimate the reflectance of the bottom of lakes and used this as a comparison with the previously estimated bed albedo for the model (Chapter 5).

6.2 Lake volume estimates

In order to estimate the volume of water stored on the lakes previously used for depth estimates based on the water reflectance model (Chapter 5), lake area quantification is needed. The area selection technique used was as follows; selected pixels that for which $R_w \leq A_d$, meaning that the surface reflectance must be smaller than the bed albedo otherwise the *Bouguer-Lambert-Beer law* would generate positive depth values, which would violate the physics of the equation (Figure 6.1). An uncertainty was hence introduced due to the mixed pixels of water-ice at the edge of the lake in the ASTER image.

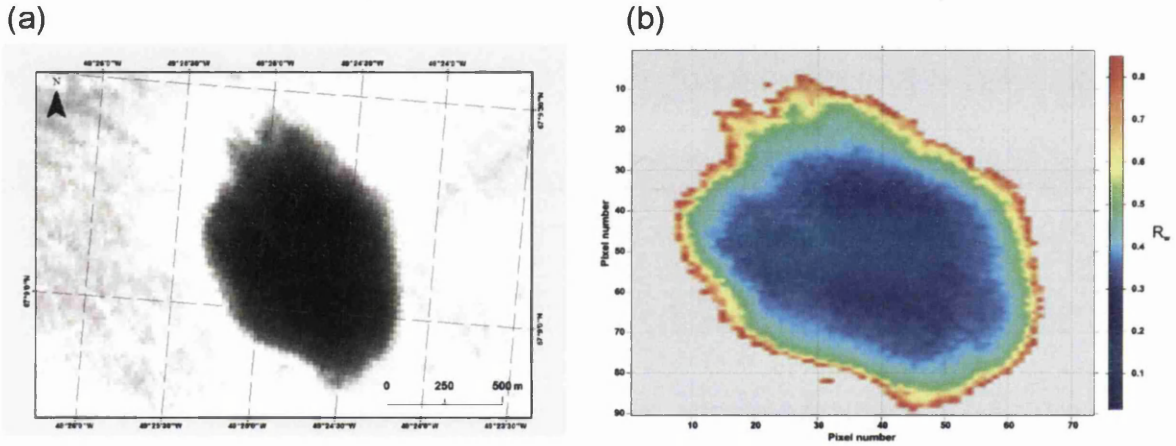

Figure 6.1: (a) Snapshot of one of the lakes used in this Chapter (ASTER Band 1); (b) Reflectance values for Band 1 of the same lake after applying a band threshold value to image (a). From (b) the area and hence the lake volume is estimated. The band threshold is applied for $R_w \leq A_d$, otherwise the model would give positive values of depth, which is a not physically possible.

The equation used to derive lake volume calculates the volume of each water column underneath each pixel by multiplying the pixel size by the depth derived from the water reflectance model for each pixel. The total volume is the sum of all the volumes of each column. To estimate the uncertainty in the volume for each column of water the propagation of errors rule for the product was used, since the variable errors are considered independent random errors (Sánchez del Río, 1989). This assumption could substantially underestimate volume errors because one of the

assumptions for the water reflectance model was homogeneous bottom, *i.e.* fixed albedo, which would mean that the errors could be correlated. The reason for choosing independent errors was for simplification, therefore the uncertainties in the volume should be considered with caution. The uncertainty in the pixel area was assumed negligible in comparison with the error induce in the depth determination, which was taken as half of the IQR derived from the Monte Carlo approach derived previously (Chapter 5).

The resulting volume estimates are presented in Table 6.1. Notice that there are two relative error estimates, δV_{range} and δV_{iqr}, which corresponds to assuming the depth absolute error as half of the range or the IQR respectively, with both magnitudes obtained from the Monte Carlo simulation. In both cases the uncertainty is insignificant in comparison with the magnitude of the volume, with the largest error being less than the 10%. It is also worth noting that the error is not a function of the volume quantity, which is due to the fact that the error in the area was neglected. Therefore the error is related exclusively with the depth uncertainty.

Table 6.1: Table showing the area and volume of each of the lakes used for the optimisation model.

Lake ID	Area (km^2)	V_{optim} (x 10^6 m^3)	δV_{iqr} (%)	δV_{range} (%)
1	0.99	3.87	0.15	0.52
2	0.32	0.61	0.43	1.50
3	0.51	1.54	0.24	0.86
4	0.89	2.49	0.20	0.67
5a/5b	0.19	0.21	0.97	3.18
6	1.57	2.28	0.25	0.25
7	0.85	2.19	0.72	0.72
8	0.17	0.36	0.56	1.91
9	0.31	0.13	1.88	5.99
10	0.53	0.61	0.54	1.78

6.2.1 Comparison with ICESat derived volumes

There are no *in situ* measurements of the selected lakes to validate the volume estimates derived above (Table 6.1). Nevertheless an approximation was applied in order to obtain two independent volume estimates from remote sensing observations; ICESat reference profiles were used for this purpose, although it was already known beforehand that the results were not going to be precise and not completely realistic. As described previously, the ICESat dataset consists of tracks crossing the lake with footprint spacing of around 172 m. Because only tracks on the same year as the ASTER image used were chosen for the calculations, one track was available for each lake, which does not provide a direct volume estimate, rather a 2D transect of the lake.

Two approximations to derive volume were used; the first approximation is applied to the lake shape definition. After some testing with different geometrical objects and their volume, a spherical cap was chosen as the approximate shape for the lakes (Figure 6.2). Two main reasons determined this choice; the first one was that looking at all the lakes studied, the length of the lake appear to be larger than the depth with an averaged ratio of 270:1 (approximated from Figure 5.2 in Chapter 5). This ratio is estimated by measuring the length of each of lake in that figure (given by the X-axis) and the maximum depth of each lake. The second reason was the simplicity of the equations needed for the spherical cap volume estimation, where only two variables were required. Looking at Figure 6.2 and the volume equation on it, the following terms were identified: h = maximum lake depth derived from the water reflectance model and r = radius of the lake area, considered a circle.

The second approximation used for the determination of the lake volume based on ICESat data is related to the selection of the right circle radius (r) for the spherical cap equation. Since lake shape is often random, although with tendency to be circular/oval in plan form, three different choices for r were selected and from them

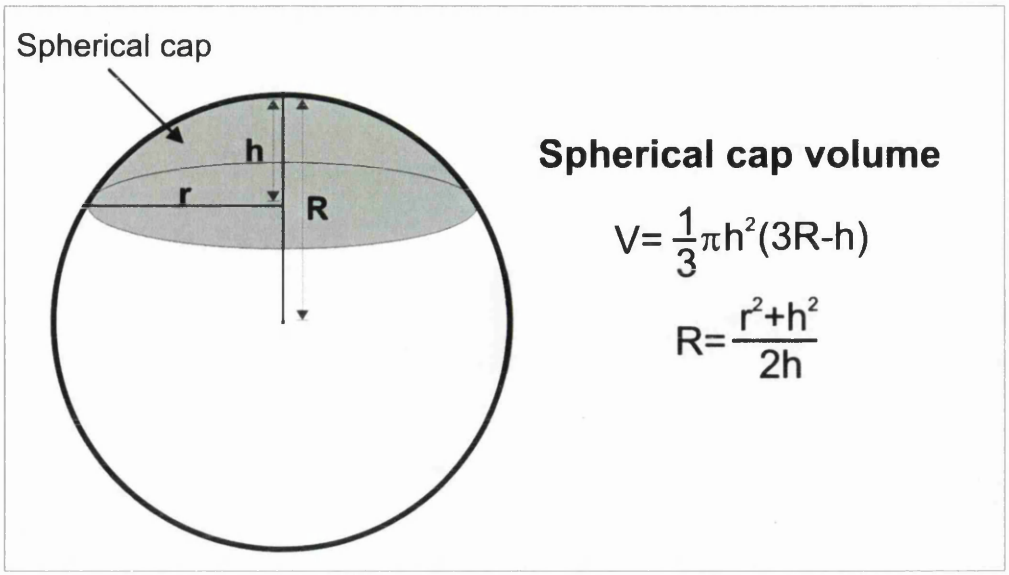

Figure 6.2: Geometric shape chosen to define the lake volume from the ICESat track, where it was assumed it had a spherical cap shape.

derive three different independent volume estimates, in order to see which one was closer to the volume results obtained for the ASTER imagery in the previous section (Figure 6.4).

The first r choice was taking the half of the shortest possible length (d_{min}) and estimate then the volume. Secondly, the longest possible length on the lake and taken $d_{max}/2$ as the radius was selected. Finally the third choice consisted in taking the radius as half of the length of the ICESat track crossing the lake (Figure 6.3). For the three cases the centre of the circle is taken as the maximum depth value given by the ICESat track (h in Figure 6.2).

Figure 6.4 summarises the results obtained from the approximations described above. The three volume estimates for ICESat are compared with the volume obtained in the previous section (V_{optim}), *i.e.* selected from ASTER scenes. The graph shows no clear relationship with the volumes derived from the ASTER reflectance values; a linear fit model was applied and for the three cases R^2 is smaller than 0.4, which means lack of linearity.

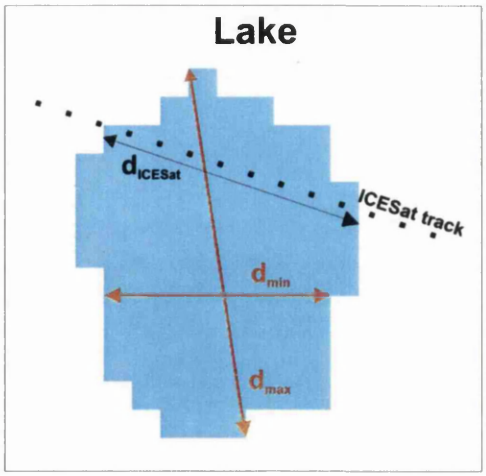

Figure 6.3: Theoretical lake shape, showing an example of an ICESat track crossing the lake (d_{ICESat}) and the maximum and minimum diameters of the lake (d_{max} and d_{min} respectively). Three different volume estimates are obtained from each of the diameters.

Table 6.2: Table showing the total volume of all the lakes selected for the optimisation model showed for the different estimation approaches. The relative error is also shown (ϵ) and the Residual, which is the difference between the three different V_{ICESat} estimates and the reference value, taken as V_{optim}.

Volume ID	V_{total} (x10^6 m^3)	ϵ (%)	V_{optim}/V_{ICESat}
V_{optim}	17.79	16.24	1
V_{ICESat} for d_{max}	23.23	23.25	1.31
V_{ICESat} for d_{min}	7.29	19.49	0.41
V_{ICESat} for d_{ICESat}	12.17	21.34	0.68

Theoretically it would be expected to find that $V_{ICESat}/V_{optim}=1$, but looking at Table 6.2 this relationship is not evident. ICESat volume results were not used as a validation of the volumes derived from the water reflectance model. This experiment was intended to be a comparison of different approaches that potentially could be used for future volume estimations of supra-glacial lakes. Table 6.2 shows the comparison of the total volume of water stored in the ten lakes for the different estimates. There is an average residual of 20 % between the total ICESat derived

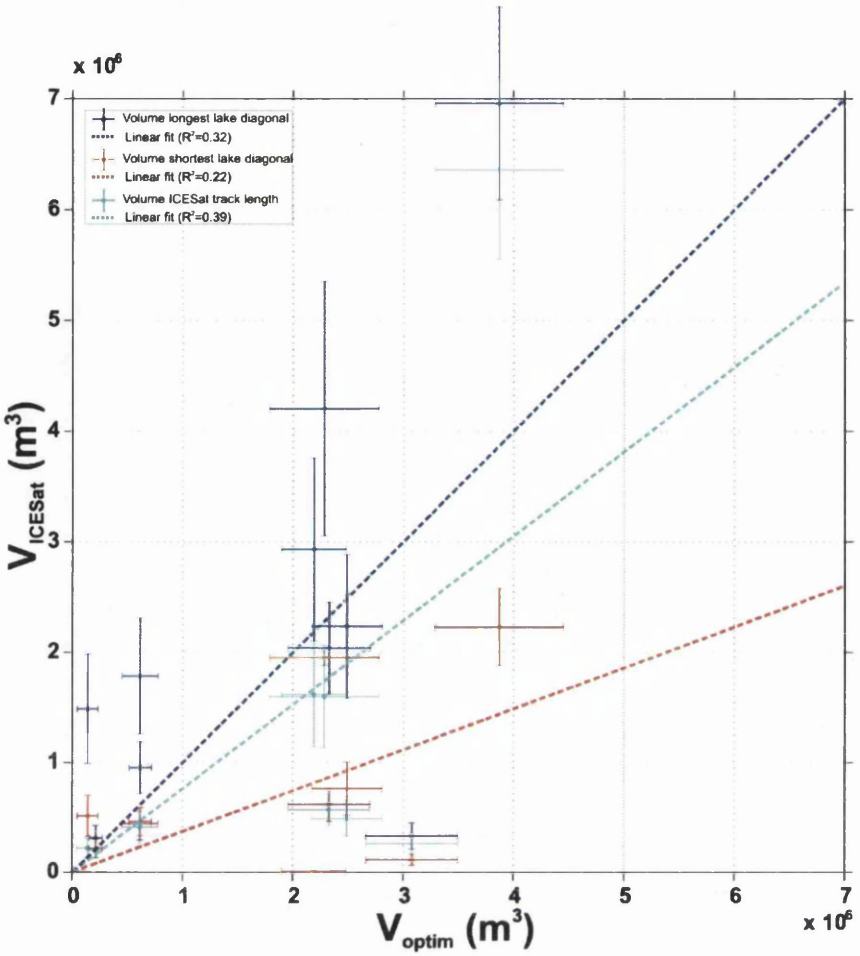

Figure 6.4: Comparison of lake volume derived from ASTER (V_{optim}) vs. the volume derived from ICESat measurements (V_{ICESat}). The three different colours correspond to different assumptions when deriving V_{ICESat} (see Figure 6.3, all of them estimated assuming a spherical cap lake shape. The lines correspond with the uncertainties derived from the propagation of errors approach.

volume and the optimised ones. For the case of d_{max} (Figure 6.3) there is an overestimation of the volume with respect V_{optim}; whereas for the cases of d_{min} and d_{ICESat} (Figure 6.3) there is an underestimation of the volumes. For example, for individual lakes, if interannual ICESat campaigns are available and after removing the elevation changes due to accumulation/ablation and other considerations like firn densification correction, it could be possible to obtain the lake geometry from the combinations of the different ICESat tracks. Nevertheless, in the current study only one ICESat track per lake was considered, therefore the spherical cap volume estimation is an approximation. Despite this approximation, in all the lakes the different volume estimates present the same order of magnitude, which shows that

the approximation could be valid with further lake observations. For a precise statistical validation of the optimised volumes, *in situ* calibrations are needed, since in this section results made from approximations were compared.

6.2.2 Volume estimates derived from the water-reflectance model up-scaled at regional level

In this section the results derived from a regional up-scaling of the water reflectance model are presented. The up-scaling was not done globally across the GrIS; this is because the optimisation model was only developed in south-west Greenland (see blue dots in Figure 6.5 in Chapter 5) due to data availability. In Chapter 4 some assumptions were considered before applying the water reflectance model for lake depth estimations; for example non-presence of particulate matter on the water column was assumed. Moreover, since there are not any field observations that could test the results obtained from the optimisation model (Chapter 5), nor water quality and composition across lakes, the up-scaling was restricted to the same region as for where the results from Chapter 5 were obtained (Figure 6.5). From this regional up-scaling the amount of uncertainties derived from comparing lakes of different regions could be ignored and assume that within this selected area of interest the properties of water will not vary. A total of thirty lakes were found for the up-scaling (see red dots in Figure 6.5), which together with the ten lakes used for the optimisation model (Chapter 5), give forty lakes to study.

For this section there are no *in situ* data from the forty lakes that provide lake volume estimates as a validation for the results obtained in this section. Moreover there are no ICESat data that could be used as an approximation as done in the previous section. The relationship that might exist between area, volume and depth of the lakes was studied in this section, assuming that at least the order of magnitude and the uncertainties are realistic. As explained in the introduction of the current

chapter, it is expected to find a positive relationship between area and volume, and it may be possible to use this elsewhere to infer lake depths.

Figure 6.6 summarises the results obtained in this section. The water reflectance model was applied to forty lakes distributed across the south-west of Greenland, using the optimised parameters obtained in the previous Chapter (Chapter 5). For this purpose available ASTER images were selected and for lake identification, the distribution map produced by Selmes (2011) as part of his thesis.

There is a positive relationship between depth and volume, as shown in Figure 6.6; nevertheless it is not clear which curve could define that relationship. Moreover, the depth values plot in Figure 6.6 are just the deepest pixel for each of the forty lakes, which means that the lake shape and the rest of the pixel values are being ignored. A lake could present a V shape, which would mean the lake volume for that lake would not be the greatest, despite being the lake with deepest points. On the other hand, smoother lake shapes (U shape) could store more water volume and at the same time not be the deepest lakes. Further research is needed to better understand the relationship between the two variables. The uncertainties in the volume results are calculated as in Section 6.2, using the propagation of errors approach (Sánchez del Río, 1989); for the depth uncertainty, half of the IQR values derived from the Monte Carlo simulation were taken. Some data points do not have error bar, this is because the error was insignificant in comparison with the data point value.

Looking now at area-volume curve in Figure 6.6, the trend seems to be more clear. Lake volume is a function of lake area, although the relationship is not linear. Further analysis could try to find a function that defines that relationship; which if it was found then lake depth estimates would not be needed for a quatinficaiton of water stored on the GrIS. For this purpose preliminary results regarding this poten-

tial relationship are introduced. Once more, this results are not enough to establish the relationship, but it is a valid approximation and it could be used to test other independent results.

Area-volume relationship test

Figure 6.7 is an example of two types of function that could define the relationship between lake area and lake volume. Two different fitting functions were applied and both present very similar results, showing the possibility of a non-unique solution to the problem. The exponential fit gives an equation of the form $A = 87.6 * exp(1.4 * log_{10}V)$ with a $RMSE = 3.6 * 10^5$ (Root Mean Square Error). In the case of the potential fit, the equation is $A = 87.6 * (log_{10}V)^{0.63}$, with $RMSE = 3.6 * 10^5$.

Despite the high R^2 for both fitting functions (Figure 6.7) of around 0.8, it is yet not possible to conclude about the area-volume relationship. The main reason is that there are only forty samples, against thousands of lakes distributed across Greenland. Even more, looking at Figure 6.7 it can be seen that at the top right of the graph there are only two data points, which means that the curve shape end is determined for a not representative number of data points, comparing it with the sample number. In the discussion (Chapter 8) previous A$\propto$V relationships (Krawczynski *et al.*, 2009) will be introduced and their accuracy analysed.

6.3 Water-reflectance model applied to MODIS dataset

Following the up-scaling of the water-reflectance model to a regional scale, MODIS imagery is used to compare the spectral behaviour of ASTER and MODIS satellites

and also to show if the difference in spatial resolution, *i.e.* pixel size, can mask the results. For this purpose MODIS images of the same day and time as the ASTER images were selected to be able to accurately compare both results based only in the spectral and pixel size differences and not illumination influences, cloud cover or different lake size and depth. Sixteen lakes out of the forty lakes from the previous section (Figure 6.5) were selected for this study, merely due to the MODIS images that were available to use at that time. Nevertheless for a simple comparison between satellite characteristics the samples are enough, as it will be shown below.

Figures 6.8 and 6.9, show the exponential decay of depth (z) with the surface reflectance (R_w). There are sixteen figures and in each of them the pixel depths derived from ASTER (Z_{ASTER}) are plotted together with the pixel depths derived from MODIS (Z_{MODIS}). The first thing to notice is the difference in pixel numbers between satellites; this is explained by the fact that the ASTER product used presents a 15x15 m spatial resolution, against the 250x250 m that the MODIS product has. This results in a narrower window of R_w values for MODIS, this is due to the fact that this satellite presents more mixed pixels than ASTER, therefore more pixels are subjected to different substrate. It is also worth noticing that ASTER tends to give deeper lake values than MODIS for most of the cases presented. Only three lakes show deepest values with the MODIS results.

The exponential curves for all the lakes are of the same shape because all the estimates are derived with the optimised set of parameters (Chapter 5), thus only X and Y values vary. The uncertainties were derived from the Monte Carlo approach, using half of the IQR value given by the simulation. Remember that each pixel depth value was taken as the median of all the samples generated based on the error range of the parameters driving the water reflectance equation (Equation 4.5, Chapter 5).

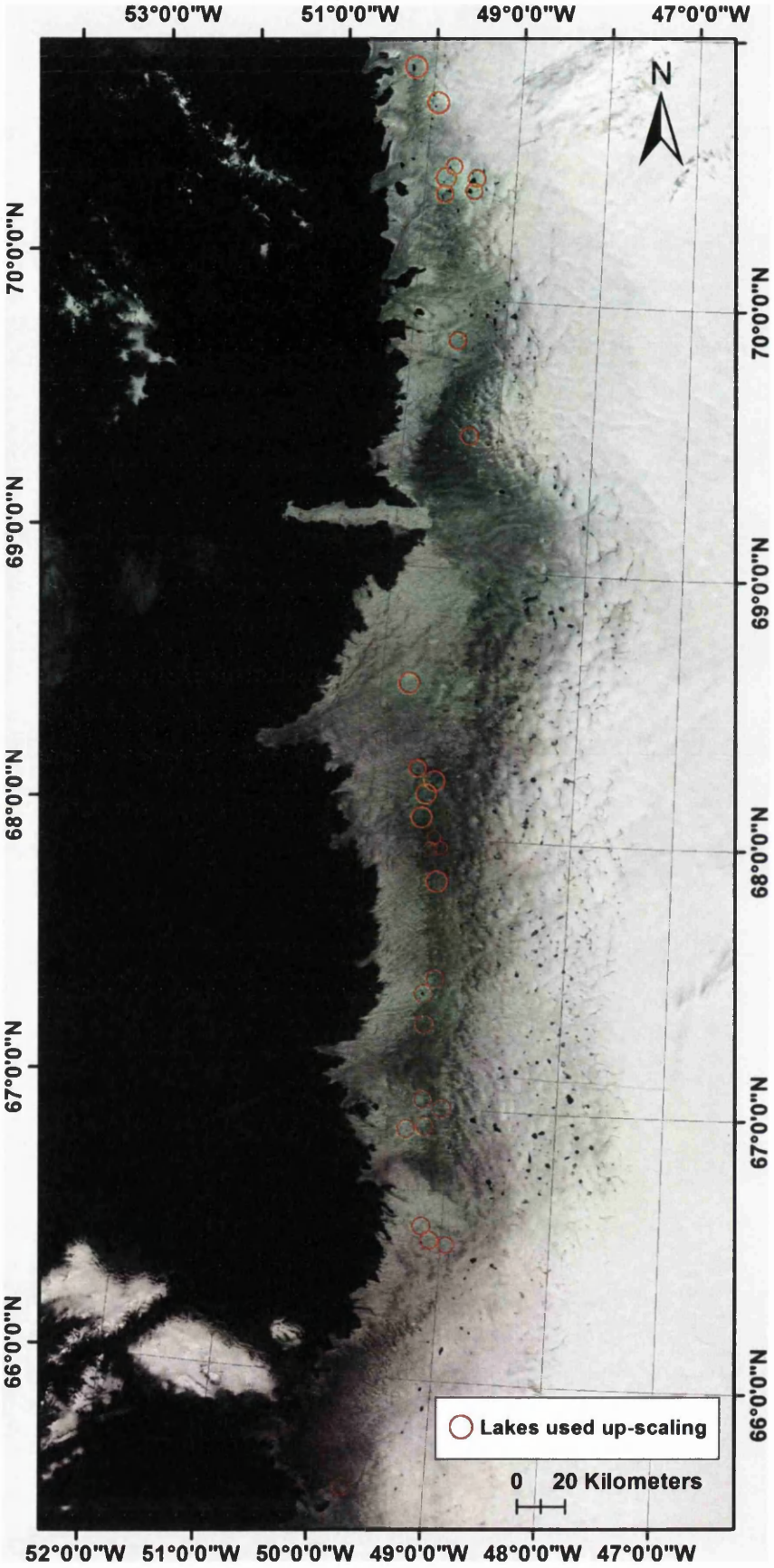

Figure 6.5: Location lake map showing the thirty lakes included in the up-scaling.

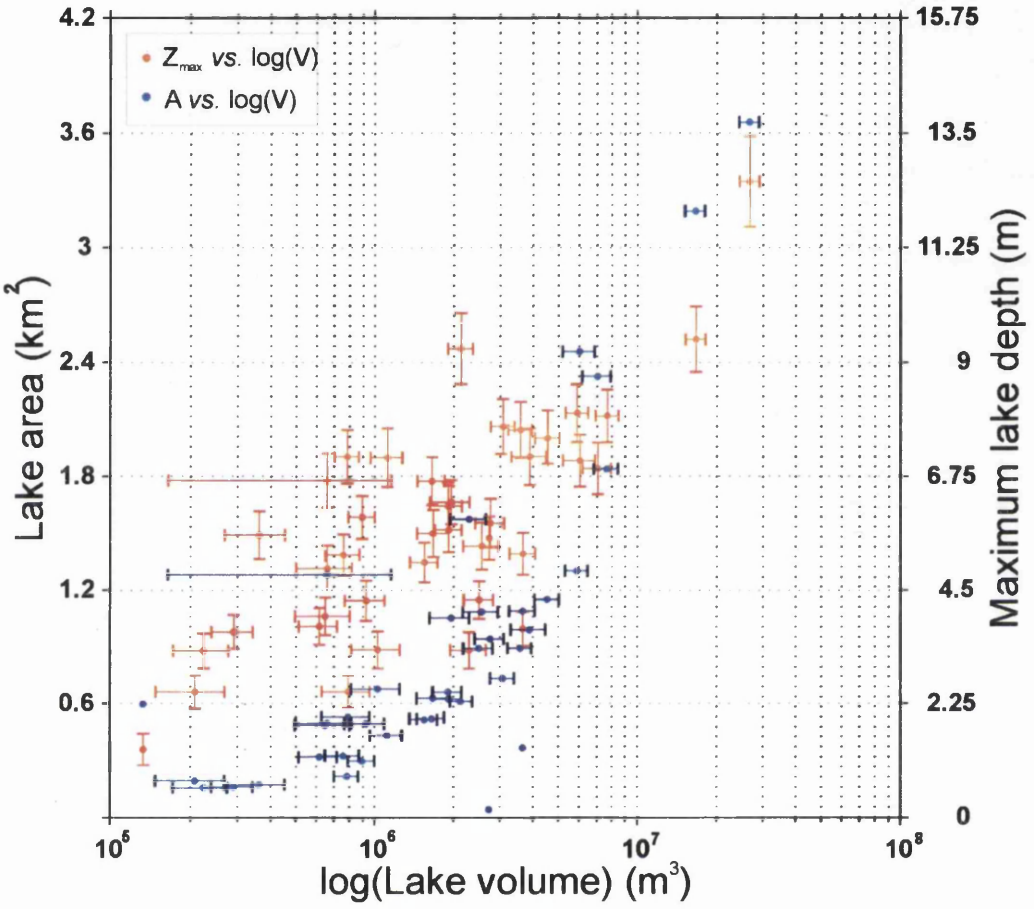

Figure 6.6: Graph summarising the volume estimates derived from the up-scaling. Blue dots correspond with lake area (left Y axis) *vs.* lake volume for the lakes in Figure (6.5). Red dots correspond the maximum depth values of each lake (right Y axis) *vs.* lake volume. Lake volume is plotted in logarithmic scale since many points are concentrated in small volume range.

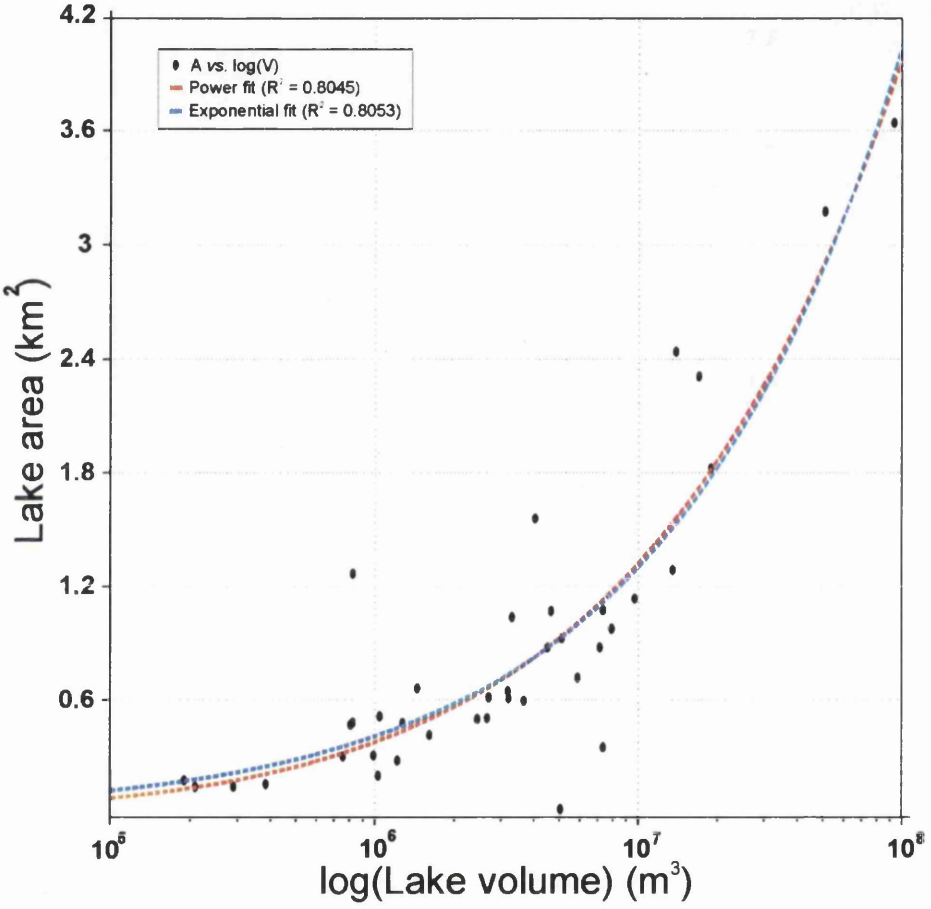

Figure 6.7: Graph showing two possible fitting models for A-log(V) relationship.

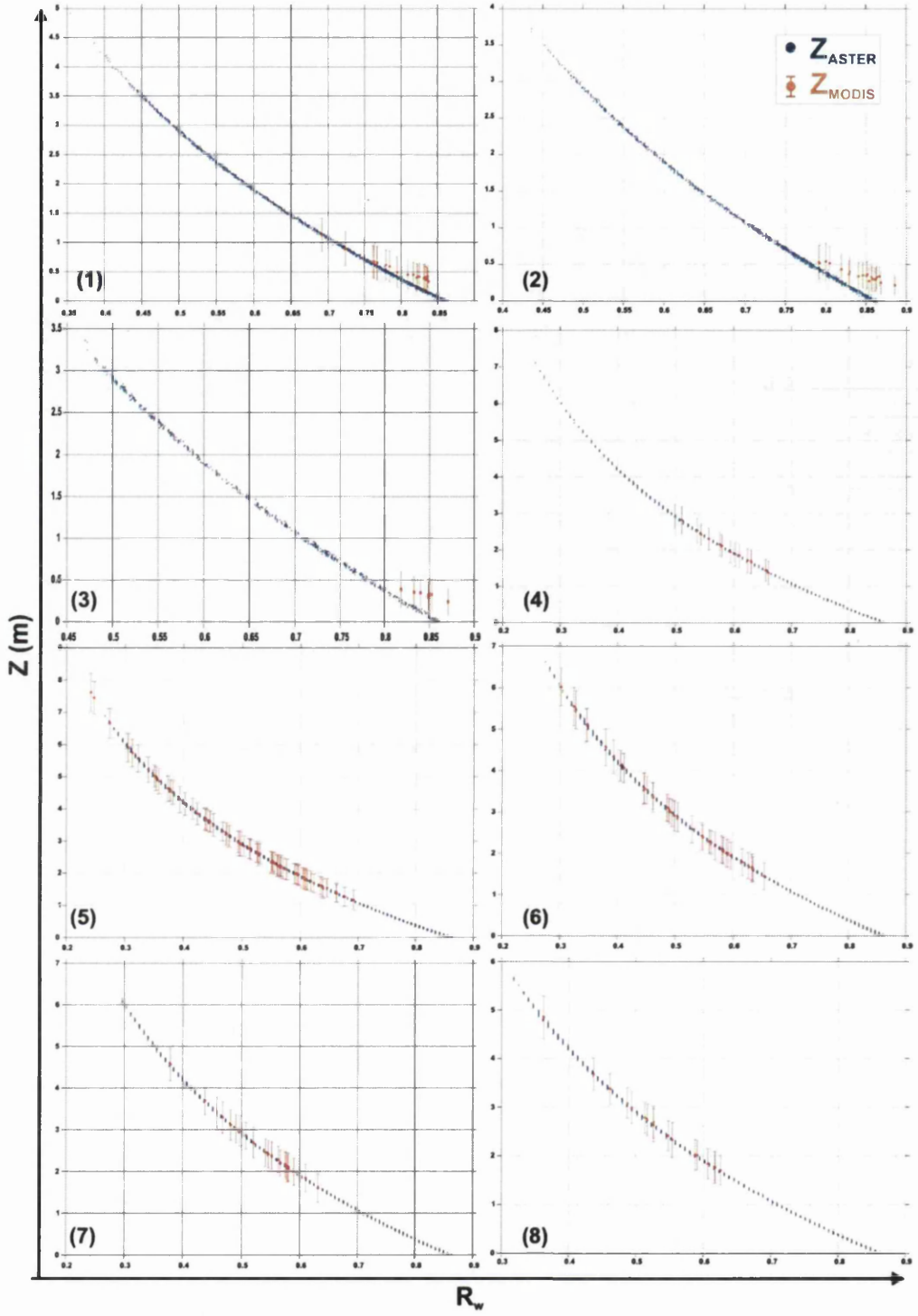

Figure 6.8: Graphs comparing depth estimates derived from ASTER scenes (blue dots) and MODIS scenes (red dots). Both datasets of depths are plotted against the surface reflectance value of each pixel (R_w). Both depth estimates are derived from water-reflectance model, using the set of parameters derived from the optimisation model in the previous chapter. The uncertainties in Z_{MODIS} are shown as red error bars. The error bars for the case of ASTER were excluded due to the high density of data and because they were of the same range as the MODIS errors (Continued overleaf).

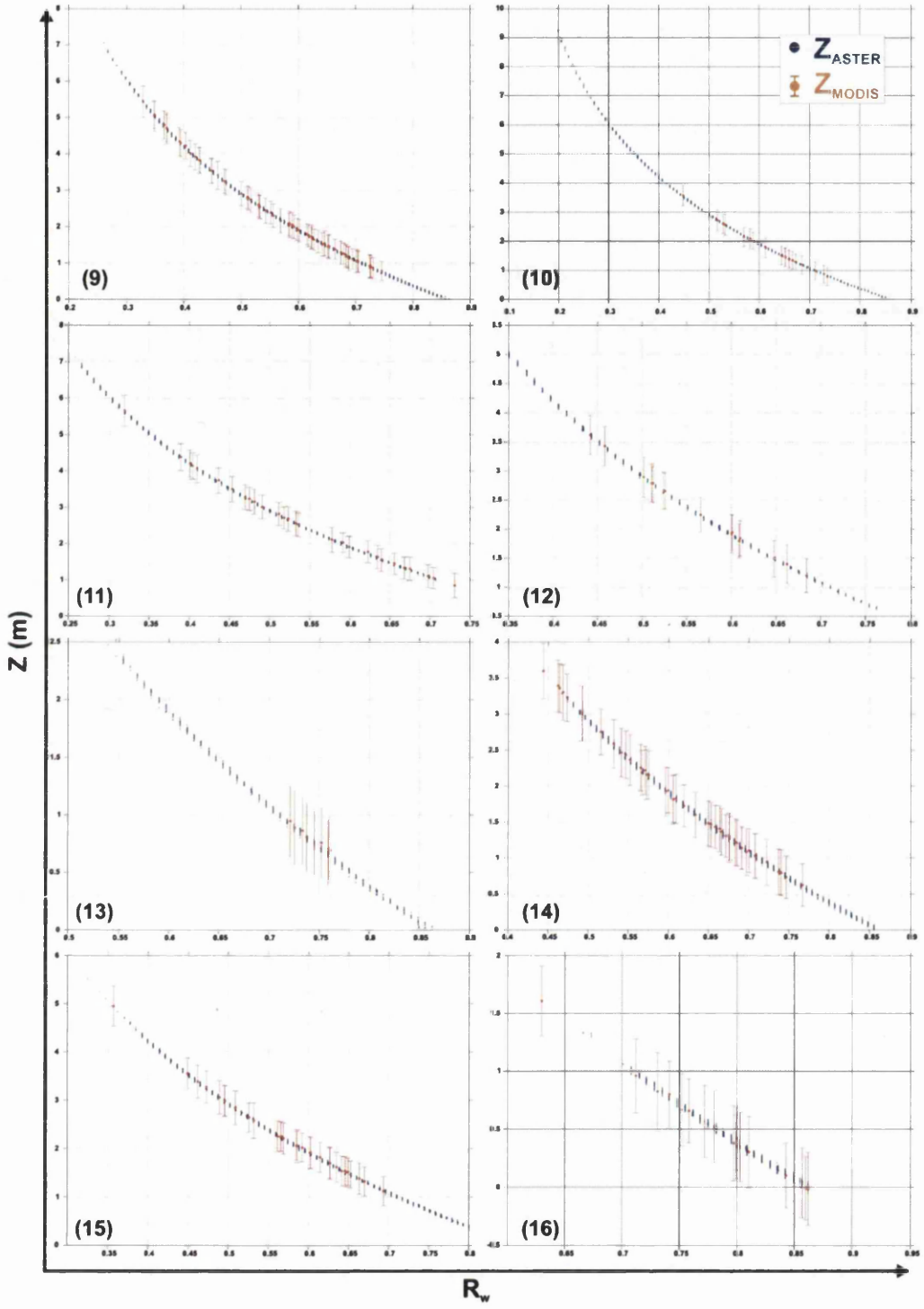

Figure 6.9: Graphs comparing depth estimates derived from ASTER scenes (blue dots) and MODIS scenes (red dots). Both datasets of depths are plotted against the surface reflectance value of each pixel (R_w). Both depth estimates are derived from water-reflectance model, using the set of parameters derived from the optimisation model in the previous chapter. The uncertainties in Z_{MODIS} are shown as red error bars. I excluded the error bars for the case of ASTER because of the high density of data and because they were of the same range as the MODIS errors (Continued from previous page).

Figure 6.10 presents a summary of all the elements involving the volume estimation for both ASTER and MODIS.

Firstly, the deepest pixel of MODIS was plotted against ASTER (a) showing an underestimation of the deepest points with the MODIS dataset. In Chapter 5 the depth estimates of ASTER imagery for the optimisation model tended to underestimate the results compared with the ICESat depths, used as reference depths. From Figures 6.8 and 6.9, the reflectance values of MODIS did not reach as smaller values as ASTER in most of the cases, which explains why the lakes do not appear as deep.

Secondly, lake area for both satellites was compared (Figure 6.10(b)). The linear trend fits with $R^2 = 0.93$, although there is a persistent underestimation of the area in ASTER in comparison with MODIS. Previous studies have shown that this is not necessarily the case and despite the different spatial resolution both MODIS and ASTER can give very similar area estimates (Liang *et al.*, 2012). This disagreement could be explained as follows; ASTER area was determined as explained previously in this chapter. On the other hand MODIS, area was selected applying the region of interest selected for an individual ASTER lake, to the MODIS scene. This produced an overestimation of the lake domain, because the software used tried to fill the region of interest following the coordinates of the ASTER point but the pixel size is different. Therefore when a pixel falls within the domain, is counted as part of the area, even though that point had previously an area of 225 m^2, and in the MODIS scene has a 62,500 m^2 area.

MODIS areas determined by the technique explained in the previous paragraph, produced an increase in area of around 50% in comparison with the ASTER area; this will influence in the volume determination (Figure 6.10(c)). Some of the lakes show agreement between V_{MODIS} *vs.* V_{ASTER}, especially for the smallest lakes. However for the deepest lakes given by MODIS, ASTER presents the smallest values, and

vice versa. This lack of trend might be due to the area determination method used above. Despite this, both satellites present the same order of magnitude for all the variables investigated in this section (depth, area and volume).

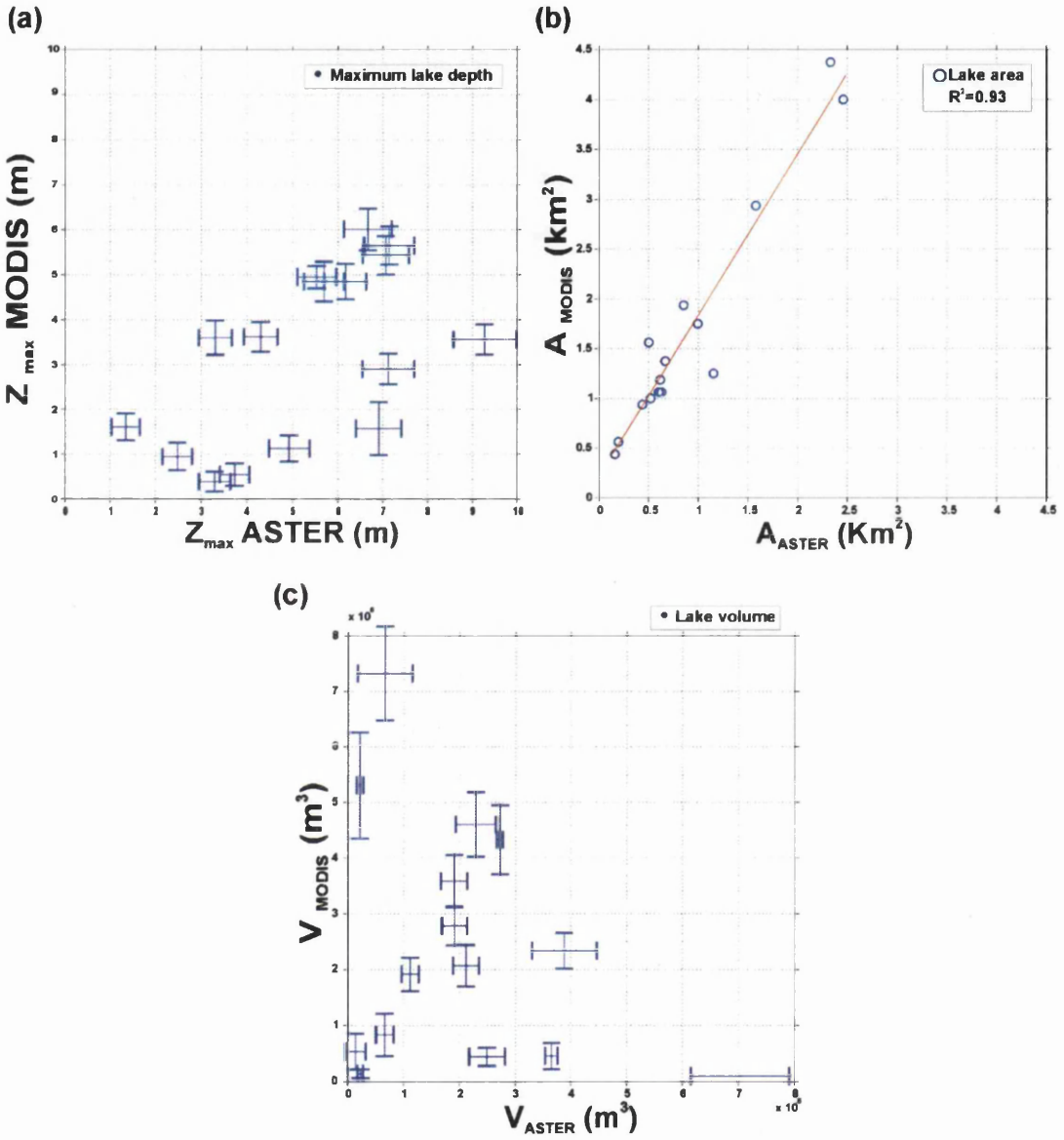

Figure 6.10: Summary of the results obtained by using ASTER and MODIS scenes for lake characterisation. (a) compares the maximum depth of each lake (Z_{MODIS} *vs.* Z_{ASTER}). (b) compares the lake area for both ASTER and MODIS; showing a linear fit (red line) with $R^2 = 0.93$, although there is a consistent overestimate of the area in the case of MODIS of around double the ASTER size.(c) compares the volume estimates for both ASTER and MODIS. For all the graphs error bars are shown, except for graph (b), where no error was associated pixel area determination.

6.4 The role of spectral band choice for the water-reflectance model

In the methods chapter it was justified why ASTER Band 1 was chosen as the spectral reflectance (R_w) for the water reflectance model (Chapter 5). In this section the water reflectance model was applied for each of the visible near infrared red bands from ASTER (Band 1, Band 2 and Band 3N). The reason was to see how the model behaves with different wavelengths, since one of the ideas why the optimised model still underestimates depths in comparison with ICESat was that the chosen band range could be limiting deep lake values.

Figure 6.11 shows the results obtained after applying the water reflectance model for the three ASTER spectral bands. The three graphs show once more the exponential decay of depth with reflectance. An exponential fit function was plotted for a better visualisation of the trend. The decay is however quite different; while for Band 1 there is a pronounced decline in depth of around 5 m for a range in R_w of around 0.3, the decline with increasing wavelengths seem to be less significant. For Band 2, the curve decays only 2 m for a similar range of reflectance; and finally for Band 3N the difference between the maximum and minimum depths is just of 0.3 m for the same R_w range. This results show that depth is more sensitive to variations in the water reflectance for wavelengths between 520-600 nm than for any of the other two (630-690 nm for Band 2 and 760-860 nm for Band 3N). Moreover the satellite signal suffers more absorption for Band 2 and Band 3N. As an example the attenuation coefficient (g) used for Band 3N is 4.14 m^{-1} in comparison with 0.196 m^{-1} for Band 1 (Smith and Baker, 1981).

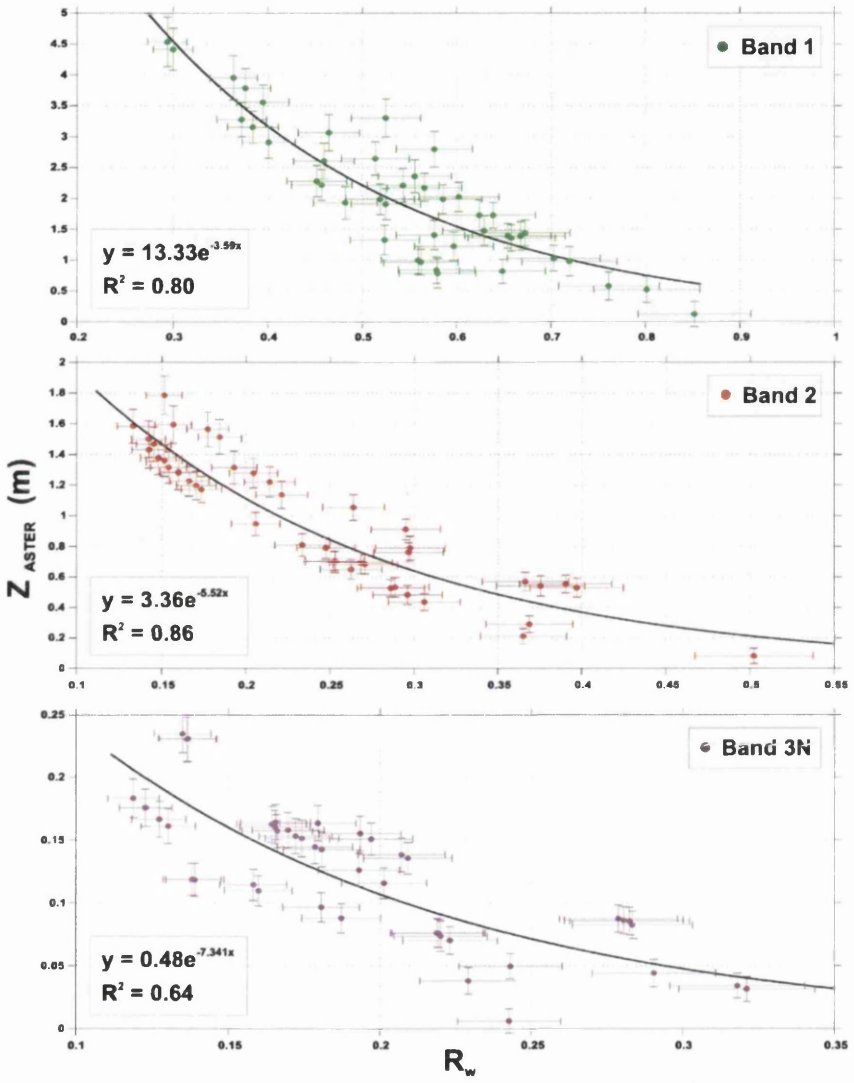

Figure 6.11: Graphs showing the exponential relationship between lake depth (Z_{ASTER}) and the surface water reflectance (R_w). The three graphs correspond with the three visible bands of ASTER imagery. The uncertainties in each estimate is shown with error bars.

Finally, in Figure 6.12 $Z_{ASTER}(\lambda)$ is plotted against Z_{ICESat}. This figure confirms what it was discussed previously; with Band 3N there is almost no depth variation and the values are close to zero, meaning the attenuation coefficient is driving the depth equation, instead of the bed albedo like in Band 1. This is due to the high attenuation coefficient, and hence the signal does not reach the bottom so it is not influenced by it. As showed in Chapter 4, Band 1 appears to be the most suitable band of the three visible near-infrared spectral bands of ASTER.

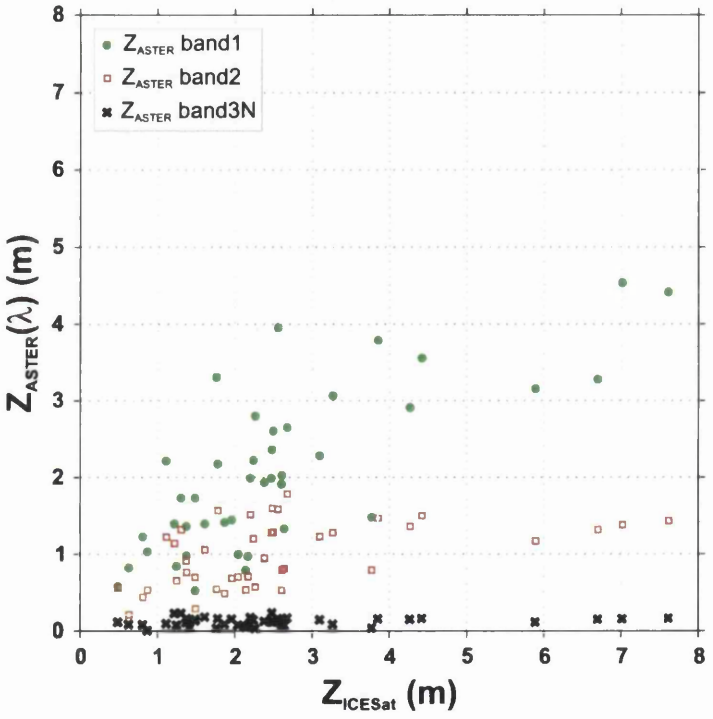

Figure 6.12: Graph comparing the depth values for ICESat (Z_{ICESat}) and ASTER as a function of the wavelength used ($Z_{ASTER}(\lambda)$).

6.5 Pixel reflectance over empty lakes

In this last section of the current chapter the reflectance values that empty lakes present were investigated and compared with the bed albedo values that were used for the water reflectance model. It is worth recalling that the water reflectance model is more sensitive to changes in bottom albedo value in comparison with the other parameters as shown previously (Chapter 5). For this purpose ASTER scenes with empty lakes on them were selected and the pixel reflectance values of the area that was covered by water before drainage analysed. Empty lakes are easy to detect if they have recently drained, because the pixels within the lake area look brighter than the surrounding pixels. This might be due to dust accumulated on the surface free of lakes; whereas the areas that were water covered before, are not exposed to dust or wind transportation. It could also be due to different crystal structure at the lake bed due to melt.

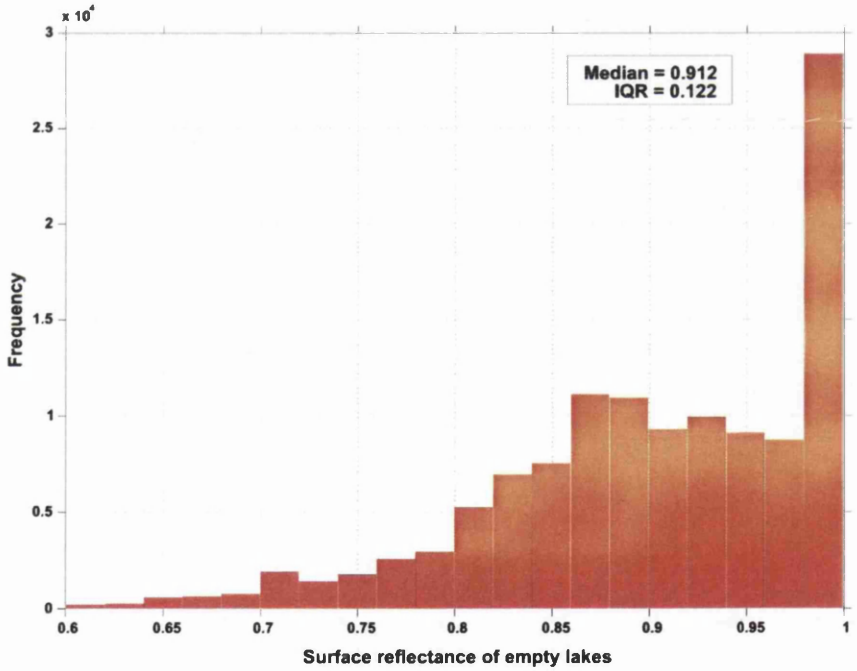

Figure 6.13: Histogram showing the pixel distribution in terms of the bed reflectance in selected empty lakes.

Figure 6.13 shows the spectral distribution of all the pixels within the lake area for

the fourteen examples found. There is a statistically significant number of pixels with reflectance values of around 0.999. From the graph it can be seen it is not a Gaussian distribution, therefore for statistical analysis the median is estimated, being of 0.912 ± 0.055. This value is higher than the bed albedo value obtained from the optimisation model, which is expected because the reflectance in the empty lake is not influenced by the column of water above it, like when the bed albedo is estimated. this means that the spectral characteristics of the bottom have varied.

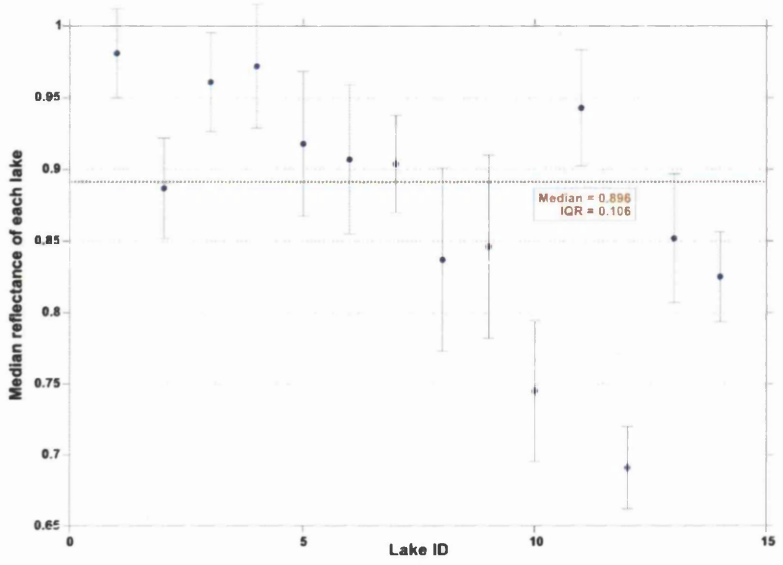

Figure 6.14: Scatter plot showing the median reflectance for each of the empty lakes and the uncertainty derived.

The next step was to look at each of the empty lakes, to investigate whether there are any anomalous reflectance values. For that purpose the median of the empty bottom reflectance was again estimated, but this time for each lake (Figure 6.14). Two of the lakes present a low median of around 0.7 in reflectance, but the rest agree with the previous result, with most of the medians varying around 0.9. When calculating the median of the lakes median, the value is slightly lower than when the median was estimated globally, 0.896 ± 0.053. Nevertheless both error ranges cover the other's value. Further discussion about the reflectance of empty lakes is presented in Chapter 8.

6.6 Chapter summary

In this chapter the optimised water reflectance model developed previously (Chapter 5) was used for further applications regarding the supra-glacial lakes. The main result obtained from this chapter was the quantification of the volume regionally stored around the lakes of the south-west Greenland. These results were compared with estimates based on ICESat imagery. The application of the Monte Carlo approach for the volume uncertainties regarding depth estimates is a unique tool that accurately provides the error in the estimates. The comparison with ICESat volumes is a first approximation, since only a 2D picture is derived from ICESat data. Nevertheless in all the cases the order of magnitude of the volume is in agreement with the ICESat estimates, which gives confidence in the approach.

The use of MODIS imagery for volume derivation and comparison with ASTER derived volumes gives an alternative source of data, and the study of this gives a better picture of the importance of the spatial resolution of the satellite used. MODIS satellites underestimate lake depths, probably due to the mixed reflectance values, which is caused by mixed pixels. Also this underestimation can be due to the fact that the parameters used as an input to the MODIS estimates were derived from the water reflectance model. Although only spectral bands with the same value range were chosen for the study (Band 1 for ASTER and Band 4 for MODIS).

A proof of concept was included in this chapter, where depth estimates derived from the different visible near infrared bands of ASTER imagery were compared. This was done to further understand how the exponential decay of depth behaves with the chosen wavelength. It was shown how Band 2 and especially Band 3N present very strong absorption and that the attenuation coefficient dominates the water reflectance equation.

Finally results derived from empty lakes were presented, showing how the reflectance values in empty lakes cannot be approximated to bed albedo values when the lake is filled, since the spectral properties of the return signal is different. Also it is important to know when the lakes drained to see whether the reflectance characteristic of the surface changed with time.

Chapter 7

Application of the water reflectance model to water-filled crevasses

7.1 Introduction

The objective of this chapter was to explore the possibility of applying the water-reflectance model for the quantification of water-filled crevasse depths, using a high spatial resolution hyperspectral satellite: CASI sensor mounted on the UK NERC's Airborne plane. The specific characteristics of this sensor were described previously (Chapter 4). In this case the dataset includes water-filled crevasses and a supra-glacial lake on Helheim Glacier in south-east Greenland (Figure 7.1). Two different experiments are described using atmospherically corrected Landsat 7 scenes, CASI geocorrected scenes and *in situ* measurements (pers. comm. W. Sneed, 2012).

The first experiment (Section 7.2) compares CASI datasets with those from Landsat and field observations measurements; and further investigates the influence of spatial resolution on water-depth estimations. The CASI dataset has a spatial resolution

between 2 and 10 m, although for the present experiment 10x10 m pixel resolution was chosen. The pixel size selection was chosen based on the geocorrection applied to the CASI scenes and its settings, which were described in Chapter 4. Depth and volume estimates are shown for one lake, from which there were data available from both CASI and Landsat 7 taken one year apart, and also *in situ* measurements from Sneed and Hamilton (2011). ICESat elevation footprints were also available over this lake (see Figure 7.2), although from different years to the other data so it was not possible to directly compare them.

The second experiment was surface water quantification of water-filled crevasses close to the ice front of Helheim (Section 7.3). In this case there are no *in situ* data that can be used to validated these results. Nevertheless this is first approach to depth estimation of water-filled crevasses from remote sensing satellites, which was possible to detect due to the high spatial resolution of CASI scenes. Knowledge of the water-filled crevasses depth is important for calving models because they predict that calving will occur where the depth of surface crevasses equals ice height above sea level (Benn *et al.*, 2007). Krawczynski *et al.* (2009) calculated that lakes with a diameter of 250-800 m and 2-5 m deep store enough volume of water to drive a water-filled crack to the base of an ice sheet of 1 km thickness. Cook *et al.* (2012) highlighted that calving rate depends on the depth on water-filled crevasses, hence the importance of depth knowledge. The quantification of the water stored in crevasses presented here is a first approach that could be used as an input to calving models.

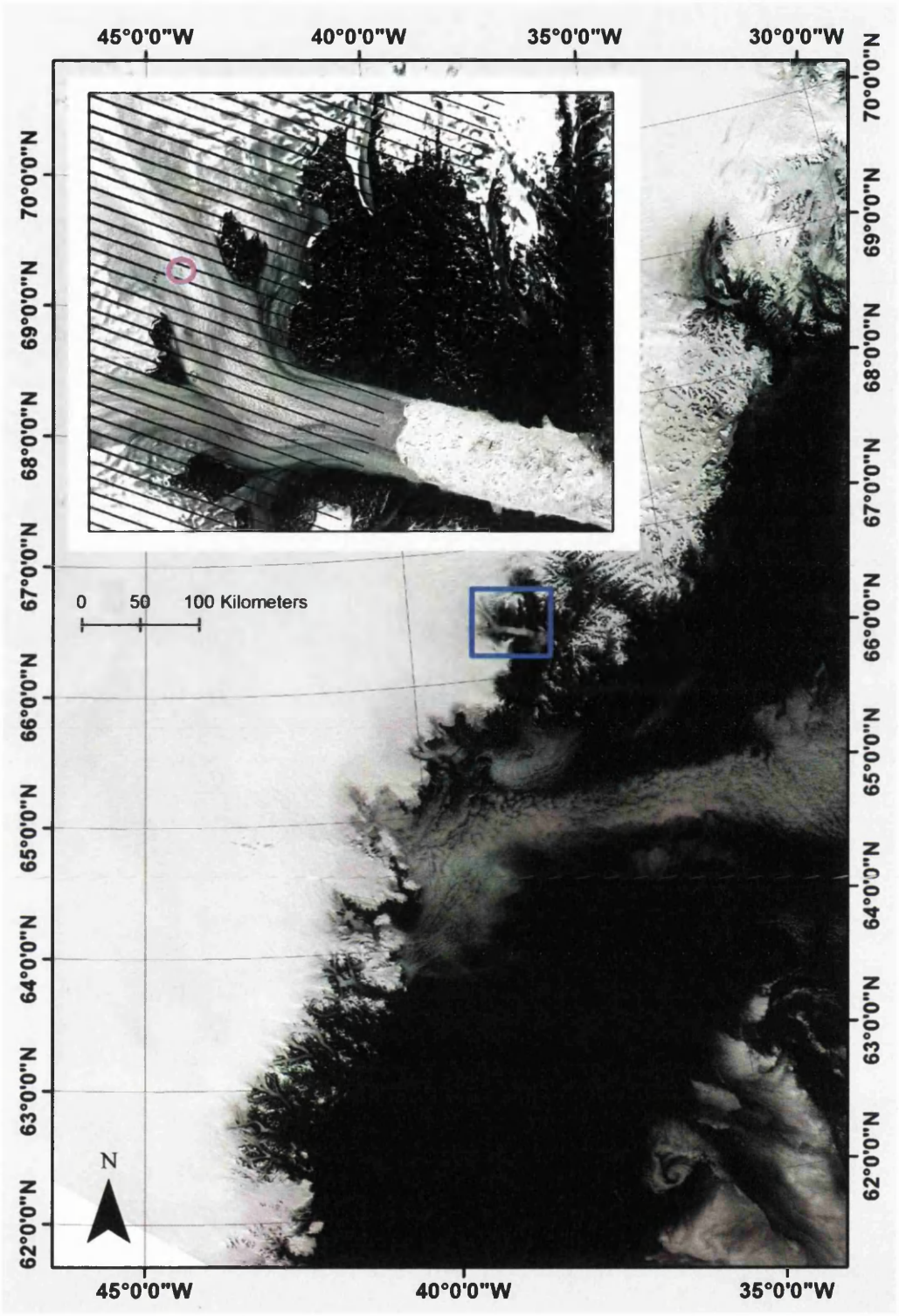

Figure 7.1: Location map showing the lake used in the current section for spatial resolution comparison. The Helheim image corresponds to a Landsat 7 scene 20 July 2008. The pink circle locates the position of the supra-glacial lake used in this section.

7.2 Application of the water reflectance model to CASI and Landsat 7 datasets

In this section the water reflectance model is applied to an individual lake. The lake location is shown in Figure 7.1. Two different optical sensors presented data from that lake, Landsat 7 and CASI. CASI is a new tool for this purpose and was selected due to its high spatial resolution, 10x10 m for the present geocorrection applied.

Table 7.1: Summary of the different data sources and acquisition dates (*pers. comm. W. Sneed, 2012).

Date	Type of measurement
02 July 2007	Landsat 7 atmospheric corrected surface reflectance
19 July 2007	CASI geocorrected surface reflectance
24 July 2007	CASI geocorrected surface reflectance
25 July 2007	Landsat 7 atmospherically corrected surface reflectance
19 August 2007	Landsat 7 atmospherically corrected surface reflectance
11 July 2008	Bathymetry measurements*
20 July 2008	Landsat 7 atmospherically corrected surface reflectance

The lake was chosen because there were *in situ* measurements (on 11 July 2008) of it published previously (Sneed and Hamilton, 2011). That study used a digital fathometer to measure lake depth with an accuracy of 0.03 m and they measured a maximum depth of 3 m within their transect profile, although it does not necessary mean that it was the deepest point of the lake. The Landsat 7 scene (on 20 July 2008) was also used in Sneed and Hamilton (2011), therefore their results could be compared with those obtained using the model developed in this thesis. The CASI scene (on 19 July 2007) was taken almost exact one year before the Landsat one and the *in situ* measurements. There were also three Landsat scenes from July 2007 of the lake; Table 7.1 summarises all the different data sources.

There were no ICESat data from 2007/2008 that could be used as a reference measurements of the empty lake as it was done in Chapter 5. However as shown in Figure 7.2, there are lake profiles for the years 2005/2006, showing a difference of almost 15 m between early melt season (20 June 2005) and late November (20 November 2005). With no extra data, it is not possible to conclude whether 15 m difference in elevation are caused by the drainage of the lake or by melting. It is also interesting that in the next year during spring (24 March 2006) and early melt season (23 June 2006) the elevation is slightly lower than in the previous November and then around around 3 m higher in the next late autumn (24 November 2006). The year 2005 was reported to be very dynamic on Helheim glacier, showing sudden acceleration an retreat, with a change in acceleration from 6 to 11 km/yr between 2002 and 2005 (Luckman *et al.*, 2006; Howat *et al.*, 2007; Stearns and Hamilton, 2007). As the lake location is fixed, rapid surface change can occur by ice advert through the lake basin. Moreover, strain thinning was also occurring (pers. comm. N. Selmes, 2012). Therefore 15 m of elevation change could be due to the previous dynamic changes. This implies that for outlet glaciers like Helheim ICESat elevation interannual measurements could be bias by ice dynamics. This confirms the usefulness of relative depth measurements in those situations.

The comparison between the reference depth estimates (Sneed and Hamilton, 2011) and CASI dataset was done indirectly using Landsat 7 as a link; this was due to the lack of temporal overlap between CASI and *in situ* measurements. The steps taken were as follows;

1. Depths derived from the water reflectance model with Landsat 7, scene 20 July 2008 (Figure 7.3) were compared with depth points measured by Sneed and Hamilton (2011).

2. Landsat from 20 July 2008 was compared with Landsat from 2 and 25 July 2007 (Figure 7.3); in this case spectral characteristics were compared and

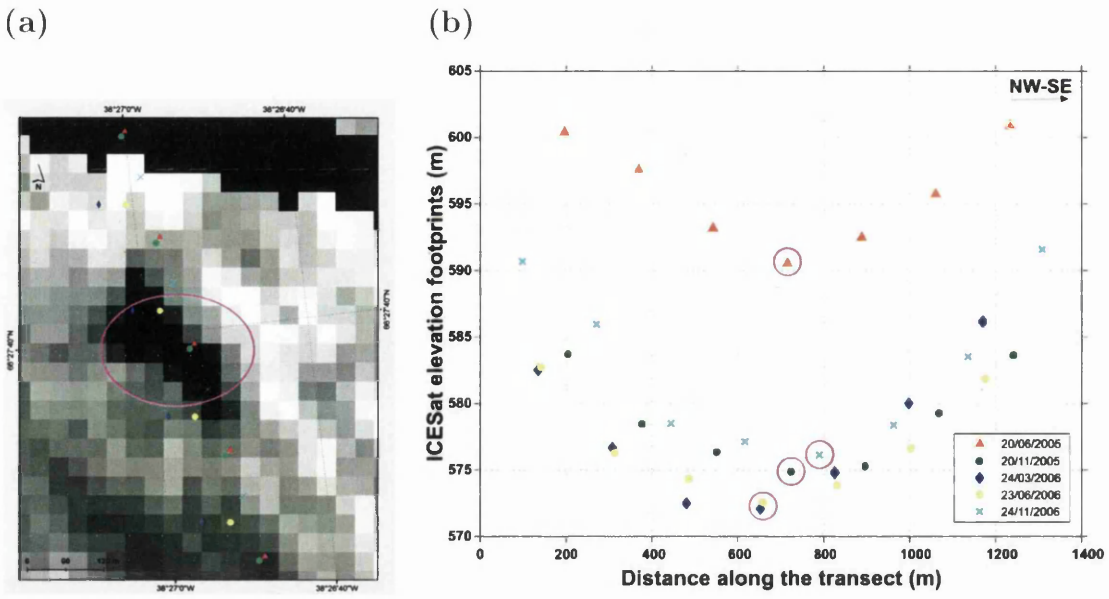

Figure 7.2: (a) Snap shot of the lake from Figure 7.1. The coloured dots correspond to the different ICESat campaigns that passed over the lake. (b) ICESat profiles from the studied lake. The pink circles show the footprints that fall within the pixels corresponding with the lake.

also the deepest points and their location, since it is expected to be different between years.

3. Landsat 2007 (2 and 25 July) is compared with CASI 2007 (19 and 24 July) (Figure 7.3); in this step depth estimates will be compared together with the surface reflectance ranges given for both sensors.

4. Volume estimates were calculated for all the dates summarised in Table 7.1.

7.2.1 Validation of the water-reflectance model with *in situ* bathymetry measurements

The input data used for the water-reflectance model are shown in Figure 7.4, where the distribution of the reflectance of each pixel within the lake is plotted for Landsat Band 2. All the Landsat 7 scenes were atmospherically corrected as showing in the methodology (Chapter 4).

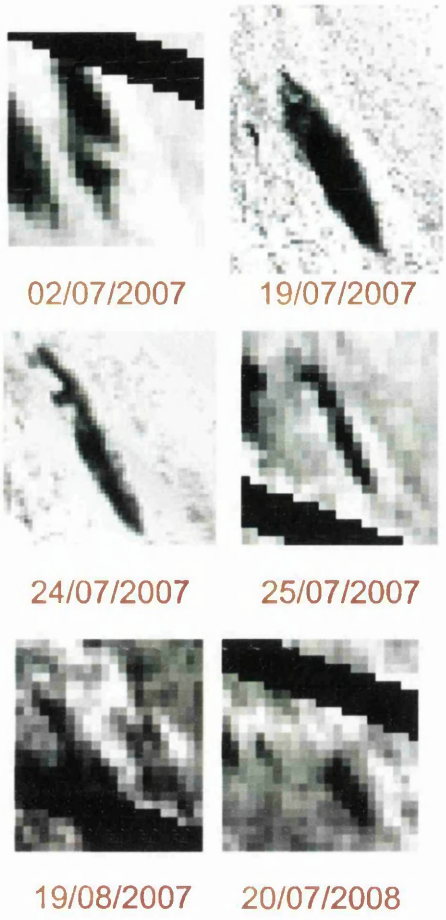

Figure 7.3: Snapshots of the evolution of the lake studied in this section. The second and third scene correspond to CASI Band 3 (547.0-555.8 nm) and the rest are Landsat 7 Band 2 (520-600 nm).

To obtain lake depth from the reflectance values in Figure 7.4, the water reflectance model was applied once more including the Monte Carlo simulation to derive the uncertainties of the results, as done in the previous chapters. To retrieve the values of the three parameters needed as an input to the model (g, A_d and R_∞), the same approach followed by Sneed and Hamilton (2007) and the current study was taken. The set of the input parameters and their absolute error are summarised in Table 7.2, which includes the parameters applied for each scene in the current chapter. Since there were no data to optimise the model as done previously (Chapter 5), it was decided to independently estimate the parameters for each scene.

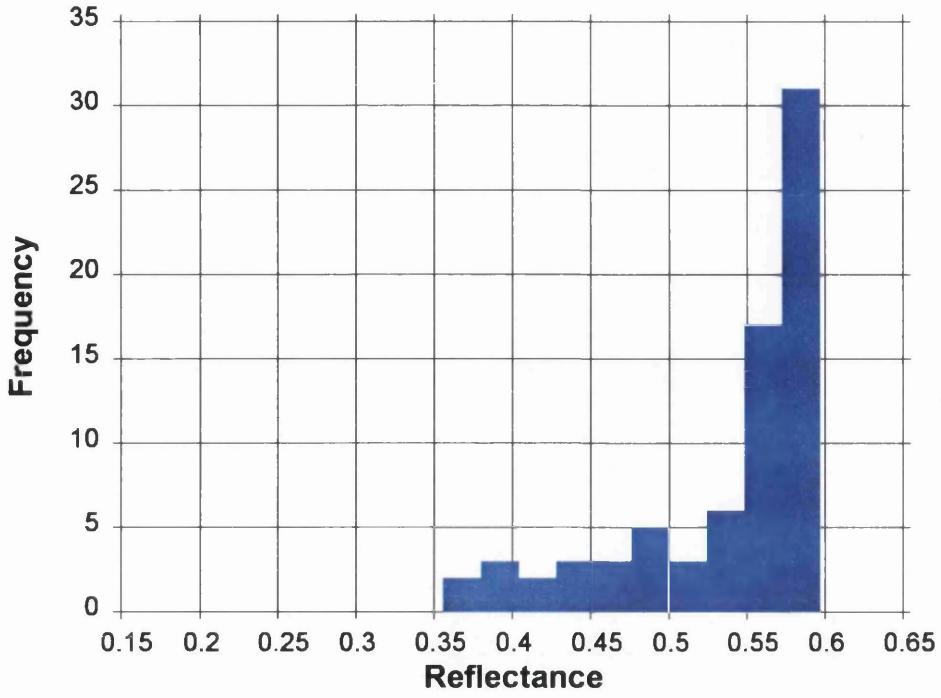

Figure 7.4: Distribution of the surface reflectance of the lake domain for Band 2 Landsat 7.

Table 7.2: Values of each of the input parameters for the water-reflectance model for different scenarios and their absolute errors.

Scenario ID	g (m^{-1})	A_d	R_∞
02/07/2007 (Landsat)	0.197 ± 0.030	0.588 ± 0.038	0.03 ± 0.01
19/07/2007 (CASI)	0.128 ± 0.030	0.496 ± 0.069	0.08 ± 0.01
24/07/2007 (CASI)	0.128 ± 0.030	0.327 ± 0.021	0.08 ± 0.01
25/07/07 (Landsat)	0.197 ± 0.030	0.610 ± 0.033	0.03 ± 0.01
20/07/2008 (Landsat)	0.197 ± 0.030	0.599 ± 0.057	0.03 ± 0.01

After applying the water reflectance model, depth measurements for the whole lake domain are shown in Figure 7.5. The next step was to compare these measurements with the reference depth points previously published (Sneed and Hamilton, 2011). In that study *in situ* measurements give the depths at two points on the lake taken on the 11 July 2008; one at 66° 27' 44,32" N 38° 27' 3.6" W, 0.7 ± 0.03 m deep, and the other at 66° 27' 41,22" N 38° 26' 9.86" W, 3 ± 0.03 m deep. The study says that the 3 m is not necessarily the deepest part of the lake since they took a

random profile of the lake. Despite this, these two points can be directly compared with the Landsat derived depths for the same lake on the 20 July 2008. 9 days of difference are enough to cause major changes, since it has been shown that a lake can drain within hours (Selmes *et al.*, 2011) (See Appendix A Figure A.2). For the point of 0.7 m there are two Landsat pixels within those coordinates and the water reflectance model applied to the Landsat gives the depths between 0.34 ±0.22 m and 1.22 ±0.24 m, which give a mean depth value of 0.78 m, around 1% deeper than the reference measurement. For the 3 m measured point, the model gives a depth between two pixels of 2.20±0.26m and 2.9±0.3 m respectively. The mean of these depths is 2.55 m, around 15% shallower than the given measured point. These estimations are within the uncertainties of the depths, which confirms the validity of the approach applied in this study, although more *in situ* points would give further confidence.

The previous comparison showed that Landsat 7 atmospherically corrected data provide a valid approximation of lake depth, thus in the next subsection modelled Landsat depth measurements will be taken as the reference depth.

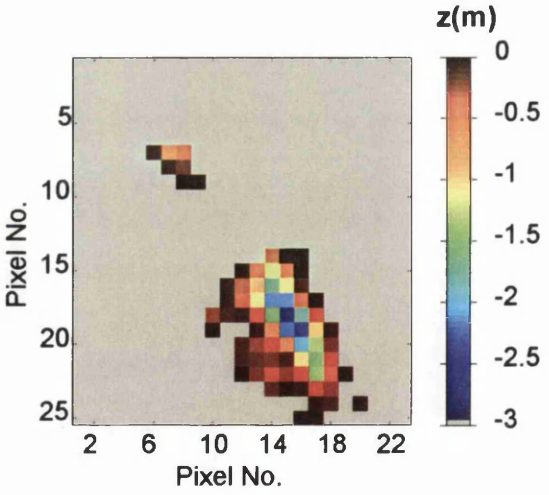

Figure 7.5: Depth measurements of the studied lake for the Landsat 7 scene 20 July 2008. The input to the model were the reflectance from Figure 7.4 and the input parameters from Table 7.2.

7.2.2 Comparison of CASI and Landsat

Following the previous subsection, Landsat results (2008) are now compared with Landsat for 2007. Then as explained before, Landsat 2007 will be compared with CASI 2007 so it can be analysed whether CASI data is also valid for depth estimations or not.

Figure 7.6 shows the reflectance distribution for both CASI ((b) and (c)) and Landsat 7 ((a) and (d)). The lake drained completely by the 19 August 2007 (pers. comm. N. Selmes, 2012) (See Appendix A Figure A.1) , which by chance coincides with the Landsat 7 scene shown in Figure 7.3 (bottom left snap shot). This could explain the higher surface reflectance values given in the late July image in comparison with the Landsat scene of 2 July 2007 (Figure 7.6(a)), where the range is of around 0.3 and the interval is [0.27,0.58]. This could mean the lake was deeper on the earlier dates, indeed the area of the lake is bigger in the earlier image. This hypothesis is demonstrated in Figure 7.7, where the smallest lake area corresponds with the latest Landsat scenes, as does the shallowest lake. In 2007, it is shallower than the early July scene and also presents smaller area.

The next step was the introduction of CASI data for a complete analysis. Focussing on Figure 7.6, the first impression is that the CASI reflectance data presents lower values than Landsat 7, which in theory should not happen if both scenes were atmospherically corrected; although the atmospheric correction method was different for each sensor (see Chapter 4), therefore that could influence the reflectance. Where both satellites agree is in the temporal evolution of the reflectance; in the first CASI scene (Figure 7.6(b)) the reflectance range is bigger than in Figure 7.6(c), and even though higher reflectance values would be expected because the lake is smaller, that is not the case. The small range in the latest CASI scene (around 0.15) can be explained because the lake is shallower but at the same time smaller so less shallowest parts of the lake will be covered with water.

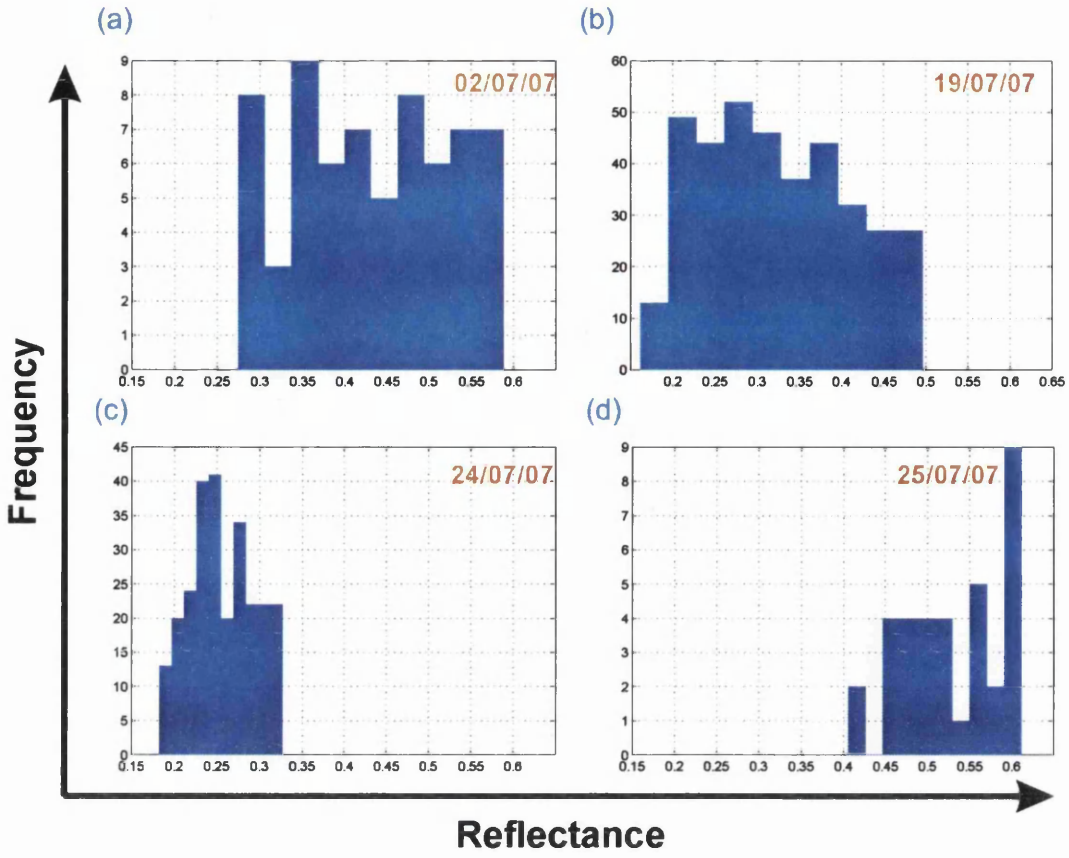

Figure 7.6: Reflectance distributions for the four different scenes during the melting season in 2007. (a) and (d) are from Landsat 7 whereas (b) and (c) correspond to CASI.

Figure 7.7 shows the modelled depths for the four scenes derived from Table 7.2 and Figure 7.6. CASI and Landsat models based on the water reflectance approach present very different depth ranges. CASI's maximum depth estimated is from 19 July 2007 where the values are around 12 m deep, whereas the deepest Landsat point is around 5 meters in early July. Without further information, this could be explained with the lake filling with water. However when looking at the scenes from 24 and 25 of July, which correspond with CASI and Landsat respectively the differences in depth are significant (more than 3 m).

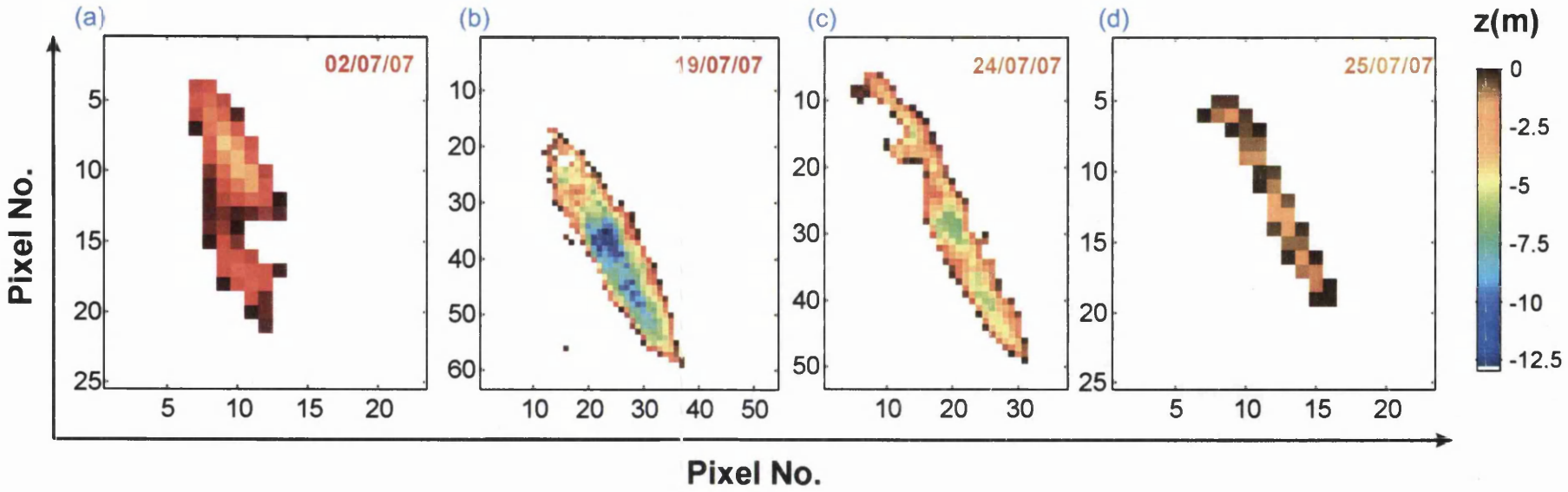

Figure 7.7: Depth estimates for the lake studied for four different scenes. (a) and (d) are derived from Landsat 7; Figures (b) and (c) correspond to the depths derived from CASI data. The input to the model where the reflectance from Figure 7.6 and the input parameters from Table 7.2.

7.2.3 Volume evolution of the supra-glacial lake derived from CASI and Landsat scenes

The last part of this section is the estimation of water volume of the lake for the different scenes. Table 7.3 summarises these results. The largest lake area corresponds with the Landsat 7 scene of 2 July 2007, which was expected looking that the snapshots in Figure 7.3 where it appears flooded around the main lake area. The consecutive scenes from 24 and 25 July show that the area in the later day is 15% bigger than in the previous image, even though the lake depth estimates are deeper in the earlier image. This difference is easily explained with the difference in pixel size, because at the edge of the lake a pixel that is part of the lake can present a percentage of ice, hence increasing the lake area. In 2008 the lake has its smallest area coverage.

Table 7.3: Summary of the results obtained in the current section, showing the volume estimates from the five different scenes, with their relative error derived from the Monte Carlo simulation. The area for each scenario is also shown.* ϵ referrers to the uncertainty in the volume estimations.

Scene date	Area (x10^4 m^2)	Volume (x10^5 m^3)	ϵ* (%)
02/07/2007 (Landsat)	6.75	1.082	1.4
19/07/2007 (CASI)	5.94	1.774	17.2
24/07/2007 (CASI)	3.15	0.740	18.4
25/07/2007 (Landsat)	3.71	0.252	21.7
20/07/2008 (Landsat)	2.58	0.677	65.6

Looking at the volume, it is interesting to see how the lake volume increases between early and mid July (2007) by almost 40%, and then loses half of its volume in less than a week. The substantial difference in volume between 24 and 25 July is explained once more with the difference in surface reflectance between the two sensors obtained in this thesis. The uncertainty in the volume for 2008 is more than 50%,

this is due to the fact that of the three Landsat scenes, that one has the deepest point and hence the uncertainty is bigger, since it is proportional with depth. And even though CASI scenes gave deeper lakes, the pixel area for Landsat is bigger and hence the relative error bigger too.

7.3 Application of CASI hyperspectral data for water quantification on Helheim glacier front

In this section the water reflectance model previously applied to supra-glacial lakes was tested with water-filled crevasses on the glacier front of Helheim glacier (Figure 7.8). The depth estimates from this study are the first made of water depth in crevasses from optical imagery; therefore a detailed discussion is needed to conclude whether it is possible to apply the water reflectance model on crevasses or not.

The first step was to do a water classification across the glacier front, because unlike supra-glacial lakes that have been mapped and located previously (Selmes *et al.*, 2011; Leeson *et al.*, 2012), crevasses are influenced by ice dynamics and they advance with the glacier front and within hours/days the geometry can change. After the water classification, the water reflectance model is applied to the reflectance of the water-filled crevasses, obtaining water depths and from there an estimate of the volume of water stored on the surface of Helheim glacier front.

7.3.1 Water classification across Helheim front

To obtain a water classification a band ratio method was applied. This method is useful for this purpose because it enhances the spectral differences between bands. It consists of dividing one spectral band by another producing relative bands inten-

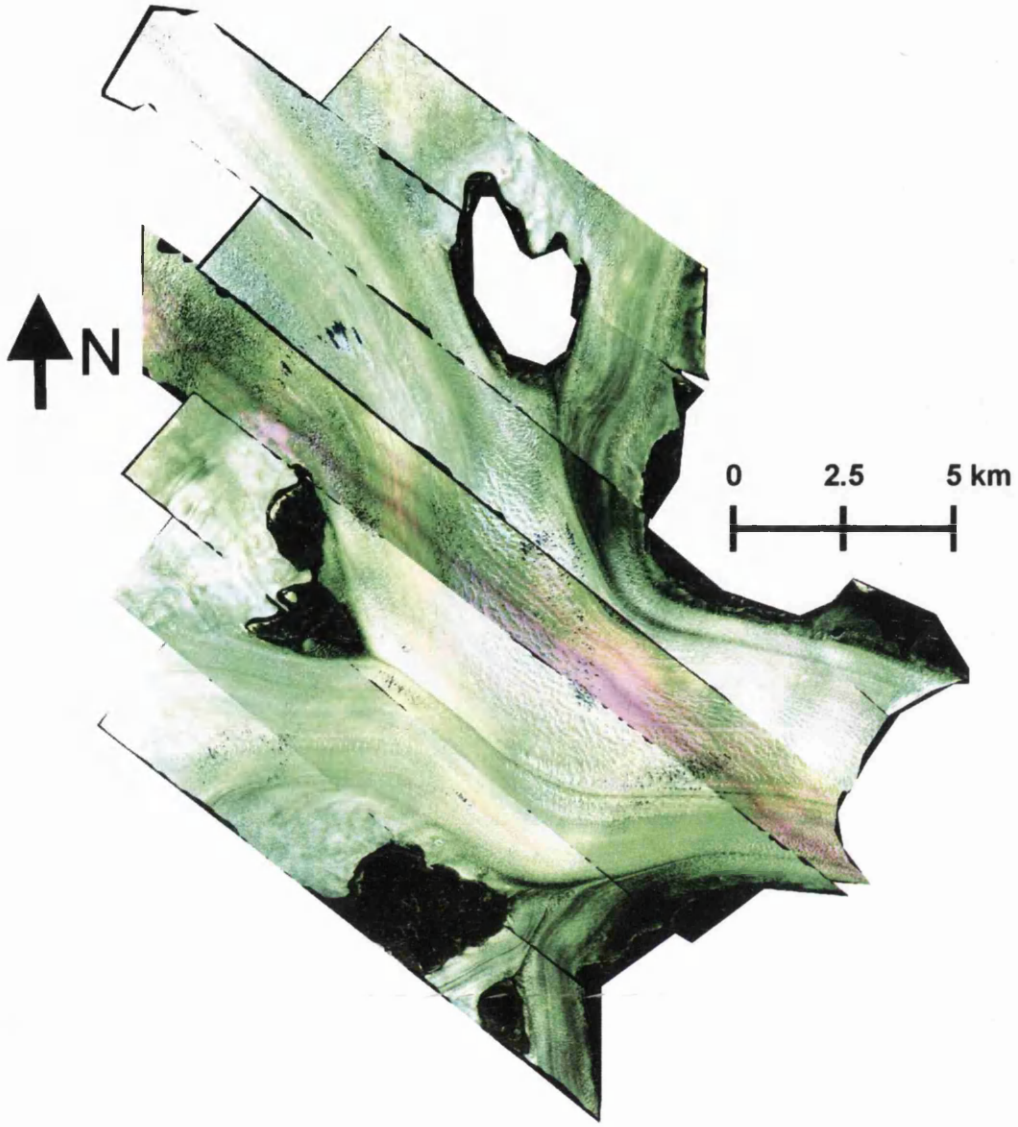

Figure 7.8: Composite image of Helheim glacier composed by the combination of the different flight lines of CASI on 24 July 2007. The colour composition chosen is (R:B6, G:B4, B:B1) because this differentiates water from ice effectively.

sities. Bands that behave completely different for the chosen target are needed. In the present study the target is water, and it is known that blue and red bands have different spectral characteristics for water surfaces. Figure 7.9 shows where the blue and red bands are and how the CASI reflectance varies with the wavelength. The biggest change in reflectance is between the blue range and the red near-infrared. The lowest range of the blue corresponds with Band 1 CASI (431.6-449.0 nm), which is the first of the bands chosen. Band 4 CASI (676.5-681.8 nm) did produced a con-

trast with Band 1, but produced errors of classification, therefore the ratio method was tried again with another combination, using CASI Band 6 (735.4-740.7) in this case. Figure 7.10 shows that the difference in reflectance between R6-R1 it is bigger than with R4-R1, therefore the ratio band combination R6/R1$\in$[0.001,0.6] was chosen for the water classification method.

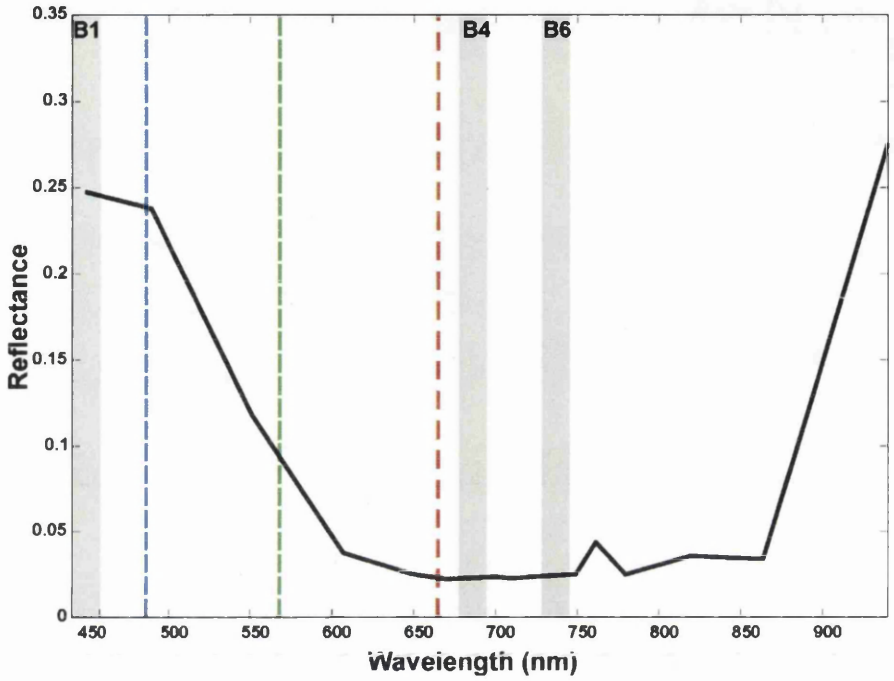

Figure 7.9: Reflectance profile over water in a crevassed taken from one of the CASI scenes from Figure 7.8. The visible centre wavelengths are shown by coloured lines and the CASI wavelengths intervals used in Figure 7.8 are shown in grey stripes (B1, B4, B6)

The CASI scenes used for the water classification are shown in Figure 7.8. The colour composite of the figure (Band 6, Band 4 and Band 1) was chosen to help visualise the water on the surface, in this case with a dark blue tone. After applying the band ratio R6/R4 to Figure 7.8, the water classification is shown in Figure 7.11 in red colour.

The total area of Helheim glacier front is 1,139.15 km^2, which was computed adding up the number of pixels that compose Figure 7.11 multiplied by the pixel area 10x10 m. The number of pixels that are part of the water classification ratio, *i.e.* the ones

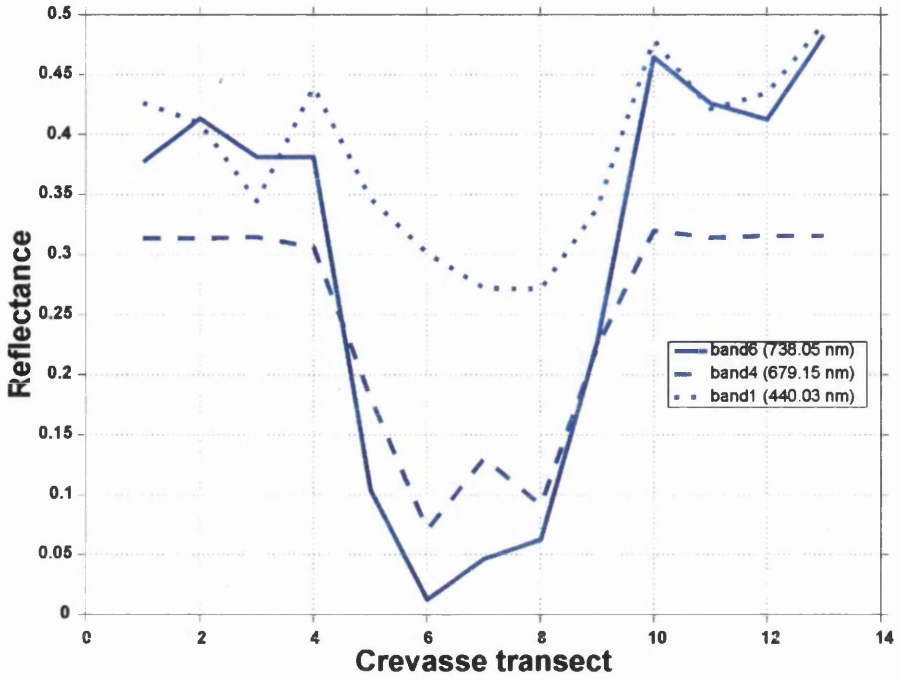

Figure 7.10: Spectral profile through a crevasse. Note that the three spectral bands used in this profile are the same ones as in the previous figures (B1, B4, B6). Note the similar curves in B4 and B6 in comparison with B1, and how B6 shows the biggest spectral difference with respect to B1.

that meet R6/R1$\in$[0.001,0.6], is 24,041; the relative area covered by water is then around 0.2%, which is insignificant with respect to the total area of the glacier front. This result could have major impact in the current calving models, which assumed water-filled crevasses on the glacier front for calving to happen (Cook *et al.*, 2012). However investigating the distribution of water-filled crevasses could be more interesting for the influence on calving. Water-filled crevasses distribution will be discussed in the following chapter (Chapter 8).

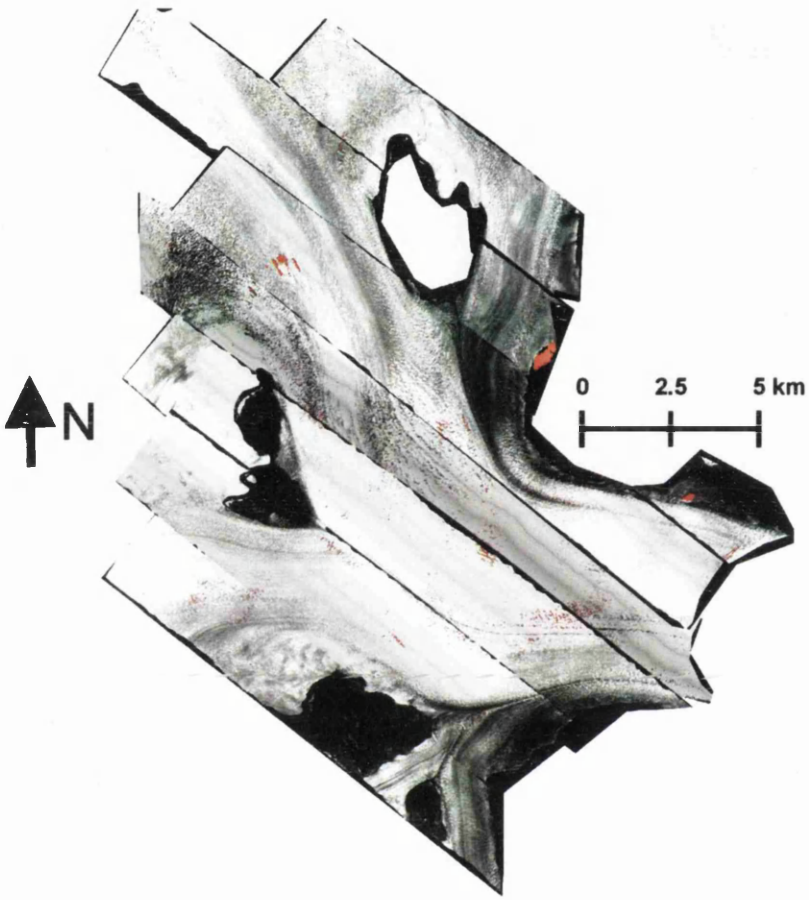

Figure 7.11: Helheim glacier showed with the composition of CASI flight lines as in Figure 7.8. In this case the image is shown in one band colour (Band 3) and the red points corresponds to the water detected by the ratio classification used in this section R6/R1.

7.3.2 Water-filled crevasses depth estimations

As mentioned before the quantification of water-filled crevasse depths is important for calving models, therefore in this section the water reflectance model was applied to the CASI scenes from the previous section. For this purpose, the surface reflectance from the pixels that fall within the water classification in Figure 7.11 was selected (Figure 7.12); once more the surface reflectance is used as input to the water reflectance model to derive water depth. The set of the input parameters chosen for this example are taken from Table 7.2, selecting the ones derived for the CASI image 4 July 2007, since it is the same one used in the current section (g = 0.1284 ± 0.03; A_d = 0.3273 ± 0.0208; R_∞ = 0.08 ± 0.01).

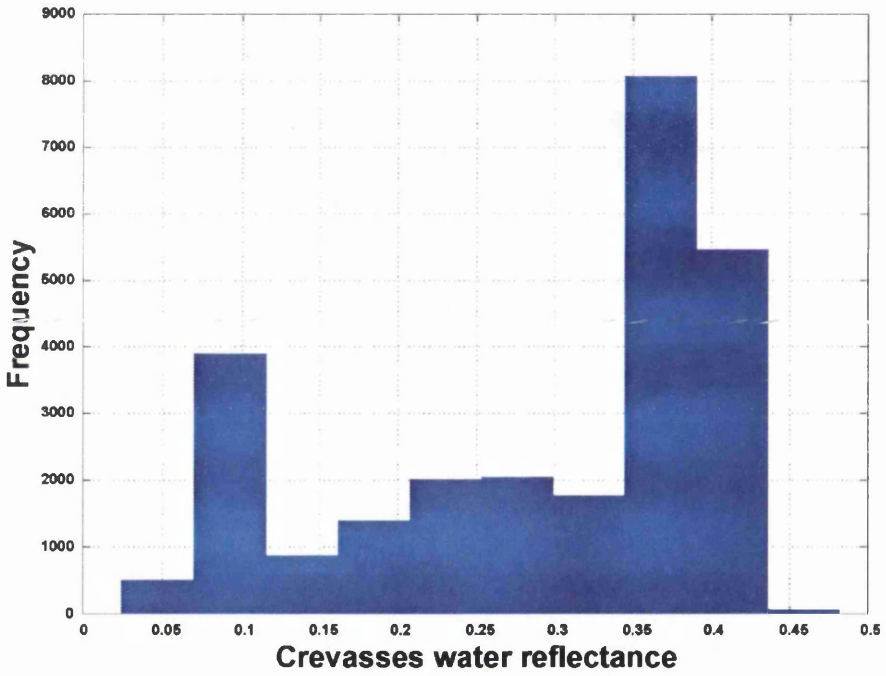

Figure 7.12: Surface reflectance distribution of all the water pixels detected by the ratio classification approach from Figure 7.11.

Figure 7.13 shows the distribution of the depth of water in crevasses Helheim glacier. The values of each pixel are the median of the depths generated from the Monte Carlo simulation, as previously (Chapter 5). Notice that around 39% of the pixels fall within depth values greater than zero, which means they are out of the water area domain. That is a big proportion of the total number of pixels, reducing

considerably the water covered area percentage estimated previously; reducing that percentage of the total area to almost 0.1 %. This result could be caused by various factors;

1. The set of parameters used to derived crevasse depth are not adequate for this purpose, because they underestimate crevasse area and hence depth, since it is proportional to the reflectance.

2. The ratio water classification made does not reflect realistically the water stored on the surface of the glacier, *i.e.* another ratio needs to be chosen in order to meet this.

3. Water in crevasses cannot be detected from optical sensors as in the case of lakes, because the geometry of the crevasses is completely random, with spikes of ice combined with very deep parts. The sharp crevasse walls influence in the returning signal, therefore distorting the true water reflectance given by the sensor. The shadowing effect will be discussed in Chapter 8).

From the previous scenarios that could cause the positive depth values, scenario two would be the first to be dismissed, because when selecting the most appropriate ratio (R6/R1), an underestimation of the water pixels was made, because if not many new pixels free of water would appear as water. Therefore, the final pixels are with high probability inside the water area domain.

Despite the uncertainties on the water-filled crevasses depth estimates, it is still interesting to calculate the total volume of water stored through the glacier front of Helheim. For that purpose the pixels with positive depth values in Figure 7.13 were excluded. The total volume for the area 694.88 km^2 (61% of the total area derived from the ratio method) is $10.77 \text{x} 10^6 \pm 2.70 \text{x} 10^6$ m^3. The relative error is around 27%.

The uncertainties of the depth estimates derived from the Monte Carlo simulation are calculated from half of the IQR for each median depth value. Figure 7.14 shows

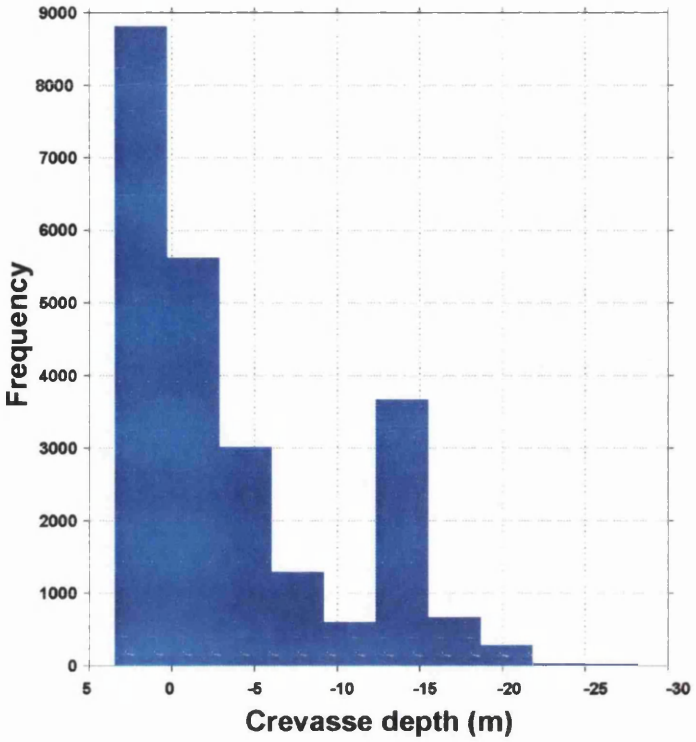

Figure 7.13: Depth distribution of all the CASI pixels from Figure 7.12. Notice that there 9,344 pixels ($\approx 39\%$ of the total)that give positive depths, which were removed from the analysis.

how the error in depth estimates increases as depth increases, which has been already reported (Hedley and Mumby, 2003). It is interesting how the relationship between depth estimates and errors changes; it seems that there is an inflexion point where the relationship changes. Until 15 m deep the error increases exponentially with depth; for deeper values the points scatter around the plot, still with a positive relationship but the exponential curve disappears. Does the model behave different for deeper lakes? Is there an inflexion point after which the relationship between depth and reflectance ceases being exponential? It is known that the water reflectance models, like the one used in the current study are limited to shallow waters. If that is the case and that value is 15 m like in Figure 7.14, that would imply that the water reflectance model is not applicable to crevasses. Further discussion is provided in Chapter 8.

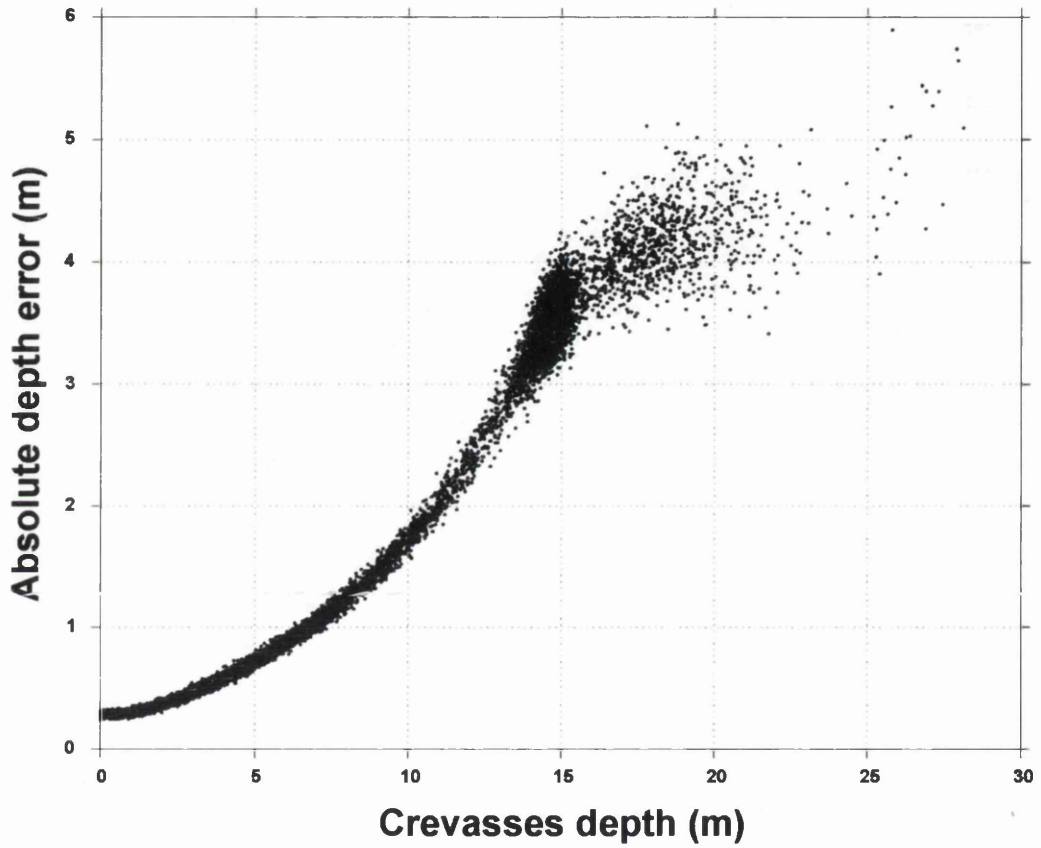

Figure 7.14: Uncertainty in depth estimates *versus* crevasses depth for all the pixels that give z < 0 in Figure 7.13.

7.4 Chapter summary

In the current chapter the water reflectance model was used for the first time to derive water-filled crevasse depth. For this purpose a hyperspectral satellite was used (CASI), with a spatial resolution of 10x10 m. To validate the results obtained from CASI dataset, Landsat 7 was used. The reason for choosing this sensor was that Sneed and Hamilton (2011) validated depth estimates from Landsat 7 with *in situ* measurements. To sum up, *in situ* measurements were used to validate Landsat 7 depth values over the lake in Figure 7.1 for the year 2008; Landsat 7 for 2008 was compared with Landsat scene of 2007; finally CASI data was compared with Landsat 7 for 2007.

The differences between Landsat 7 depth estimates and CASI shown in Figure 7.7 could be explained either by the differences in the measurement of water reflectance from both sensors and the different atmospheric correction methods used (Figure 7.6) or by at the evolution of the lake, from the early stages where it was growing, when it started draining and when it was drained. Nevertheless, a full bathymetry profile of the lake would be needed to contrast these results and from Sneed and Hamilton (2011) only two data points were available, and none of them represented the deepest point of the lake.

The second major result from this chapter was the water quantification derived from CASI data using a band ratio algorithm. This is a novel result and could contribute towards the improvement of current calving models (Cook *et al.*, 2012; Nick *et al.*, 2010; Otero *et al.*, 2010). The current estimations predict that less than 0.2% of the total area of Helheim is covered with water, which does not seem significantly crucial for calving processes. However, further analysis of water-filled crevasses distrubution across Helheim could provide useful information about water presence at the calving front, where calving events occurr. This analysis will be presented in Chapter 8.

The last section of this chapter corresponded with water filled crevasses depth estimations. The results obtained there are not conclusive, because the model predicts no water where water is visible. Moreover, crevasse geometry is not like that of supra-glacial lakes; crevasses present almost vertical walls and the bottom is not homogeneous, it could present water crystals from melt or ice spikes that will interfere in the surface reflectance values, making the satellite signal to have multiple refractions. Even more, the depth on the crevasses might be deeper than the maximum permitted by the water reflectance models, which were developed for shallow waters. Despite all this uncertainties, there is no doubt that the use of CASI hyperspectral data for water quantification across Helheim could be a big step forward for the better understanding of its influence on calving events.

Chapter 8

Discussion

8.1 Introduction

In this chapter a general view of the different sources of limitations derived from the results chapters are introduced and discussed.

Firstly the water reflectance model performance is presented (Section 8.2). The main limitation found from the water reflectance model is that it tends to underestimate water depths of shallow lakes in comparison with ICESat dataset, which was used as the reference depth. Due to these differences in depth estimates, further investigation about how representative ICESat is for this purpose is needed. The use of ASTER water reflectance as an input to the model highlighted the importance of the choice of the physical parameters (Chapter 5). The derivation of A_d (bottom albedo) in Chapter 5 is analysed and compared with reflectance values of empty lakes found in some ASTER (Section 8.5). However, these reflectance values of empty lakes cannot directly be compared with A_d obtained for the water reflectance model, because of the different times of the drainage events for each lake, which will effect the spectral characteristics of the substrate.

For the estimation of the uncertainties a Monte Carlo simulation was applied. This proved to be an useful tool for this purpose, because it takes into account the influence of each of the parameters in the model in a way that can be tuned. Section 8.3 presents further analysis of the Monte Carlo performance.

In Section 8.4 the potential uncertainties that could influence the water reflectance model are listed. Starting from ICESat as a depth validation tool; then how the water reflectance and the parameters could be limiting the model to a certain critical depth; followed by how the input parameters add uncertainties to depth calculations; and finally how these uncertainties influence on the total volume estimates.

Section 8.5 introduces a phenomenon that is not yet well understood; this is the dark zone that appears in the ablation area in the south west of the GrIS during the late melt season, causing a remarkable decrease in surface reflectance. The striking finding is that over the areas where supra-glacial lakes formed previously and then partially or totally drained, the dark ice does not appear, leaving the ice previously water covered, with reflectance values similar to fresh snow. The implications of this dark zone over the depth estimates from optical imagery is discussed.

In Section 8.6 the volume estimations are compared with previously published estimations. Further analysis of the potential relationship between volume and area introduced in Chapter 6 is included here. The results showed in that chapter could help in understanding the limitations of remote sensing for a quantification of water stored on the surface of the GrIS.

The estimation of the depth of water-filled crevasses from remote sensing is also discussed in this chapter, taking into account the expected geometry of a crevasse in comparison with a lake. This discussion can be found in Section 8.7.

Finally, Section 8.8 discusses the glaciological implications that this thesis could have for future studies.

8.2 Further justification of satellite choice for the water reflectance model

8.2.1 Resolution effects

Previous studies of supra-glacial lakes on the GrIS have showed that MODIS imagery can be a valid data source for lake detection and area measurement. Furthermore, due to the high temporal resolution, it is possible to monitor the evolution of lake area during each melt season; also as lakes form in the same position each year, it is possible to monitor interannual variations of lake area (Liang *et al.*, 2012; Selmes *et al.*, 2011; Sundal *et al.*, 2009). Despite this, from Figure 8.1 MODIS is not adequate for a detailed lake perimeter identification, due to it coarse spatial resolution. The importance of accurately determined area for volume measurement is discussed in Section 8.4.

Masking the ASTER scene from lake 2 (Figure 8.1(2a)) with the seven pixels of the corresponding MODIS scene (Figure 8.1(2b)), a distribution of the reflectance values of ASTER falling within each MODIS pixel was produced (Figure 8.2). There is no clear probability distribution, although the wide range of ASTER reflectance within each MODIS pixel is interesting. This range could come not only from ice but also from both shallow and deep water. It could also be that as ASTER has higher resolution, it will resolve better the water and lake bottom characteristics: for example reflectance could be lowered if a patch of cryoconite appeared within a particular pixel. Figure 8.2 shows the major implication that these results will have in the depth estimations. Further discussion about what can influence the satellite reflectance at the surface will appear later in this chapter (Section 8.4).

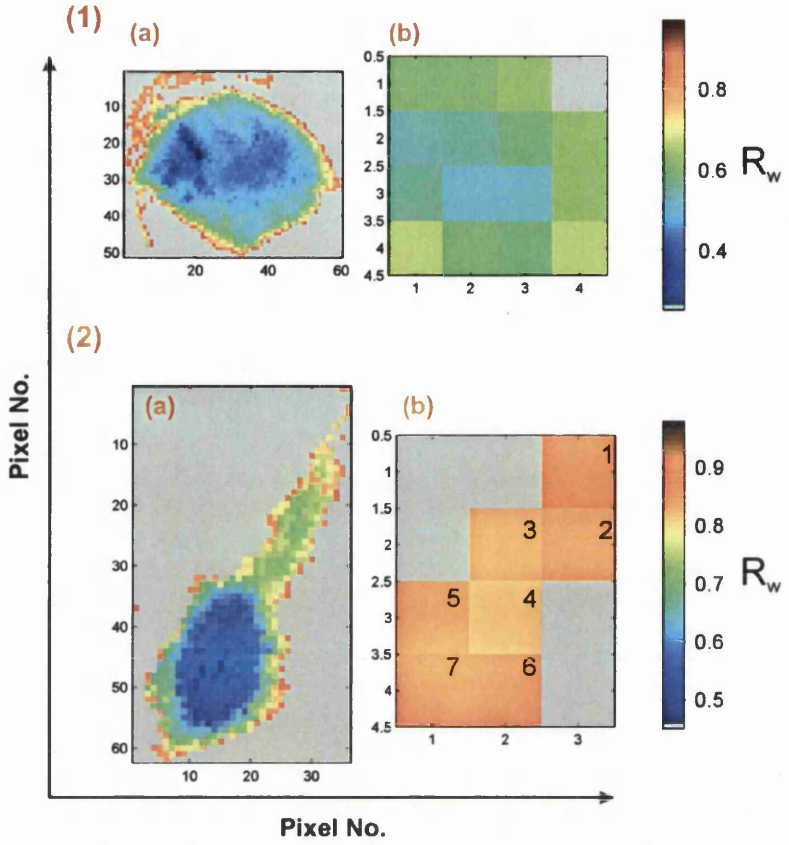

Figure 8.1: Example of two lakes (1 and 2 in the figure) where the pixel reflectance is compared for ASTER and MODIS; (a) corresponds with the surface water reflectance for the ASTER scene (15 by 15 m); (b) corresponds to the MODIS reflectance applying the region of interest of the ASTER image to the MODIS (250 by 250 m).

The main conclusion that can be made from this is that, firstly ASTER spatial resolution is more precise for lake perimeter specification and for a more accurate depth derivation because there are fewer mixed pixels than in MODIS. The differing spectral characteristics of the two satellites is shown in Figure 8.3, where the surface reflectance along a transect of the ablation area in south west of the GrIS is plotted for both satellites. The narrower values of reflectance given by MODIS were already introduced in Chapter 6, where ASTER and MODIS lake volumes were calculated.

MODIS maximum reflectance value for the transect in Figure 8.3 is 0.815 whereas ASTER's is 0.999; whereas the minimum value is 0.533 and 0.481 respectively (Fig-

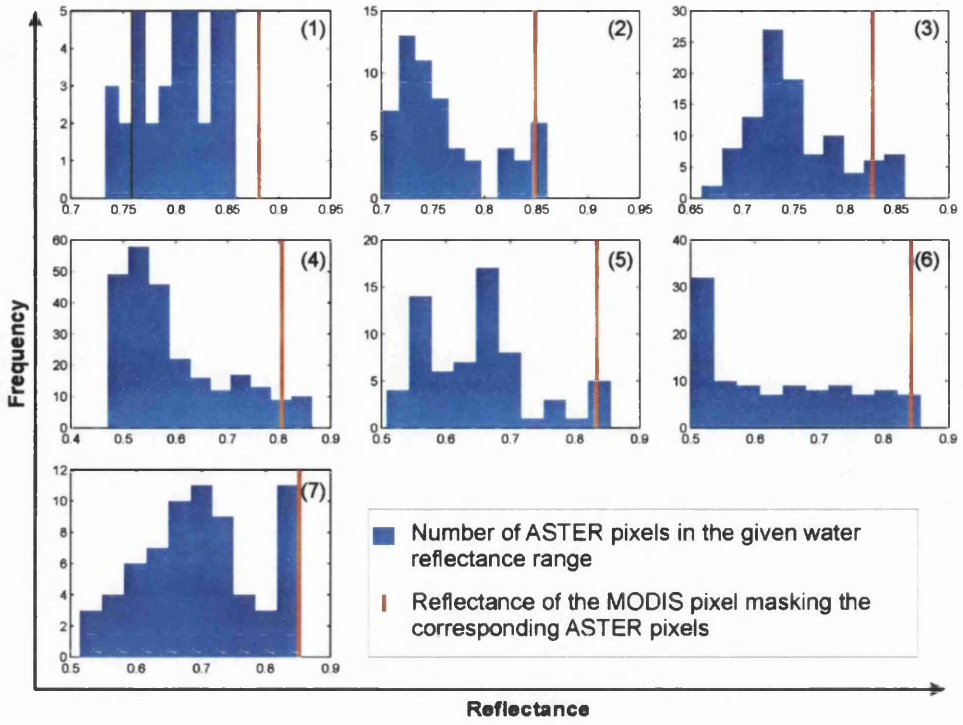

Figure 8.2: Histograms showing the water reflectance distribution of the ASTER pixels (Figure 8.1(2)) masked with each of the seven MODIS pixels.

ure 8.4). The maximum reached by MODIS does not mean that is the maximum value detectable by the satellite; taking a transect around the centre of the ice sheet from the same MODIS scene the reflectance is around 0.980. Once again it is likely the varied surface types of the ablation zone are mixed, making the reflectance values less extreme. Figure 8.2 also shows that in the south west Greenland a dark zone appears, in comparison with the centre of the ice sheet. A thorough discussion about the dark zone will appear later in the current chapter (Section 8.5).

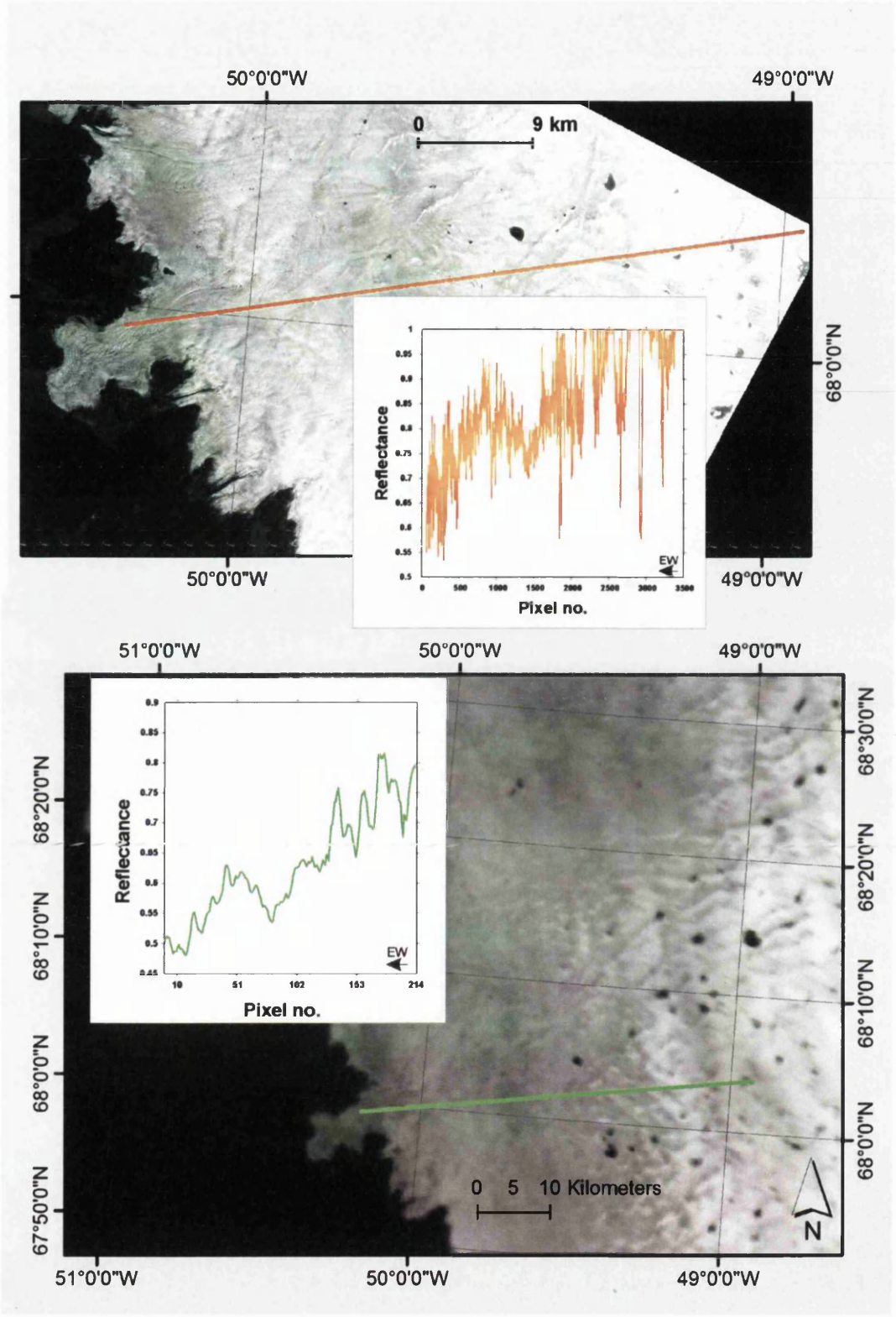

Figure 8.3: Snapshots of an ASTER band 1 (above) and a MODIS band 4 (below) images. Both scenes were taken on the 11 July 2005 at 15:10 UTC (MODIS) and 15:11:45 (ASTER) UTC . The red and green lines across the scenes correspond with the location of the transect profiles shown in the graphs for ASTER and MODIS respectively, which show the surface reflectance along the profiles.

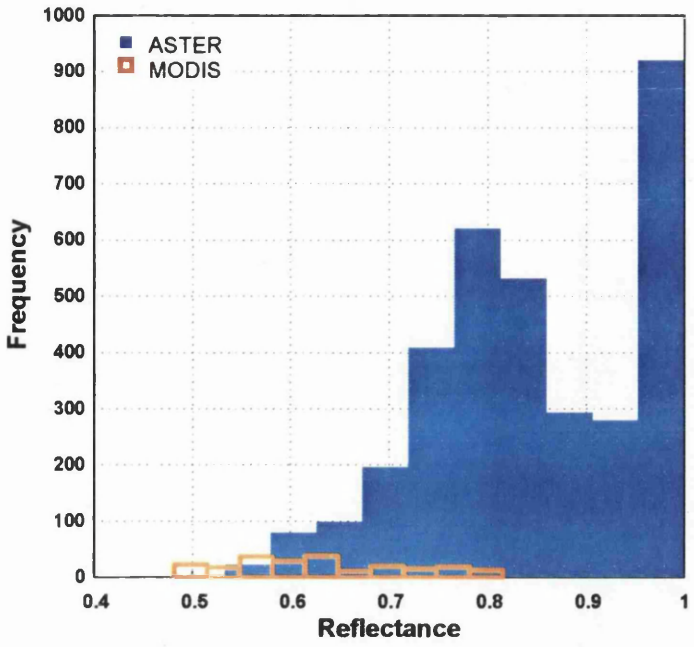

Figure 8.4: Distribution of the reflectance corresponding to the transects from Figure 8.3. Note the lower range of MODIS (red) data in comparison with ASTER (blue).

8.2.2 Limitations of data availability

ASTER optical imagery is a useful dataset for lake depth estimations (Chapter 5), but due to the infrequent measurements only for specific locations and dates. Both ASTER and Landsat are carried by satellites with orbital repeat cycles of 16 days. However, ASTER can modify the direction of view, in contrast to MODIS and Landsat, which cannot modify their look-angle; therefore observations with ASTER could in theory be made more frequently, even every three days. Nevertheless, ASTER is operated "on demand" so data archives are limited to previously requested data, so in reality data availability is very sparse.

On the other hand MODIS is good for repeated area measurements but not for depth estimations or for an precise lake perimeter determination. MODIS has a wider swath than ASTER (2,330 km *vs.* 60 km), meaning that MODIS can image a site daily. In the area of interest of the current study, *i.e.* in polar regions, MODIS can image several times per day due to the convergence of the satellites' orbital paths

(Terra and Aqua). This wide swath acquisition method permits global data collection, hence frequent repeated data is available from the archives. Various studies have made used of the high temporal resolution of MODIS to monitor supra-glacial lakes over time: Liang *et al.* (2012), Selmes *et al.* (2011) and Sundal *et al.* (2009) developed automated models for lake detection based on MODIS observations.

To sum up, ASTER can be applied for depth-volume estimates whereas with MODIS an extended time series can be produced, therefore time series of depths are not yet viable with the currently available data. As an example, Figure 8.20 (Section 8.5.1) shows the area evolution of a particular lake during a period of around hundred days; it shows more than thirty MODIS observations against two from ASTER. This means that even if it was possible to accurately quantify the volume of water for those two ASTER observations, in this particular example the maximum area extent would be missed using ASTER data. Hence as a future reference, for next generation sensors a compromise between time series and accurate volume estimates could be achieved. Figure 8.5 shows how lake area from ASTER scenes used in the current study (Chapter 6) do not show the maximum area extent as recorded for the same year from repeated MODIS observations (pers. comm N. Selmes, 2011). From the seven sampled lakes, six show ,as expected, how ASTER observations do not represent the maximum lake area. One lake shows that the ASTER derived area was bigger than that obtained from MODIS; looking at the table in Figure 8.5, there is only one day separating the ASTER and MODIS observations. This area difference between ASTER and MODIS might be due to the different approaches used for both MODIS and ASTER area determination. MODIS area is derived by spectral classifications ratio methods, whereas ASTER area is determined by the pixels that give positive depth values after applying the water reflectance model, which are physically incoherent.

Because there is still no satellite that can both produce accurate depth measurements at the same time as repeated observations, some studies used an assumed

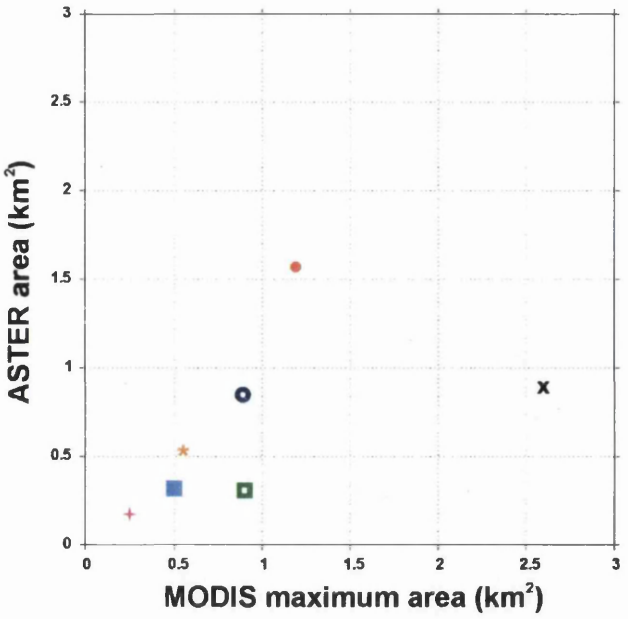

ASTER (Julian day)	MODIS (Julian day)	ΔA (%)
200	190	36.0
192	210	65.8
177	178	-31.9
192	200	4.5
171	165	32.0
206	209	65.6
206	210	3.6

Figure 8.5: Comparison of lake area for ASTER and MODIS. ASTER areas are derived from the scenes available for depth derivations. MODIS areas are from the same year as ASTER but for the maximum detected area from MODIS (pers. comm N. Selmes, 2011). The right side table shows the dates for both ASTER and MODIS observation and also the difference in area of ASTER with respect to the maximum extend given by MODIS, presented in percentage.

depth-area relationship to derive lake depth and hence volume. Various studies followed the assumption of a conical shape lake with 100:1 diameter-depth relationship (Krawczynski *et al.*, 2009; Leeson *et al.*, 2012). The area from ASTER observations of forty lakes was plotted against the maximum lake depths, calculated earlier in the current study (Chapter 6), and is shown Figure 8.6. This figure shows several candidate fits to these data and all of these fits give high residuals (SSE). The residuals from each of the fits are almost identical, diverging at the extreme values, and no clear relationship is apparent. The correlation between lake area and depth (red dots in Figure 8.6) is 0.631, which is not a strong correlation. If the most extreme two points on the right side of Figure 8.6 are excluded as outliers, then the correlation of the new sample is even lower, 0.386. From these results it can be concluded that lake area is a poor proxy for volume and that depth estimation is necessary for accurate volume quantification. In Section 8.6 further discussion of the potential area-relationship will be presented, analysing previous studies approaches.

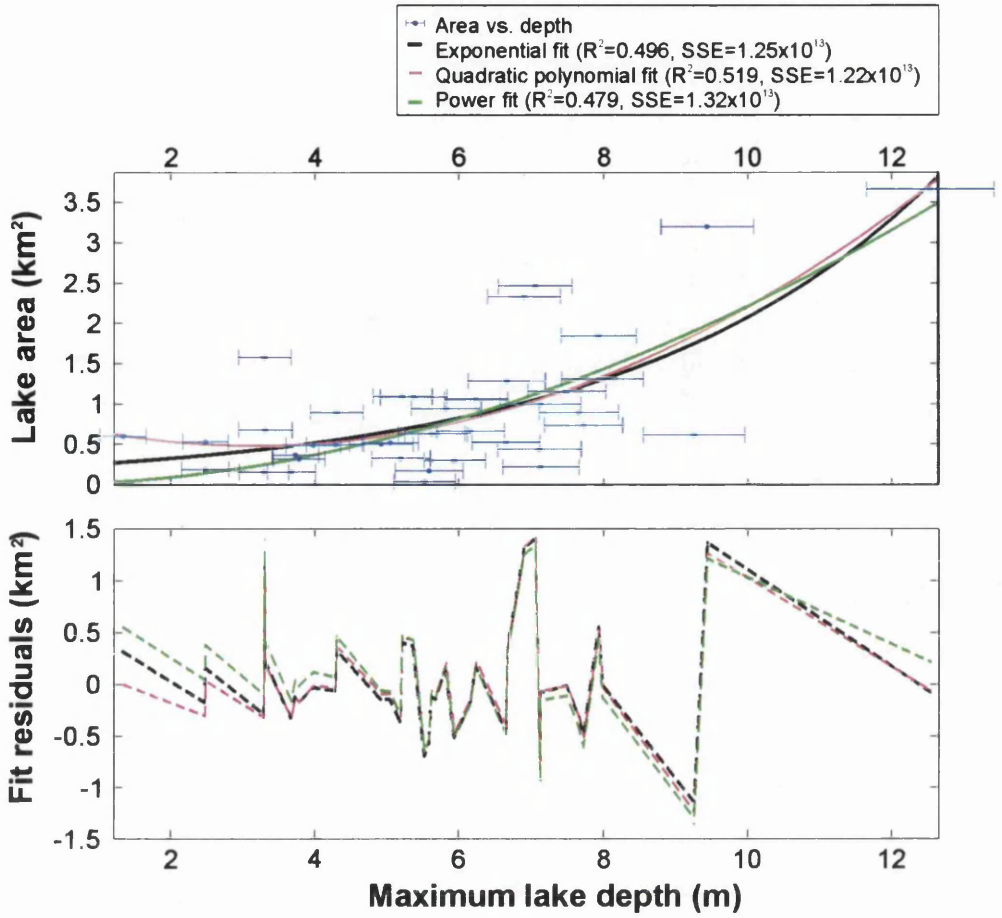

Figure 8.6: Lake area plotted against maximum estimated depth; error bars for depth estimates are shown in blue, area uncertainties too small to plot at this scale. The colour lines correspond with three sample fitting models; note that both the R^2 and SSE are almost identical for the three models. The bottom graph corresponds with the residuals for each model; the residuals only vary between models at extreme depth values, where they diverge.

8.3 Performance of Monte Carlo optimisation

The Monte Carlo simulation was used in Chapter 5 to obtain a robust depth uncertainty estimations based on the water reflectance model and using the absolute errors of each of the input parameters as an input. There a minimisation model was applied, which objective was to minimise the difference in depth between ICE-Sat depths ("true" depths) and the depths from the water reflectance model for ASTER observations. The minimisation model worked by varying randomly the input parameters within their error range and assuming either a Box or a Gaussian distribution.

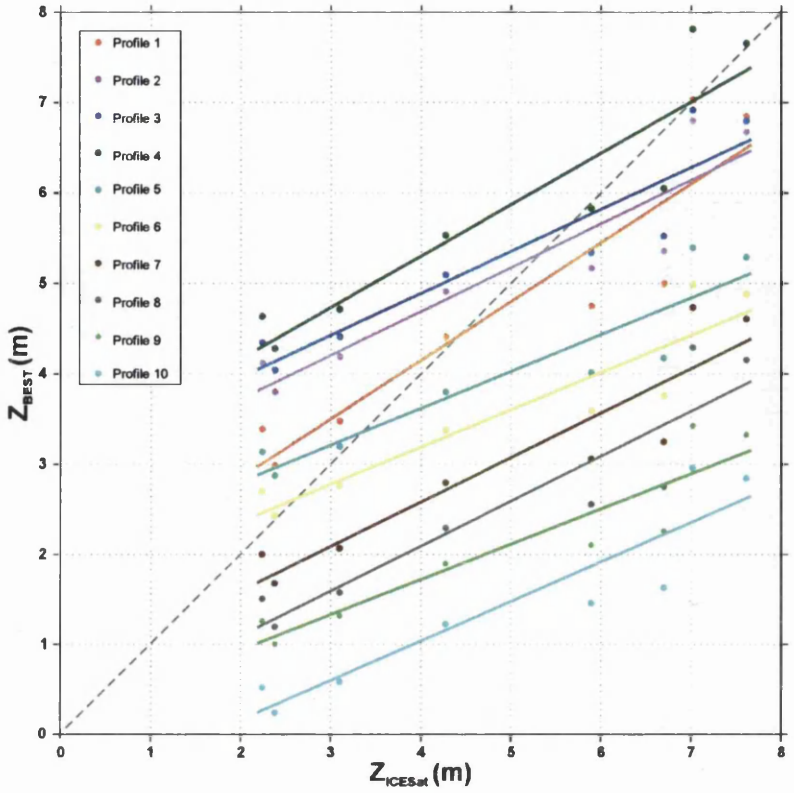

Figure 8.7: Profiles from the ten best iterations of the minimisation mode from one of the lakes used in Chapter 5. Profiles with the smallest SSE are ranked highest. The red dots and line correspond with the best profile giving the smallest residuals.

The minimisation model ranks each iteration according to the minimum residuals (SSE). To demonstrate the suitability of the Monte Carlo approach Figure 8.7 shows the best ten minimisation solutions from the Monte Carlo approach for one of the lakes used in the current study (Chapter 5). In that figure the red line corresponds with the best profile, and hence with the equivalent chosen profiles for all the lakes in the study. Further statistical analysis is shown in Table 8.1, where the Sum Squared Error (SSE = $\sum(Z_{ICESat} - Z_{model})^2$) is shown for the first ten best profiles. The best profile presents SSE=6.62 m and from then the subsequent value is almost double the first one. The tenth SSE=107.50 m, which is more than ten times bigger than the best profile. These results clearly show the effectiveness of the Monte Carlo approach for minimisation. In the next subsection the variation of the input parameters in the Monte Carlo simulation is shown.

Table 8.1: Table summarising the root Sum of Squared Error (SSE) for the profiles plotted in Figure 8.7.

Best profiles order	SSE (m)
1^{st}	6.62
2^{nd}	10.41
3^{rd}	11.99
4^{th}	14.66
5^{th}	19.15
6^{th}	26.59
7^{th}	37.91
8^{th}	54.20
9^{th}	76.90
10^{th}	107.50

8.4 Water reflectance model potential uncertainties

The uncertainties derived from the Monte Carlo simulation for the optimisation model are one of the main achievements of this thesis. The depth uncertainties depend on the absolute errors of each of the input parameters to the water reflectance model, *i.e.* surface reflectance, bed albedo, attenuation coefficient and the reflectance of optically deep water. Nevertheless, the overall performance of the water reflectance model and of the optimisation model based on ICESat reference depths can be further analysed by introducing all the source of uncertainties that could have influenced the results obtained in this thesis.

8.4.1 ICESat elevation measurements as a proxy to lake depth

The use of ICESat data as a proxy to lake depth is a novel approach developed in this thesis. Previous studies have used ICESat elevation data to locate and characterise sub-glacial lakes on Antarctica, since the ice surface responds to variations in water volume (Fricker *et al.*, 2007). Therefore there are no other studies with lake depths from ICESat that could be compared with the approach followed in this thesis.

ICESat depths have proved to be a useful approach for this thesis, taking into account the uncertainties of the technique. In Chapter 4 a 0.65 m vertical uncertainty was given to ICESat depth measurements, obtained from the vertical resolution of ICESat laser, 0.15 m (Fricker *et al.*, 2005b; Siegfried *et al.*, 2011), plus 0.5 m of uncertainty assigned to the depth estimation from ICESat elevations. Only ICESat data from the same year as ASTER observations were used, which limited the number of lakes that could be studied. This data shortage was increased by the fact that ICESat measurements needed to be made when lakes were empty.

There is one issue that should have been take into account if ICESat data had been used for inter-annual variations, this is the fluctuations in rates of snow accumulation and ablation, which is reported to be between 1 to 2 m for this region of the ice sheet (Box *et al.*, 2006). This rate of changes was assumed for McMillan *et al.* (2007) because they were studying the seasonal variation of lakes using airborne LIDAR. For this thesis that is not necessary because depths derived from ICESat are relative, even if the lake is covered with snow during the ICESat spring campaign, the depth of the lake is calculated relative to the lake margin, therefore assuming equal snow thickness for both margin and lake bed, it can be assumed no uncertainty derived from this fact.

The effects of firn densification over ice sheet mass balance calculations has been widely reported (Cuffey, 2001; Arthern and Wingham, 1998). Nevertheless different firn densification models (McConnell *et al.*, 2000; Reeh, 2008; Wingham, 2000; Alley, 1987) can be applied to account for this effect densification, where they consider ice and snow densities separated to compute volume changes (Slobbe *et al.*, 2009) derived from ICESat data. For this thesis uncertainties due to firn densification are unlikely to have influence because there were not any interannual comparison of ICESat measurements, therefore no firn correction was applied.

As mention before, the main ICESat uncertainty results from depth determination, especially from margin location; this is due to the sparse footprint separation around 172 m. This prevents from an exact margin location. Future laser satellites could overcome this by decreasing footprint separation. Also even if ICESat track density was higher in the thesis study area due to orbit convergence at the poles, because lakes area is insignificant in comparison with ICESat track separation, which is around 30 km in south Greenland (Sørensen *et al.*, 2011), the probability of an ICESat track crossing an empty lake over the middle is low.

8.4.2 Depth limit of the model

Before applying the water reflectance model, one of the assumptions was that the model would be depth limited, because the passive methods are limited to shallow waters; the true bottom cannot be detected in > 15 m of water (Stumpf *et al.*, 2003). This shows a fundamental limitation of depth estimation by optical systems, regardless of method. In this section that maximum depth limit will be tested for ASTER scenes and the water reflectance model used in Chapter 5. Depth is estimated for a set of reflectance values spaced uniformly from 0.01 to 1. These reflectance values are theoretical; for the water reflectance model used in this thesis the set of parameters used had a reflectance of optically deep water (R_∞) was 0.099. If this

R_∞ was used for the theoretical reflectance values, the physical assumption would be violated; it is not possible to get reflectance values lower than the optically deep water reflectance. Therefore since this is a theoretical test, R_∞ was set to 0.001, so it is smaller than the theoretical surface reflectance.

Figure 8.8 shows the resultant curve of depth *vs.* water surface reflectance. The maximum depth value was around 25 m. The depth is also limited in the lower part, since R_w must be $\leq$ to the bed albedo, otherwise the model will give positive values, which is not physically possible. It is worth noticing that bellow 5 m deep, the depth curve increases in depth very fast, even if the reflectance range of changes is less than 0.1; before that from 0-5 m deep the range in reflectance varies from 1-0.1.

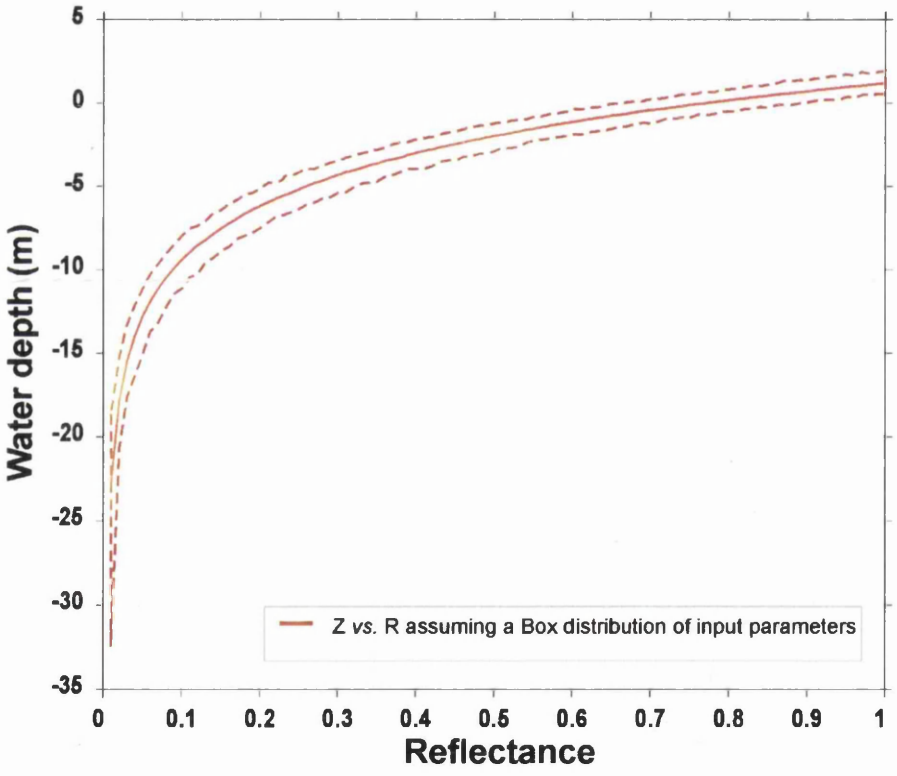

Figure 8.8: Median of lake depths derived from the water reflectance model against water reflectance values. The red dotted lines correspond with the depth uncertainties. These results were from the set of parameters derived from Chapter 5, although R_∞ value was changed to be smaller than 0.01 so the model could be run for a bigger range of R_w.

From these results it can be concluded that the water reflectance model, even if it is limited to shallow waters, is not limiting the results obtained in the current thesis. This can be said with confidence as all observed depths were within the optimal shallower pat of the curve shown in Figure 8.8. Therefore the water reflectance is what limits the minimisation model, since there are no low enough values of the reflectance to give deeper lakes. The limitation of the water reflectance model to shallow waters could prevent the application of the model for water-filled crevassed depth estimations, which will be discussed in Section 8.7.

8.4.3 Potential uncertainties derived from the input parameters

The input parameters used for the water reflectance model (A_d, g and R_∞) obtained in Chapter 4 could be compared with other studies (Maritorena *et al.*, 1994; Philpot, 1989; Georgiou *et al.*, 2009; Sneed and Hamilton, 2011; Tedesco and Steiner, 2011), although this is would not be a direct comparison, because the parameters are either derived from other satellites or from *in situ*. Nevertheless later in this chapter the results obtained from this thesis will be compared with previous studies (Section 8.6), including the input parameters (Table 8.6). The questions that arise from this comparison are: do the differences come from using different satellites even if they have the same sensor characteristics or equivalent? or are the differences due to the water characteristics and hence the physical parameters are specific for each lake? Before the studies are compared, in this subsection a thorough analysis of each of the three physical parameters (bed albedo, attenuation coefficient and reflectance of optically deep water) is detailed.

Bed albedo

The primary source of error in the water reflectance model is the A_d (Georgiou *et al.*, 2009); for example Sneed and Hamilton (2007) showed that an $\approx 1\%$ decrease in A_d resulted in a $\approx 16\%$ decrease in calculated melt-water volume. Therefore the choice of the parameter value is very important. However, it is also the parameter most difficult to obtain with accuracy. For this thesis the approximation used by Sneed and Hamilton (2007) was followed, which as mentioned previously (Chapter 4) was done by finding pixels at the lake's edge that are just barely covered with water. At 780 nm (Band 3 in ASTER) with 10 cm of water covering ice, R_w is approximately 40% less than the reflectance of ice with no water cover. Searching for adjacent pixels that show rapid decrease in R_w and then finding the same in Band 1 we can arrive at a value for the bottom albedo. This technique was tested by Tedesco and Steiner (2011) where they obtained a 10% difference between the bed albedo obtained as just explained and from *in situ* measurements, which translates to a depth underestimation of 15.9% for Landsat Band 2 (equivalent to ASTER Band 1).

Another important factor ignored in many studies, including this thesis, is the ablation that occurs at the bottom of the lakes. Ablation will not only can have hydrological implications for the ice sheet, but also and more importantly for this thesis, melting at the bottom could affect estimates of lake depth from optical satellites, because it can alter the reflective properties of the signal (Tedesco *et al.*, 2012). It is also possible that the bed albedo could vary with time as the melt season advances; Selmes *et al.* (2011) concluded that this phenomenon could be especially important for lakes that do not drain, which they will have a longer life span and hence likely have more melt at the bottom. Since it is not possible to obtain the bed albedo from optical imagery without using the approximations described above and in the absence of *in situ* data, the only thing one can do with the data available is to look at the spectral reflectance of the bottom albedo for drained or partially drained lakes; this will be done in Section 8.5.

Reflectance of optically deep water

Previous studies showed that the images used for depth estimation needed to contain deep-water pixels from the ocean in order to obtain R_∞ (Sneed and Hamilton, 2007), although Georgiou *et al.* (2009) used adjacent scenes along track including sea water at a depth greater than 40 m and later on Sneed and Hamilton (2011) demonstrated that is not necessary that the image used shows deep water. For the present study there were no ASTER scenes with pixels from the ocean, therefore looking at MODIS scenes for the same date and time as the ASTER, the value of R_∞ was selected from the MODIS image. Nevertheless from the water reflectance model and the Monte Carlo simulation, it can be stated that this parameter does not have a crucial role on depth estimation uncertainty.

Despite the fact that the water reflectance model is not driven by the value of R_∞ - in Chapter 5 was shown how broad the range of it was and how little the depth varied with those variations - it is still one of the physical parameters governing the water reflectance model. Therefore in order to minimise the uncertainties due to these parameters it would be preferable if a more rigorous technique were available to future studies to determine R_∞ values. This would not only reduce the depth uncertainties, but would allow the use of satellite observations that do not contain deep water; or if *in situ* measurements are taken there would not be a need to use satellite values of R_∞. As an example, Tedesco and Steiner (2011) measured *in situ* multispectral (surface leaving reflectance values) and bathymetry (water depths) data and tested the procedure followed by Sneed and Hamilton (2007). Fitting an exponential decay of the surface leaving reflectance with water depth, they obtained a fitted set of parameters (A_d, g and R_∞). The results are shown in Figure 8.9, which stresses the importance of *in situ* measurements for the validation of the parameters derived from optical satellites, like in the present study.

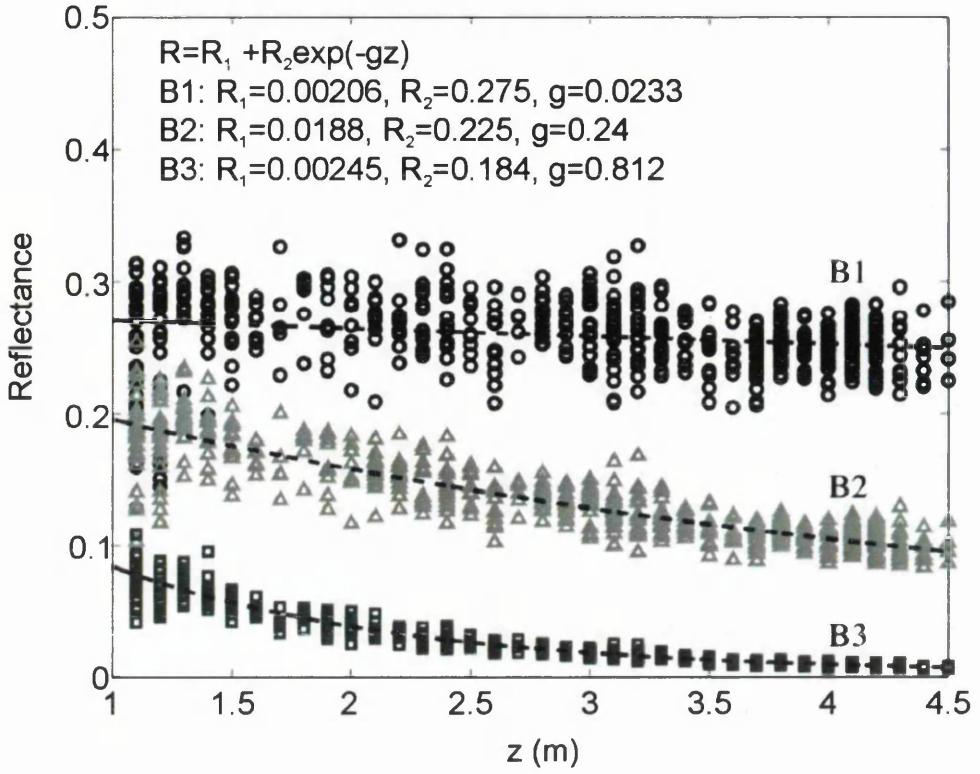

Figure 8.9: *In situ* measured surface water reflectance *vs.* lake depth for Landsat Band 1 (450-550 nm), Band 2 (520-600 nm) and Band 3 (630-690 nm). The fitting equation used for the graph is $R=R_\infty+(A_d-R_\infty)exp(-gz)$ (Figure modified from Tedesco and Steiner (2011)).

Specific attenuation coefficient

The last physical parameter is g, which was obtained based on studies of optically clear water (Smith and Baker, 1981), where g has a value for each 10 nm wavelength interval (Chapter 4). For this study the mean value of all the intervals within the selected band was taken. This assumption could lead to uncertainties, as presented by Georgiou *et al.* (2009) where they showed that the averaging lead to an uncertainty of 9.5% in the derived depth. To overcome this effect when applying the Monte Carlo simulation, g was allowed to vary within a maximum and minimum value corresponding to the spectral band used. Nevertheless, there is another factor that can lead to further uncertainty, g was estimated assuming that the parameter $\alpha \approx 2$, where $g \approx \alpha K_d$. This assumption can lead to an underestimation of the actual attenuation (Tedesco and Steiner, 2011; Maritorena *et al.*, 1994), which implies an

overestimation of depth. Tedesco and Steiner (2011) obtained *in situ* data and they obtained a 15% diference between the observed α values and those from literature.

Apart from the use of ground-truth measurements to improve the water reflectance model - like shown by Tedesco and Steiner (2011) - the attenuation coefficient could be further refined with the application of a semi-analytical model like the one proposed by Lee *et al.* (1999), where they developed an inversion method to estimate bottom depth from the optical properties of water for different water characteristics. Also if the water column diffuse attenuation coefficient was known from field observations for each spectral band and the water depth were measured independently, the surface reflectance of the submerged substrate could be estimated, hence allowing a spectral classification of the lake (Hedley and Mumby, 2003), which would improve the present spectral classification of water in supra-glacial lakes.

8.4.4 Influence of area uncertainty on the estimation of the volume of water

In Chapter 6, lake volume estimates were shown together with their uncertainties. As a reminder, the volume uncertainties were derived using the propagation of errors approach (Sánchez del Río, 1989) taking only into account depth uncertainties, which were obtained from the Monte Carlos simulation. Area uncertainties derived from the pixel size of the satellite (ASTER and MODIS) were consider insignificant with respect to depth induced uncertainties, therefore they were not included in the volume uncertainties. However the uncertainties derived from the estimation of lake area could be attributed to other factors, which are included in this section.

Previous authors have used several approaches to estimate the error in area calculations as a result of pixel resolution. Some studies assumed a circular lake area

equivalent to the mean of all the considered lakes and the uncertainty given to that area was applied to all the lakes' area uncertainties (Sundal *et al.*, 2009; McMillan *et al.*, 2007). The uncertainties estimated from this approach were 4% for Sundal *et al.* (2009) and 8-9% for McMillan *et al.* (2007). Another study combined the area of 100 lakes for ASTER and MODIS data set, giving an area difference of 1.77% and using the RMSE (0.11 km^2) as the area uncertainty per lake, assuming no variation or errors between years (Selmes *et al.*, 2011). All these approaches seem reasonable, although further analysis of the area uncertainties should be made.

In this subsection a new method of area uncertainty is introduced to replace those used previously. The technique is as follows; for each lake an automatic script is run, which counts the number of pixels on the lake perimeter. The script counts the pixels with at least one side on the border and also the pixels touching the border diagonally. The reason for this approach is that it is assumed that for each pixel at the border of the lake, there will be a ± half pixel of uncertainty; assuming that this uncertainty is then taken into account the mixed pixels at the lake edge. This is equivalent to ± 112.5 m^2 per pixel at the edge. Table 8.2 shows the results obtained from this approach for both lake area and volume for five random lakes of the current study. In the table volume uncertainties used previously (Chapter 6) are also shown for comparison.

The average area uncertainty is 9.67%, which is of the same order and similar value as in previous studies (Selmes *et al.*, 2011; Sundal *et al.*, 2009; McMillan *et al.*, 2007). For the lake volume, the averaged uncertainty taken from Chapter 6 is 8.54%, whereas for the current case is 25.76%, which is one order of magnitude bigger than the first case. The averaged dV_2 (Table 8.2) is within the range of previous studies (see Table 8.4), where the range of volume uncertainty is 20-50%.

From these findings it can be concluded that the new area error determination devel-

Table 8.2: Table showing area and volume uncertainties for five sample lakes of the current study. dV_1 correspond to the uncertainties obtained in Chapter 6 assuming no area error; dA and dV_2 assuming the error derived assuming ± half pixel of uncertainty as the area uncertainty.

A ($x10^5 m^2$)	dA ($x10^5 m^2$)	V ($x10^6 m^3$)	dV_1 ($x10^6 m^3$)	dV_2 ($x10^6 m^3$)
3.65	0.61	3.64	0.11	0.19
1.56	0.23	2.23	0.05	0.17
6.60	0.41	1.89	0.24	0.81
24.55	1.33	5.99	0.83	1.37
6.10	0.32	2.11	0.23	1.06

oped in this subsection meets the results from previous studies and that the previous assumption used in Chapter 6 is too optimistic. Therefore that approach should be rejected for future research and the present one should be used instead. Nevertheless for the calculations in Chapter 6, it was considered as a first approach, therefore is still taken into account.

In Chapter 6 the errors in the depth estimation for each column of water was considered independent for the volume uncertainty calculation. As mentioned previously, this assumption could substantially underestimated the error in the volume, therefore for future studies it is recommended to consider the errors correlated.

8.5 Reflectance of empty lakes and the dark zone

Late in the melt season, some lakes drain fully or partially, while others refreeze or just overflow on the ice surface. ASTER scenes including partially drained lakes were found for the south west Greenland (see Figure 8.10), therefore further investigation about the spectral characteristics of the bare ice of the empty lakes was

performed. A striking finding was the values of the surface reflectance over empty or semi-empty lakes, in comparison with the surrounding ice. Before analysing that difference, the values of the lake reflectance after draining are investigated (Figure 8.11). The identification of lakes that had recently drained was very simple because the spectral characteristics between the bare ice and the ice outside of the lakes are visually very different (Figure 8.19). The pixels previously covered by water are much brighter than the pixels of the surrounding ice and the delimitation of the lake margin when it was full of water is very obvious for all the lakes found. Applying a mask to pixels outside the bright area, the result is shown in Figure 8.11.

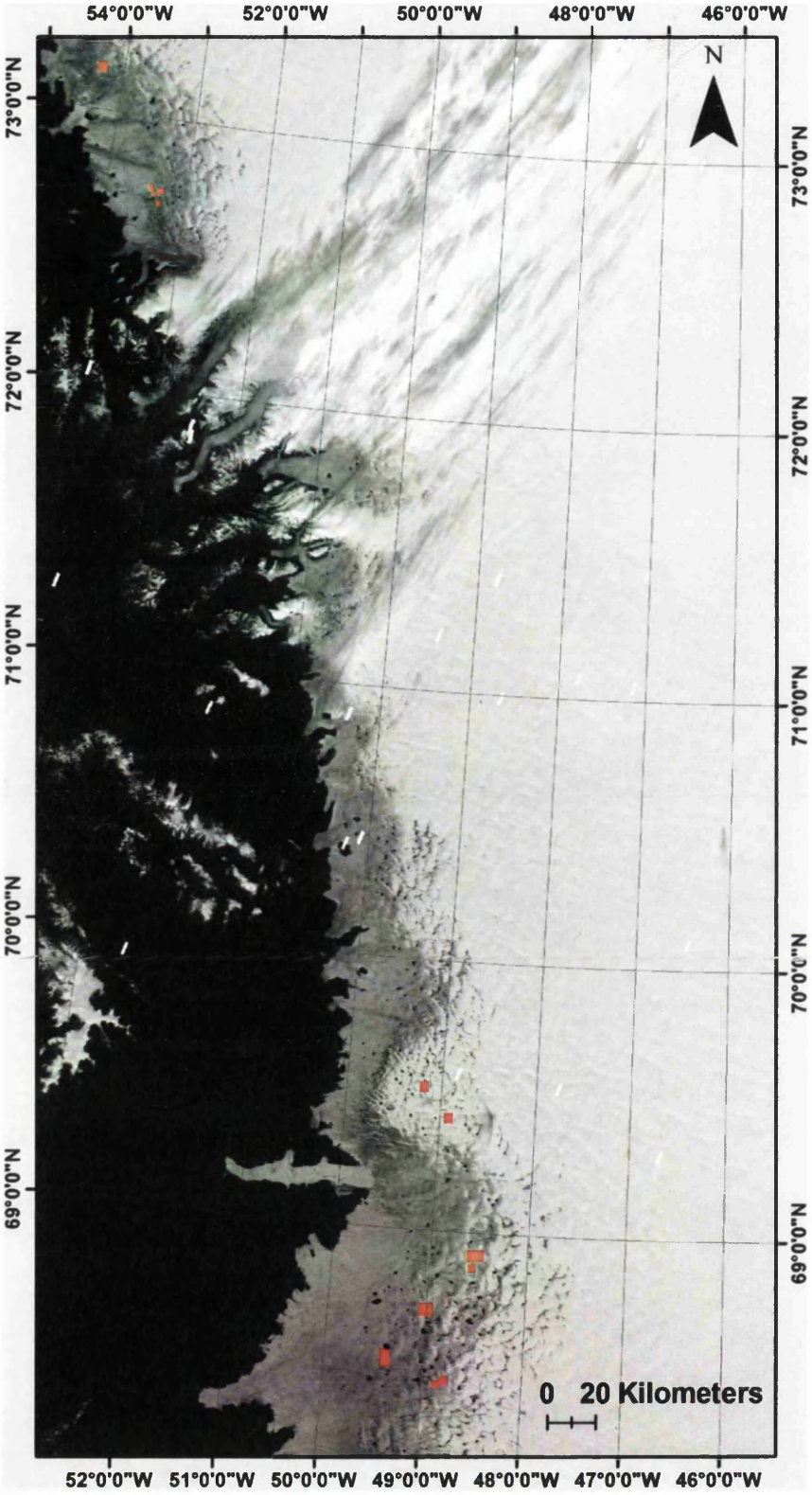

Figure 8.10: Location map of the partially/fully empty lakes found in south west Greenland (red dots) used in this section. The background image corresponds to a MODIS band 4 scene.

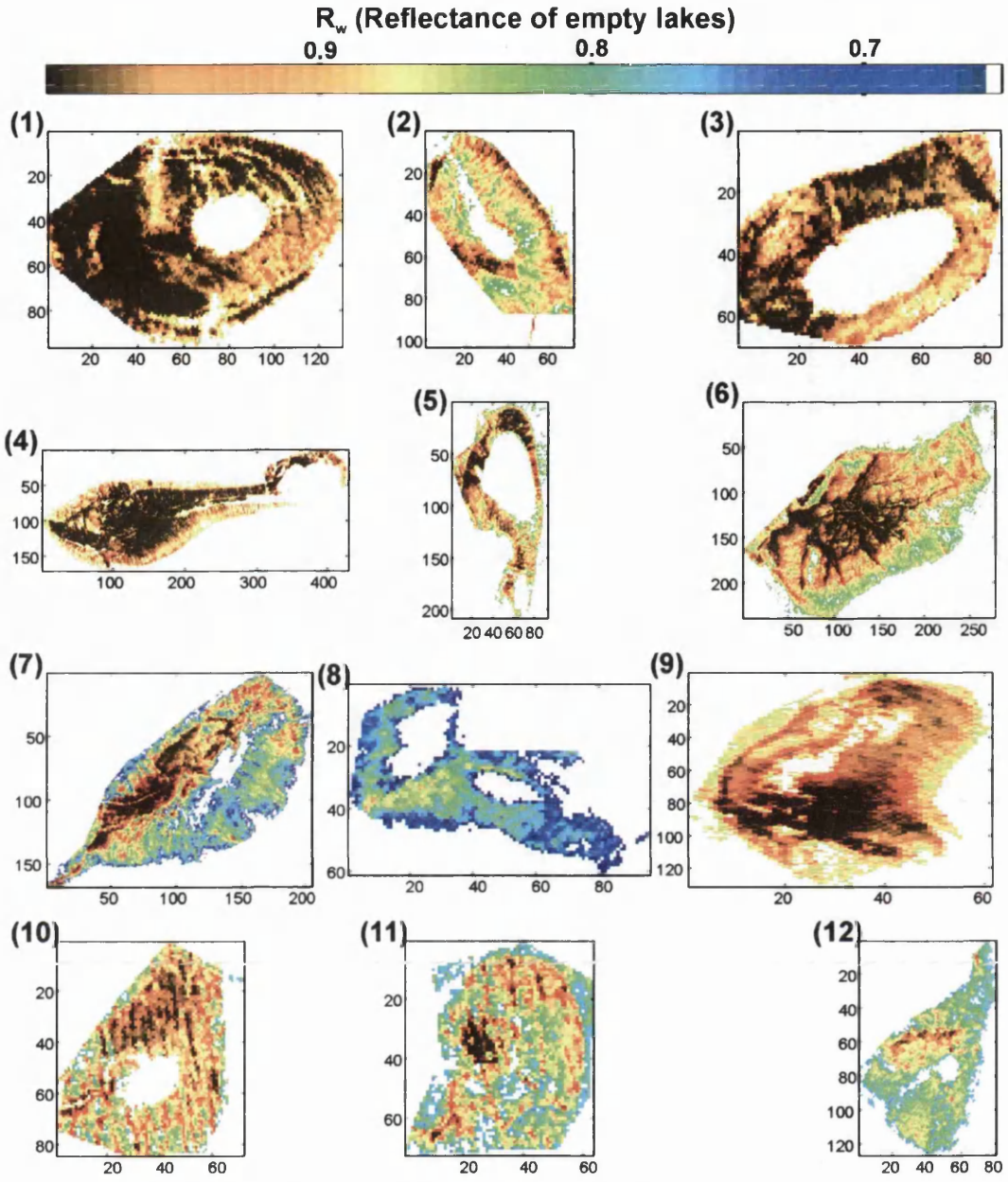

Figure 8.11: Example of twelve drained or semi-drained lakes from ASTER Band 1 scenes. Most of them are not completely drained, that is why there is a grey area on most images with no data. The images show the value of the surface reflectance after drainage.

The idea was to investigate if there was a pattern in the reflectance of empty lakes, for instance to see if the brightness decreased with the time since the pixels were free of water. The majority of the lakes in Figure 8.11 tend to show higher reflectance where the empty lake had previously been deepest, for example lakes 4, 5, 6, 7, 8 and 9 in Figure 8.11, but it is not conclusive. Figure 8.12 shows the distribution of the reflectance of those lakes and again the pattern is very random with no clear distribution shape. From the previous figure (Figure 8.11), there can also be noted a difference in reflectance between lakes. It is possible that this is due to the different drainage days, so to analyse this the median of the reflectance for each lake was plotted against the number of days since the draining was detected, which can be seeing in Figure 8.13.

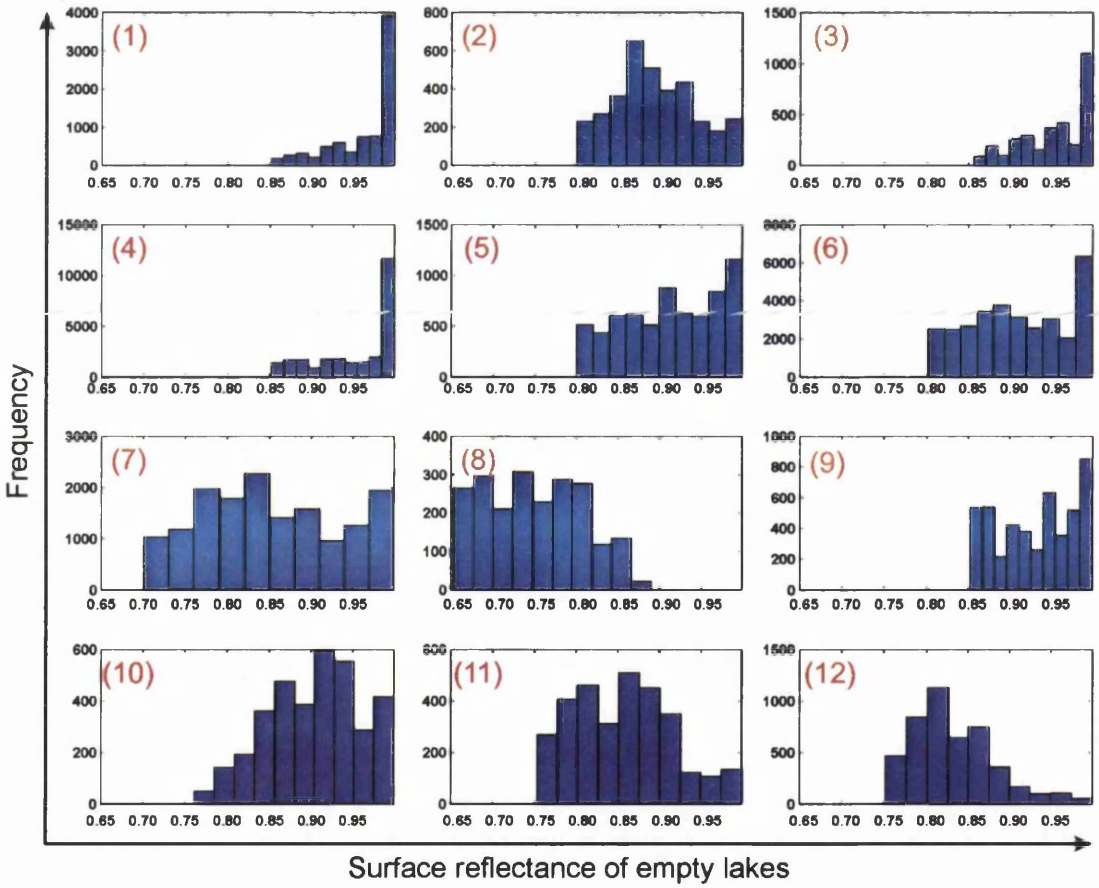

Figure 8.12: Histograms showing the distribution of the surface reflectance of the twelve lakes from Figure 8.11.

MODIS scenes where the drainage events can be followed are used to estimate the day of each lake's drainage (Appendix B). Figure 8.13 shows the relationship between reflectance of the empty lakes and the days since drainage, with a correlation coefficient of -0.475. However, if the last two data points on that graph are treated as outliers and ignored (with number of days since drainage bigger than 26), it seems that the median of the reflectance decreases as the number of days since drainage increases and it presents a correlation coefficient of -0.791, a robust inverse relationship. This result could be interpreted as that the reflectance at the surface of recently drained lakes is very high, of the order of the reflectance of bare ice (around 0.9-0.99), and as the time passes since the drainage the reflectance values reduce, which could perhaps be due to dust accumulation for example. The discussion about the dust presence is introduce in the dark zone subsection (Section 8.5.1) . Table 8.3 summarises the days the ASTER images were taken and the days when based on MODIS images, the lake drainage approximately occurred.

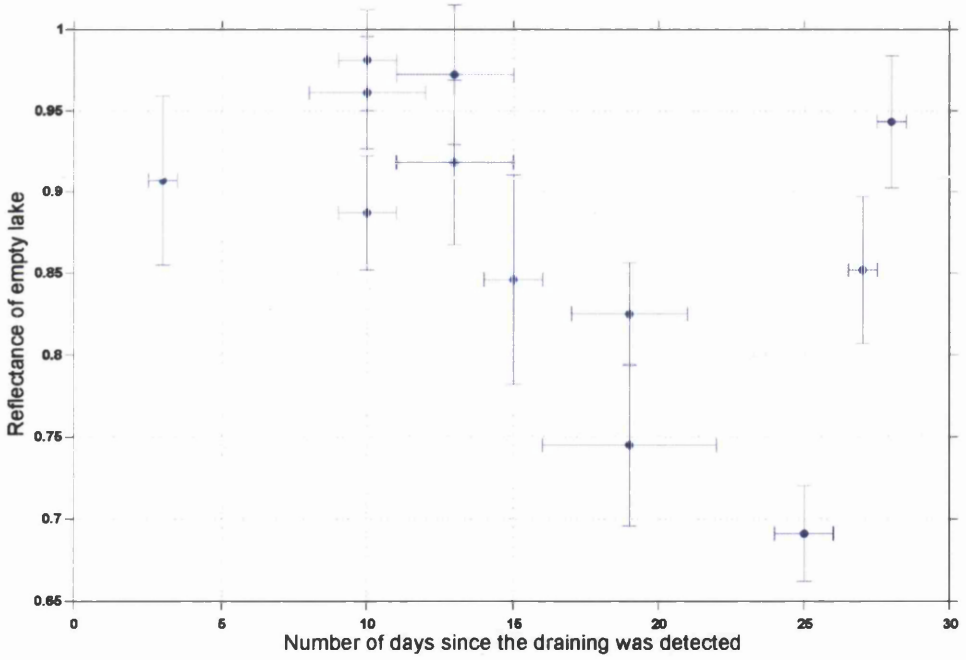

Figure 8.13: Evolution of the median of the reflectance from all the lakes in Figure 8.12 with the time passed since the drainage was detected. Vertical lines are the absolute error of the median (IQR/2), and the horizontal lines is the uncertainty in the drainage day selection, due either to the lack of MODIS scenes, or to not very clear scenes.

Table 8.3: Table summarising the dates for the ASTER and MODIS scenes used in this section. ASTER images acquisition time in UTC; whereas there is not time for the MODIS dates, rather drainage is know to have occurred between two scenes, therefore the data is an approximation.

Lake No	ASTER image (Empty lake date)	MODIS image (Drainage date)
1	11/08/2008 15:18:25	01/08/2008
2	11/08/2008 15:18:25	01/08/2008
3	11/08/2008 15:18:25	01/08/2008
4	12/08/2005 15:11:32	30/07/2005
5	12/08/2005 15:11:32	30/07/2005
6	12/08/2005 15:11:32	09/08/2005
7	12/08/2005 15:11:32	28/07/2005
8	03/08/2008 16:06:39	15/07/2008
9	03/08/2008 16:06:39	06/07/2008
10	03/08/2008 16:06:39	09/07/2008
11	03/08/2008 16:06:39	07/07/2008
12	03/08/2008 16:06:39	15/07/2008

8.5.1 The dark zone surrounding empty lakes on the SW of Greenland

MODIS and ASTER scenes show a phenomenon that is not yet well understood; looking at the location map of the empty lakes (Figure 8.10), a shadowed or dark area can be noticed on the ablation zone of the west of Greenland. Previous literature has already reported the formation of the dark zone (Wientjes and Oerlemans, 2010; Wientjes *et al.*, 2011; Boggild *et al.*, 2010; Greuell, 2000). This darkening of the surface appears to increase as the melt season advances. Figure 8.14 shows the temporal evolution of the dark zone for MODIS observations. For a more detailed view of the spectral characteristics of this dark zone, a longitudinal transect is drawn across the the dark zone for three different melt season dates (Figure 8.15). The latitude of the transect is around 67° 50" N and it seems that the dark zone is concentrated between 49.7°- 48.2° W. The minimum reflectance values of the dark zone on the latest scene (purple dots) is around 0.3, which corresponds with Paterson (1994) definition of *slightly dirty ice*, whereas the surface reflectance of the earlier scene in the same location (blue dots) is around 0.8, which is between the classification of *dry snow* and *melting snow* by Paterson (1994).

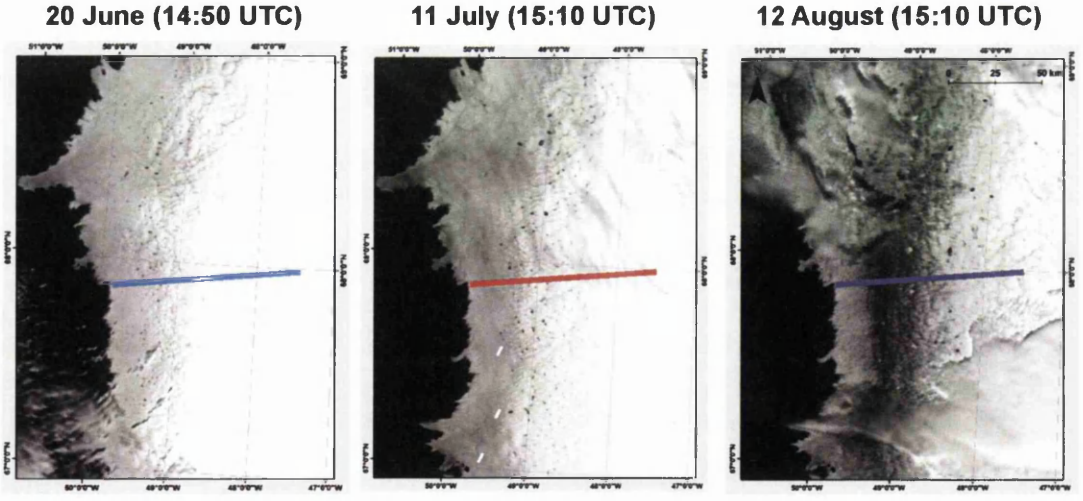

Figure 8.14: MODIS band 4 (545-565 nm) snapshots showing the temporal evolution of the dark zone from late June to mid August during the melt season of 2005. The coloured lines locate the transverse reflectance profiles plotted in Figure 8.15.

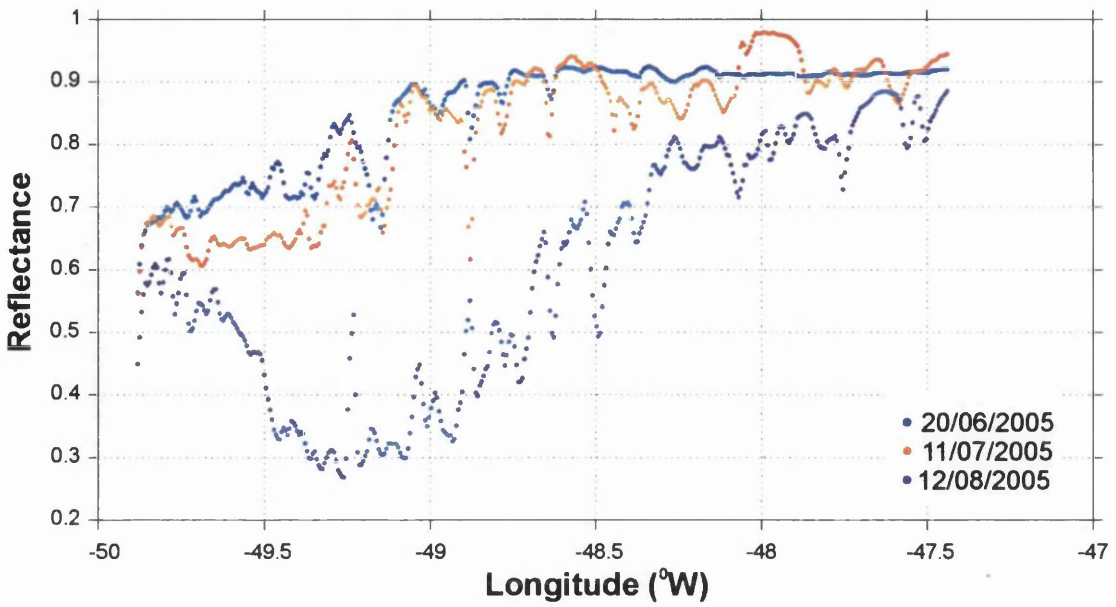

Figure 8.15: MODIS surface reflectance plotted against longitude for the three different MODIS band 4 scenes from Figure 8.14.

All the studies that have investigated this dark zone (Wientjes and Oerlemans, 2010; Wientjes *et al.*, 2011; Boggild *et al.*, 2010; Greuell, 2000) agree in the location of the dark zone, which is between 64.5°-70.5° N. This dark zone also happens in the north east of Greenland, as reported by Boggild *et al.* (2010), although this section focuses on the south west dark zone. The dark zone is thought to appear only during the part of the season with intensive melting (July and early August) (Greuell, 2000). The darkness is believed to appear from outcropping dust layers (Wientjes and Oerlemans, 2010), and the increase in melt-water seems to be a result of the darkening rather than the cause, as was previously thought (Greuell, 2000). More recently, chemistry and sedimentological analysis concluded that the dust originated locally (Wientjes *et al.*, 2011).

ASTER scenes can be also used to detect this dark zone; due to its high spatial resolution (15 by 15 m) further analysis of the lakes used previously in the empty lakes Section (Figure 8.12) is done. Looking at the spectral characteristics of each of the lakes between ice outside and inside the empty lake area, striking differences are found (Figures 8.16, 8.17, 8.18). Plotting a transverse profile of the reflectance

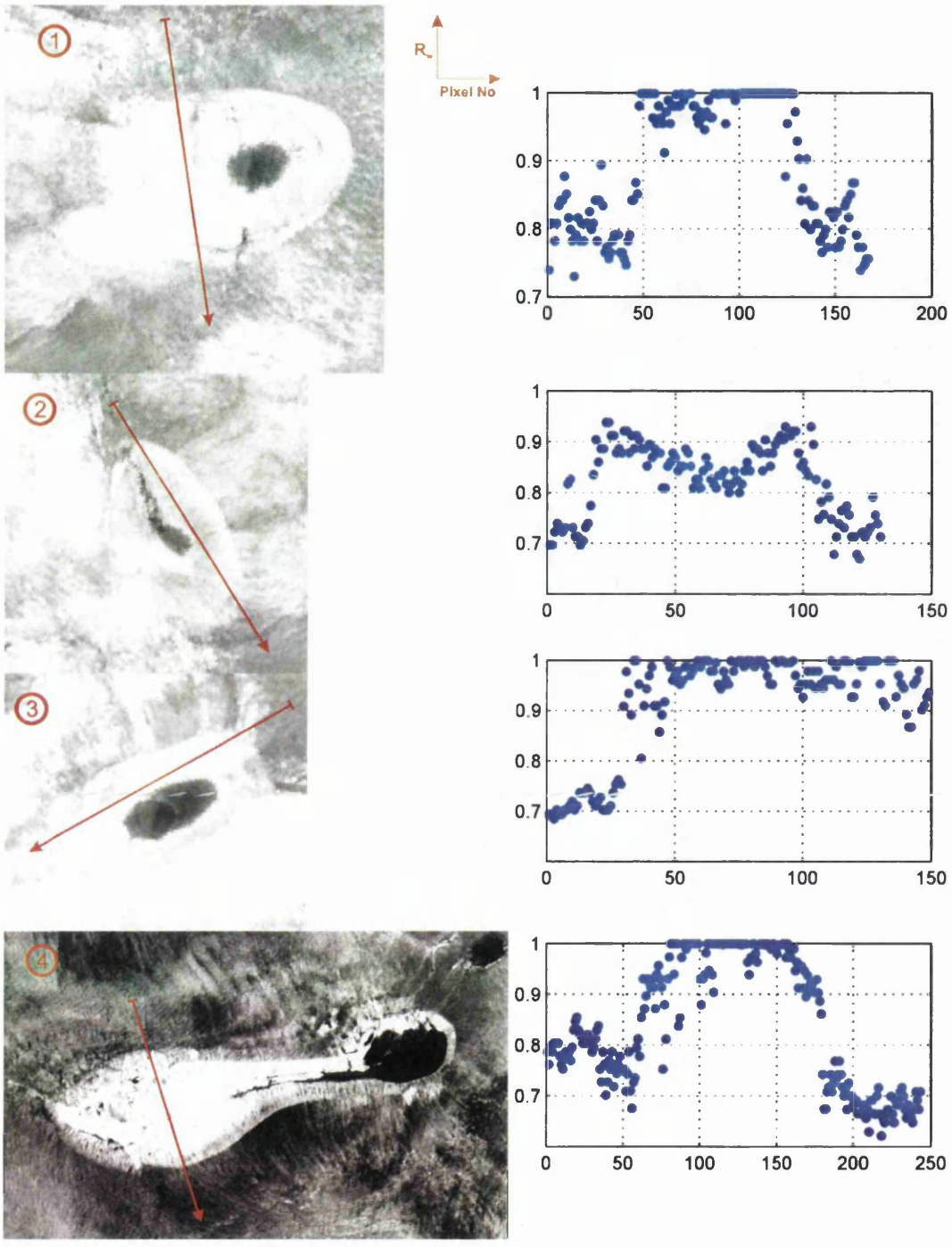

Figure 8.16: ASTER snapshots of the lakes from Figure 8.11. The scatter plots on the right side of each snapshot correspond with the transverse reflectance profile from the red arrow in the left side (continued overleaf).

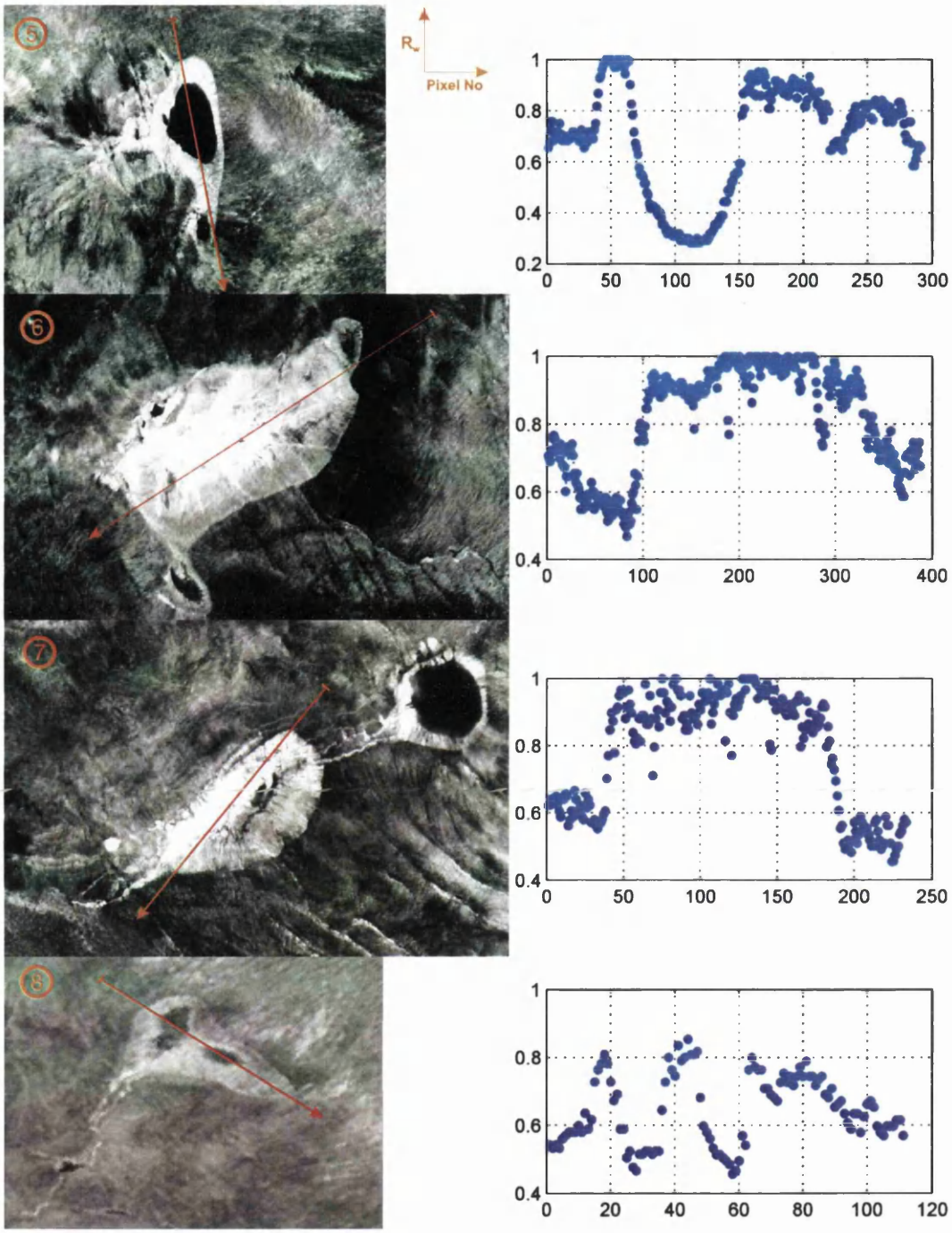

Figure 8.17: ASTER snapshots of the lakes from Figure 8.11. The scatter plots on the right side of each snapshot correspond with the transverse reflectance profile from the red arrow in the left side (continued overleaf).

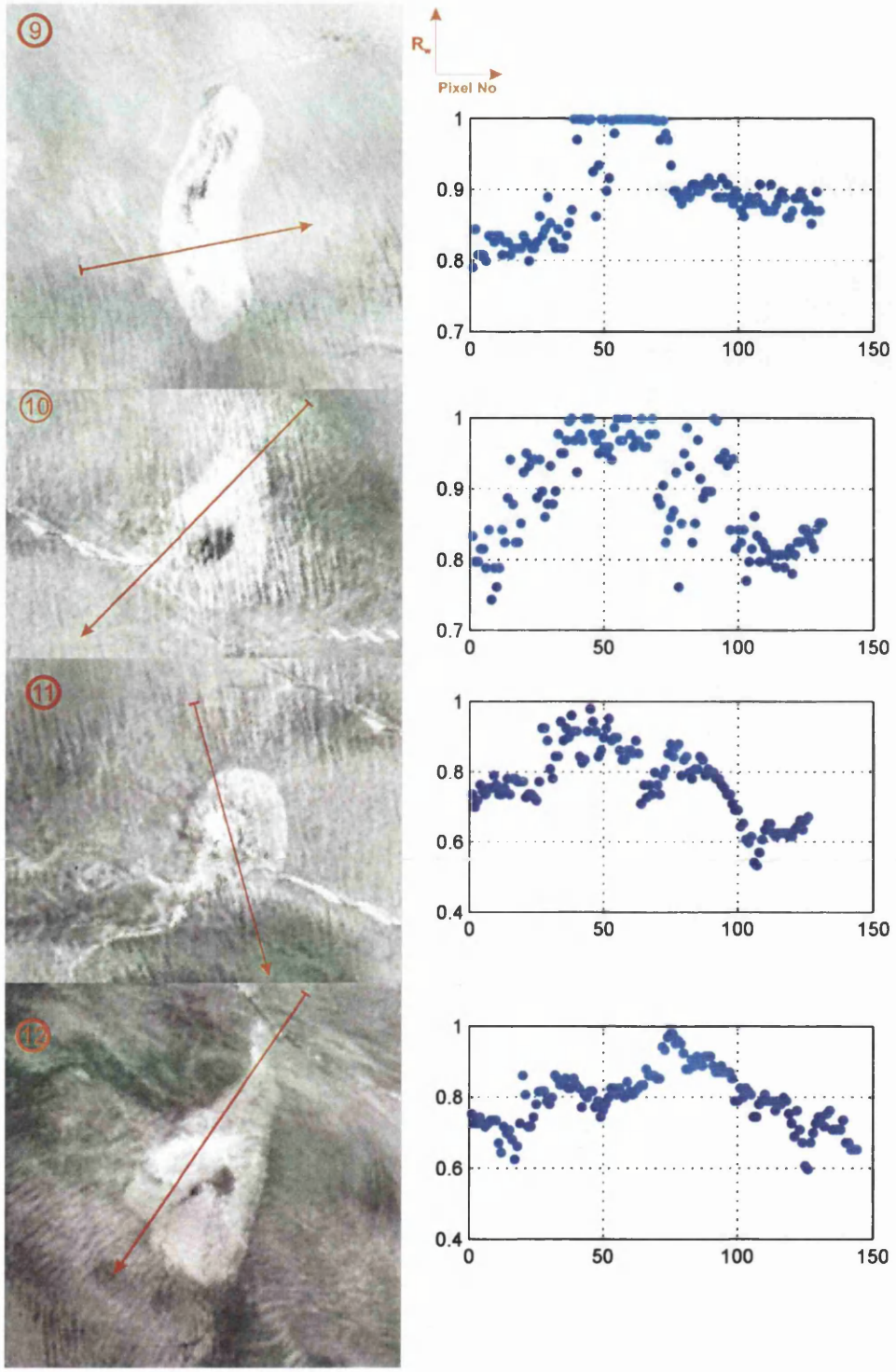

Figure 8.18: ASTER snapshots of the lakes from Figure 8.11. The scatter plots on the right side of each snapshot correspond with the transverse reflectance profile from the red arrow in the left side.

including pixels from outside and inside of the empty lake, allows us for a better visualisation of this phenomenon (Figures 8.16, 8.17, 8.18). In all the cases the surrounding lake ice has lower reflectance (lower than 0.8), in comparison with the ice inside the empty lake area, which presents a reflectance higher than 0.9. The values of the latter are similar to the expected reflectance values of fresh snow for that wavelength range (520-600 nm) (Rees, 1993), regardless of time since drainage.

What is intriguing is that the dark zone defined above is not present on the area where the water filled the lakes previously, and comparing consecutive MODIS images (Appendix B), the high reflectance values in comparison with the dark zone do not change significantly. The cause if this is still unknown, and there are not previous studies that report this phenomenon on lakes. Various hypotheses are proposed here;

1. The dust from the dark zone gets suspended in the melt-water of the lakes and when they drain it washes off the surface.

2. The dust was transported while the lakes were filled and thus the water "protected" the lake bottom from the dust, although if this was the case the water would contain suspended dust, hence darkening the satellite signal and deepening the depth results from the water reflectance model.

3. The empty lakes contain holes filled with the dust, like the cryoconite holes that are mostly narrow and vertical. This means the albedo derived from nadir-view satellites (like Landsat or ASTER) will bias the reflectance. This was reported by Boggild *et al.* (2010). This effect in the lakes analysed here would produce higher reflectance, despite having holes filled with the dust. But if this was the case, the lake area would be completely covered in holes, and looking at Figures 8.16, 8.17, and 8.18 the area looks very smooth, although the spatial resolution of ASTER would not resolved the holes. Also if that was the case, we would expect to see holes also outside the lake area, and this is not the case and even if they where there, the holes would still be too

small to resolve.

Figure 8.19 shows in more detail the characteristics of the dark region. It is interesting to note that the region covered with dust presents an almost Gaussian distribution of reflectance, with a mean of 0.831 and a median of 0.835 and an IQR of 0.043. Figure 8.19 shows the development of the dark zone as the melt season advances, which agrees with Greuell (2000), because it can be seen that the dark zone is not there at the beginning of the melt season, there are patches of dust but its maximum extent occurs at the end of the melting season. It is also interesting that the distribution of the water reflectance is very homogeneous for the first image but for the partially empty one there is a zone of very low reflectance in the centre of the lake, even though the water-covered area is quite similar, between 0.9 to 0.7 km^2 (Figure 8.20). The maximum lake area extent for 2005 is around 28/07/2005 with more than 2.5 km^2 covered by water. The dark pixels on the later image of 12/08/2005 could be caused by bottom ablation as reported by Tedesco *et al.* (2012), which would deepen the lake. Another hypothesis is that the dust could be accumulated at the centre coming from the surrounding lake while it drained.

The key findings from this section are the dark zone appearing during the melt season and how the dark pixels do not appear in the former sites of lakes drained during the melting period. This means that the mechanism with which the dark zone develops does not affect the bottom of the lakes. In other words the water covering the lakes could be preventing the dark zone to extend to the bottom of the lakes or is removed by their drainage. If this is caused by the seasonal melting and the darkness appears from outcropping dust layers (Wientjes and Oerlemans, 2010), then the bottom of the lakes should not be influenced by it, and hence there would not be any repercussion for the application of the water reflectance model on melt lakes. Future field studies should investigate why the dark zone seems not to affect areas that where previously covered with water, by analysing the spectral characteristics of the bottom before and after the drainage, and the studies should

be extended for the duration of the melting season.

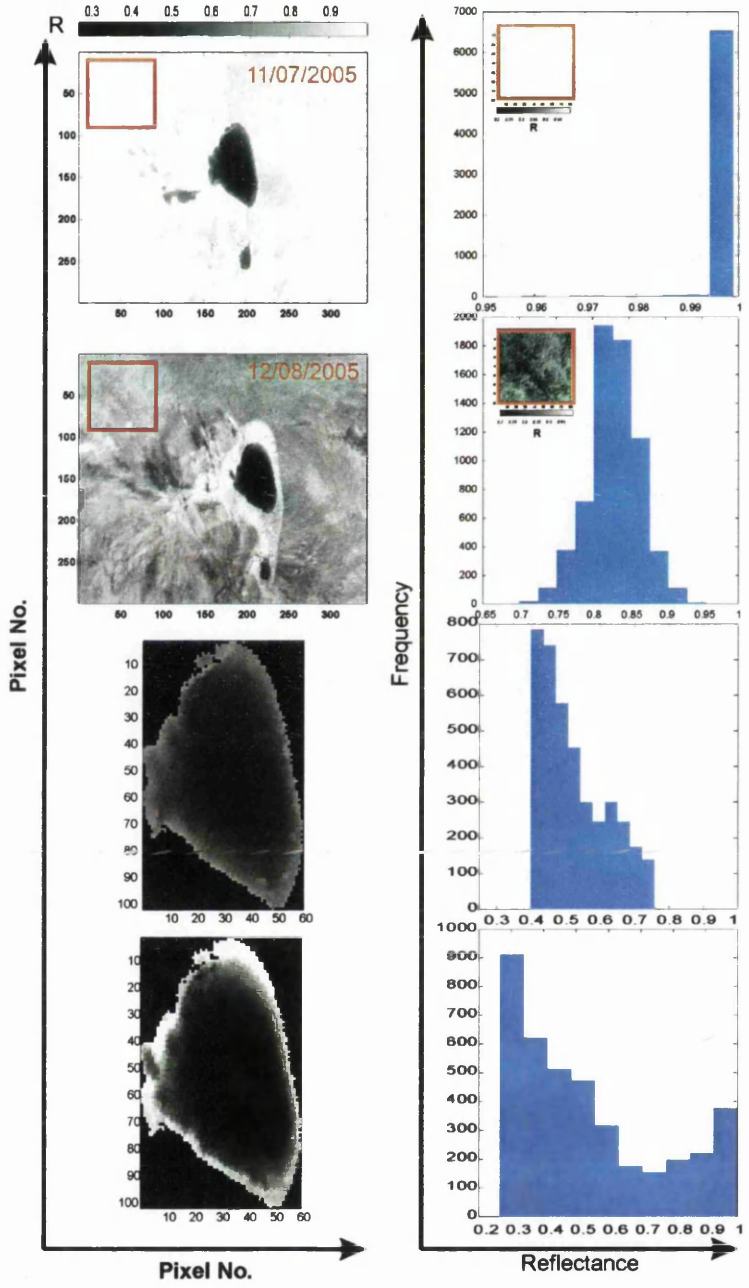

Figure 8.19: Figure showing lake 5 from previous graphs in this section. The first image on the top correspond to the ASTER image that was used as an input for the water reflectance model in previous chapters (Chapter 5). On its right there is a histogram of a random square of pixels from the snow/ice, with an area of around 1.6 km^2. The second graph from above is the same lake but showing it partially empty. the histogram on its right if from the same square area of bare ice covered with dust. The two bottom snapshots show the only the lake area of the previous graphs for a deeper look and also on their right the histogram of the lake area reflectance.

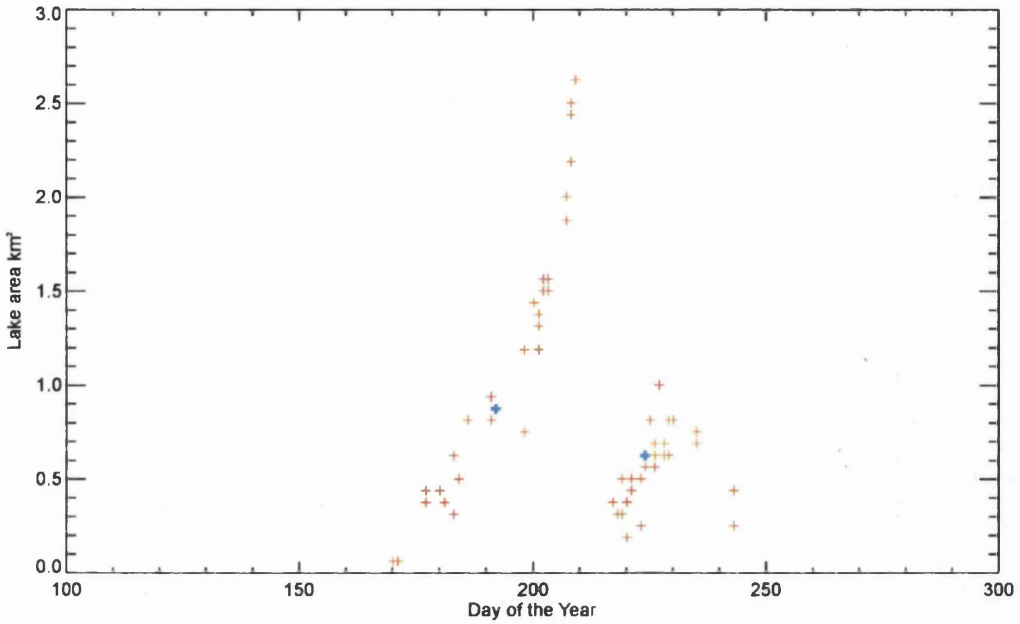

Figure 8.20: Figure showing the area distribution of lake 5 derived from MODIS images for 2005 melt season. The blue crosses correspond with the area of the dates where the two ASTER scenes from Figure 8.19 were taken (Figure modified from Selmes (2011)).

8.6 Comparison with previous studies

the use of remote sensing observations is not a new tool for quantifying the water stored in supra-glacial lakes across Greenland, although there are different approaches for this purpose. In this section different results from previous studies will be shown and compared with the results obtained in the current study. The differentiation between four types of studies that focus on supra-glacial lakes could be made for an easier comprehension;

1. Studies attempting to develop automated lake detection to study temporal evolution of its coverage over a large region (Liang *et al.*, 2012; Selmes *et al.*, 2011; Sundal *et al.*, 2009). All of these studies used MODIS observations, despite its coarse spatial resolution (250 by 250 m) to measure lake area. The fact that supra-glacial lakes form in depressions that are linked to the bedrock

topography, means that they form always in the same location and they do not are not displaced with ice flow. This facilitates the lake detection algorithms.

2. Studies that used optical sensors to derive water lake depth, mainly based on Sneed and Hamilton (2007) approach (Sneed and Hamilton, 2011; Tedesco and Steiner, 2011; Georgiou *et al.*, 2009), or other model-fitting approaches, still based on the exponential decay of surface water reflectance with depth (Box and Ski, 2007). Generally these models present a volume quantification of water stored based on depth calculations, either in individual lakes or at a catchment area scale.

3. Studies that monitor the evolution of supra-glacial lakes using satellite imagery in combination with regional data of accumulation and ablation and also PDD (Positive Degree Days) models as a proxy to lake depth (McMillan *et al.*, 2007) or Digital Elevation Models (DEMs) as a proxy for depth (Lüthje *et al.*, 2006; Leeson *et al.*, 2012).

4. Studies based on *in situ* observations (Echelmeyer *et al.*, 1991) of lake formation or drainage events monitored with GPS or other equipment (Das *et al.*, 2008).

From the studies mentioned above Table 8.4 summarises the results obtained for each of them, including area, volume and/or maximum depth estimations. Unless otherwise specified, all the results are from the south west Greenland, which is the same location this thesis covered for the application of the water-reflectance model. It is worth noting that the majority of the studies do not include uncertainties in the estimates, which are necessary for the development of any model and for a statistical analysis. Since each study gives results for specific lakes, direct comparison would not be constructive and few of the estimates have been validated with *in situ* measurements. Nevertheless, in this section the relationship between each of the three estimates (A, V and z) will be tested.

The last row in Table 8.4 shows the median and IQR for the lakes used in this section (see Table C.1). Depth values correspond with the deepest pixel for each lake and the water reflectance model was applied, using the optimised set of parameters obtained in Chapter 5. The median and the IQR are used, since it is not a normal distribution and extreme values were excluded. From those values it can be seen that the lakes from this study are uniformly shallow, despite the large area coverage (62.8 km^2) compared with other studies. Which again shows a potential underestimation of lake depth. Nevertheless the results obtained from other studies shown in Table 8.4 vary in one order of magnitude, implying that lakes across Greenland vary in shape and size, hence for an accurate between studies, same lakes should be studied.

Some studies used area-volume relationships to overcome the lack of validated depth estimates. This is the case of Krawczynski *et al.* (2009), who approximated lake volume assuming that lakes had a conical shape. They also assumed that the diameter and depth follow the aspect ratio 100:1. This assumptions have not yet been validated, although other studies have used them too due to the lake of depth estimations. Therefore using Krawczynski *et al.* (2009) for the studies from Table 8.4 showing estimates of area, volume and depth, the diameter-depth ratio will be tested. Using the formula of the area of a circumference ($A = \pi\ r^2$), the diameter value can be worked out ($\phi = r/2$), using A from Table 8.4. Then to estimate the depth, the formula of the volume of a cone ($V = (\pi\ r^2 z)/3$) is solved for z, using V from Table 8.4. The results are in Table 8.5, where A, V and z_{max} are from previous studies (Table 8.4); whereas $\phi_{conical}$ and $z_{conical}$ correspond to the results obtained using Krawczynski *et al.* (2009) approach. If the assumptions made by Krawczynski *et al.* (2009) are correct, then the ϕ-z ratio should be 100:1; looking at the last column of Table 8.5 it can be seen that the obtained aspect ratio for those thirteen lakes from previous studies does not meet the expected value. The range goes from 88:1 to 1436:1, with a median of 203:1; therefore both assumptions of conical lake shape and ϕ-z ratio $\equiv$ 100:1 are not valid for the sample lakes.

Table 8.4: Table summarising the different lake area and volume reported by previous studies. The last row corresponds with the results obtained in this thesis using the water reflectance model with ASTER data, median and IQR taken from Table C.1

Study	Specifications	A (km^2)	V (x10^6 m^3)	z_{max} (m)
(Selmes *et al.*, 2011)	Median lake A	0.56±0.01	-	-
(Sneed and Hamilton, 2011)	Max. z, not necessarily deepest	-	-	4
(Tedesco and Steiner, 2011)	Mean z for MODIS and Landsat	-	-	2.1±0.92
				3.47±0.95
(Georgiou *et al.*, 2009)	Max. A/V	3.4	18.6 ± 3.7	9.6±1.0
(Sundal *et al.*, 2009)	Max. lake A range (SW, NE, NW)	0.16-0.99	-	
(Das *et al.*, 2008)	Max. lake A/V extend	5.6	44±10	10
(Box and Ski, 2007)	SW	1.8	10.3	12.1
		8.5	21.7	4.8
		1.8	5.4	5.1
		2.2	8.3	8.0
		3.3	24.3	11.5
		6.8	32.9	10.8
		6.5	21.7	6.2
(McMillan *et al.*, 2007)	Max. lake A/V modelled	40.6±3.4	157±42	3.9±1.1
		13.6±	20±11	1.5±0.7
		30.9±2.6	45±21	1.5±0.7
		9.6±0.8	14±7	1.5±0.7
(Sneed and Hamilton, 2007)	Max. z, not necessarily deepest	-	-	4
(Lüthje *et al.*, 2006)	Modelled	-	-	10.28
(Echelmeyer *et al.*, 1991)	From *in situ* observations	10	-	20*
Current study (ASTER data)	Water reflectance model	62.8±31.4	1.9±1.4	5.8±1.5

Further investigation was carried out using the lakes from this thesis selected for volume estimations (Chapter 6). Figure 8.21 shows the depth results for the lakes of this thesis assuming conical shape lakes plotted against the maximum depths obtained from the water reflectance model. The comparison is also plotted for the lakes from Table 8.5. None of the datasets meet the assumptions of conical shaped lakes. Appendix C shows the equivalent Tables C.1 and C.2 for the lakes used in the current study (Chapter 6). The aspect ratio for this dataset varies from 23:1 to 1304:1, with a median of 110:1. If it was assumed that Krawczynski *et al.* (2009)

Table 8.5: Table summarising the different lake area, volume and depth reported by previous studies; the last three columns of the table correspond to the diameter, depth and diameter-depth ratio that those lakes would have assuming a conical shape volume (using A and V from column one and two).

A (km^2)	V ($x10^6$ m^3)	z_{max} (m)	$\phi_{conical}$ (m)	$z_{conical}$ (m)	ϕ-z ratio
3.4	18.6	9.6	1954	18.6	105:1
5.6	44	10	2670	23.6	113:1
1.8	10.3	12.1	1514	17.2	88:1
8.5	21.7	4.8	3290	7.7	430:1
1.8	5.4	5.1	1514	9.0	168:1
2.2	8.3	8.0	1674	11.3	148:1
3.3	24.3	11.5	2050	22.1	93:1
6.8	32.9	10.8	2943	14.5	203:1
6.5	21.7	6.2	2877	10.0	287:1
40.6	157	3.9	7190	11.6	620:1
13.6	20	1.5	4161	4.4	943:1
30.9	45	1.5	6272	4.4	1436:1
9.6	14	1.5	3496	4.4	799:1

ratio was and average/median of other values, then the approximation could be considered, although taking into account the big grade of uncertainties.

Figure 8.21 presents the regression parameters for both dataset if the relationship was $z_{conical}/z_{estimated}$. For the data set from Table 8.5, R^2 is negative, which is an indicator that there are not enough observations for the regression (blue dots). In the case of the dataset from the current study R^2 is 0.48, which indicates a weak linear fit.

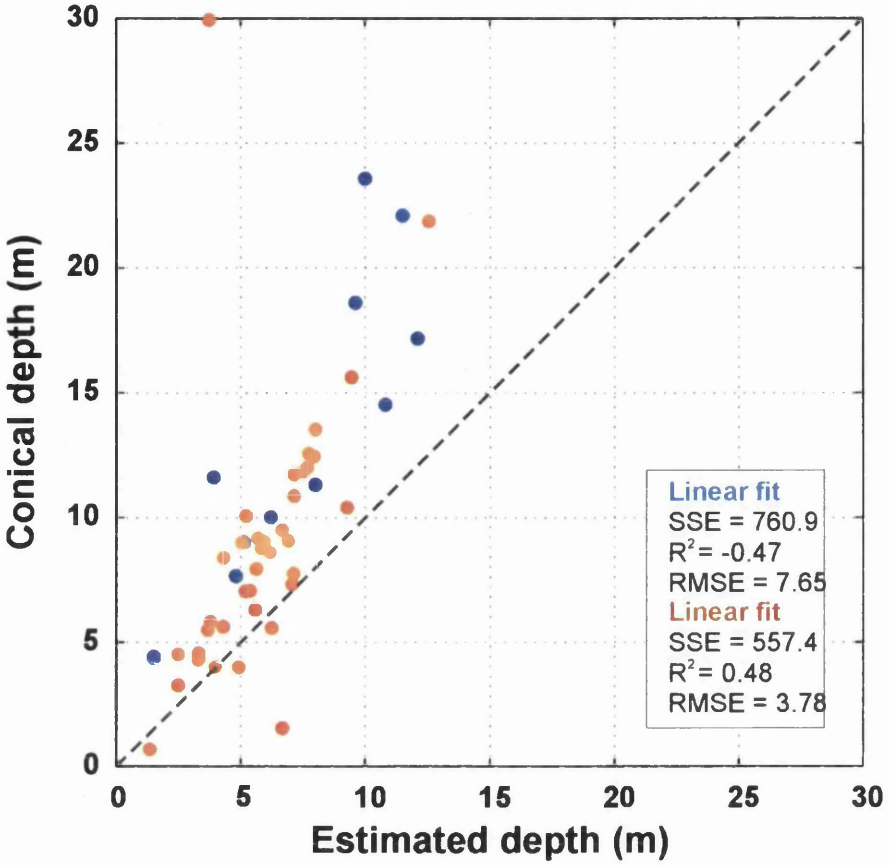

Figure 8.21: Depth estimates derived from assuming a conical lake shaped *vs.* estimated depths; red dots correspond with the lakes used in the current study, whereas blue dots correspond with the lakes used in previous studies (Table 8.5). Both linear fits correspond to the ideal case where x=y, which is the dash line on the figure.

8.6.1 Summary of the water reflectance model parameters used in previous studies

Apart from depth, volume or area comparisons with previous studies, the physical parameters used for depth derivation drive the accuracy of the estimations as well as the uncertainties derived from them. For this reason a summary of previous studies' set of parameters is shown in the current subsection (Table 8.6). The last row of the table corresponds to the set of parameters obtained for this thesis in Chapter 5. There are not enough studies that used Sneed and Hamilton (2007) for a robust statistical analysis. However with the available data, the correlation coefficients can be estimated, to see whether there is any correlation between the parameters and their variation with the studies. The correlation coefficients are 0.2575 (A_d-g),

0.1848 (g-R_∞) and 0.6732 (A_d-R_∞). From these coefficients it can be concluded that the first two pairs of parameters are uncorrelated, whereas the last pair shows a weak linear correlation. This means that of the number of different studies that are available from Table 8.6, there is not a clear relationship between each set of parameters and the variations within studies.

Table 8.6: Table summarising the different input parameters for the water reflectance model in previous studies. The last row corresponds with the set of parameters derived from the optimisation model using a Monte Carlo approach assuming a box distribution of the input parameters (Chapter 5).

Source	Methodology	A_d	g (m^{-1})	R_∞
Georgiou *et al.* (2009)	ASTER observations based on Sneed and Hamilton (2007)	0.76 ± 0.17	0.206 ± 0.01	0.105 ± 0.035
Tedesco and Steiner (2011) (*free fitting parameter to equation)	Landsat observations based on Sneed and Hamilton (2007)	0.34 ± 0.062	0.21	0.0188*
Sneed and Hamilton (2011)	Landsat observations based on Sneed and Hamilton (2007)	0.5639	0.1180	0.0380
Current study	Monte Carlo approach assuming a Box distribution based on Sneed and Hamilton (2007)	0.864 ± 0.032	0.222 ± 0.011	0.099 ± 0.002

This section can be synthesised as follows: there is a lack of field studies that estimate lake depth in a regional scale. This fact prevents a more accurate water reflectance model. With this lack of reliable depth estimates, some studies made use of an approximation of area-volume relationship to calculate lake volume from just the satellite derived area. As shown above, this assumption would work for the results included in this thesis if the ratio was assumed as the median of all the lakes, although for previous studies this was not the case. This result stresses the need of *in situ* depth measurements to improve current models and to get a more adequate set of parameters. There is another source of uncertainties that should be discussed in this section, this is related with scene selection, which is analysed next.

8.6.2 Data selection procedure and uncertainties

When looking at previous literature, apart from the results they presented, the data sources used was also taken examined. For all the studies from the previous section, it was checked whether the same scenes were available in the archive that was used for this thesis. None of the lakes that the previous studies used coincided with the lakes that this thesis studied owing to the lack of ICESat data for these lakes. However the same scenes that some studies used were found in the archive. Therefore those scenes were checked to investigate if with the model developed in this thesis, similar results could still be found as in those studies. This is the case of two of the ASTER scenes used by Georgiou *et al.* (2009). They used ten summertime scenes recorded by ASTER between 2002 and 2005 to analyse temporal variations of lake reflectance. They focused on the evolution of a lake located at 69° 18' 2" N, 48° 54' 31" W.

One of the scenes used is from 2 July 2005 15:17 UTC, and the lake snapshot can be seeing in Figure 8.22 (a). With the colour composition chosen a significant part of the lake appears ice covered and most of the ASTER pixels seem to present mixed water-ice. Tracing a rough region of interest following the perimeter of the lake, Figure 8.22 (b) shows the distribution of the pixels corresponding to lake coverage; more than 80% of the pixels show a reflectance higher then 0.878 (for ASTER Band 1). Georgiou *et al.* (2009) used a value of the lake bed reflectance of 0.76±0.17, which means all the water pixels with reflectance larger than that of the bed albedo will give positive values with the depth equation. Solving the water reflectance model for depth using the input parameters given by Georgiou *et al.* (2009), the results are shown in Table 8.6. The depth profile is shown in Figure 8.22 (c), with only 9% of the total pixels inside the lake area being represented as water; this gives an area of the lake covered by water of 0.18 km^2, against the total considered lake area with

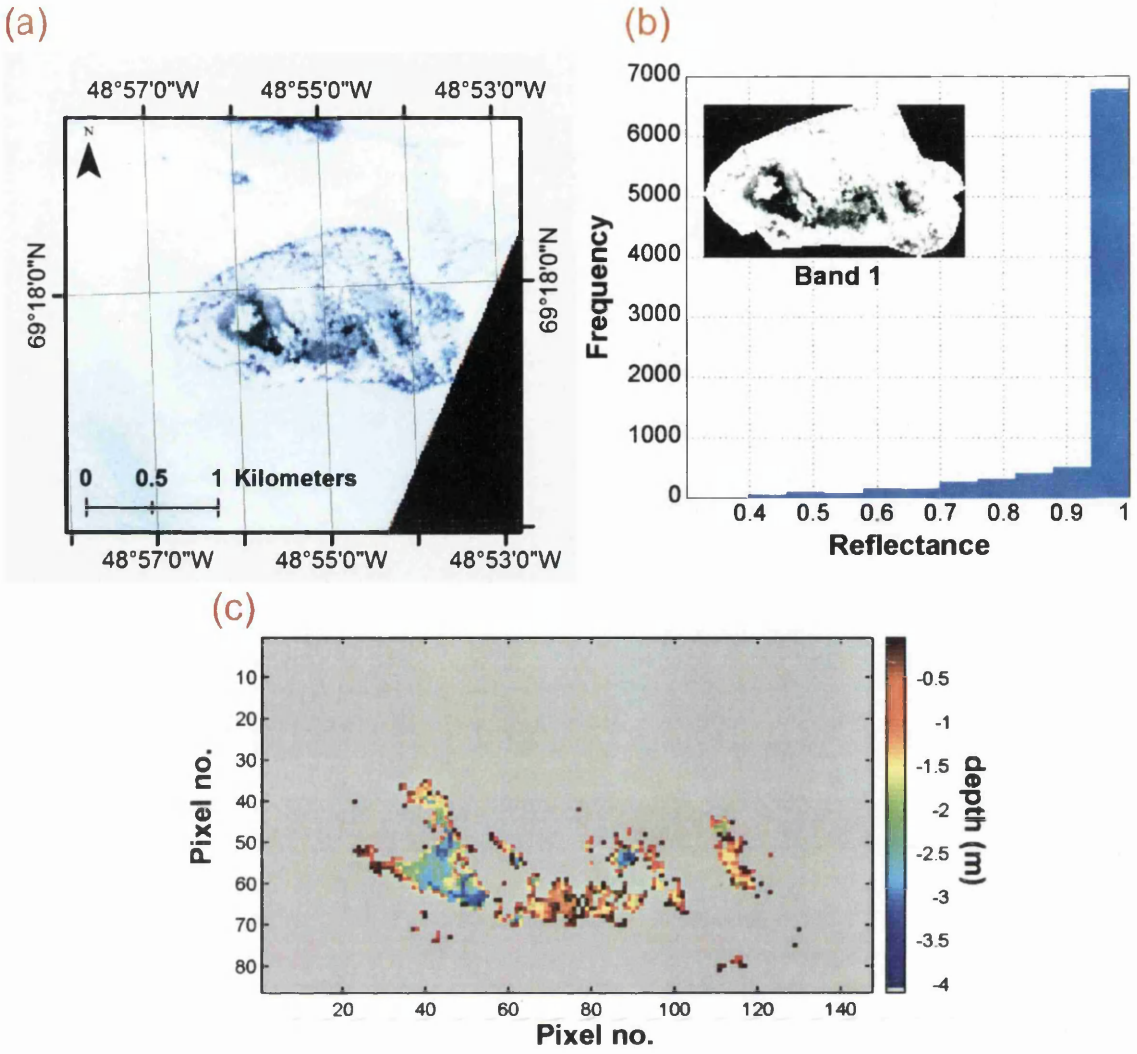

Figure 8.22: Graphs showing one of the lakes used by Georgiou *et al.* (2009); (a) ASTER colour composite snapshot (R:3, G:2, B:1) from 2 July 2005; (b) Histogram shows the reflectance distribution of the pixels inside the lake area, which is shown in the small snapshot on the top left corner; (c) Depth estimates derived after applying the water reflectance model and using the input parameters derived from Georgiou *et al.* (2009).

and without ice, which is 2 km^2. Georgiou *et al.* (2009) estimated a lake area of 1.9 km^2 for the same lake scene, which means that for their lake volume estimations they took in account the whole lake, ignoring the fact that the majority of the pixel were covered by ice and the rest could be considered mixed pixels. The maximum lake depth is 4 m, which is within the higher range estimated by Georgiou *et al.* (2009), where the maximum depth was 3.2 $\pm$ 1.9 m.

Despite the results shown in Figure 8.22, which tried to emulate Georgiou *et al.* (2009) results for that ASTER scene, those values could be biased. Even more, when doing the lake selection for the current study, that lake was selected and rejected after seen the percentage of ice covered pixels. One of the uncertainties that can affect not only depth measurements but also an accurate area detection is the presence of ice. In the case of depth estimates the ice could bias the reflectance values detected by the sensor, therefore underestimating lake depth, as will increase the reflectance of the pixels. Therefore, for future studies, the use of lakes with ice present is not recommended, especially if it is almost entirely covered. Nevertheless, it might still possible to estimate lake area looking at Figure 8.22 (a), because at the margins the ice from the surroundings of the lake is well differentiated from the perimeter of the lake, but without further data it is not possible to determine lake depth, nor volume without adding significant uncertainties to the estimations.

Apart from mixed ice-water pixels over a lake, cloud cover is another important source of depth estimates uncertainties. Another ASTER scene of the same lake as above was found in our archive, and that scene was also used by Georgiou *et al.* (2009). It is the scene from 12 August 2005, which was the scene that study made most of their analysis from. The full ASTER scene is shown in Figure 8.23 (image on the left). Cloud assessment of satellite imagery is important for better image selection and higher-level processing. For this reason a cloud classification mask algorithm was applied to the ASTER scene (Tonooka, 2008); the result is shown in Figure 8.23 (right hand side). The spatial resolution of the mask is quite coarse (around 86 by 86 m), in comparison with ASTER scenes (15 by 15 m). Nevertheless it is shows a borderline zone where the lake is located; the cloud mask algorithm divided the scene into four squares, and the left bottom corner square corresponds with where the lake is. The algorithm estimated that 76% of that square is cloud covered, whereas the average cloud cover for the whole scene is 82%. These percentages seem very high to be ignored, therefore as it was recommeneded for the ice-covered lake scene (Figure 8.22), this scene should not be use for lake depth

estimations, because the clouds could bias the lake reflectance.

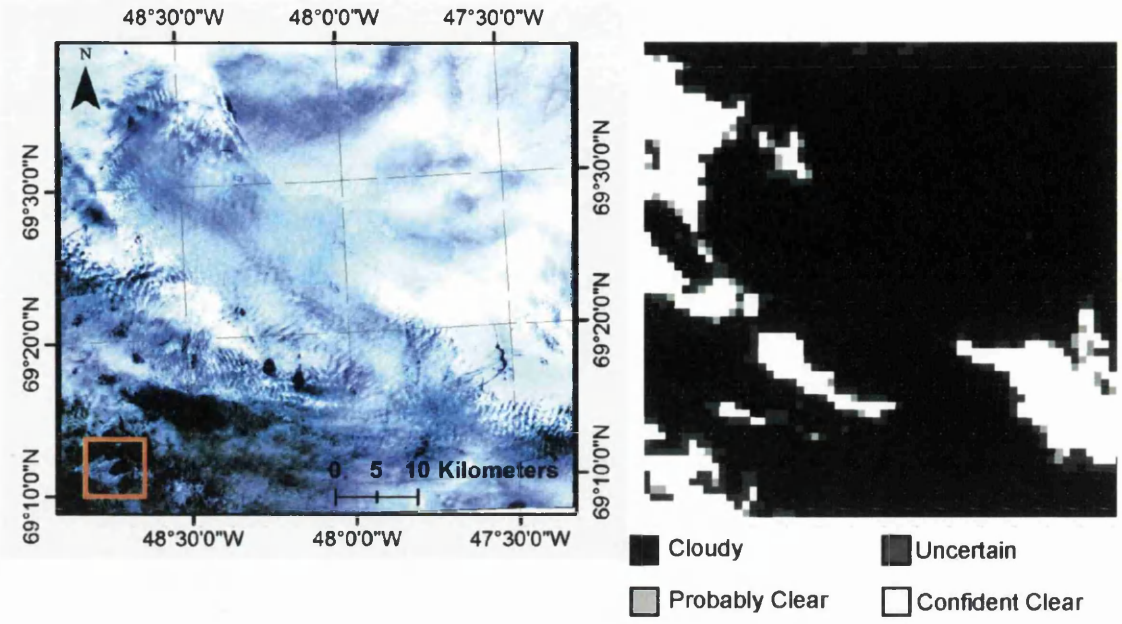

Figure 8.23: ASTER colour composite snapshot (R:3, G:2, B:1) from 12 August 2005 used by Georgiou *et al.* (2009) to determined the maximum area extend of the studied lake, shown inside the red squared (figure on the left); Cloud mask derived from an algorithm developed by Tonooka (2008). Note how the lake is on borderline area, where the algorithm predicted around half of the pixels to be *confident clear* and other *half uncertain/cloudy*.

From this section it is concluded that satellite imagery selection should be performed more rigorously, and also the potential uncertainties like cloud cover or ice-water mixed pixel should be taken into account when estimating area or lake volume.

8.7 Discussion about crevasse depths derived from the water-reflectance model: Is it feasible?

The results obtained in Chapter 7 are further discussed in this section. In that chapter the high spatial resolution (10 by 10 m) hyperspectral airborne data from CASI was used as an input to the water reflectance model and water-filled crevasse depth was obtained from it. As previously mentioned knowing the depth of water in crevasses is important for calving models because they predict that calving will occur where the depth of surface crevasses equals ice height above sea level (Benn *et al.*, 2007). Water-filled crevasses can penetrate cold glaciers within hours or days, depending on ice thickness and availability of the surface water (van der Veen, 2007). Hence in the models for calving to occur, water in crevasses is a prerequisite. Krawczynski *et al.* (2009) calculated that lakes with a diameter of 250-800 m and 2-5 m deep store enough volume of water to drive a water-filled crack to the base of an ice sheet of 1 km thickness. They also showed that if a crack is water-filled during its evolution, then the crack propagation depth is only limited by the volume of water available to fill the crack. This is possible for example when the crack is the base of a supra-glacial lake. However there are not supra-glacial lakes on the glacier front of Helheim, the first group of lakes are around 20 km from the calving front in the main flow line. Therefore in the case of calving fronts supra-glacial lakes might not play an important role in the dynamics of the front, at least directly: if one of these lakes drained to the bed, it could contribute to the acceleration of the glacier front. This is unlikely since in the case of Helheim there are not many lakes. Moreover, as Selmes *et al.* (2011) reported drainage events on the GrIS are not linked with areas where acceleration and retreat have been reported in recent years (Luckman *et al.*, 2006).

Due to the location of crevasses, it is dangerous to monitor them with field observations and satellite images present usually too low spatial resolution to resolve crevasses. Also, due to the uneven surface at the glacier front, optical satellites can

not accurately differentiate the spectral characteristics of the surface, due mainly to shadowing. In shadow areas the radiance detected by the sensor is a small non-zero signal, because the total radiation signal at the sensor contains a direct (beam) and a diffuse (reflected skylight) component (Ritcher and Schäpfer, 2012). The shadowing can also occurre when the level of the water in the crevasse is not to the surface level, therefore the reflectance signal is scattered on a vertical wall, similar to the shadowing effect. Nevertheless an accurate water depth detection for crevasses is necessary for a better refinement of calving models: it has being found that modelled calving rate is highly sensitive to changes in crevasse water depths, varying from 0 to 10 m (Cook *et al.*, 2012). It has been reported that glacier acceleration and retreat could be provoked by fracturing and deepening of crevasses caused by the availability of surface melt-water. This feedback increases calving rates (Cook *et al.*, 2012).

In Chapter 7 it was calculated from a water classification approach of CASI scenes on the 25 July 2007, that only 0.1% of the total area of Helheim front covering around 20 km length of the glacier from the calving front (see Figure 7.11 from previous Chapter). However, since calving events occur at the front, it would be convenient to estimate the water-filled crevasses depth focussing on the calving front. On the north side of the Helheim calving front (Figure 8.24 (a) red line) more calving events are reported because it is the fastest flowing part of the glacier and also it is connected to the glacier bed so all the water could have drained higher up the glacier (pers. comm. T. James, 2012).

Figure 8.24 shows the water depth of the crevasses at the calving front. The maximum depth is 6.94 $\pm$ 1.07 m. The reflectance values vary from 0.073 to 0.419 and a mean value of 0.333 $\pm$ 0.033.

Looking at the distribution of crevasse depths at the front, it can be seeing that

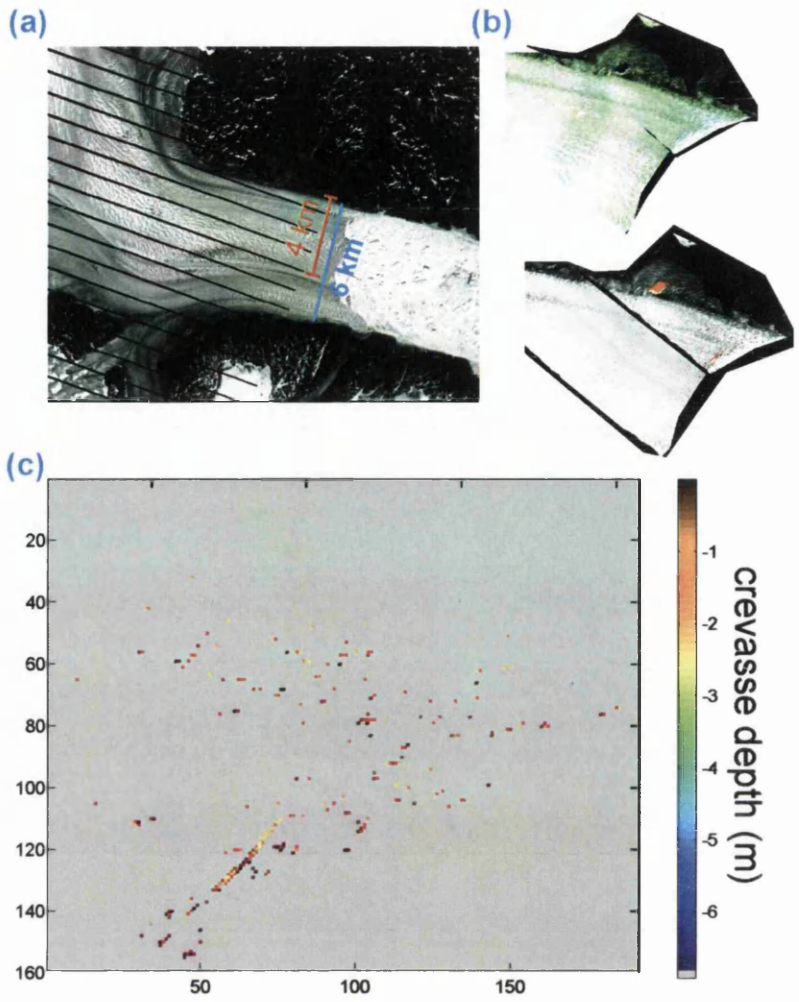

Figure 8.24: Close up selection of crevasses on the glacier front of Helheim; (a) Landsat band 2 snapshot from Helheim front showing the wideness of the front (6 km) and the length of the front where water was detected by CASI water classification method (4 km); (b) CASI snapshots of the 4 km calving front on the 24 July 2007 (around 12:00 UTC (Coordinated Universal Time)), the top one is a colour composite (R:6, G:4, B:1) and the bottom one shows in red the pixels that have water from the ratio band classification applied in Chapter 7; (c) crevasse depths of the calving front from that 4 km zone derived using the Monte Carlo approach with the water reflectance model.

they are very shallow (Figure 8.25), with a median of 1.18 m. These results do not necessarily follow the calving model theory. In Chapter 7 crevasse depths were distributed between 0 to 25 m (Figure 7.14, Chapter 7) for the whole Helheim front area. A question rises from these results, and that is whether the water-filled crevasses contain more water higher up the glacier and as they get closer to the calving front that water drains forming cracks through the ice, and since there are

not supra-glacial lakes at front, those cannot act water storage sources to fill the crevasses. The implication could also be that because the crevasses are not filled to the surface, optical imagery as CASI hyperspectral signal, would be biased by scattering in the narrow walls of the crevasses. That is, crevasses will penetrate to the depth at which the net longitudinal stress becomes zero. In the absence of water in the crevasses, at this depth the longitudinal tensile stress equals the compressive ice overburden pressure (Nick *et al.*, 2010). If the crevasse contains the sufficient water, the crevasse could start increasing deepening and once water crevasse propagation is started, the growth rate is determined primarily by the amount of water flowing into the crevasse (van der Veen, 2007).

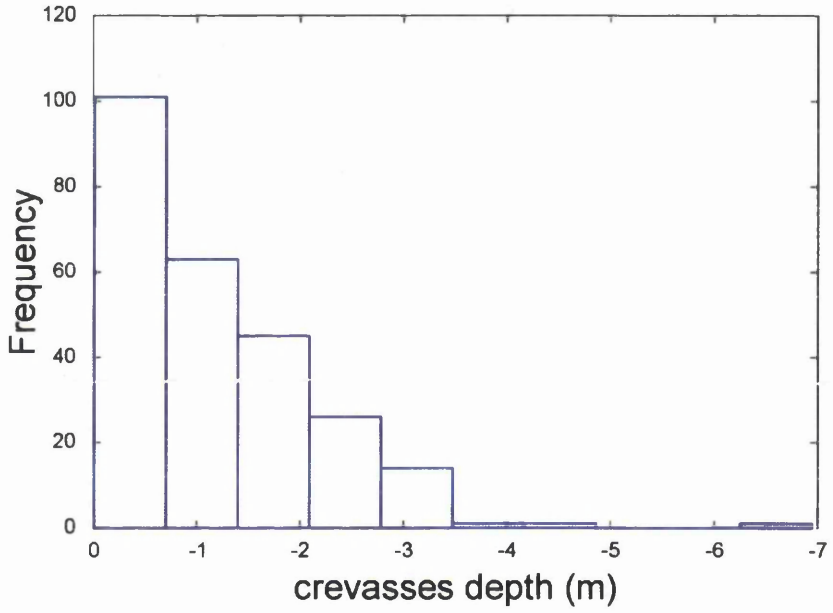

Figure 8.25: Distribution of crevasse depth of water within crevasses at the front of Helheim calving front estimated from CASI hyperspectral dataset (Figure 8.24).

As shown previously the water reflectance model is limited to shallow waters, but the depth at which the model stops working varies with the parameters. The model will stop being valid when R_w=R_∞, *i.e.* when the reflectance given at the water surface equals the reflectance of optically deep water. Therefore, this is one of the reasons why the water reflectance model might not be suitable for water-filled crevasse depth estimations. There even if at the calving front the crevasses are very shallow following the water reflectance model depth estimates (Figure 8.25) those

results might an underestimation of the real crevasse depth at the glacier front.

There are no field studies in Helheim that have water-filled crevasse depth estimates; nevertheless Mottram and Benn (2009) compared *in situ* crevasse depths from a glacier in Iceland (Breidamerkurjökul glacier) with crevasse depths derived from Nye crevasse model (Nye, 1957) and from the Linear Elastic Fracture Mechanics (LEFM) model (van der Veen, 1998b,a). The models predict crevasse depth of maximum 40 m, whereas the field observations from Mottram and Benn (2009) show depths of maximum 20 m, although mainly below 14 m, as shown in Figure 8.26. These field results are very similar to the crevasse depth estimations obtained in the previous chapter (Chapter 7) based on CASI reflectance and the water reflectance model, as shown in Figure 8.27, which is repeated from the previous chapter for a direct visual comparison. Mottram and Benn (2009) concluded that predicted depths in both Nye and LEFM models might be closer to actual crevasse depth than estimated with field observations; this could be due to the fact that the measurements were minimum depths because the device used was prevented from accessing the narrowest and deepest of the crevasses. Also, van der Veen (1998b) proposed that cracks may penetrate to deeper levels due to the overburden pressure, without the fracture at the surface separating, which would imply that optical or field observations would not account for the depth of that crack.

To sum up, field observations are limited not only by the location of the crevasses, which is dangerous, but also by the current devices used to measure crevasse depth. In terms of the result obtained in Chapter 7, there have been found various limitations to that approach. These limitations were mainly due to shadowing, which is pronounced around outlet glaciers due to the mountainous areas and with low sun angles in late summer observations. In addition, the crevasses are not necessary filled to the top surface, therefore the sensor might be detecting not the water, but only narrow ice walls, which would underestimate the amount of water-filled crevasses on the glacier. The bottom of the crevasse is another source of errors, and

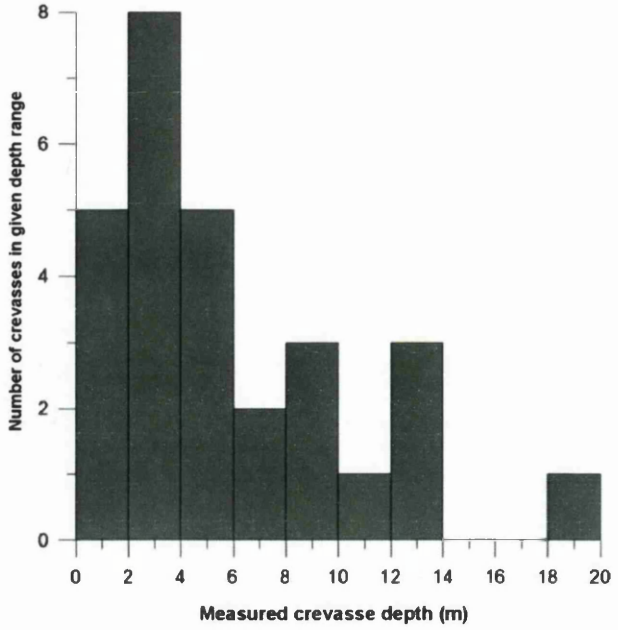

Figure 8.26: Distribution of crevasse depths measured at Breidamerkurjökul (Mottram and Benn, 2009)

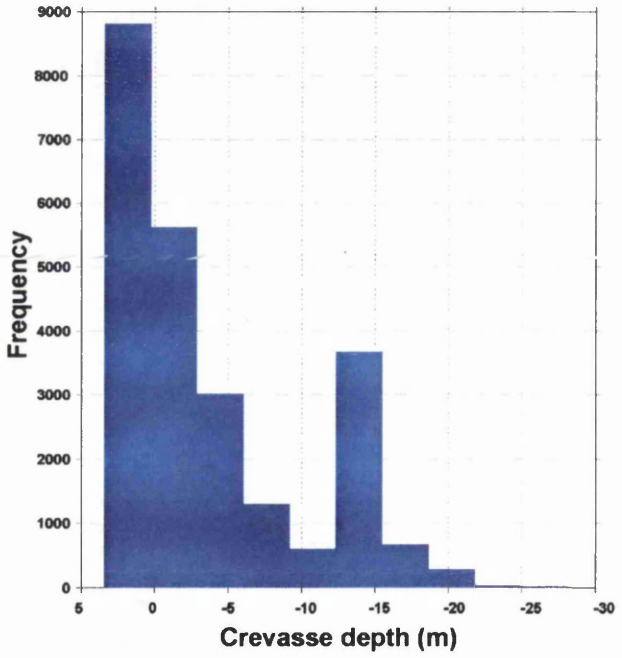

Figure 8.27: Depth distribution of all the crevasses depth detected with CASI hyperspectral data. Notice that there 9,344 pixels ($\approx$ 39% of the total) that give positive depths, which were removed from the analysis.

that is when it can actually be detected by the sensor signal. This might not be possible, since the crevasses can present a very uneven bottom. Finally, crevasses are not in a constant position from year to year, as supra-glacial lakes are: crevasses

move within days, which prevents the use of satellite observations from monitoring changes in depth of crevasses with time. Also this movement will deform the geometry of the crevasse. From all of these limitations, it could be concluded that crevasse depth determination from optical satellites is at the moment not reliable. However, the estimates obtained in this thesis are of the range of previously published field observation (Mottram and Benn, 2009), which can potentially be useful for further field campaigns of CASI airborne over Helheim or elsewhere.

8.8 Glaciological implications of this thesis

The motivation of this thesis was to test the current methods of estimating lake depth on supra-glacial lakes that form on the surface of the GrIS. The implications of this study on the glaciological community could help clarify the theory developed by Zwally *et al.* (2002a); the so called Zwally effect was thought to be the cause of the increased dynamic loss by drainage to the bed, lubricating the glacier and accelerating it. However, recent studies have dismissed this theory showing the areas with highest mass loss are not areas with highest number of drainage events. If further investigation was done, either with field observations or with the launch of a satellite that met adequate spatial and temporal resolutions, more accurate estimates of lake volume could be produced.

The optimisation of the water reflectance model developed in this study was regionally up-scale to forty lakes in south west Greenland. These lakes correspond to the 3% of the total lakes mapped by Selmes *et al.* (2011), who mapped 1,430 lakes on the southwest (south west area from Figure 2.4). From this it can be stated that the regional up-scaled is not significant. Time limitations prevented from a full volume estimation of the whole south west area. However, this study could be a first step towards a global quantificaiton of the volume stored at catchment area, which could

add further information to previous studies (Selmes *et al.*, 2011; Leeson *et al.*, 2012). This volume of water could be compared with the location of the lakes with drainage events, reported by Selmes *et al.* (2011). The implication of these findings could be applied to further explore the potential link between drainage events and glacier dynamics. Since area and volume are somehow related, it would be expected that in regions with highest lake concentration, the highest amount of volume would be found. Future research could help explain the role of supra-glacial lakes on seasonal acceleration and also it could be possible to link lake volume with drainage events and hence hydrofracture to the glacier bed, which could dismiss the Zwally effect theory.

8.9 Chapter summary

The water reflectance model used in this thesis has been widely used to derive water depth across the supra-glacial lakes on the GrIS, specifically in the south west of Greenland (Sneed and Hamilton, 2007, 2011; Tedesco and Steiner, 2011; Georgiou *et al.*, 2009). One of the aims of this thesis was to test whether an optimised version of the water reflectance model could be applied simultaneously in a regional/global scale to obtain water depth. The main achievement of this thesis was the inclusion of a robust analysis of the model by applying a Monte Carlo simulation (Chapter 4). For this purpose ICESat elevation measurements over empty lakes was transformed as a reference depth for the optimisation model, as shown in Chapter 5. Throughout this section all the factors driving the water reflectance model are discussed. One of the main sources of error is the selection of the physical parameters used as an input to the water reflectance model; also their uncertainties and the assumptions that need to be made to be able to compute the model (Chapter 4). In that regard the Monte Carlo simulation appeared to be an adequate approach for a better understanding and quantification of these uncertainties. Finally the use of ICESat data as the observed depth for the minimisation and optimisation of the model

was discussed and what it can be interpreted from the results obtained, since it was not possible to generate a global model that agrees with the expected measurements.

Further analysis should be done with regard to the dark zone and field observations should be taken in consideration to understand the phenomenon. Also more extended field measurements are needed for a better understanding for the area-volume relationship, since at the moment the chosen approximations by Krawczynski *et al.* (2009) are not correct. Another factor to take in consideration in the future is the image selection procedure, since it has been proved that cloud cover and ice mixed pixels can influence in depth estimates cause bias.

Chapter 9

Conclusions and future work

9.1 Summary

In recent years supra-glacial lakes have been in the spotlight of studies interested in the mechanisms that govern the recent mass loss at the margins of the GrIS. Drainage events to the bed through hydrofractures were thought to enhance glacier flow velocities by lubricating the ice sheet bed. Recent studies have shown that there is not a direct link between drainage to the bed and the recent observed mass losses, like in the south west of Greenland. Nevertheless field studies have confirmed how melt-water from supra-glacial lakes plays an important role in hydrofractures and establishing a connection between the surface and bed hydrological systems over short time scales; peak velocities of the ice are found to be positively correlated with the degree of melting. Therefore supra-glacial lakes are of interest for a better understanding of the dynamic response of the GrIS to recent climate change in a short term scale and to the future predicted warming.

The aim of this research was to investigate the performance of current water reflectance models applied to optical imagery for melt-water depth/volume quantification. These water reflectance models are based on the *Bouguer Lambert Beer*

law, which represents the exponential decay of the reflectance at the surface with water depth. The ASTER sensor was chosen owing to its high spatial resolution, which allows for a more accurate lake delimitation and for more precise reflectance values that minimised the amount of mixed pixels, which bias the reflectance and hence depth calculations. A MODIS inventory of lakes across the GrIS developed in a previous research (Selmes, 2011) was used to locate the lakes. For the water reflectance model three physical parameters were needed as an input; bed albedo (A_d), attenuation coefficient (g) and reflectance of optically deep water (R_∞). Various assumptions had to be made to obtain the parameters using previous approaches. To validate the depth estimations from the water reflectance model, ICESat elevation measurements were transformed into lake depth when ICESat tracks crossed an empty lake. Only eleven lakes were selected for the model validation; this was due to the lack of overlapping between ASTER observations and ICESat tracks crossing empty lakes over the same year. Further investigation consisted of an optimisation model applied to minimise the difference between ICESat and ASTER modelled depth profiles. For this purpose a Monte Carlo simulation was applied to the water reflectance model, which produced a robust uncertainties analysis of the modelled depths.

9.2 Conclusions

- The optimised model provides an improvement with respect to the original model, which was based on previous literature. Despite the improvement, the difference between the expected depths and the modelled depths is significant, especially in the deepest parts of the lakes, where there is a systematic underestimation of depth from the model.

- In order to understand the factors that prevent the optimisation model to meet ICESat reference depths, different model scenarios were tested. The different

scenarios give an insight into how the model behaves; from those results a Box distribution of the parameters applied to a global model seemed more appropriate. One of the objectives of this thesis was to derive an optimised set of parameters that could be applied elsewhere, in a regional or global scale across the GrIS; for that a global minimisation model appeared to be more realistic.

- The parameters that govern the water reflectance model together with the water reflectance need to be obtained from field observations in higher spatial scale than individual lakes. Moreover, other factors might be influencing depth modelled from satellite observations; for example the dark zone introduced in Chapter 8, could be causing bias on depth estimations during the time when the darkening is present.

- The Monte Carlo Simulation provides a new method of accurately calculating an optimised depth based on the water reflectance model and using ICESat depth estimates as reference depths. Taking into account the Monte Carlo-derived uncertainties, it is possible to model depths at a regional scale using the optimised model.

- It is possible to accurately determine lake volume from optical imagery, although due to the lack of compromise between spatial-temporal resolution of the current sensors, it is yet not feasible to study the evolution of lake volume throughout the melt season. For interannual variations of volume bathymetry field observations could help validating the modelled volumes and hence gain a better understanding of the difference in spectral characteristics of lakes, since if the bathymetry was known, then the optical signal could entirely be attribute to water characteristics and depth.

- Up-scaling the optimisation model elsewhere in the ice sheet is not recom-

mended without further research, since water and lake bottom characteristics could vary spatially.

- The application of the the water reflectance model for the quantification of water-filled crevasse depth on Helheim glacier, was a novel approach and therefore tested. Crevasse geometry is not like that of supra-glacial lakes; crevasses present almost vertical walls and the bottom is not homogeneous, it could prevent water from melt or ice spikes that will interfere in the surface reflectance values, making the satellite signal have multiple refractions. Even more, the depth of the crevasses might be deeper than the maximum permitted by the water reflectance models, which were developed for shallow waters. Despite all these uncertainties, there is no doubt that the use of CASI hyperspectral data for water quantification across Helheim could be a big step forward for the better understanding of its influence on calving events.

9.3 Suggestions for further work

As a future reference, for next generation of sensors a compromise between time series and spatial resolution could be useful for accurate volume estimates and temporal variations of the melt-water stored on the ice sheet. Also even if in this thesis satellite comparison was mainly focussed on ASTER and MODIS differences, similar comparisons could be made between other combinations of high resolution sensors.

The Monte Carlo optimisation model could be applied with field observations, therefore the reference depths used in the minimisation model would be precise and hence a robust statistical analysis could be achieved once the optimised parameters are obtained. If field observations could be made in a catchment scale, then different sensors covering that catchment during the field season, could be optimised with the those *in situ* measurements and then a detailed comparison of the performance of each satellite could be made.

Further analysis should be done with regard to the dark zone and field observations should be taken in consideration to understand the phenomenon. Also more extended field measurements are needed for a better understanding for the area-volume relationship, since at the moment the chosen approximations by Krawczynski *et al.* (2009) are not correct. Another factor to take in consideration in the future is the image selection procedure, since it has been proved that cloud cover and ice mixed pixels can influence depth estimates causing bias.

The CASI hyperspectral sensor is a potential candidate for further studies over lakes and over crevasses. Nevertheless first validation of the geocorrection methods is needed, since CASI reflectance was significantly lower than expected. If the geocorrection process and the atmospheric correction were reviewed, CASI data could be applied to other glacier fronts where narrower storage of water occurs.

Further studies on water-filled crevasse depth are crucial to better understand the dynamics that govern calving events, also field observations could make the current calving models more realistic.

Recent studies have proved that drainage events from lakes are not directly linked with the variations in mass balance, although they are linked with the seasonal peaks of flow speed up. Both field studies and satellite observations have detected those drainage events; however is still not well understood why some of the lakes drain and why others do not or why the refreeze instead. Hence there is a need to find the factor that makes lakes more likely to drain. Quantification of lake volume across the GrIS could help finding the trigger of these events, by knowing the distribution of water on the ice sheet and how it could influence the draining.

References

Abrams, M. (2000). The advanced spaceborne thermal emission and reflection radiometer (ASTER): Data products for the high spatial resolution imager on nasa's terra platform. *International Journal of Remote Sensing*, **21(5)**:847–859.

Ackleson, S. and V. Klemas (1986). Two-flow simulation of the natural light field within a canopy of submerged aquatic plants. *Applied Optics*, **25(7)**:1129–1136.

Alley, R. (1987). Firn densification by grain-boundary sliding: A first model. *Journal of Physique*, **3(48)**:249–256.

Alley, R., P. Clark, P. Huybrechts, and I. Joughin (2005a). Ice-sheet and sea-level changes. *Science*, **310**:456–460.

Alley, R., T. Dupont, B. Parizek, and S. Anandakrishnan (2005b). Access of surface meltwater to beds of sub-freezing glaciers: preliminary insights. *Annals of Glaciology*, **40**:8–14.

Arthern, R. and D. Wingham (1998). The natural fluctuations of firn densification and their effect on the geodetic determination of ice sheet mass balance. *Climatic Change*, **40**:605–624.

ASTER (2002). *ASTER Higher-Level Product User Guide, Version 2.0, JPL D-200062.*

ASTER (2005). *User's Guide Part I General (Ver.4.0).* Earth Remote Sensing Data Analysis Centre.

AZGCORR (2005). *Airborne Remote Sensing Hyperspectral Direct Georeferencing package. User's manual. azgcorr version 5.0.0, azexhdf version 3.0.3.* AZIMUTH SYSTEMS UK.

Bae, S. and B. E. Schutz (2002). Geoscience laser altimeter system (GLAS). algorithm theoretical basis document, version 2.2: Precision attitude determination (pad). *Centre for Space Research, The University of Texas at Austin.*

Bamber, J., R. Alley, and I. Joughin (2007). Rapid response of modern day ice sheets to external forcing. *Earth and Planetary Science Letters*, **257**:1–13.

Bartholomew, I., P. Nienow, A. Sole, D. Mair, T. Cowton, S. Palmer, and J. Wadham (2011). Supraglacial forcing of subglacial drainage in the ablation zone of the Greenland Ice Sheet. *Geophysical Research Letters*, **38(L08502)**:1–5.

Bell, R. (2008). The role of subglacial water in ice-sheet mass balance. *Nature*, **1**:297–304.

Benn, D., J. Gulley, A. Luckman, A. Adamek, and P. Glowacki (2009). Englacial drainage systems formed by hydrologically driven crevasse propagation. *Journal of Glaciology*, **55(191)**:513–523.

Benn, I., N. Hulton, and R. Mottram (2007). Calving laws, sliding laws and the stability of tidewater glaciers. *Annals of Glaciology*, **46**:123–130.

Bierwirth, P., T. J. Lee, and R. Burne (1993). Shallow sea-floor reflectance and water depth derived by unmixing multisprectral imagery. *Photogrammetric Engineering and Remote Sensing*, **59(3)**:331–338.

Boggild, C., R. Brandt, K. Brown, and S. Warren (2010). The ablation zone in northeast Greenland: ice types, albedos and impurities. *Journal of Glaciology*, **56(195)**:101–113.

Boon, S. and M. Sharp (2003). The role of hydrologically-driven ice fracture in drainage system evolution on an arctic glacier. *Geophysical Research Letters*, **30(18)**:1–4.

Boon, S., M. Sharp, and P. Nienow (2003). Impact of an extreme melt event on the runoff and hydrology of a high arctic glacier. *Hydrological Processes*, **1**:1051–1072.

Booth, A., R. Clark, and T. Murray (2011). Resolution and precision of semblance-based gpr velocity analysis by monte-carlo simulation. *Near Surface Geophysics*, **9(5)**:399–411.

Box, J., D. Bromwich, B. Veenhuis, L.-S. Bai, J. Stroeve, J. Rogers, K. Steffen, T. Haran, and S.-H. Wang (2006). Greenland ice sheet surface mass balance variability (1988-2004) from calibrated polar mm5 output. *Journal of Climate*, **19**:2783–2800.

Box, J. and K. Ski (2007). Remote sounding of greenland supraglacial melt lakes: implications for subglacial hydraulics. *Journal of Glaciology*, **53(181)**:257–265.

Brenner, A., J. DiMarzio, and H. Zwally (2007). Precision and accuracy of satellite radar and laser altimeter data over the continental ice sheets. *IEEE Transactions on Geoscience and Remote Sensing*, **45**(2):321–331.

Brenner, A., H. Zwally, C. Bentley, B. Csatho, M. Harding, D.J. ad Hofton, B. Minster, L. Roberts, J. Saba, R. Thomas, and D. Yi (2003). *GLAS Algorithm Theoretical Basis Document Version 4.1: Derivation of Range and Range Distributions From Laser Pulse Waveform Analysis for Suface Elevations, Roughness, Slope, and Vegetation Heights.*

Chrysoulakis, N., M. Abrams, H. Feidas, and K. Arai (2010). Comparison of atmospheric correction methods using ASTER data for the area of Crete, Greece. *International Journal of Remote Sensing*, **31(24)**:6347–6385.

Colgan, W., K. Steffen, W. McLamb, W. Abdalati, H. Rajaram, R. Motyka, T. Phillips, and R. Anderson (2011). An increase in crevasse extent, west greenland: Hydrologic implications. *Geophysical Research Letters*, **38(L18502)**:1–7.

Cook, S., T. Zwinger, I. Rutt, S. O'Neel, and M. T. (2012). Testing the effect of water in crevasses on a physically based calving model. *Annals of Glaciology*, **53(60)**:90–96.

Cuffey, K. (2001). Interannual variability of elevation on the greenland ice sheet: effects of firn densification, and establishment of a multi-century benchmark. *Journal of Glaciology*, **47(158)**:369–377.

Das, S. B., I. Joughin, M. D. Behn, I. M. Howat, M. A. King, D. Lizarralde, and M. P. Bhatia (2008). Fracture Propagation to the Base of the Greenland Ice Sheet During Supraglacial Lake Drainage. *Science*, **320**(778):778–781.

Echelmeyer, K., T. Clarke, and W. Harrison (1991). Surficial glaciology of jakobshavns isbrae, west greenland: Part i. surface morphology. *Journal of Glaciology*, **37(127)**:368–381.

ENVI (2009). *Atmospheric Correction Module: QUAC and FLAASH USer's Guide*. Atmospheric Correction Module Version 4.7, ITT Visual Information Solutions.

Fricker, H., T. Scambos, R. Bindschadler, and L. Padman (2007). An active subglacial water system in west antarctica mapped from space. *Science*, **315**:1544 – 1548.

Fricker, H. A., J. N. Bassis, and B. Minster (2005a). ICESat's new perspective on ice shelf rifts: The vertical dimension. *Geophysical Research Letters*, **32**:L23S08.

Fricker, H. A., A. Borsa, B. Minster, C. Carabajal, K. Quinn, and B. Bills (2005b). Assessment of ICESat performance at the Salar de Uyuni, Bolivia. *Geophysical Research Letters*, **32**:L21S06.

Georgiou, S., A. Shepherd, M. McMillan, and P. Nienow (2009). Seasonal evolution of supraglacial lake volume from aster imagery. *Annals of Glaciology*, **50(52)**:95–100.

Greuell, W. (2000). Melt-water accumulation on the surface of the greenland ice sheet: effect on albedo and mass balance. *Geografiska Annaler*, **82(4)**:489–498.

Hedley, J. and P. Mumby (2003). A remote sensing method for resolving depth and subpixel composition of aquatic benthos. *Limnology and Oceanography*, **48(1, part 2)**:480–488.

Hoffman, M., G. Catania, T. Neumann, L. Andrews, and J. Rumrill (2011). Links between acceleration, melting, and supraglacial lake drainage of the western greenland ice sheet. *Journal of Geophysical Research*, **116(F04035)**:1–16.

Howat, I., I. Joughin, and T. Scambos (2007). Rapid changes in ice discharge from Greenland outlet glaciers. *Science*, **315**(5818):1559–1561.

Johansson, A. (2012). *Remote sensing of supra-glacial lakes on the west Greenland Ice Sheet.* Ph.D. thesis, Stockholm University, Faculty of Science, Department of Physical Geography and Quaternary Geology.

Krauth, W. (2006). *Statistical Mehcanics: Algorithms and Computations.* Oxford University Press 1st Edition.

Krawczynski, M. J., M. D. Behn, S. B. Das, and I. Joughin (2009). Constraints on the lake volume required for hydro-fracture through ice sheets. *Geophysical Research Letters*, **36**:L10501, doi:10.1029/2008GL036765.

Lee, Z., K. L. Carder, C. D. Mobley, R. G. Steward, and J. S. Patch (1999). Hyperspectral remote sensing for shallow waters: 2. deriving bottom detphs and water properties by optimization. *Applied Optics*, **38(18)**:3831–3843.

Leeson, A., A. Shepherd, S. Palmer, A. Sundal, and X. Fettweis (2012). Simulating the growth of supra-glacial lakes at the western margin of the greenland ice sheet. *The Cryosphere*, **6**:1077–1086.

Lemke, P., J. Ren, R. B. Alley, I. Allison, J. Carrasco, G. Flato, Y. Fujii, G. Kaser, P. Mote, R. H. Thomas, and T. Zhang (2007). Observations: changes in snow, ice and frozen ground. in: Climate change 2007: The physical science basis. contribution of working group i to the fourth assessment report of the intergovernmental panel on climate change. *Cambridge University Press, Cambridge, United Kingdom and New York, NY, USA.*, **Chapter 4**:996pp.

Liang, Y., W. Colgan, Q. Lv, K. Steffen, W. Abdalati, J. Stroeve, D. Gallaher, and N. Bayou (2012). A decadal investigation of supraglacial lakes in west greenland using a fully automatic detection and tracking algorithm. *Remote Sensing of Environment*, **123**:127–138.

Luckman, A., M. T., R. de Lange, and E. Hanna (2006). Rapid and synchronous ice-dynamic changes in East Greenland. *Geophysical Research Letters*, **33**:1–4.

Lüthje, M., L. T. Pedersen, N. Reeh, and W. Greuell (2006). Modelling the evolution of supraglacial lakes on the West Greenland ice-sheet margin. *Journal of Glaciology*, **52(179)**:608–618.

Lyzenga, D. (1978). Passive remote sensing techniques for mapping water depth and bottom features. *Applied Optics*, **17(3)**:379–383.

Lyzenga, D. R., N. P. Malinas, and F. J. Tanis (2006). Multispectral Bathymetry Using a Simple Physically Based Algorithm. *IEEE Transitions Geoscience and Remote Sensing*, **44(8)**:2251–2259.

Maritorena, S., A. Morel., and B. Gentili (1994). Diffuse reflectance of oceanic shallow waters: Influence of water depth and bottom albedo. *Limnology and Oceanography*, **39(7)**:1689–1703.

Masek, J., E. Vermote, N. Saleous, R. Wolfe, F. Hall, F. Huemmrich, F. Gao, J. Kutler, and L. T.K. (2012). Ledaps landsat calibration, reflectance, atmospheric correction preprocessing code. model product. available on-line [http://daac.ornl.gov] from oak ridge national laboratory distributed active archive center, oak ridge, tennessee, u.s.a.

McConnell, J., R. Arthern, E. Mosley-Thompson, C. Davis, R. Bales, R. Thomas, J. Burkhart, and J. Kyne (2000). Changes in greenland ice sheet elevation attributed primarily to snow accumulation variability. *Nature*, **406**:877–879.

McMillan, M., A. Nienow, P. Shepherd, T. Benham, and A. Sole (2007). Seasonal evolution of supra-glacial lakes on the Greenland Ice Sheet. *Earth and Planetary Science Letters*, **262**:484–492.

Metropolis, N. and S. Ulam (1949). The Monte Carlo Method. *Journal of the American Statistical Association*, **44(247)**:335–341.

Mishra, D., S. Narumalami, M. Lawson, and D. Rundquist (2004). Bathymetric mapping using ikonos multisprectral data. *GIScience and Remote Sensing*, **41(4)**:301–321.

Mitchell, S. (2009). Geoscience laser altimeter system: Validation of altimetry and atmospheric backscatter data. *University of Colorado at Boulder, ASEN 5235.*

Miura, T., H. Yosioka, K. Fujiiwara, and H. Yamamoto (2008). Intercomparison of aster and modis surface reflectance and vegetation index products for synergistic applications to natural resource monitoring. *Sensors*, **8**:2480–2499.

Mobley, C. (1994). *Light and Water: Radiative Transfer in Natural Waters.* San Diego: Academic Press.

Morassutti, M. and E. Ledrew (1996). Albedo and depth of melt ponds on sea-ice. *International Journal of Climatology*, **16**:817–838.

Mottram, R. and D. Benn (2009). Testing crevasse-depth models: a field study at Breiethamerjurjökull, Iceland. *Journal of Glaciology*, **55(192)**:746–752.

Nick, F., C. van der Veen, A. Vieli, and D. Benn (2010). A physically based calving model applied to marine outlet glaciers and implications for the glacier dynamics. *Journal of Glaciology*, **56(199)**:781–794.

Nye, J. (1957). The distribution of stress and velocity in glaciers and ice-sheets. *Proc. R. Soc. Lond., Ser. A*, **239(1216)**:113–133.

Otero, J., F. Navarro, C. Martin, M. Cuadrado, and M. Corcuera (2010). A three-dimensional calving model: numerical experiments on Johnsons Glacier, Livingston island, Antarctica. *Journal of Glaciology*, **56(196)**:200–214.

Palmer, S., A. Shepherd, P. Nienow, and I. Joughin (2011). Seasonal speedup of the greenland ice-sheet linked to routing of surface water. *Earth and Planetary Science Letters*, **302**:423–428.

Paterson, W. (1994). *The physics of Glaciers*. Butterworth-Heinemann, Oxford.

Pavlis, N., S. Holmes, S. Kenyon, and J. Factor (2008). An Earth Graviational Model to degree 2160: EGM2008. Pers. comm.

Philpot, W. (1989). Bathymetric mapping with passive multispectral imagery. *Applied Optics*, **28(8)**:1569–1578.

Ray, R. (1999). A global ocean tide model from topex/poseidon altimeter: Got99.2. *NASA Technical Memorandum*, **209478**:58 pp.

Reeh, N. (2008). A nonsteady-state firn-densification model for the percolation zone of a glacier. *Journal of Geophysical Research*, **113(F03023)**:1–13.

Rees, W. (1993). *Physical principles of remote sensing. Topics in Remote sensing 1.* Cambridge University Press.

Rignot, E., J. E. Box, E. Burgess, and E. Hanna (2008). Mass balance of the Greenland ice sheet from 1958 to 2007. *Geophysical Research Letters*, **35**:L20502.

Rignot, E. and P. Kanagaratnam (2006). Changes in the Velocity Structure of the Greenland Ice Sheet. *Science*, **311**(5763):986 – 990.

Sánchez del Río, C. (1989). *Análisis de errores.* EUDEMA Universidad: Textos de apoyo.

Ritcher, R. and D. Schäpfer (2012). *Atmospheric / Topographic Correction for Airborne Imagery. ATCOR-4 User Guide, Version 6.2 BETA.*

Russell., A., J. Carrivick, J. Ingeman-Nielsen, and M. Williams (2011). A new cycle of jökulhlaups at russell glacier, kangerdlugssuaq, west greenland. *Journal of Glaciology*, **57(202)**:238–246.

Sasgen, I., M. van den Broeke, J. Bamber, E. Rignot, L. Sørensen, B. Wouters, Z. Martinec, I. Velicogna, and S. Simonsen (2012). Timing and origin of recent regional ice-mass loss in greenland. *Earth and Planetary Science Letters*, **333-334**:293–303.

Schrama, E., B. Wouters, and B. Vermeersen (2011). Present day regional mass loss of greenland observed with satellite gravimetry. *Surveys in Geophysics*, **32**:377–385.

Schrama, E. J. O. and B. Wouters (2011). Revisiting Greenland ice sheet mass loss observed by GRACE. *Journal of Geophysical Research*, **116**:B02407.

Schutz, B. (2002). *Geoscience Laser Altimeter System (GLAS), Algorithm Theoretical Basis Document Version 3.0: Laser footprint location (geolocation) and surface profiles.* Spot Geolocation ATBD.

Schutz, B. and H. Zwally (2008). Icesast overview. laser ranging workshop. Pers. comm.

Schutz, B. E., H. J. Zwally, C. A. Shuman, D. Hancock, and J. P. DiMarzio (2005). Overview of the icesat mission. *Geophysical Research Letters*, **32**:L21S01.

Selmes, N. (2011). *Remote Sensing of Supraglacial Lakes on the Greenland Ice Sheet.* Ph.D. thesis, Department of Geography, Swansea Unviversity.

Selmes, N., T. Murray, and T. James (2011). Fast draining lakes on the Greenland Ice Sheet. *Geophysical Research Letters*, **38**:L15501.

Shepherd, A., A. Hubbard, P. Nienow, M. King, M. McMillan, and I. Joughin (2009). Greenland ice sheet motion coupled with daily melting in late summer. *Geophysical Research Letters*, **36(L01501)**:1–4.

Shuman, C. A., H. J. Zwally, B. E. Schutz, A. Brenner, and DiMarzio (2006). Icesat antarctic elevation data: Preliminary precision and accuracy assessment. *Geophysical Research Letters*, **33**:L07501.

Siegfried, M., R. Hawley, and J. Burkhart (2011). High-resolution ground-based gps measurements show intercampaign bias in icesat elevation data near summit, greenland. *IEEE Transactions on Geoscience and Remote Sensing*, **49(9)**:3393–3400.

Sirota, J., S. Bae, P. Millar, D. Mostofi, and C. Webb (2005). The transmitter pointing determination in the geoscience laser altimeter system. *Geophysical Research Letters*, **32**:L22S11.

Slobbe, D., P. Ditmar, and R. Lindenbergh (2009). Estimating the rates of mass change, ice volume change and snow volume change in greenland from icesat and grace data. *Geophysical Journal International*, **176**:95–106.

Smith, R. and K. Baker (1981). Optical properties of the clearest natural waters. *Applied Optics*, **20(2)**:177–184.

Sneed, W. and G. Hamilton (2011). Validation of a method for determining

the depth of glacial melt ponds using satellite imagery. *Annals of Glaciology*, **52(59)**:15–22.

Sneed, W. A. and G. S. Hamilton (2007). Evolution of melt pond volume on the surface of the Greenland Ice Sheet. *Geophysical Research Letters*, **34**:1–4.

Sørensen, L., S. Simonsen, K. Nielsen, P. Lucas-Picher, G. Spada, G. Adalgeirsdottir, and C. Forsberg, R.mand Hvidberg (2011). Mass balance of the greenland ice sheet (2003-2008) from icesat data - the impact of interpolation, sampling and firn density. *The Cryosphere*, **5**:173–186.

Stearns, L. and G. Hamilton (2007). Rapid volume loss from two east greenland outlet glaciers quantified using repeat stereo satellite imagery. *Geophysical Research Letters*, **34(L05503)**:1–5.

Stumpf, R., K. Holderied, and M. Sinclair (2003). Determination of water depth with high-resolution satellite imagery over variable bottom types. *Limnology and Oceanography*, **48(1)**:547–555.

Sundal, A., A. Shepherd, P. Nienow, E. Hanna, S. Palmer, and P. Huybrechts (2009). Evolution of supra-glacial lakes across the greenland ice sheet. *Remote Sensing of Environment*, **113**:2164–2171.

Sundal, A., A. Shepherd, P. Nienow, E. Hanna, S. Palmer, and P. Huybrechts (2011). Melt-induced speed-up of greenland ice sheet offset by efficient subglacial drainage. *Nature*, **7331**:521–524.

Tedesco, M., X. Fettweis, M. R. van den Broeke, R. S. W. van de Wal, C. J. P. P. Smeets, W. van de Berg, M. Serreze, and J. Box (2011). The role of albedo and accumulation in the 2010 melting record in greenland. *Environmental Research Letters*, **6**:1–6.

Tedesco, M., M. Lüthje, K. Steffen, N. Steiner, X. Fettweis, I. Willis, N. Bayou, and A. Banwell (2012). Measurement and modeling of ablation of the bottom of supraglacial lakes in western greenland. *Geophysical Research Letters*, **39(L02502)**:1–5.

Tedesco, M. and N. Steiner (2011). In-situ multispectral and bathymetric measurements over a supraglacial lake in western greenland using a remotely controlled watercraft. *The Cryosphere*, **5**:445–452.

Thomas, R., C. Davis, E. Frederick, W. Krabill, Y. Li, S. Manizade, and C. Martin (2008). A comparison of Greenland ice-sheet volume changes derived from altimetry measurements. *Journal of Glaciology*, **54**(185):203–212.

Thome, K. (1999). Algorithm theoretical basis document for aster level 2b1 - surface radiance and aster level 2b5 - surface reflectance.

Thome, K. (2001). ASTER Higher-Level Product User Guide, Version 2.0, Surface Reflectance. *JPL*, **D**:20062.

Thome, K., F. Palluconi, T. Takashima, and K. Masuda (1998). Atmospheric correction of aster. *IEEE Transactions on Geoscience and Remote Sensing*, **36(4)**:1199–1211.

Tonooka, H. (2008). Aster night-time cloud mask database using modis cloud mask (mod35) produts. *Proc. SPIE*, **7107**.

Urban, T. and B. Schutz (2005). Icesat sea level comparisons. *Geophysical Research Letters*, **32**:L23S10.

van der Veen, C. (1998a). Fracture mechanics approach to penetration of bottom crevasses on glaciers. *Cold Regions Science and Technology*, **27**:213–223.

van der Veen, C. (1998b). Fracture mechanics approach to penetration of surface crevasses on glaciers. *Cold Regions Science and Technology*, **27**:31–47.

van der Veen, C. (2007). Fracture propagation as means of rapidly transfering surface meltwater to the base of glaciers. *Geophysical Research Letters*, **34(L01501)**:1–5.

Velicogna, I. (2009). Increasing rates of ice mass loss from the Greenland and Antarctic ice sheets revealed by GRACE. *Geophysical Research Letters*, **36**:L19503.

Vermote, E. F., N. El Saleous, C. Justice, J. Kaurman, J. Privette, L. Remer, J. Roger, and D. Tanré (1997). Atmospheric correction of visible o middle-infrared eos-modis data over land surfaces: Background, operational algorithm and validation. *Journal of Geophysical Research*, **102(14)**:17131–17141.

Vermote, E. F. and A. Vermeulen (April 1999). MODIS Algorithm Technical Background Document, Atmoshperic correction algorithm: Spectral reflectances (MOD09). *NASA contract NAS5-96062*:Version 4.0.

van de Wal, R. S. W., W. Boot, M. R. van den Broeke, C. J. P. P. Smeets, C. H. Reijmer, J. J. A. Donker, and J. Oerlemans (2008). Large and Rapid Melt-Induced Velocity Changes in the Ablation Zone of the Greenland Ice Sheet. *Science*, **321**(5885):111–113.

Wang, X., X. Cheng, P. Gong, H. Huang, Z. Li, and X. Li (2011). Earth science applications of icesat/glas: a review. *International Journal of Remote Sensing*, **32(23)**:8837–8864.

Weertman, J. (1973). Can a water-filled crevasse reach the bottom surface of a glacier? *IASH Publ. 95 (Symposium at Cambridge 1969 - Hydrology of Glaciers)*:139–145.

Wientjes, I. and J. Oerlemans (2010). An explanation for the dark region in the western melt zone o the greenland ice sheet. *The Cryosphere*, **4**:261–268.

Wientjes, I., R. Van de Wal, G. Reichart, A. Sluijs, and J. Oerlemans (2011). Dust from the dark region in the western ablation zone of the greenland ice sheet. *The Cryosphere*, **5**:589–601.

Wingham, D. (2000). Small fluctuations in density and thickness of a dry firn column. *Journal of Glaciology*, **46(154)**:399–411.

Yamaguchi, Y., A. Kahle, H. Tsu, T. Kawakami, and M. Pniel (1998). Overview of advanced spaceborne thermal emission and reflection radiometer (aster). *IEEE Transactions on Geoscience and Remote Sensing*, **36(4)**:1062–1071.

Yi, D., H. J. Zwally, and X. Sun (2005). Icesat measurement of greenland ice sheet surface slope and roughness. *Annals of Glaciology*, **42**:83–89.

Zaneveld, J. and E. Boss (2003). The influence of bottom morphology on reflectance: Theory and two-dimensional geometry model. *Limnology and Oceanography*, **48(1)**:374–379.

Zwally, H., W. Abdalati, T. Herring, K. Larson, J. Saba, and K. Steffen (2002a). Surface melt-induced acceleration of greenland ice-sheet flow. *Science*, **297**(5579):218–222.

Zwally, H. J., B. Schutz, W. Abdalati, J. Abshire, C. Bentley, A. Brenner, J. Bufton, J. Dezio, D. Hancock, D. Harding, T. Herring, B. Minster, K. Quinn, S. Palm, J. Spinhirne, and R. Thomas (2002b). Icesat's laser measurements of polar ice, atmosphere, ocean, and land. *Journal of Geodynamics*, **34**:405–445.

Appendix A

Lake evolution from MODIS

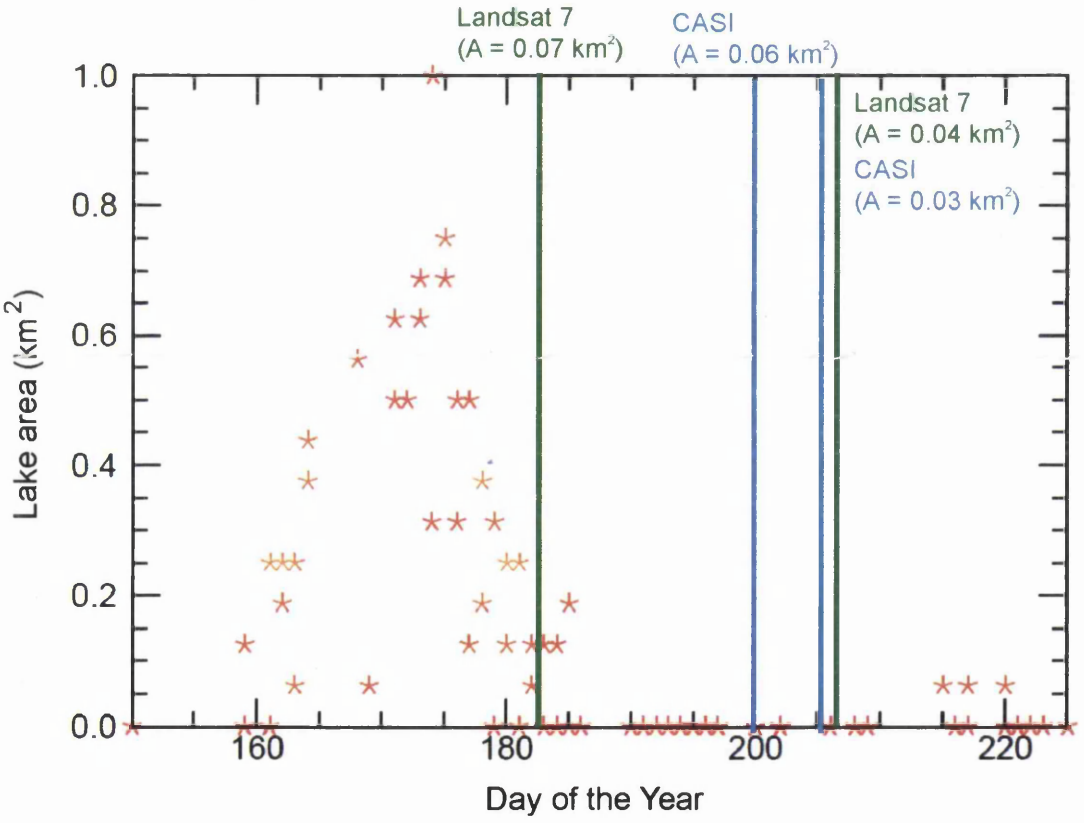

Figure A.1: Figure showing the area distribution of the supra-glacial lake studied in Chapter 7. The area distribution was derived from MODIS images for 2007 melt season. Blue lines correspond with the CASI scenes used to estimate depth from the water reflectance model and also lake area derived from is shown. Green lines correspond with the Landsat 7 scenes used to estimate depth from the water reflectance model and also lake area derived from is shown Figure modified from Selmes (2011).

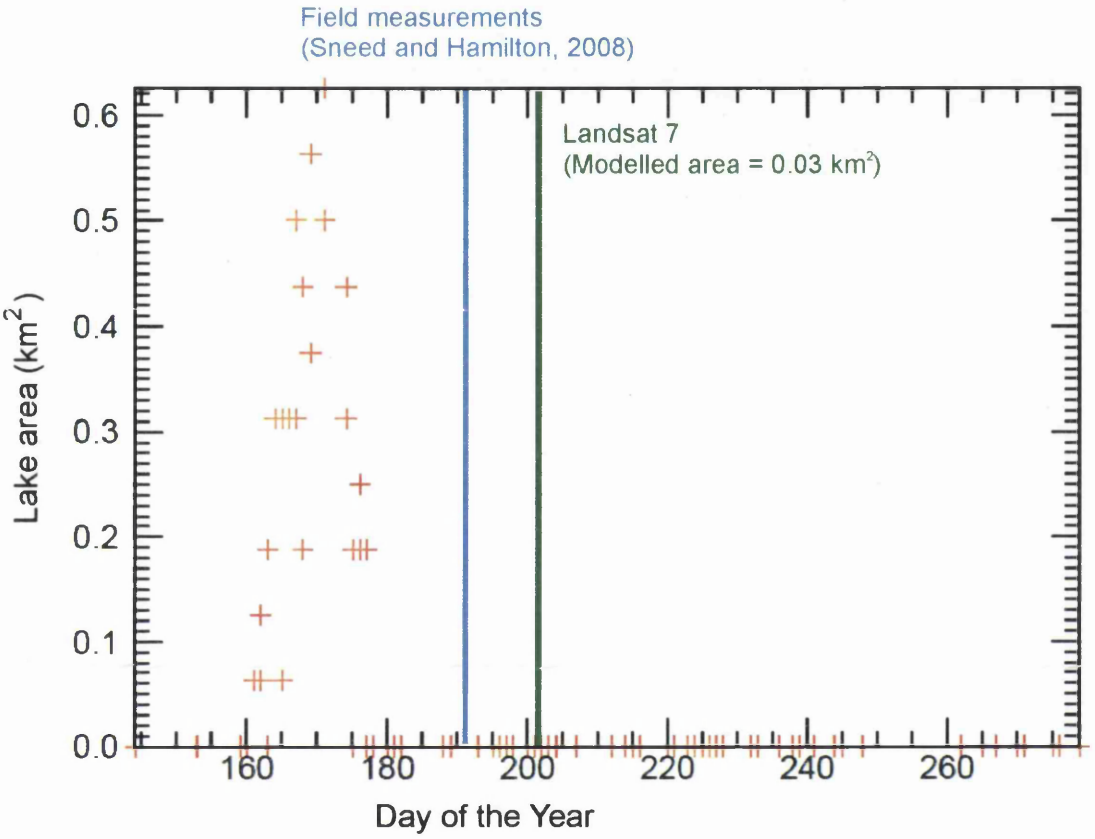

Figure A.2: Figure showing the area distribution of the supra-glacial lake studied in Chapter 7. The area distribution was derived from MODIS images for 2008 melt season. The blue line corresponds with the day of the field observations by Sneed and Hamilton (2011). The green lines corresponds with the Landsat 7 scenes used to estimate depth from the water reflectance model and also lake area derived from is shown Figure modified from Selmes (2011).

Appendix B

Drainage evolution from MODIS

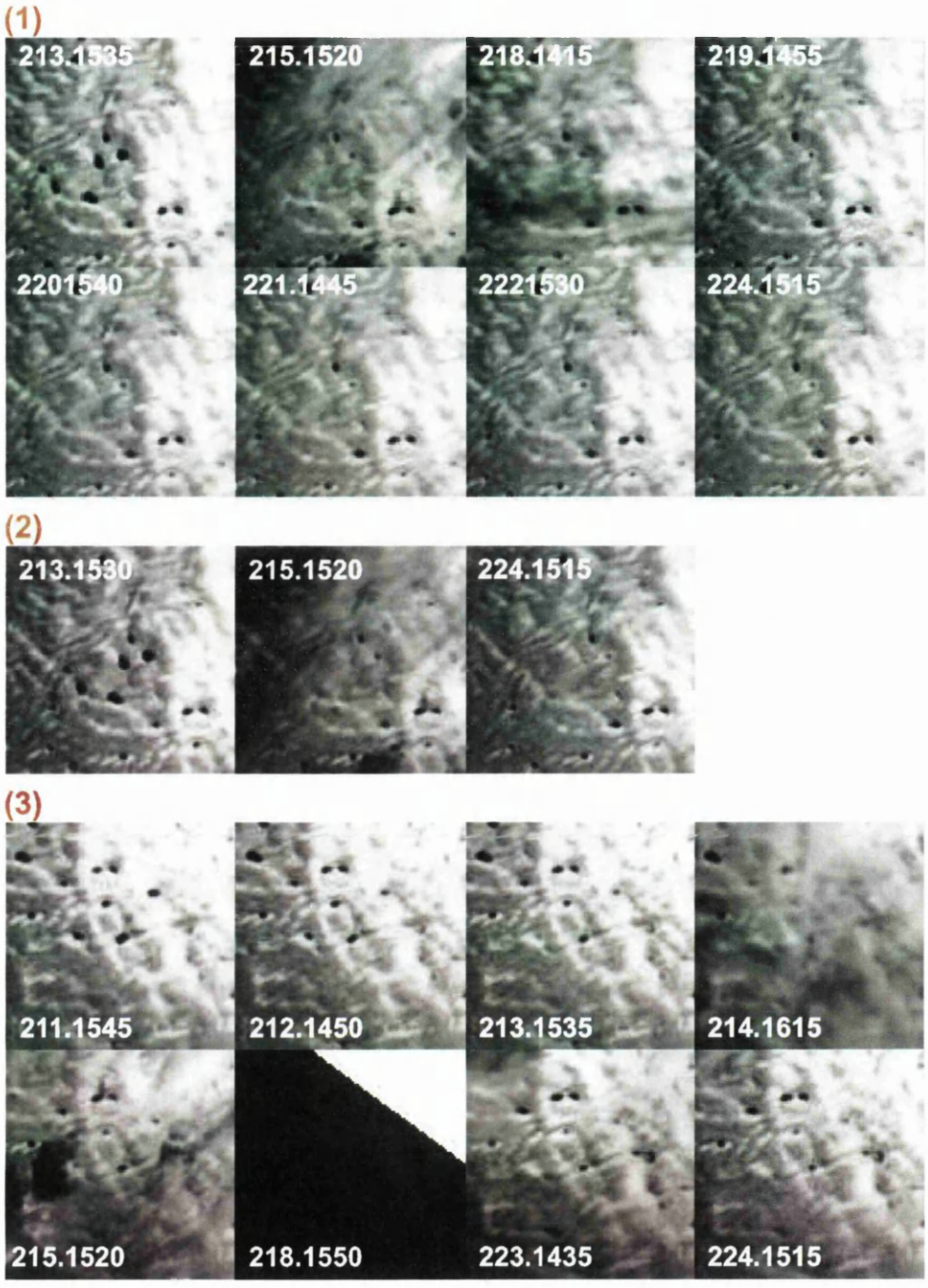

Figure B.1: MODIS scenes showing the evolution of the twelve lakes studied in Section 8.5 (Chapter 8). The lake number in the graphs corresponds with the numbers in Figure 8.11. From these snapshots the day that the lakes drained was approximated. Continued in Figures B.2, B.3, B.4, and B.5.

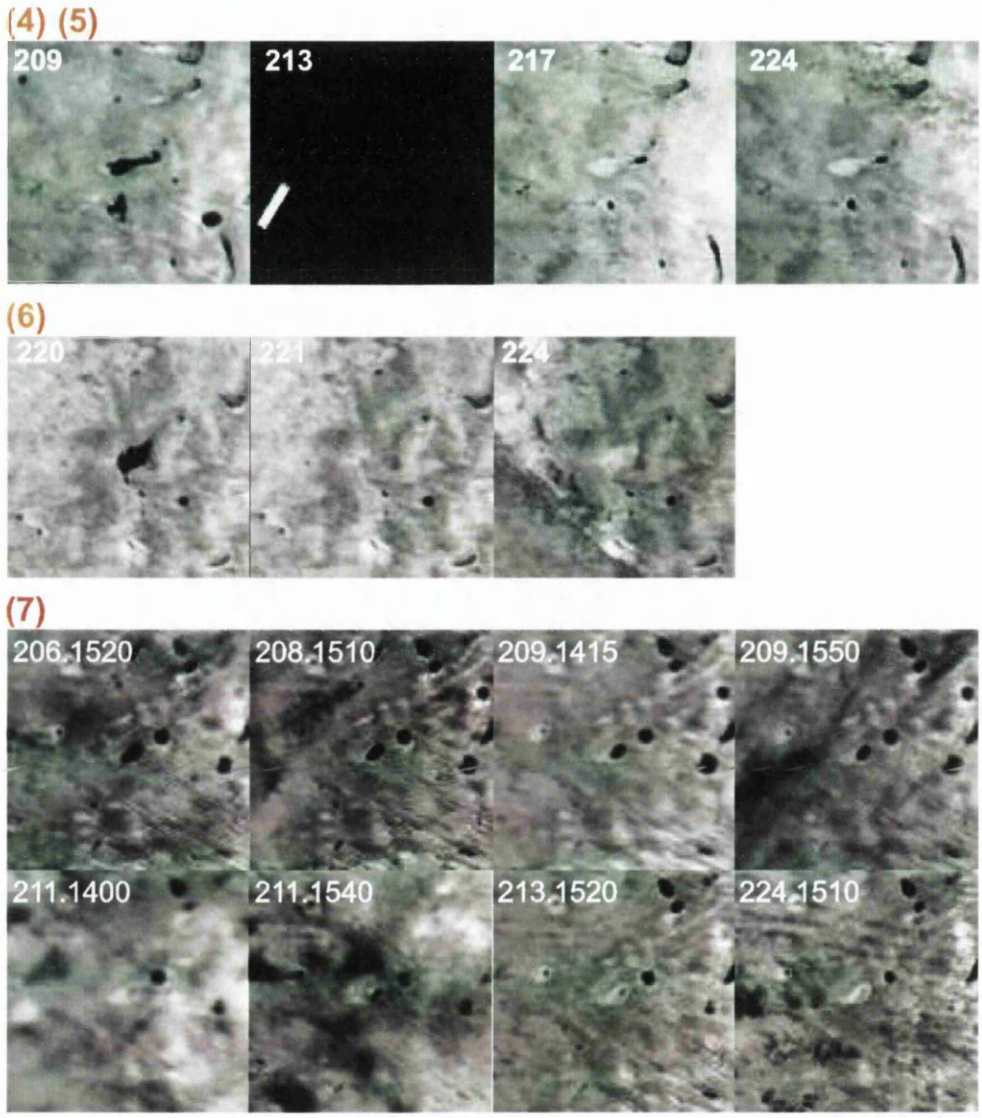

Figure B.2: Continued Figure B.1. MODIS scenes showing the evolution of the twelve lakes studied in Section 8.5 (Chapter 8). The lake number in the graphs corresponds with the numbers in Figure 8.11. From these snapshots the day that the lakes drained was approximated (continued overleaf).

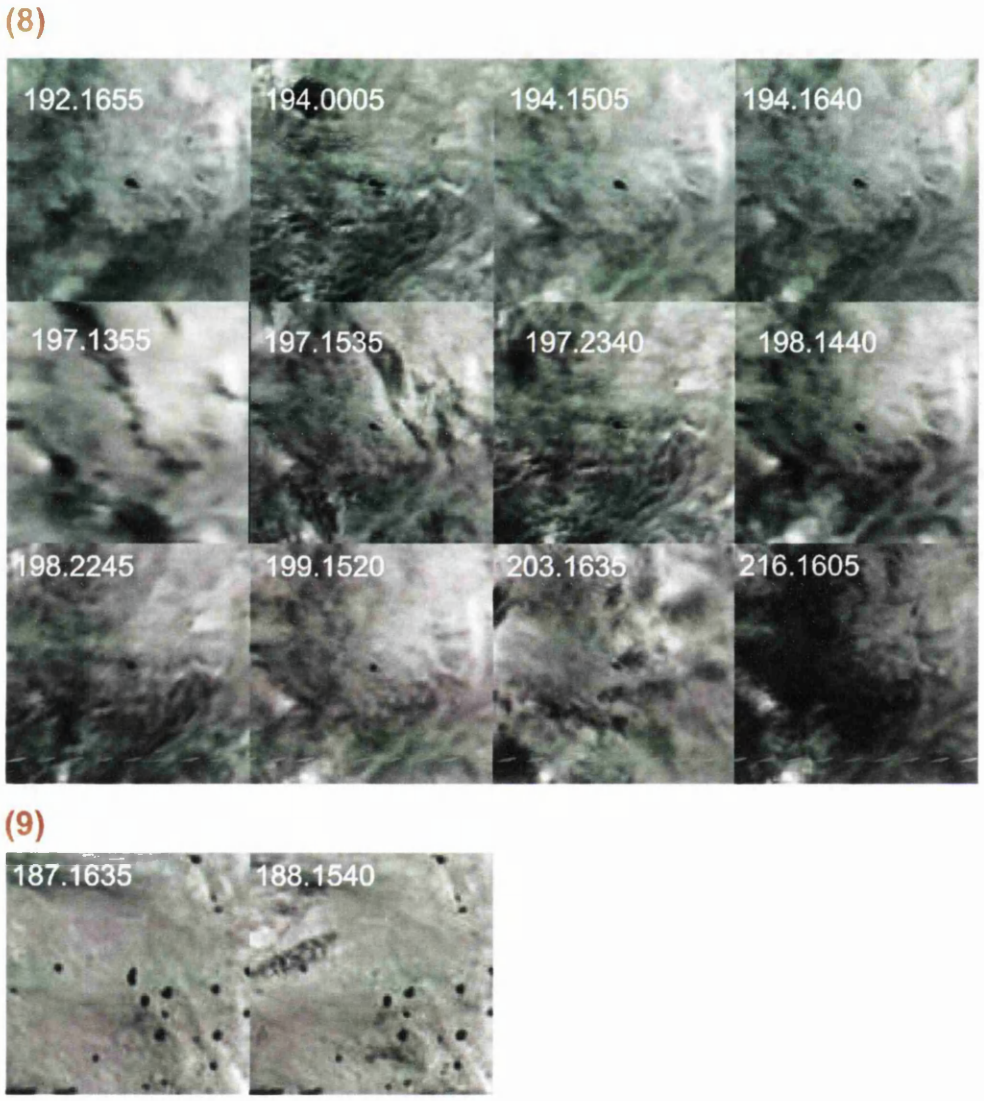

Figure B.3: Continued Figure B.1. MODIS scenes showing the evolution of the twelve lakes studied in Section 8.5 (Chapter 8). The lake number in the graphs corresponds with the numbers in Figure 8.11. From these snapshots the day that the lakes drained was approximated.

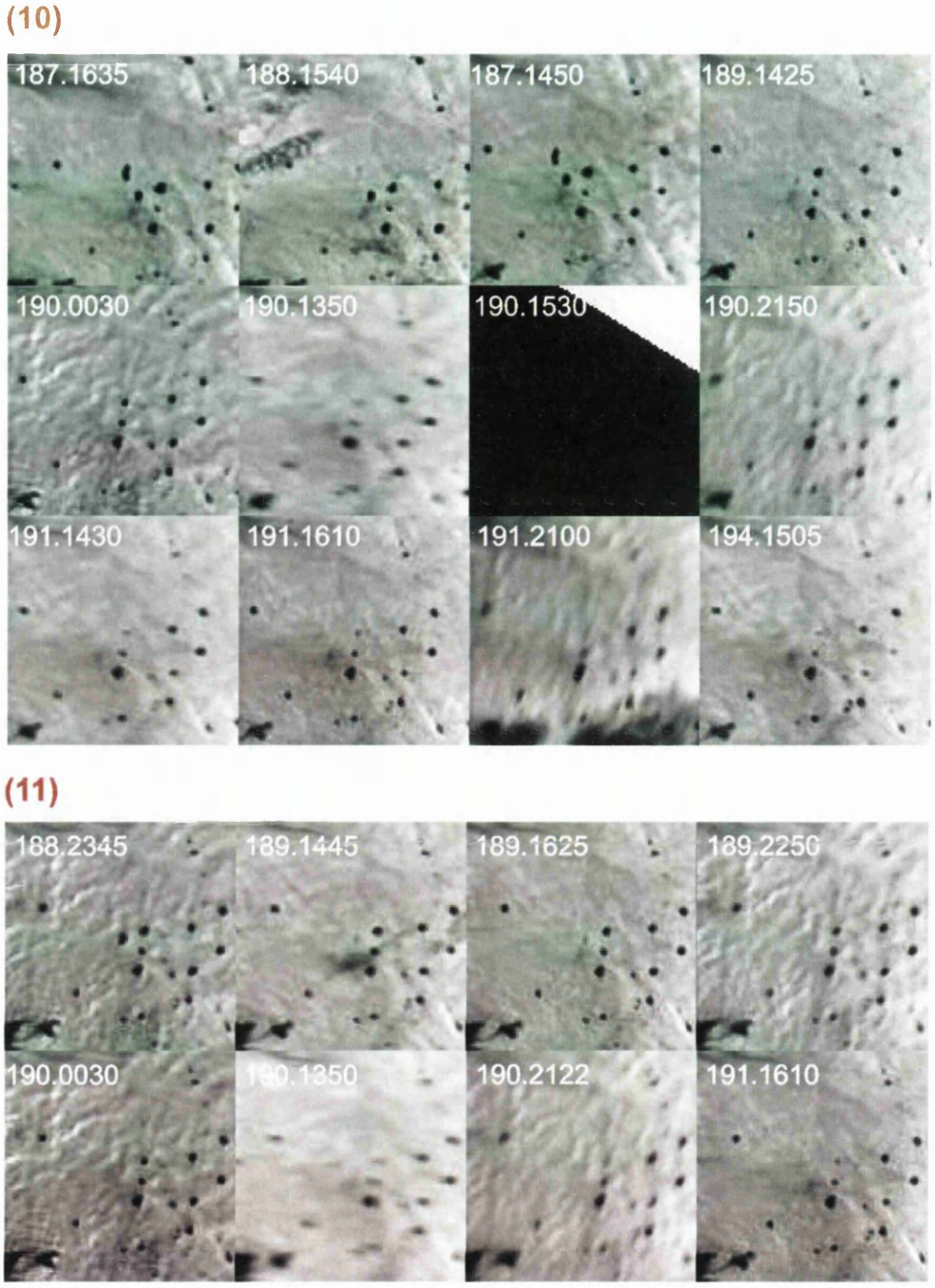

Figure B.4: Continued Figure B.1. MODIS scenes showing the evolution of the twelve lakes studied in Section 8.5 (Chapter 8). The lake number in the graphs corresponds with the numbers in Figure 8.11. From these snapshots the day that the lakes drained was approximated.

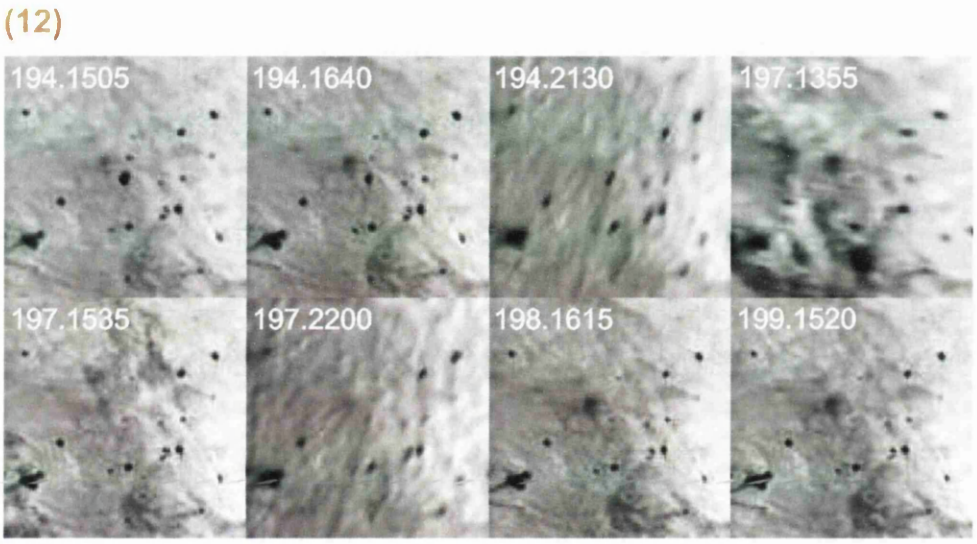

Figure B.5: Continued Figure B.1. MODIS scenes showing the evolution of the twelve lakes studied in Section 8.5 (Chapter 8). The lake number in the graphs corresponds with the numbers in Figure 8.11. From these snapshots the day that the lakes drained was approximated.

Appendix C

Conical ratio

Table C.1: Table summarising the different lake area, volume and depth obtained from this study; the last three columns correspond to the diameter, depth and diameter-depth ratio that those lakes would have assuming a conical shape volume (using A and V from column one and two), following Krawczynski *et al.* (2009). These results were introduced in Section 8.6 (Chapter 8). Continued in Table C.2.

A (km^2)	V (x10^6 m^3)	z_{max} (m)	$\phi_{conical}$ (m)	$z_{conical}$ (m)	ϕ-z ratio
98.93	3.87	7.1	1122	11.7	96:1
31.75	0.62	3.8	636	5.8	110:1
51.30	1.54	5.0	808	9.0	90:1
89.01	2.49	4.3	1065	8.4	127:1
19.10	0.21	2.5	493	3.3	152:1
157.32	2.28	3.3	1415	4.4	325:1
17.17	0.36	5.6	468	6.3	74:1
59.56	0.13	1.3	871	0.7	1304:1
52.74	0.79	2.5	819	4.5	183:1
49.52	0.66	4.9	794	4.0	200:1
36.52	3.64	3.7	682	30.0	23:1
15.64	0.22	3.3	446	4.3	104:1
15.84	0.29	3.7	449	5.5	82:1
49.37	0.92	4.3	793	5.6	141:1
32.27	0.76	5.2	641	7.0	91:1
67.57	1.023	3.3	928	4.5	204:1
48.40	0.65	4.0	785	4.0	196:1
105.10	1.95	6.2	1157	5.6	208:1
73.08	3.06	7.7	965	12.6	77:1
29.59	0.89	5.9	614	9.03	68:1
108.79	3.64	5.2	1177	10.0	117:1
62.78	1.66	5.6	894	7.9	113:1

Table C.2: Continued Table C.1. Table summarising the different lake area, volume and depth obtained from this study; the last three columns correspond to the diameter, depth and diameter-depth ratio that those lakes would have assuming a conical shape volume (using A and V from column one and two), following Krawczynski *et al.* (2009). These results were introduced in Section 8.6 (Chapter 8).

A (km^2)	V (x10^6 m^3)	z_{max} (m)	$\phi_{conical}$ (m)	$z_{conical}$ (m)	ϕ-z ratio
43.04	1.11	7.1	7403	7.7	96:1
232.52	7.02	6.9	1721	9.1	190:1
128.12	0.66	6.7	1277	1.5	831:1
66.04	1.89	6.2	917	8.6	107:1
62.33	1.90	5.7	891	9.2	97:1
365.56	26.63	12.5	2157	21.9	99:1
114.89	4.53	7.5	1209	11.8	102:1
89.15	3.56	7.7	1065	12.0	89:1
130.03	5.86	8.0	1287	13.5	95:1
183.89	7.63	7.9	1530	12.4	123:1
319.12	16.60	9.4	2016	15.6	129:1
21.58	0.78	7.1	524	10.9	48:1
93.94	2.74	5.8	1094	8.8	125:1
245.52	5.99	7.0	1768	7.3	241:1
61.00	2.11	9.3	881	10.4	85:1
51.84	1.64	6.6	812	9.5	86:1
108.27	2.55	5.4	1174	7.05	166:1